Title
Cloud Formation and Circulation in Planetary Tropospheres from Remote-Sensing Data

Author
Molter, Edward Mischel

Publication Date
2022

Peer reviewed|Thesis/dissertation

Cloud Formation and Circulation in Planetary Tropospheres from Remote-Sensing Data

by

Edward Mischel Molter

A dissertation submitted in partial satisfaction of the

requirements for the degree of

Doctor of Philosophy

in

Astrophysics

in the

Graduate Division

of the

University of California, Berkeley

Committee in charge:

Professor Imke de Pater, Co-chair
Professor William Drew Collins, Co-chair
Assistant Professor Courtney Dressing
Associate Professor William Boos

Summer 2022

Cloud Formation and Circulation in Planetary Tropospheres from Remote-Sensing Data

Abstract

Cloud Formation and Circulation in Planetary Tropospheres from Remote-Sensing Data

by

Edward Mischel Molter

Doctor of Philosophy in Astrophysics

University of California, Berkeley

Professor Imke de Pater, Co-chair

Professor William Drew Collins, Co-chair

The technology used to observe solar system planets continues to advance, increasing the spatial resolution, time cadence, and spectral coverage of observations and permitting the discovery of new phenomena in the atmospheres of worlds near and far. Comparative planetology is a powerful framework to help characterize and explain these newly-discovered phenomena: the similarities and differences between the composition, structure, and dynamics of planetary atmospheres test the robustness of the theories we use to understand and predict the weather and climate of atmospheres. This dissertation uses a comparative planetology framework to understand the physical processes underlying new observations of the atmospheres of Uranus and Neptune and new statistical analyses of observed storms on Earth. Although qualitatively dissimilar, the atmospheres of Uranus, Neptune, and Earth lie in a similar fluid-dynamical regime in many respects, allowing much of our physical intuition to translate across those three atmospheres. In particular, this dissertation focuses on using remote-sensing data to probe processes relevant to cloud formation and precipitation.

Higher bulk densities and strong enrichment in carbon and oxygen distinguish Uranus and Neptune from the gas giants Jupiter and Saturn, placing them into their own category, the ice giants. Exoplanet statistics reinforce this distinction: a gap in the size distribution of known exoplanets has been observed between the Jupiter-sized and Neptune-sized exoplanets. Uranus and Neptune are therefore of primary importance for understanding the different types of worlds that fill our galaxy; however, their distance from Earth also makes them very challenging to study in detail. The first three chapters of this dissertation tackle that observational challenge. Using near-infrared data from Keck Observatory and optical data from the Hubble Space Telescope (HST), I characterize a newly-observed storm at the equator of Neptune, including derivations of drift rates from cloud tracking and cloud-top pressures from radiative transfer modeling. I then apply the physics of deep convection

and planetary waves to infer the drivers of the storm. Making use of millimeter-wavelength observations from the Atacama Large (sub)-Millimeter Array (ALMA) and mid-infrared observations from the Very Large Telescope (VLT), I observe the thermal component of the Uranian ring system for the first time. I apply the radiative transfer equation to the ring particles to derive their surface temperature and show that they rotate slowly compared to their radiative cooling time. I use the same dataset in conjunction with centimeter-wavelength Very Large Array (VLA) data to study the deep troposphere of Uranus from 1-50 bar. Applying intuition based on Earth's Hadley-Walker circulation, I link the observed enrichment and depletion of volatile species in Uranus's deep troposphere to Uranus's planetary-scale circulation.

Although the instrumentation and radiative transfer models are similar between observations of Earth and the ice giants, the technical challenges that arise in observing these bodies are somewhat opposite. Earth observations exemplify a data-rich regime in which millions of new data points are recorded every hour at spatial resolutions of order 1 kilometer, whereas ice giant studies are comparatively data-starved: $\sim$10 images at 100-kilometer resolution may constitute a full dataset. The second half of this dissertation tackles the data-rich observational challenge, concerning itself with the observed statistics of extratropical extreme storms on Earth from remote-sensing data. Using Doppler radar data, I show that the return values of extreme precipitation are strongly autocorrelated over the Eastern and Midwestern United States up to scales of $\gtrsim$100 kilometers, and that rain gauges can accurately estimate extreme precipitation only if interpolated with a particular eye toward capturing extremes. I then compile a suite of hourly data at 8-km resolution over the Eastern and Midwestern United States that simultaneously probes the synoptic-scale dynamical context of storms, the structure of clouds within storms, and the precipitation produced by storms. I demonstrate the utility of this unique data combination by examining the precipitation efficiency of storms, showing that precipitation efficiency increases with equivalent potential temperature over the contiguous United States (CONUS) in both the warm and cool seasons.

Taken as a whole, this dissertation showcases the ways in which recent advances in remote sensing technology and computational power can be applied to study atmospheres across the solar system, with a particular focus on cloud and precipitation processes. The types of questions that can be answered in the data-rich regime underscore the massive potential for advances in our understanding of the Solar System planets (and exoplanets) as data from new observatories and missions arrive in the next decades.

Contents

List of Figures

List of Tables

Acknowledgments

Some of the data presented herein were obtained at the W. M. Keck Observatory, which is operated as a scientific partnership among the California Institute of Technology, the University of California and the National Aeronautics and Space Administration. The Observatory was made possible by the generous financial support of the W. M. Keck Foundation.

I wish to recognize and acknowledge the very significant cultural role and reverence that the summit of Maunakea has always had within the indigenous Hawaiian community. I am most fortunate to have the opportunity to conduct observations from this mountain.

Portions of this research are based on observations made with the NASA/ESA Hubble Space Telescope (OPAL program GO14756). obtained from the data archive at the Space Telescope Science Institute. STScI is operated by the Association of Universities for Research in Astronomy, Inc. under NASA contract NAS 5-26555

Some of the data presented herein were obtained at Lick Observatory. Research at Lick Observatory is partially supported by a generous gift from Google.

Partial support for the work presented in Chapter 2 was provided by the Keck Visiting Scholar Program at W.M. Keck Observatory.

The work presented in Chapter 2 was supported in part by the National Science Foundation, NSF Grant AST-1615004 to UC Berkeley.

I thank the referees of the published version of Chapter 2, Amy Simon and one anonymous person, for their insightful comments, which substantially improved the manuscript.

I thank Conor McPartland, as well as the Keck Observing Assistants, for executing our volunteer observing program during their observing time at Keck Observatory.

I thank Geoff Chen, Ian Crossfield, Donald Gavel, and Robert de Rosa for executing our volunteer observing program during their observing time at Lick Observatory.

This thesis makes use of the following ALMA data: ADS/JAO.ALMA#2017.1.00855.S. ALMA is a partnership of ESO (representing its member states), NSF (USA) and NINS (Japan), together with NRC (Canada), MOST and ASIAA (Taiwan), and KASI (Republic of Korea), in cooperation with the Republic of Chile. The Joint ALMA Observatory is operated by ESO, AUI/NRAO and NAOJ. The National Radio Astronomy Observatory (NRAO) is a facility of the National Science Foundation operated under cooperative agreement by Associated Universities, Inc.

This thesis makes use of thermal-infrared VISIR observations acquired at the ESO Very Large Telescope Paranal UT3/Melipal Observatory, with program ID 0101.C-0073(B)

This thesis makes use of the following VLA data: VLA/2014-06-232. The National Radio Astronomy Observatory (NRAO) is a facility of NSF operated under cooperative agreement by Associated Universities, Inc. VLA data used in this report are available from the NRAO Science Data Archive at https://archive.nrao.edu/archive/advquery.jsp.

The research presented in Chapters 3 and 4 was supported in part by NASA Grant NNX16AK14G through the Solar System Observations (SSO) program to the University of California, Berkeley.

The research presented in Chapters 3 and 4 was supported in part by NRAO Student Observing Support grant #SOSPA6-006.

I thank the staff at the 2018 NRAO Synthesis Imaging Workshop for providing advice on calibration of the ALMA data used in Chapters 3 and 4.

The research presented in Chapters 5 and 6 was supported by the Director, Office of Science, Office of Biological and Environmental Research of the U.S. Department of Energy under Contract No. DE-AC02-05CH11231 and used resources of the National Energy Research Scientific Computing Center (NERSC), also supported by the Office of Science of the U.S. Department of Energy, under Contract No. DE-AC02-05CH11231.

I thank the staff of the California-Nevada, Colorado Basin, and Northwest NOAA River Forecast Centers, particularly John Lhotak, Dan Kozlowski, and Kyle Lerman, for their help accessing data and implementing the Mountain Mapper algorithm presented in Chapter 5.

I thank Bill Boos and Travis O'Brien for their detailed and insightful comments on Chapter 5, which substantially improved that chapter.

This thesis would never have existed without:

Dr. Imke de Pater, my primary adviser on the planetary science sections of this thesis, for too many things to list, but in particular for letting me explore and guiding me back when I got lost.

Dr. Bill Collins, my primary adviser on the Earth science sections of this thesis, for too many things to list, but in particular for giving me his full confidence even when I didn't have confidence in myself.

Drs. Courtney Dressing and Bill Boos, for agreeing to actually read this thesis, and for their very constructive comments in my qualifying exam and before submission.

Dr. John Cannon, my first adviser in science, for giving me a career direction, seeking out opportunities for my professional growth, writing recommendation letters, and modeling professional excellence and etiquette.

Drs. Conor Nixon, Colin Dundas, and Carlos Alvarez, the other three advisers I've had in science; each was fun to work with, made me feel welcome and cared for during our relatively short time together, and went the extra mile to help my career afterward.

Chris "Muti" Möckel, my closest friend at work, for always finding time to read my proposals, to argue about scientific topics, to grab a beer and commiserate, or almost die of exhaustion descending Tunemah Peak.

Statia, Katherine, Josh, and the other current and former members of Imke's research group, for productive scientific discussions, helpful advice, and companionship at AGU and DPS meetings.

The CASCADE team, for productive scientific discussions.

The faculty and staff of the Berkeley Astronomy and EPS departments, for organizing engaging classes, seminars, and workplace social events.

Maggie, Will, Mom, Dad, and Kayla—my family—for too many things to write down; let's just say for your love through the whole six years.

Fatima, David, Kareem, Kara, and Siyao, my first-year cohort, for helping to pull me through this, especially in the early stages.

Alyssa, Nick, Nico, Caroline, Jane, Tom, Wren, Scott, Drew, Jasper, Kat, Sky, Ellen, Mark, Maggie, Tina, Adam, and all of my other Bay Area friends, for fun adventures that kept me sane.

The Berkeley Ironworks, Great Western Power Company, and Lake Tahoe climbing communities, for giving me a home away from home.

Chapter 1

Background: Physics of Planetary Tropospheres

In the five main chapters of this thesis, I discuss three different planets (Earth, Uranus, and Neptune) and a planetary ring system, each observed with different instruments and to answer different specific science questions. Taking this information at face value, this document epitomizes the so-called staple thesis: it is much more easily read as a collection of scientific short stories than as a novel, and each of the five chapters introduces itself separately. Basic physics, though, cannot be avoided no matter which planet you are on, and despite these seemingly scattered topics, this thesis can also fairly be said to focus primarily on understanding cloud and precipitation processes at various spatial and temporal scales using remote-sensing data. In this introductory chapter, I remind the reader of the basic physics universal to all planets with atmospheres and to all remote-sensing observations. This chapter concerns primarily radiative transfer and atmospheric circulation, which, fittingly, parrots the two required courses for all astronomy graduate students at Berkeley: radiative processes and fluid dynamics.

The first section of this background chapter (Section 1.1) focuses on the global circulation patterns that lead to instabilities and the generation of storm systems. I discuss the similarities and differences in the fluid-dynamical regimes present on the three planets of interest, and their consequences for the observed global circulation patterns. These concepts are critical both to understanding precipitation on Earth from a statistical point of view (as is done in Chapters 5 and 6), and to interpret observations of Uranus and Neptune when the resolution element of the telescope is insensitive to scales smaller than a few hundred kilometers (as is the case in the other three chapters). In the second section (Section 1.2), I focus on the slightly smaller spatial scales of convective cells themselves, discussing moist convection and how deep convective storms behave energetically. These concepts are expanded upon in the Discussion section of Chapter 2 in particular, as that chapter tries to understand the origin of a large and unusual equatorial storm on Neptune. In Section 1.3, I focus on how clouds and precipitation form at microphysical scales, which is particularly relevant to the cloud models I apply to Uranus's atmosphere in Chapter 4 and to the combined

precipitation and cloud data presented in Chapter 6. Finally, Section 1.4 presents the basics of radiative transfer modeling required to observe and interpret all of these phenomena from remote-sensing data. This section also ties in Chapter 3, seemingly the odd duck, which presents radiative transfer calculations applied to a swarm of small airless bodies in space (i.e., a planetary ring).

This background chapter presents many well-accepted ideas in the field of atmospheric science that can be found in almost any atmospheric science textbook or lecture notes. These safely fall under the purview of "common knowledge" in the field and are not cited individually. I referenced the following textbooks while writing this chapter: Bohren et al. (2006), Holton (1973), Marshall et al. (1989), Rybicki et al. (1991), Thomas et al. (2002), Vallis (2019), and Wallace and Hobbs (2006). The interested reader is referred to those sources for more detailed derivations and discussion.

1.1 Large-Scale Atmospheric Circulation

The motion of a planetary atmosphere is governed by the fluid equations for a rotating thin shell. These equations, their special cases, and their implications for the atmospheric system are entire sub-fields on their own, and the reader is referred to any atmospheric science textbook for more details; a few good ones are listed above. Instead of repeating derivations here, I make a few comments on the similarities and differences between Earth, Uranus, and Neptune from a fluid dynamical standpoint, with an eye toward the inception of precipitation events. Some first-order comparisons between these three planets are given in Table 1.1, and they show that all three planets are in a similar dynamical regime in many ways, being relatively fast rotators with similar gravitational accelerations and atmospheric stratifications. On the other hand, Earth's atmosphere is warmer, denser, and has lower typical wind speeds than either Uranus or Neptune; the implications of some of these differences are discussed below.

Earth's atmospheric circulation is forced by the uneven solar heating of the planet. Near the poles, more energy is emitted than absorbed, whereas near the equator, more energy is absorbed than emitted. Therefore, energy must be transported meridionally to maintain radiative balance, and the atmospheric circulation carries out that transport. The heat and moisture transport from the tropics to the extratropics takes place primarily in longitude-resolved eddies (Barry et al. 2002); the coherent high-moisture filamentary structures carrying out over 90% of Earth's meridional vapor transport are known as atmospheric rivers (Ralph et al. 2004; Zhu et al. 1998). These eddies arise from baroclinic instability, and their characteristic size is given by the Rossby deformation radius:

$$L_{Ro} = \frac{NH}{f} \tag{1.1}$$

where N is the Brunt-Väisälä frequency ($N^2 = (g/\theta)(d\theta/dz)$ for potential temperature θ), $H = RTg^{-1}$ is the scale height, and $f = 2\Omega \sin\phi$ is the Coriolis parameter at planetary

Planet	ρ (kg m^{-3})	Ω (10^{-5} rad s^{-1})	H (km)	T (k)	g m s^{-2}	N (10^{-2} s^{-1})	L_{Ro} (km)	U m s^{-1}	L_{Rh} (km)
Earth	1.2	7	9	290	9.8	1.1	1000	10	800
Uranus	0.42	10	28	76	8.9	1.0	2000	100	4300
Neptune	0.45	11	20	72	11	1.3	1700	100	4000

Table 1.1: Global atmospheric parameters at 1 bar pressure and 45° latitude for Earth, Uranus, and Neptune. Mathematical symbols are defined in the text.

rotation rate Ω and latitude ϕ (g denotes the gravitational acceleration, R denotes the gas constant, and T denotes temperature). In weather forecasting, these eddies are called "high-pressure" and "low-pressure" systems and govern local weather. At an extratropical latitude of, say, 45° on Earth, the Rossby deformation radius comes out to roughly 1000 km, which agrees with the characteristic size of pressure systems on weather charts. In the low-pressure systems (i.e., negative near-surface pressure anomalies), net convergence drives upwelling and therefore condensation and precipitation. Because the combination of data products we present in Chapter 6 includes information about the large-scale flow, i.e., the behavior of the eddies, it will allow a more detailed exploration of the type and behavior of precipitation events that arise under different synoptic-scale conditions. The utility in making this link between local-scale extreme storms and their large-scale dynamical context for climate change prediction is discussed further in the Discussion section of Chapter 6.

In models of rapidly-rotating thin atmospheres (Rossby number $\ll 1$) like the Earth or the giant planets, planetary jets arise spontaneously due to the inhomogeneous mixing of potential vorticity (PV), which leads to the sharpening of PV gradients (for a review, see Dritschel et al. 2008). The so-called "PV staircase" that arises consists of zonal bands of similar potential vorticity values separated meridionally by narrow regions with very sharp gradients in PV. The sharp PV gradients are coincident with narrow jets in the cyclonic (typically, eastward) direction and the uniform-PV regions are associated with broader anticyclonic (westward) winds. The wind profiles from these models share strong qualitative similarities to Jupiter's observed zonal wind profile (Kaspi et al. 2020). The spacing between jets can be estimated theoretically using the shallow-water fluid equations and making the β-plane approximation, which says that the Coriolis parameter varies linearly with latitude. Mathematically, the β plane is constructed via a first-order Taylor approximation of the Coriolis parameter about a given latitude ϕ_0: $f = f_0 + \beta y$, where $\beta = 2\Omega \cos \phi_0 / a$ for a planet of rotation rate Ω and radius a. Making this assumption, the jet spacing should be

$$L_{Rh} = \left(\frac{U}{\beta}\right)^{1/2} \tag{1.2}$$

where U is a characteristic wind speed associated with the turbulence; the quantity L_{Rh} is known as the Rhines length (Rhines 1975). The Rhines lengths for our three planets of interest are given in Table 1.1. In Chapter 4, we observe alternating bright and dark bands both between 25°N and 25°S as well as in the north polar spot of Uranus. The spacing of the near-equator bands is roughly 25°, which translates to ∼10000 km, and at 25°N or S the Rhines length is roughly 4000 km. So the Rhines length is a factor of two too small, but nevertheless yields an acceptable order-of-magnitude estimate. This factor-of-two difference likely arises from uncertainty in the eddy wind speeds, which are hard to determine accurately. It is thus reasonable to assume that the alternating bands we observe are indeed a manifestation of a Jupiter-like PV staircase, at least at some pressure level in the atmosphere. Alternating prograde and retrograde winds have not been observed on Uranus (see, e.g., Sromovsky, de Pater, et al. 2015), but cloud tracking observations are

difficult given Uranus's thick haze, and most of the clouds that have been tracked to date are upper-tropospheric and stratospheric methane clouds.

The alternating prograde and retrograde jets set up by the PV staircase are associated with alternating regions of net upwelling and subsidence. On Earth, the intertropical convergence zone (ITCZ) at the equator is associated with retrograde (westward) winds and upwelling of moist air, which leads to an abundance of deep convective storms that supply precipitation to the tropical rainforests. By contrast, the subtropics, which are bounded on the poleward side by the eastward (westerly) subtropical jet streams, are associated with dry, subsiding air and overlie the Earth's deserts. Similarly, the extratropics are wetter than the polar regions. As the above suggests, the ITCZ and extratropics have a higher column humidity on average than do the subtropics and poles. Reversing this statement, the presence or absence of vapor at a given latitude can be used as a tracer for the global circulation cells on other planets: dry air suggests subsidence, while moist air suggests upwelling. We interpret the aforementioned alternating bright and dark bands on Uranus as arising from a similar alternating excess and paucity of condensing species, further corroborating a Hadley-Walker-like circulation on that planet. These ideas are discussed more in Chapter 4.

1.2 Moist Convection

Several chapters of this thesis focus on extreme weather triggered by deep convection. The summertime extreme precipitation over the Continental United States that is a central focus of both Chapter 5 and Chapter 6 is associated with extratropical thunderstorms, and the best explanation for the infrared-bright equatorial cloud system observed on Neptune in Chapter 2 is a tropical convective complex. To understand how these extreme events are produced, one must understand the conditions in an atmospheric column before, during, and after it becomes convectively unstable, and those are laid out here.

In the absence of diabatic heating and cooling, i.e., for an atmosphere in hydrostatic equilibrium, the vertical temperature profile of an atmosphere follows an adiabatic lapse rate, denoted Γ. An adiabatic lapse rate is the natural configuration of an atmosphere in radiative-convective equilibrium, if it is assumed that any radiative heating and cooling is very rapidly counterbalanced by convection. The assumption of an adiabatic lapse rate is used in Chapters 2 and 4, and tested to some extent in the Appendix to Chapter 4. However, in the tropospheres of both Earth and the giant planets, the deeper layers of the troposphere tend to warm up in relation to the higher layers due to either the presence of an absorbing surface (such as the ocean and land surface on Earth), more efficient absorption of sunlight by gases in the deeper layers, or a deep interior heated by the friction of differentiation, isotopic decay, and residual heat from the initial accretion process[1]. These diabatic heating processes force the atmospheric temperature away from an adiabatic profile, making dT/dz

[1]The internal heat of Uranus has been measured to be much smaller than in Neptune or the other giant planets, and is actually consistent with zero based on available measurements; nevertheless, the deeper atmosphere warms by absorbing sunlight more efficiently than the upper atmosphere

more negative. This configuration can become unstable and convection may occur. In the absence of moisture, the condition for dry convective instability can be written

$$-\frac{dT}{dz} = \Gamma_d > \frac{g}{c_P} \tag{1.3}$$

where g is the gravitational acceleration and c_P is the specific heat capacity. However, atmospheres contain trace species that undergo phase transitions and alter the temperature structure of the atmosphere via latent heat of condensation and evaporation. The condition for moist convective instability can be derived by assuming conservation of moist static energy during moist adiabatic motion. The result is:

$$-\frac{dT}{dz} = \Gamma_s > \Gamma_d - \frac{1 + \frac{L_c q}{RT}}{1 + \frac{\epsilon L_c^2 q}{c_P R T^2}} \tag{1.4}$$

where L_c is the latent heat of condensation, R is the ideal gas constant, q is the specific humidity, and ϵ is the mass ratio between a molecule of the condensing species (e.g. H_2O for Earth) and the average mass of the ambient air.

To understand the energy balance of an atmospheric column before and after Equation 1.4 is satisfied, it is convenient to define the virtual temperature,

$$T_V = T\frac{1+\eta}{1+\epsilon\eta} \tag{1.5}$$

where η is the mole mixing ratio of the condensable species (e.g., water) and ϵ is the mass ratio of the condensable species to the dry air. T_V is the temperature at which dry air would have the same temperature as moist air at a given pressure, thus the difference in T_V between a parcel and its environment can be used as a proxy for buoyancy. When the condition for instability is not satisfied, convection is inhibited. The extra energy needed to lift that parcel to a level at which it would convect freely (i.e., the Level of Free Convection or LFC) is given by the convective inhibition (CIN):

$$CIN = \int_0^{\text{LFC}} g\Big(\frac{T_{V,\text{parcel}} - T_{V,\text{env}}}{T_{V,\text{env}}}\Big)dz \tag{1.6}$$

where g is the gravitational acceleration. Equation 1.6 is basically the integrated negative buoyancy. In the part of an atmospheric column where the parcel would satisfy Equation 1.4, i.e. above the LFC, the integrated positive buoyancy or Convective Available Potential Energy (CAPE) can instead be defined:

$$CAPE = \int_{\text{LFC}}^{\text{LNB}} g\Big(\frac{T_{V,\text{parcel}} - T_{V,\text{env}}}{T_{V,\text{env}}}\Big)dz \tag{1.7}$$

where LNB refers to the level of neutral buoyancy, the height at which a rising parcel attains the same density as its environment.

As stated before, the upper troposphere radiates to space more efficiently than it warms up via shortwave absorption in both the terrestrial and gas giant atmospheres. As this heating at the bottom and cooling at the top of an atmospheric column proceeds, Γ increases, CIN decreases, and CAPE increases. Once Equation 1.4 is satisfied for an air parcel, it becomes energetically favorable for it to rise. If CIN is small and CAPE is positive, it does so. As a moist parcel rises, it cools and its vapor condenses, releasing latent heat that serves to further increase the parcel's buoyancy relative to its surroundings. A very simple estimation of the conversion of potential energy due to buoyancy ($PE = g\Delta z\Delta T/T$) into kinetic energy ($KE = w^2/2$) yields fairly realistic estimates for the maximum vertical velocity $w = 2\sqrt{PE} \approx 25$ m s^{-1} for a deep convective plume of height $\Delta z = 10$ km on Earth. The same back-of-the-envelope estimate is revisited for methane convection on Neptune in Chapter 2. However, it should be stated that this oft-used estimation of vertical velocity has been shown to be an overestimate by an order of magnitude in theoretical calculations and simulations of deep convection on Earth. Calculations of the entropy budget show that the conversion of potential energy to mechanical work is highly inefficient; most of the potential energy goes to diffusion of water vapor, irreversible phase changes, and frictional dissipation (Pauluis et al. 2002).

The physics of moist convection has been developed and tested extensively with Earth's atmosphere in mind. The way that moist convection proceeds on the giant planets, of course, remains subject to all the same physics, but the dramatically different compositions and temperatures of these atmospheres as compared with Earth leads to many qualitative differences, too. As pointed out by, e.g., Li and Ingersoll (2015) and Sánchez-Lavega, Pérez-Hoyos, et al. (2004), one important difference is that a moist parcel of air in giant planet atmospheres is much heavier than a dry parcel: dry air is composed primarily of hydrogen and helium, with an average molar mass of $\mu \approx 2$, and the condensable species are methane (μ=16), hydrogen sulfide (μ=34), ammonia (μ=17), and water (μ=18) depending on the pressure of interest. For example, at the water cloud layer on Saturn, the virtual temperature decreases with increasing temperature for water mixing ratios $\gtrsim$0.01 since $\epsilon \approx 8$. Equation 1.5 then has two solutions: that is, two parcels at the same temperature but different water mixing ratios can have the same virtual temperature.[2] Li and Ingersoll (2015) consider a situation in Saturn's atmosphere in which the atmosphere is cooling from the warmer moist adiabat to the cooler moist adiabat with the same T_V at the water cloud base and a vapor mixing ratio of more than 1%. During this cooling, paradoxically, the virtual temperature would actually increase at first, and a less dense layer of air would sit atop the denser, deep atmosphere for fairly long timescales, inhibiting convection and allowing CAPE to build up. That layer cools until the convective inhibition vanishes and the warm moist air beneath ascends, accelerated by latent heat release, in a massive convective upwelling event that overshoots into the stratosphere. The upwelling air and subsequent geostrophic adjustment also advect ammonia upward to its condensation temperature, triggering additional condensation, precipitation, and latent heat release. This mechanism may explain the periodic giant storms on Saturn like the

[2]This is possible because η depends on ϵ

planet-encircling Great Northern Storm on Saturn in 2010 (see, e.g., Fletcher, Hesman, et al. 2011), although this mechanism has not been studied in a three-dimensional circulation model.

It is reasonable to suggest that this mechanism may have also triggered the nearly planet-encircling storm on Neptune we analyze in Chapter 2, and certainly qualitative similarities between that storm and Saturn's great storms are abundant. However, episodic convection has not yet been studied in ice giant atmospheres, and many differences between Neptune and Saturn may alter or inhibit this mechanism; more work is needed to apply the model of Li and Ingersoll (2015) to the ice giants. For example, Neptune is expected to be 5-10 times more abundant in water than Saturn, and the water cloud layer is expected to sit much deeper in the atmosphere (>100 bar pressures), where even the ideal gas law starts to be substantially violated. If such a convective upwelling event did erupt in the water cloud, it remains unclear how high into the atmosphere the convective plumes would extend: would they be stopped at another stable layer, e.g. the NH_4SH layer, or break through and even push parcels of NH_3- and H_2S-moist air to their levels of free convection? Could a water-cloud convective tower substantially alter the weather even at the methane layer? One might also consider applying the same mechanism to other cloud layers in Neptune, such as the H_2S cloud layer or the NH_4SH layer, but the mixing ratios of $\lesssim$0.1% we derive for these species in Chapter 4 on Uranus and those derived by Tollefson, de Pater, et al. (2021) on Neptune appear to be too low to set up this double moist adiabat behavior. Some of the difficulties in accurately modeling convective activity in the deeper layers of Neptune are presented in the Discussion section of Chapter 2.

1.3 Microphysics of Cloud and Precipitation Formation

I discussed how the large-scale flow can induce the conditions for cloud and precipitation formation in Section 1.1, and I introduced moist convection as one important mechanism that lifts parcels of moist air above their saturation pressure. However, the observations in Chapters 2, 5, and 6 are sensitive to cloud and precipitation particles, and so the formation of these (initially) micron-scale particles within a convective cell must also be discussed.

Formation and Growth of Droplets

The Gibbs energies of vapor (G_v) and droplets (G_d) are related according to the ratio of the vapor pressure e to the saturation vapor pressure e_s at temperature T (R is the gas constant):

$$G_v - G_d = RT \ln \frac{e}{e_s} \tag{1.8}$$

Equation 1.8 says that if the vapor pressure is greater than the saturation pressure, then it is energetically favorable for water to exist in liquid phase instead of gas phase. However,

energy is required to give the droplet surface tension (denoted σ), and it can be shown that the total energy change to form a droplet of radius R from vapor is given by

$$\Delta E = 4\pi R^2 \sigma - \frac{4}{3}\pi R^3 nkT \ln \frac{e}{e_s} \tag{1.9}$$

such that the critical radius above which a droplet would form and grow spontaneously is

$$R_{\text{crit}} = \frac{2\sigma}{nkT \ln \frac{e}{e_s}} \tag{1.10}$$

where k is Boltzmann's constant. For water at typical conditions in Earth's atmosphere, R_{crit} comes out to ∼50 nm for supersaturations of a few percent. Thus, to form a droplet from pure vapor would require a spontaneous collision between roughly 10 million particles of H_2O vapor, which would of course never happen. This (hypothetical, in this case) process is known as homogeneous nucleation.

Given the limitations of homogeneous nucleation, droplets must form by adsorption onto cloud condensation nuclei (CCNs), such as dust, large organic molecules, black carbon, or sea salt. Typically, large and water-soluble nuclei are the most efficient CCNs because they are more easily wetted, meaning that lower supersaturations are required. On Earth, different sources of CCN might dominate in different regions and seasons. No matter the particular CCN, clouds and precipitation do form in large quantities on Earth, and their study at macroscopic scales is the subject of Chapters 5 and 6. Condensation nuclei are also required to form methane clouds in the ice giants, for the same reasons as outlined above. However, it has been suggested that in the extremely cold temperatures of the ice giants' upper troposphere and stratosphere, condensation nuclei are scarce (Moses et al. 1992). Heterogeneous nucleation would have to proceed directly from the ice phase and, contrary to the case for typical Earth clouds, good CCNs would be insoluble particles with specific energetically-favorable crystal structures. Furthermore, none of the dominant CCNs on Earth are relevant for a planet with no surface or oceans, and while meteoritic dust and photochemically-produced hazes from the upper stratosphere likely play a role, it remains unclear how to produce a significant amount of CCN in the stratosphere. Large supersaturations may therefore be required before cloud formation occurs, especially at the low stratospheric volume mixing ratio of $\sim 2\times10^{-4}$ for methane. Lower in the troposphere of Uranus and Neptune between ∼1 and ∼50 bar pressures, the situation is even less clear, as Moses et al. (1992) focused primarily on hydrocarbon nucleation at pressures <100 mbar. As discussed in Chapter 4 of this thesis, a tropospheric CH_4 cloud layer, an H_2S layer, and an NH_4SH precipitate layer are all expected to form in this pressure range. Large cloud particles lofted from deeper layers may serve as CCNs for higher clouds in this region (Moses et al. 1992); however, recent observational data suggests that large supersaturations of gas-phase H_2S may nevertheless be present above the H_2S cloud layer in Neptune (Tollefson, de Pater, et al. 2021). A detailed analysis of cloud formation processes in the troposphere of the ice

giants has not (to my knowledge) been carried out, and would be of particular interest in advance of an upcoming ice giant mission.[3]

Once droplets are formed at $\sim 1\mu$m scales on condensation nuclei, subsequent growth into hydrometeors proceeds in two stages: first via diffusion (up to a few tens of μm) and then via collisions between droplets. These two growth stages are interesting topics of study in their own right, but a detailed discussion strays from the core topics of this thesis; the reader is referred to Wallace and Hobbs (2006) for a more in-depth look at these processes. In the next section, I will consider the resulting cloud particles and droplets as scatterers of electromagnetic radiation and discuss how they can be observed using remote sensing.

1.4 Radiative transfer in planetary tropospheres

The interpretation of nearly every piece of observational data in this thesis requires understanding the physics of light passing through a medium, a branch of physics known as radiative transfer. In Chapters 2 and 4, we use radiative transfer modeling directly and explicitly to derive properties about the composition and vertical structure of the atmospheres of Uranus and Neptune. The specifics of radiative transfer calculations are for the most part not discussed in detail in Chapters 5 and 6. However, the derivation of precipitation amount from radar data requires understanding the interaction between radar waves and falling water droplets within Earth's troposphere, and the cloud products based on data from the GOES satellite presented in Chapter 6 are derived from a complex radiative transfer model of clouds in Earth's atmosphere. Those cloud products are presented in more detail in Section 6.2 of that chapter. The radiative transfer equation can also be applied to many physical contexts other than planetary atmospheres, and in Chapter 3 we use the principles laid out in this section to derive a simple analytical model for the radiative transfer through a swarm of small airless bodies, i.e., the Uranian ring system.

The radiative transfer equation

The radiative transfer equation reads

$$\frac{dI_\nu}{d\vec{s}} = J_\nu - \alpha_\nu I_\nu \tag{1.11}$$

where I_ν is the specific intensity of radiation, J_ν is the emission, and α_ν is the coefficient of extinction, all at frequency ν. $\vec{s}$ is the path through the atmosphere. The equation states simply that radiation passing through a medium changes spectral intensity via either absorption by the medium ($\alpha_\nu I_\nu$) or emission from the medium (J_ν). Dividing this equation

[3]The Planetary Science and Astrobiology Decadal Survey 2023-2032 (National Academies of Sciences et al. 2022) identified a Uranus orbiter and entry probe as the highest-priority flagship mission for the National Aeronautics and Space Administration (NASA) in the next decade.

by α_ν gives us the familiar

$$\frac{dI_\nu}{d\tau_\nu} = S_\nu - I_\nu \tag{1.12}$$

where τ_ν is the optical depth and S_ν is the source function. For a medium in local thermodynamic equilibrium at temperature T, S_ν is given by the Planck function $B_\nu(T)$.

To be relevant for planetary atmospheres, this equation must be generalized to include scattering, so we must separate the extinction coefficient α_ν into scattering and absorption components. We can parameterize this separation using the single-scattering albedo ϖ, defined as the ratio of the scattering efficiency to the total extinction efficiency, such that if $\varpi = 0$ then all extinction is due to absorption and if $\varpi = 1$ then all extinction is due to scattering. Scattering may deflect light from any angle Ω' into the direction of interest Ω, or similarly may deflect light from the direction of interest Ω into any arbitrary angle Ω'. Mathematically, we express the direction of scattering using the phase function $p(\Omega', \Omega)$, which is normalized such that

$$\frac{1}{4\pi}\int_{4\pi} p(\Omega, \Omega')d\Omega' = 1 \tag{1.13}$$

We can think of $p(\Omega, \Omega')$ as a probability: given that a photon arrives from direction Ω' and is scattered, what is the probability that it scatters into direction Ω?

Putting these ideas all together into the radiative transfer equation, we get

$$\frac{dI_\nu(\Omega)}{d\tau} = (1-\varpi)B_\nu(T) + \frac{\varpi}{4\pi}\int_{4\pi} I_\nu(\Omega')p(\Omega, \Omega')d\omega' - I_\nu(\Omega) \tag{1.14}$$

In practice in planetary atmospheres, Equation 1.14 quickly becomes complicated to solve: absorbers, emitters, and scatterers vary along the path in complicated ways. Subject to one or more scattering events, a photon may also take a countless number of different paths through the atmosphere, all of which much be accounted for. Thankfully, there are several simplifications that can be made to solve this equation numerically in an atmospheric model, some of which are discussed in the next subsections.

The Asymmetry Parameter

For real particles, the phase function $p(\Omega, \Omega')$ is often very complicated to express mathematically. Finding an expression for the phase function requires solving the full Maxwell equations as a particle of a given shape interacts with electromagnetic radiation, and analytical solutions can be written down only for the simplest cases. For a spherical particle, these solutions are called Mie scattering, and even in this idealized case, $p(\Omega, \Omega')$ has many peaks at different angles caused by resonances between the particle radius and the wavelength of radiation. Luckily, for macroscopic radiative transfer calculations in atmospheres, we are often not interested in the behavior of individual scattering events. We can instead average over a large number of scattered photons, and simply ask how many photons are scattered in the forward direction versus the backward direction.

Assuming that particles in the atmosphere have no preferred orientation relative to the planet,[4] we can express the angle between incidence and scattering Θ such that $\cos\Theta = \Omega\cdot\Omega'$. We then define the asymmetry parameter g as the average value of Θ over a large number of scattering events:

$$g = \frac{1}{4\pi}\int_{4\pi} p(\cos\Theta)\cos\Theta d\omega \tag{1.15}$$

Thus if all photons are scattered in the forward (backward) direction, then $g = 1$ (-1), whereas if the scattering direction is random then $g = 0$.

Sometimes we would like a better approximation to $p(\cos\theta)$ than simply "mostly forward" or "mostly backward" scattering, but still without a full description of Mie theory. In this case, g is commonly used as an input parameter to a function called the Henyey-Greenstein phase function, which takes the form

$$p_{HG}(\cos\Theta) = \frac{1-g^2}{(1+g^2-2g\cos\Theta)^{3/2}} \tag{1.16}$$

This function has the advantages that it is non-negative for all values of Θ and at least somewhat resembles real phase functions. However, it is single-peaked; that is, if $g > 0$ it scatters the most in the forward direction and the least in the backward direction. For most real phase functions, there should be an additional peak in scattering angle in the backward direction. If this is important for one's application, the double Henyey-Greenstein function may be more applicable:

$$p_{HG2}(\cos\Theta) = bp_{HG}(\cos\Theta, g_1) + (1-b)p_{HG}(\cos\Theta, g_2) \tag{1.17}$$

where b is the relative strength of the forward and backward peaks parameterized by g_1 and g_2, respectively.

The Two-Stream Approximation

In many situations relevant to atmospheric science, such as in a thick cloud or in a cloud-free atmosphere, the variation of light intensity I with angle Ω is quite small. In this case, we can make a dramatic simplification to Equation 1.14 by considering only the upward and downward directions instead of all possible values of Ω. This is called the two-stream approximation. Mathematically, we state that

$$F_U = \int_0^{-1} I_\nu(\Theta)\mu d\mu \tag{1.18}$$

and

$$F_D = \int_0^{1} I_\nu(\Theta)\mu d\mu \tag{1.19}$$

[4] this is sometimes violated, e.g., in the case of rainfall

for the upward and downward directions, respectively, where μ is the cosine of the scattering angle. The radiative transfer equation is then expressed as a system of two equations:

$$\frac{dF_D}{dt} = \frac{\varpi f}{\mu_0} F_D + \frac{\varpi(1-f)}{\mu_0} F_U - \frac{F_D}{\mu_0} \tag{1.20}$$

$$\frac{dF_U}{dt} = \frac{\varpi f}{-\mu_0} F_U + \frac{\varpi(1-f)}{-\mu_0} F_D - \frac{F_U}{-\mu_0} \tag{1.21}$$

where $f = (1+g)/2$ is the fraction of scattering that goes forward and μ_0 is the average incidence angle cosine (taken to be 1/2 for isotropic scattering).

Equations 1.20 and 1.21 are clearly more tractable than Equation 1.14, because only two angles are considered instead of infinitely many angles. In fact, these two equations can be solved analytically in many cases. The relatively low computational expense of the two-stream approximation makes it a good choice when radiative transfer calculations must be carried out many thousands of times, such as within a climate model; indeed, the ERA5 atmospheric reanalysis discussed in Chapter 6 makes use of the two-stream approximation for many aspects of its radiative transfer scheme (Morcrette et al. 2008). When higher accuracy is needed, one approach is simply to discretize Equation 1.14 into angle ranges like the two-stream approximation, but use more than two ranges. It is easy to imagine formulating a four-stream or eight-stream approximation instead, and this is indeed what is done in the `disort` radiative transfer solver underlying the `SUNBEAR` (Spectra from Ultraviolet to Near-infrared with the BErkeley Atmospheric Retrieval) code used in Chapter 2 (Ádámkovics et al. 2016).

Rovibrational Spectra and the Correlated-K Method

In the tropospheres of the solar system planets, which span pressures from roughly ∼0.1 to ∼100 bars,[5] the assumption of local thermodynamic equilibrium is an excellent one, with collisions between molecules occurring frequently enough to maintain equality between the excitation temperature, kinetic temperature, and radiative temperature of the gas. Temperatures are also cool enough that atoms tend to be neutral (as opposed to ionized), tend to remain mostly in their base electronic states, and tend to form molecules. Cold temperatures present a challenge for remote-sensing observations of atmospheres because major elemental constituents (e.g. nitrogen, oxygen, hydrogen) are locked into very weakly-emitting nonpolar diatomic molecules (e.g. H_2, N_2, O_2). We thus often rely on ro-vibrational molecular transitions in trace species (e.g. CO, H_2S, NH_3) at infrared and radio wavelengths to study these atmospheres.

Recall that molecular energy states are quantized, just like energy orbitals in individual atoms. Considering here a diatomic molecule for simplicity, one must take into account rotational and vibrational energy. The molecule may rotate about an axis perpendicular to

[5]It is difficult to define the bottom of the troposphere on the gas giant planets, so I choose 100 bars here as this is about as deep as we can observe with the methods considered in this thesis.

the bond axis with angular momentum N, and its electrons have intrinsic angular momentum L, giving rise to a (conserved) total angular momentum quantum number J with energy levels $E_{rot} = \hbar^2 J(J+1)/2I$, where $I = \mu L^2$ is the moment of inertia of the molecule. The molecule may also vibrate as a simple harmonic oscillator, with energy levels $E_{vib} = (\nu+1/2)\hbar\omega$, where ω is the vibration frequency, $\hbar$ is Planck's constant, and ν is the vibrational quantum number. The vibrational energy is much larger than the rotational energy, by a factor of roughly the square root of the nucleus-to-electron ratio, which comes out to $E_{vib} \sim 30 E_{rot}$. Because of this, pure rotational spectra ($\nu = 0$) are found at millimeter and centimeter wavelengths and dominate spectra at the ALMA and VLA wavelengths discussed in Chapter 4. Ro-vibrational spectra take on complicated band structures in the infrared; a given vibrational transition (e.g. $\nu = 2 \rightarrow 1$) will be observed at many different (but still discretized) wavelengths because the rotational energy level will change at the same time. For example, $(\nu = 2, J = 3) \rightarrow (\nu = 1, J = 3)$ and $(\nu = 2, J = 3) \rightarrow (\nu = 1, J = 2)$ and $(\nu = 2, J = 3) \rightarrow (\nu = 1, J = 5)$ will all be observed at slightly different wavelengths despite transitioning between the same vibrational quantum numbers.

The above behavior makes modeling of infrared spectra difficult. The absorption k at a given wavenumber ν takes the form $k(\nu, P, T) = \sum_i S_i(T) f_i(\nu, P, T)$, where S_i is the line intensity for the ith absorption line with normalized line shape f_i at a given temperature T and pressure P. It quickly becomes computationally expensive to account for every single one of the i ro-vibrational transitions and their line shapes in every molecule, and this complexity is exponential as larger molecules are considered. Fortunately, if one is only interested in a fairly wide frequency range $\Delta\nu$, then a transformation may be made from frequency space into absorption coefficient space that dramatically speeds up computations; this method is called the "correlated-k" method and is described here.

The average brightness $\bar{I}$ in a given atmospheric layer and spectral interval $\Delta\nu$ looks like

$$\bar{I} = \int_0^1 I(k(\nu)) d(\nu/\Delta\nu) \tag{1.22}$$

The absorption coefficients within the spectral interval can be represented by the probability distribution function $f(k)$, in which case Equation 1.22 can be written

$$\bar{I} = \int_0^\infty f(k) I(k) d(k) \tag{1.23}$$

The cumulative distribution is

$$g(k) = \int_0^k f(k') dk' \tag{1.24}$$

which is by definition a monotonic function of k, so we can write

$$\bar{I} = \int_0^1 I(k(g)) dg \tag{1.25}$$

Equations 1.22-1.25 have made a transformation between the frequency ν and the cumulative probability of absorptivity g as the independent variable in computing the average intensity. This transformation is powerful because $I(\nu)$ has a different shape over every interval $\Delta\nu$ and is difficult to approximate with simple functions, whereas $I(k(g))$ (or nearly any other radiation parameter of interest) is a smooth function of g. This fact speeds up the computation of the integral dramatically, often making accounting for absorption from tens of thousands of spectral lines as computationally intensive as computing a single line profile in a line-by-line code (Goody et al. 1989). The correlated-k method is used extensively for the radiative transfer computations within General Circulation Models (GCMs), including the ERA5 reanalysis dataset we present in Chapter 6. The `SUNBEAR` radiative transfer code we use in Chapter 2 also uses correlated-k to account for the many thousands of weak ro-vibrational lines of methane and other trace species in Neptune's infrared atmosphere (Ádámkovics et al. 2016). By contrast, the `RadioBEAR` (Radio-BErkeley Atmospheric Radiative-transfer) software implemented in Chapter 4 uses primarily line-by-line methods (de Pater, Fletcher, et al. 2014; de Pater, Sault, Wong, et al. 2019), since the separation between spectral lines tends to be much larger in the millimeter and radio portion of the spectrum than in the infrared.

Spectroscopy at High Pressures: Collision-Induced Absorption and Pressure Broadening

The pressures considered in this thesis range from roughly 0.1 to 100 bars. At these pressures, one must account for the effects of interactions between molecules on electromagnetic spectra. The two most important effects are called collisional broadening and collision-induced absorption. The principal difference between them is that the first arises from elastic collisions and the second arises from inelastic collisions. Both processes are explained in detail below.

Collisional broadening describes the effect of elastic collisions on quantum transitions. In short, a collision between an emitting molecule and another molecule in the gas shortens the timescale for the emission to occur, leading to greater uncertainty in the energy of the transition according to the Heisenberg uncertainty principle. An alternative but equally valid way of thinking about this is that the collision lends energy to (or removes energy from) the transition. The resulting spectral lines follow a Lorentzian (Cauchy) line profile. At very high gas densities, the presence of nearby molecules may also alter the quantum energy states of a given molecule quasi-statically, i.e., on timescales much longer than that of the emission process, affecting the line shape and sometimes the central wavelength of the spectral line; this is called quasistatic pressure broadening. The combination of these two effects is known collectively as pressure broadening, but at the pressures considered in this thesis, collisional broadening is most important.

Collision-induced absorption (CIA) arises when two atoms or molecules get near enough each other to interact weakly via the Van der Waals force. This interaction induces a

small dipole moment between the two atoms or molecules. Several mechanisms exist for inducing dipoles during these interactions, especially for multi-atom molecules, but let us state for now simply that a small dipole is induced. When this occurs, the two molecules may be treated as a "supramolecular system:" they behave in much the same way as a single Van der Waals molecule, and can transition between quantum energy states. Because these molecular flyby collisions occur on extremely short timescales of roughly $\sim 10^{-4}$ nanoseconds, the uncertainty principle dictates that the spectral lines produced by these transitions are orders of magnitude broader than typical ro-vibrational spectral lines. (Compare this to the typical timescale of $\sim$1 nanosecond for an electronic transition). Although the line strengths are typically weak for CIA interactions, they are crucially important to correctly modeling planetary atmospheres, especially those of the gas giants because they induce transitions in very abundant but otherwise inert species like H_2, He, and CH_4; this is discussed further in Chapter 4.

Chapter 2

Analysis of Neptune's 2017 Bright Equatorial Storm

The published version of this chapter was coauthored by the following individuals, and is included in this thesis with their express permission: Imke de Pater, Statia Luszcz-Cook, Ricardo Hueso, Joshua Tollefson, Carlos Alvarez, Agustín Sánchez-Lavega, Michael H. Wong, Andrew I. Hsu, Lawrence A. Sromovsky, Patrick M. Fry, Marc Delcroix, Randy Campbell, Katherine de Kleer, Elinor Gates, Paul David Lynam, S. Mark Ammons, Brandon Park Coy, Gaspard Duchene, Erica J. Gonzales, Lea Hirsch, Eugene A. Magnier, Sam Ragland, R. Michael Rich, Feige Wang.

We report the discovery of a large (∼8500 km diameter) infrared-bright storm at Neptune's equator in June 2017. We tracked the storm over a period of 7 months with high-cadence infrared snapshot imaging, carried out on 14 nights at the 10 meter Keck II telescope and 17 nights at the Shane 120 inch reflector at Lick Observatory. The cloud feature was larger and more persistent than any equatorial clouds seen before on Neptune, remaining intermittently active from at least 10 June to 31 December 2017. Our Keck and Lick observations were augmented by very high-cadence images from the amateur community, which permitted the determination of accurate drift rates for the cloud feature. Its zonal drift speed was variable from 10 June to at least 25 July, but remained a constant 237.4 ± 0.2 m s^{-1} from 30 September until at least 15 November. The pressure of the cloud top was determined from radiative transfer calculations to be 0.3-0.6 bar; this value remained constant over the course of the observations. Multiple cloud break-up events, in which a bright cloud band wrapped around Neptune's equator, were observed over the course of our observations. No "dark spot" vortices were seen near the equator in HST imaging on 6 and 7 October. The size and pressure of the storm are consistent with moist convection or a planetary-scale wave as the energy source of convective upwelling, but more modeling is required to determine the driver of this equatorial disturbance as well as the triggers for and dynamics of the observed cloud break-up events.

2.1 Introduction

The Voyager 2 spacecraft flyby of Neptune in 1989 revealed an extremely dynamic, turbulent atmosphere (Smith, Soderblom, Banfield, et al. 1989; Tyler, Sweetnam, Anderson, Borutzki, et al. 1989). Since then, advances in Earth-based observing, including 10m-class optical/infrared telescopes with adaptive optics systems, the Hubble Space Telescope (HST), the Combined Array for Research in Millimeter-wave Astronomy (CARMA), the Atacama Large (sub-)Millimeter Array (ALMA), and the recently-upgraded Very Large Array (VLA), have permitted multi-wavelength global monitoring of the planet's clouds and deep atmosphere. At infrared wavelengths, Neptune shows a striking pattern of bright midlatitude features against a dark background (e.g. Max et al. 2003; Roe et al. 2001; Sromovsky, Fry, Baines, and Dowling 2001). In contrast to images at visible wavelengths, in which Rayleigh scattering produces a relatively uniformly-illuminated planet disk, methane absorption and collision-induced absorption (CIA) by H_2 in cloud-free regions makes Neptune's disk dark. In the Kp band (2.2 μm), the contrast in reflectivity between reflective methane clouds and columns free of discrete upper tropospheric clouds reaches up to two orders of magnitude (e.g., de Pater, Fletcher, et al. 2014; Max et al. 2003). Infrared observations are useful to probe the conditions under which clouds and storm systems form, the structure and composition of these storms, and their evolution over time. Sromovsky, Fry, Dowling, et al. (2001b) and Sromovsky, Limaye, et al. (1995) and more recently Tollefson, Pater, et al. (2018) (along with many other authors) performed optical and infrared cloud tracking to determine Neptune's zonal wind profile. Many authors published infrared spectroscopic data with Gemini (Irwin, Fletcher, Tice, et al. 2016; Irwin, Lellouch, et al. 2014; Irwin, Teanby, et al. 2011) and Keck (de Pater, Fletcher, et al. 2014; Luszcz-Cook, de Kleer, et al. 2016; Max et al. 2003); these studies included latitudinal mapping of Neptune's methane, characterization of the stratospheric haze layer, and the observation of cloud layers both below and above the tropopause at pressures of 0.3-2 bar and 20-80 mbar, respectively.

An effort to model the circulation on Neptune paralleled these observational studies. Clouds form when humid (rich in condensible species) upwelling air reaches a low enough temperature that condensation occurs, meaning that convective upwelling results in localized cloud systems and downwelling regions tend to remain relatively cloud-free. Combining these physical principles with the observed cloud patterns and deep atmosphere brightness temperature maps led to a hypothesis for Neptune's convection in which air rises from as deep as 40 bars into the stratosphere at midlatitudes, and subsides over the poles and at the equator (de Pater, Fletcher, et al. 2014), explaining the cloud bands at Neptune's midlatitudes and the relative paucity of clouds at the equator.

In this paper, we report the discovery of a long-lived cloud complex at Neptune's equator, bright enough in the near-infrared to be observed with even amateur ($\sim$10 inch diameter) telescopes over the second half of 2017. In Section 2.2 we present observations of the cloud complex with infrared and optical telescopes over roughly seven months from June 2017 to January 2018. We track the position and morphology of the bright cloud feature and perform radiative transfer calculations to estimate the pressure of the cloud top in Section

2.3. Finally, we explore the implications of these results with respect to the fluid dynamics processes underlying the storm in Section 2.4 before summarizing our findings in Section 2.5.

2.2 Observations and Data Reduction

We obtained near-infrared and optical images of Neptune over a seven-month period from June 2017 to January 2018 with multiple telescopes; these observations are summarized in Table 2.1, which lists data from large (>3 meter) telescopes with adaptive optics (AO) systems as well as HST observations, and Table 2.5 (in the Appendix), which lists data from smaller ground-based telescopes that lack AO systems.

Keck and Lick Observations

Observing Strategy

The Keck and Lick data used in this publication were carried out via "voluntary ToO" scheduling, which we describe here. We produced an automated script to carry out short (10- to 40-minute) snapshot observations of bright solar system objects at short notice. With these in place, any observer could choose to carry out our observations during their observing time by running the script. In practice, this occurred mainly during poor weather conditions or twilight hours, when many observations (e.g. spectroscopy of faint targets at optical wavelengths) could not be carried out effectively, and relied heavily on the Observing Assistant (OA) on duty to provide both the impetus and expertise to carry out the observation. The benefits of this model are twofold: telescope time that would have otherwise gone to waste was used for science, and high-cadence short observations were made possible at a classically-scheduled observatory. However, because the observations needed to be short and easy for any classically-scheduled observer at the telescope to carry out, photometric calibration of the data could not be obtained. For this reason, only two of the Keck observations and none of the Lick observations used in this publication have been photometrically calibrated. This observing strategy was pioneered at Keck Observatory as the *Twilight Zone* program.[1] It had already been in place at Lick Observatory since 2015 and led to one previous publication (Hueso, de Pater, et al. 2017).

Data Reduction

Data were obtained on 14 nights from the Keck II telescope on Maunakea, Hawaii. We used the NIRC2 near-infrared camera coupled with the adaptive optics (AO) system, using Neptune itself as the AO guide star. Using the narrow camera on NIRC2, the instrument's smallest pixel scale, yielded a pixel scale of 9.94 mas px^{-1} (de Pater, Gibbard, and Hammel 2006), or ∼210 km px^{-1} at Neptune's distance. Data were obtained in the broadband H and

[1] https://www2.keck.hawaii.edu/inst/tda/TwilightZone.html

Telescope	UT Date & Start Time	Observer	Sub-Observer Longitude	Ang. Diam. (arcsec)	Filters
Keck	2017-06-26 14:52	TZ	298	2.31	H, Kp, CH4S
Keck	2017-07-02 12:06	TZ	214	2.32	H, Kp, CH4S
Lick	2017-07-07 09:47	Gates	324	2.32	H, Ks
Lick	2017-07-10 10:32	Gates	150	2.33	H, Ks
Lick	2017-07-13 10:36	Lynam/de Rosa	321	2.33	H, Ks
Keck	2017-07-16 15:08	Puniwai/TZ	231	2.33	H, Kp, CH4S
Keck	2017-07-24 12:53	TZ	152	2.34	H, Kp, CH4S, PaBeta
Keck	2017-07-25 15:14	TZ	21	2.34	H, Kp, CH4S, PaBeta
Keck	2017-08-03 13:25	Jordan/TZ	127	2.35	H, Kp, CH4S, PaBeta
Keck	2017-08-03 15:26	Jordan/TZ	172	2.35	H, Kp
Lick	2017-08-06 11:36	Ammons/Dennison/Lynam	256	2.35	H, Ks
Lick	2017-08-08 12:00	Rich/Lepine/Gates	258	2.35	H, Ks
Keck	2017-08-25 11:23	Sromovsky/Fry/TZ	2	2.36	H, Kp
Keck	2017-08-26 10:31	Sromovsky/Fry/TZ	159	2.36	H, Kp
Lick	2017-08-31 08:11	Crossfield/Gonzales/Gates	268	2.36	H, Ks
Lick	2017-09-01 10:42	Crossfield/Gonzales/Gates	141	2.36	H, Ks
Keck	2017-09-03 10:31	TZ	130	2.36	H, Kp, CH4S
Keck	2017-09-03 12:57	TZ	184	2.36	H, Kp, CH4S
Keck	2017-09-04 10:32	TZ	306	2.36	H, Kp, CH4S
Keck	2017-09-04 12:40	TZ	354	2.36	H, Kp, CH4S
Keck	2017-09-27 04:56	Mcllroy/Magnier	277	2.35	H, Kp, CH4S, PaBeta
Lick	2017-10-04 06:47	Duchene/Oon/Coy	112	2.35	H, Ks
Lick	2017-10-05 03:52	Duchene/Oon/Coy	224	2.35	H, Ks
Lick	2017-10-05 07:29	Duchene/Oon/Coy	304	2.35	H, Ks
Lick	2017-10-06 06:08	Rich/Lepine/Gates	91	2.35	H, Ks
HST	2017-10-06 09:02	OPAL Program	155	2.35	F467M, F547M, F657M, F619N, F763N, F845M
Keck	2017-10-06 10:54	Aycock/Ragl	197	2.35	H, Kp
HST	2017-10-07 02:40	OPAL Program	155	2.35	F467M, F547M, F657M, F619N, F763N, F845M
Keck	2017-11-08 04:14	Alvarez/Licandro	106	2.31	H, Kp, CH4S
Lick	2017-11-29 01:47	Wang/Gates	152	2.29	H, Ks
Lick	2017-11-30 02:01	Melis/Gates	334	2.29	H, Ks
Lick	2017-12-01 01:46	Melis/Gates	145	2.28	H, Ks
Lick	2017-12-02 01:47	Melis/Gates	321	2.28	H, Ks
Lick	2017-12-06 02:31	Hirsch/Gates	323	2.28	H, Ks
Lick	2017-12-29 02:08	Melis/Lynam	48	2.25	H, Ks
Lick	2017-12-31 02:22	Chen/Lynam	45	2.25	H, Ks
Keck	2018-01-10 04:38	Puniwai/McPartland	58	2.24	H, Kp, CH4S, PaBeta

Table 2.1: Description of Keck and Lick data used in this publication. "TZ" refers to the Keck Twilight Zone observing team—E. Molter, C. Alvarez, I. de Pater, K. de Kleer, and R. Campbell.

Kp filters on all 14 nights, and narrow-band observations in the CH4S and PaBeta filters were obtained when time permitted (see Table 2.1). The images are shown in Figure 2.1, and characteristics of each filter are listed in Table 2.6.

Wide-band images were processed using standard data reduction techniques of sky subtraction, flat fielding, and median-value masking to remove bad pixels. Each image was corrected for the geometric distortion of the NIRC2 detector array according to the solution provided by Service et al. (2016). Cosmic rays were removed using the `astroscrappy` package[2] (affiliated with the community-sourced `astropy` Python suite; The Astropy Collaboration et al. 2018). This package implements a version of the standard L.A.Cosmic algorithm (van Dokkum 2001), which relies on Laplacian edge detection to differentiate cosmic rays from PSF-convolved sources.

Photometric calibration was carried out on 26 June and 25 July using the photometric standard star HD1160 on both dates. This star appears in the UKIRT MKO Photometric Standards list[3]; its spectral type is A0V and it has J, H, and K band magnitudes of 6.983, 7.013, and 7.040, respectively (in the 2MASS system; Cutri et al. 2003). Due to our reliance on donated observing time, these were the only dates for which photometry could be obtained. We converted the observed flux densities to units of I/F, the ratio of the observed radiance to that from a normally-illuminated white Lambertian reflector at the same distance from the sun as the target (Hammel, Baines, et al. 1989):

$$\frac{I}{F} = \frac{r^2}{\Omega}\frac{F_N}{F_\odot} \tag{2.1}$$

where r is Neptune's heliocentric distance in AU, $\pi F_\odot$ is the Sun's flux density at Earth, F_N is the observed flux density of Neptune, and Ω is the solid angle subtended by one detector pixel. The solar flux density was determined by convolving a high-resolution spectrum from Gueymard (2004) with the NIRC2 filter passbands. Uncertainties in I/F were set to be 20% to account for errors in photometry, which we estimated by looking at the difference in flux between the three exposures taken on the standard star in each filter; this 20% uncertainty is consistent with de Pater, Fletcher, et al. (2014).

To ensure the photometric calibration in H and Kp band from HD1160 was reasonable, we used it to determine the geometric albedo of Neptune's moon Proteus. Proteus was inside the field-of-view of the narrow camera in only one image of the three-point dither on both 26 June and 25 July. The technique we employed to determine the albedo was very similar to that used by Gibbard, de Pater, and Hammel (2005) and is summarized in Appendix 2.6; the results of that calculation are given in Table 2.2. The geometric albedos we found were somewhat higher than the K-band value of 0.058 ± 0.016 reported by Roddier et al. (1997) but in good agreement with Dumas et al. (2003), who obtained 0.084 ± 0.002 in the HST F160W filter at 1.6 μm and 0.075 ± 0.010 in the HST F204M filter at 2.04 μm.

Data were obtained on 17 nights from the Shane 120-inch reflecting telescope at the UCO Lick Observatory on Mount Hamilton, California. We used the Shane AO infraRed

[2]https://github.com/astropy/astroscrappy

[3]http://www.gemini.edu/sciops/instruments/nearir-resources/photometric-standards/ukirt-standards

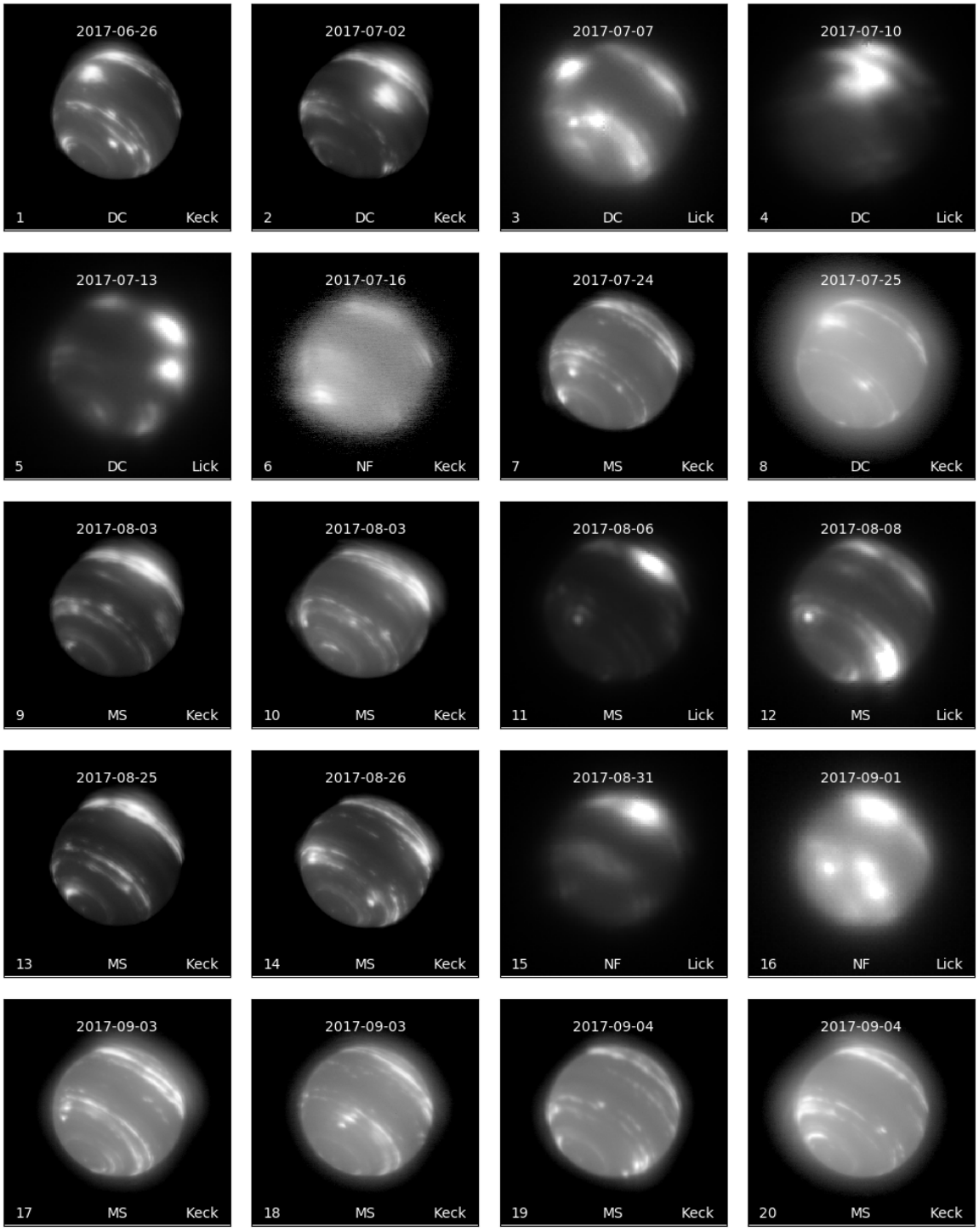
2017-06-26
1 DC Keck
2017-07-02
2 DC Keck
2017-07-07
3 DC Lick
2017-07-10
4 DC Lick
2017-07-13
5 DC Lick
2017-07-16
6 NF Keck
2017-07-24
7 MS Keck
2017-07-25
8 DC Keck
2017-08-03
9 MS Keck
2017-08-03
10 MS Keck
2017-08-06
11 MS Lick
2017-08-08
12 MS Lick
2017-08-25
13 MS Keck
2017-08-26
14 MS Keck
2017-08-31
15 NF Lick
2017-09-01
16 NF Lick
2017-09-03
17 MS Keck
2017-09-03
18 MS Keck
2017-09-04
19 MS Keck
2017-09-04
20 MS Keck

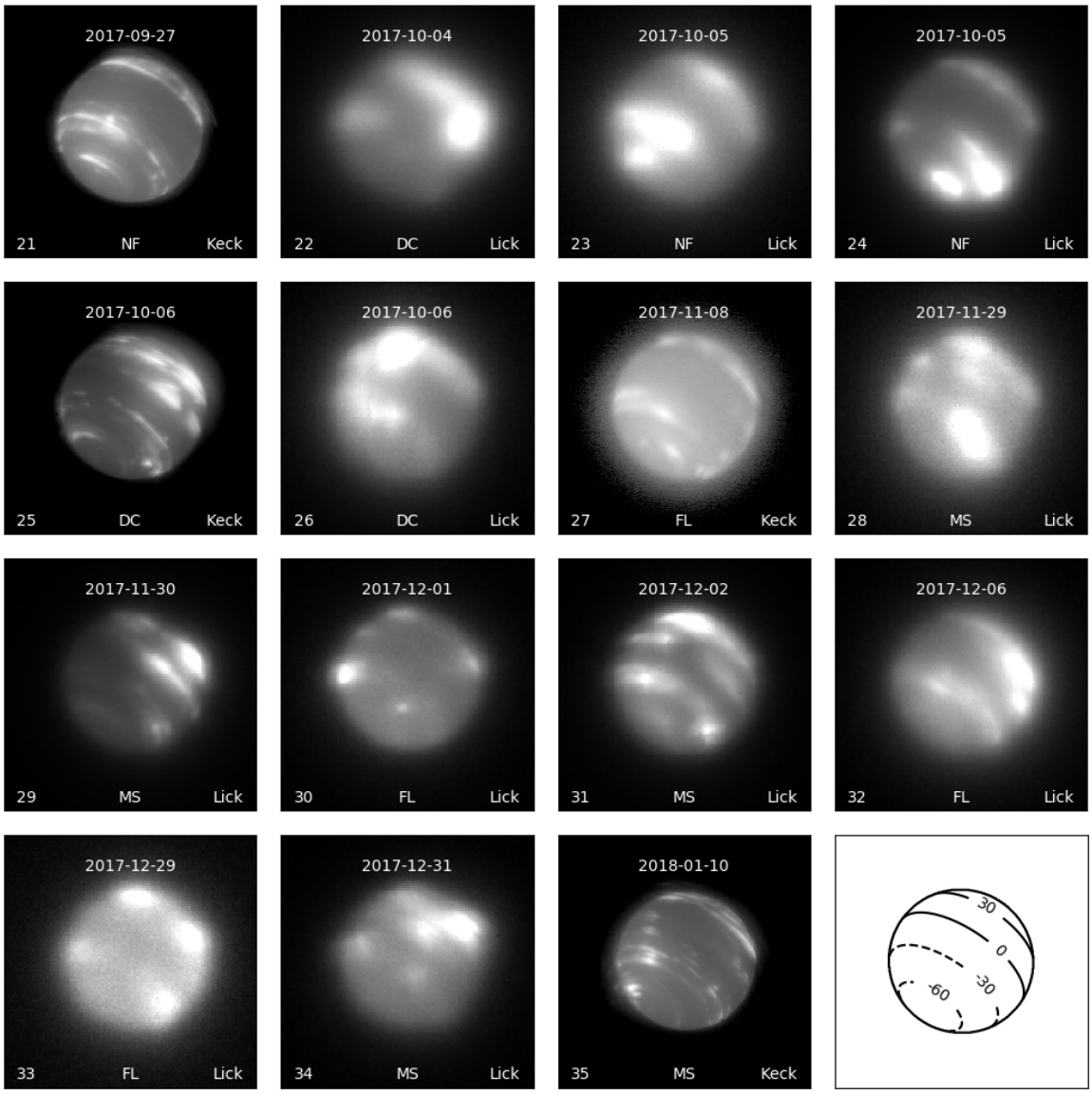

Figure 2.1: Time series of all H-band Keck and Lick images. The last panel shows the orientation of Neptune relative to the observer. The Keck observations are displayed on a logarithmic scale for better viewing of both bright and faint features. One or two bright equatorial storm features are visible in Panels 1-5, 8, 22, 25, and 26 (labeled DC for Discrete Cloud). Multiple equatorial features or bands are visible in Panels 7, 9-14, 17-20, 28, 29, 31, and 34 (labeled MS for Multiple Spots). One or more faint features are visible near the limb of the planet in panels 27, 30, 32, and 33 (labeled FL for Faint Limb). No clear equatorial features are visible in Panels 6, 15, 16, 21, 23, or 24 (labeled NF for No Features).

Date	Band	$F_{0.2}/F_{tot}$	Albedo	Error (%)	Phase Angle (°)
2017-06-26	H	0.63	0.080	21	1.8
	Kp	0.74	0.092	21	1.8
2017-07-25	H	0.30	0.073	22	1.2
	Kp	0.29	0.100	33	1.2

Table 2.2: Photometry of Neptune's moon Proteus, used to validate our standard star photometric calibration. The stated error combines the ∼20% photometry error with the estimated additional error from flux bootstrapping (see Appendix 2.6).

Camera-Spectrograph (ShARCS) camera, a Teledyne HAWAII-2RG detector, coupled with the ShaneAO system and using Neptune itself as a guide star. The pixel scale of the ShARCS images was 33 mas px^{-1}, or ∼700 km px^{-1} at Neptune. Data were obtained in the broadband H and Ks filters on all 17 nights. Data reduction was carried out using the same procedure as for the Keck data, and the images are shown along with the Keck data in Figure 2.1.

Image Navigation and Orthogonal Projection

To overlay a latitude-longitude grid onto Neptune and project its ellipsoidal surface onto a map, we followed the same general procedure as used in Sromovsky and Fry (2005); however, we have recast those codes into the Python programming language and made a few small changes. We summarize the steps here. First, an ellipsoidal model of Neptune was produced with r_{eq} = 24766 km and r_{pol} = 24342 km as found by Voyager (Lindal 1992). The model was resized, rotated, and cast into two dimensions to match the angular scale and orientation of Neptune at the time each observation was taken, making use of data from JPL Horizons[4]. Second, the model Neptune was overlain onto the image data and shifted to the location of Neptune in the image. To achieve this, we employed the Canny edge detection algorithm (implemented by the `scikit-image` Python package; Walt et al. 2014)[5] to find the edges of Neptune and then simply matched these edges to the edges of the model. The navigation error using this method was the combination of the uncertainty in the shift required to match the model and data (implemented by the `image_registration` package[6]) and the spread in the location of the edges the algorithm found as its parameters were varied over a reasonable range. We found the combined error to be < 0.1 pixels in all images with acceptable seeing conditions. Third, we interpolated this mapping between image (x, y) coordinates and physical (latitude, longitude) coordinates onto a regular latitude-longitude grid using a cubic spline interpolation (implemented by the `scipy` Python package; Jones, Oliphant, et al. n.d.)[7]. Planetographic latitudes were used here and throughout this paper. We chose the grid spacing such that one pixel in latitude-longitude space was the same size

[4]https://ssd.jpl.nasa.gov/horizons.cgi

[5]skimage.feature.canny; https://scikit-image.org/

[6] image_registration.chi2_shifts.chi2_shift; https://github.com/keflavich/image_registration

[7]scipy.interpolate.griddata; https://www.scipy.org/

as one pixel in image space at an emission angle of zero; that is, the latitude-longitude map was oversampled compared to the data away from the sub-observer point.

The code used for NIRC2 data reduction, navigation, and projection was implemented in Python and has been made publicly available on GitHub.[8]

Observations with non-AO Telescopes

We alerted the amateur community to the presence of the bright storm feature after it was imaged with Keck on 26 June. A total of 62 near-infrared amateur observations of the feature were made on 33 different nights. Amateur observers D. Milika & P. Nicholas in fact made the first observation of the storm on 10 June, though it was not recognized as noteworthy until it was later observed with Keck. The bright equatorial feature was also observed with the PlanetCam instrument (Mendikoa et al. 2016) on the 2.2m telescope at Calar Alto Observatory on 11 July. Table 2.5 (in the Appendix) summarizes the dates and characteristics of these PlanetCam and amateur observations, and sample amateur images are shown in Figure 2.13 (in the Appendix). Images were navigated in WinJupos[9] using the position of Triton as a tie-point for the Neptune latitude-longitude grid; see Hueso, de Pater, et al. (2017) for a more complete description of this technique.

HST Observations

The Hubble Space Telescope (HST) observed Neptune in Cycle 24 on 6 October as part of the Outer Planets Atmospheres Legacy (OPAL) program (Simon, Wong, et al. 2015).[10] The observations were described by Wong, Tollefson, et al. (2018), who presented a multi-year study of the southern hemisphere dark vortex SDS-2015. We processed the images following similar procedures to those described in Wong, Tollefson, et al. (2018); the images are shown in Figure 2.2.

2.3 Results

Morphological Evolution of the Storm

An ∼8500 km diameter infrared-bright cloud complex was observed at Neptune's equator on several nights from June to December 2017 (see Figure 2.1). From at least 26 June to 25 July, this bright equatorial storm remained a single discrete feature, although on 25 July the cloud had elongated compared to 26 June and 2 July and had taken on a somewhat patchy appearance (Figure 2.3). None of the Keck or Lick observations from 3 August to 27 September (13 images on 10 dates) observed a large equatorial storm, but multiple small

[8] https://github.com/emolter/nirc2_reduce
[9] http://jupos.org/gh/download.htm
[10] https://archive.stsci.edu/prepds/opal/

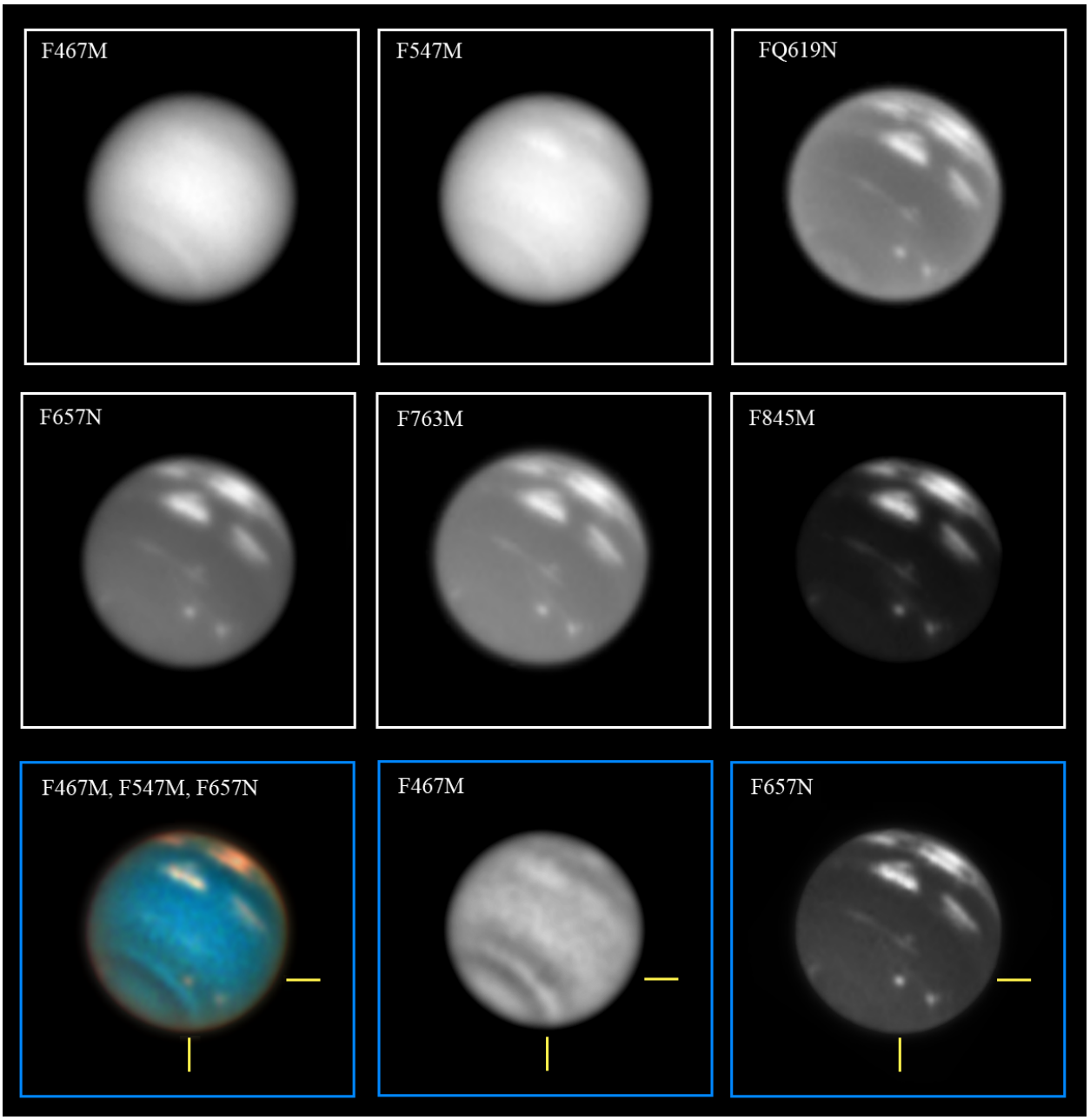

Figure 2.2: HST images of the equatorial features obtained on 6 October 2017. The two upper rows show images acquired from blue to near-infrared wavelengths, and the lower row shows high-pass versions of images at selected wavelengths. The SDS-2015 dark vortex and its associated bright cloud in red and near IR wavelengths appears highlighted with yellow lines in the color composite and blue image. The bright equatorial clouds do not show any similar dark feature.

features at different longitudes were observed at the equator in many of these images. In the first Keck image on 3 August, two relatively faint cloud complexes were seen: one thin band near the sub-observer point and another larger group of clouds on the eastern limb of the planet spanning ∼15° in both latitude and longitude, which may have been remnants of the storm. On 25 and 26 August as well as 3 and 4 September, many small, faint features were observed at various longitudes across Neptune's equator, possibly indicating that the storm sheared apart into an equatorial cloud band. The relative paucity of observations between 25 July and 4 October and the changing drift rate of the storm from 2 June to 25 July (see Section 2.3) made it difficult to determine precisely when the discrete equatorial cloud feature dissipated, since in a single snapshot the storm may have simply been hidden from view on the far side of the planet. However, if the storm maintained its drift rate of ∼202 m s^{-1} (see Section 2.3) we should have detected it with Keck on 26 August. We achieved complete longitude coverage on 25 and 26 August and again on 3 and 4 September with Keck, determining with certainty that the storm was not present on Neptune on those dates for any reasonable drift rate. Lick observations on 4 October revealed a bright discrete cloud feature again, and Keck imaging on 6 October captured this feature as well as a detached fainter equatorial cloud roughly 40° east of the main storm. In all observations in which the equatorial cloud complex was detected, it was coincident in longitude with bright cloud features at the northern midlatitudes from ∼30° to ∼50°. Multiple spots and bands were visible at the equator in 7 Lick observations and one Keck observation from 29 November 2017 to 10 January 2018, revealing that cloud activity on Neptune's equator remained heightened for several months after the reappearance of a large discrete cloud complex. However, individual features could not be tracked over this time period due to the sparse temporal coverage of the data.

The HST observations on 6 October revealed the two bright equatorial clouds observed by Keck faintly in the F467M filter and at progressively higher contrast at increasing wavelengths; the highest contrast was achieved in the F845M filter, where methane absorption is most important (see Figure 2.2). The bright equatorial storms displayed a similar morphology in the Keck H-band observations on the same date (see Figure 2.1, panel 25). Comparing the color-composite images of the equatorial storm taken on 6 October and 7 October reveals that the morphology of both the main storm and its fainter companion cloud varied significantly on timescales of $\lesssim$1 day (see Figure 2.4). The dark vortex SDS-2015 was observed near ∼45°S at blue wavelengths (see also Wong, Tollefson, et al. 2018) and its companion clouds were visible at red wavelengths, but no dark spot was observed in association with the equatorial storm nor anywhere else on Neptune. Discovery of an equatorial dark spot would have been surprising, since LeBeau et al. (1998) found that anticyclones could not survive within 15° of the equator. Their simulations predicted that vortices drifting into the equatorial region would produce extensive perturbations on a global scale, lasting for weeks. This phenomenon was observed on Uranus when the bright "Berg" storm drifted toward the equator and dissipated (de Pater, Sromovsky, Hammel, et al. 2011). Our observations of persistent equatorial features over several months is therefore also inconsistent with the dissipation of a vortex that drifted too close to the equator. However, a dark spot obscured

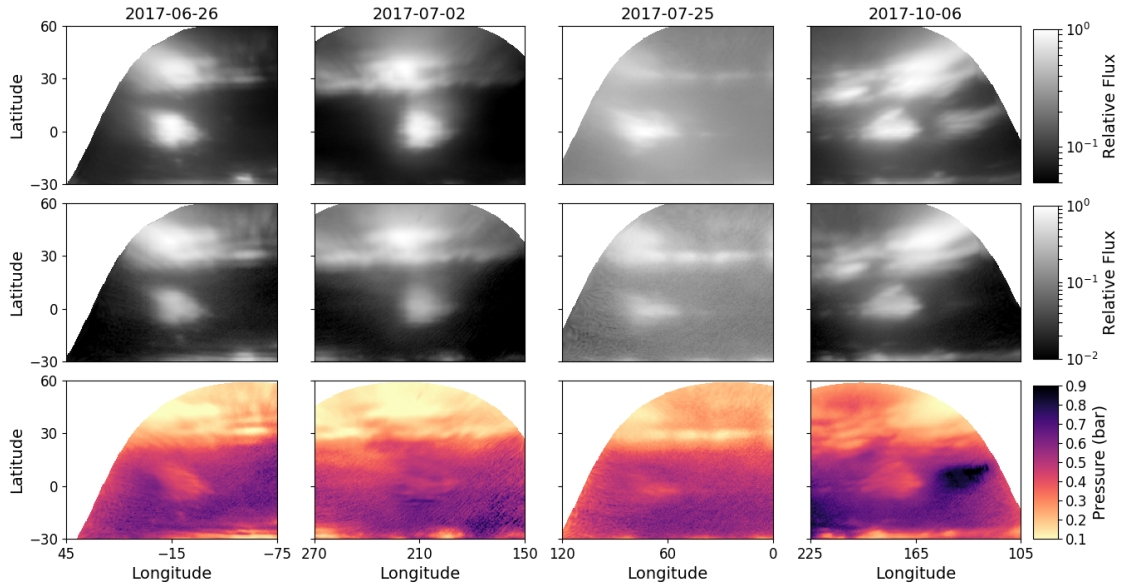

Figure 2.3: Orthogonally-projected Keck images of the equatorial and northern cloud complexes in H band (**Top Row**) and Kp band (**Middle Row**). Images are displayed on logarithmic scales for better viewing of both bright and faint features. Note that the background on 25 July appeared brighter due to poorer atmospheric seeing on that date. **Bottom Row:** Map of best-fit cloud pressures based on Kp/H ratio in each pixel. These pressures were derived from a radiative transfer model assuming a discrete optically thick cloud (see Section 2.3) and are therefore only valid in locations where clouds were visible in H band (top row).

by the equatorial cloud complex could not be definitively ruled out by our observations.

Feature size determination

To determine the physical extent of the equatorial storm, a 50% contour was laid down around the bright storm feature in the projected (onto a latitude-longitude grid) images. The longest continuous line segments in the x- and y- directions that fit inside the contour were taken to be the full widths at half-maximum of the storm feature in the zonal and meridional directions, respectively. This measurement was repeated in both H and Kp band on all four dates on which Keck observed the storm to be a discrete feature, as well as in the HST F845M filter on 6 October; the results are shown in Table 2.3.

We took the error on these measurements to be one detector pixel. The size of a detector pixel at zero emission angle was ∼210 km in the Keck images, so at any other emission

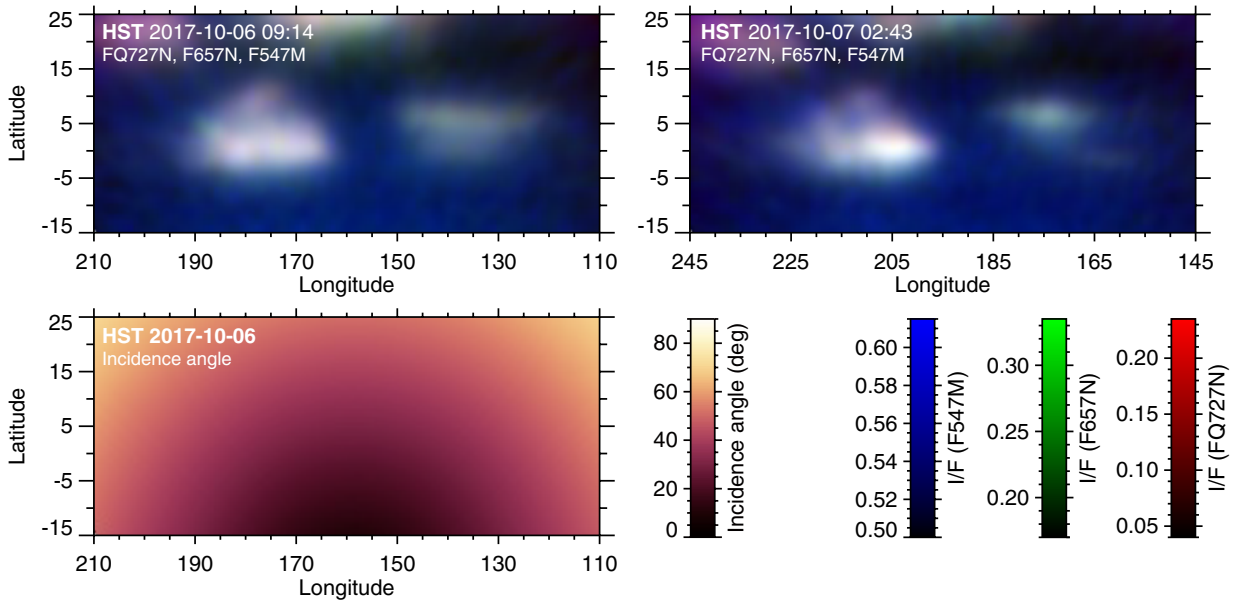

Figure 2.4: Orthogonally-projected color-composite HST OPAL images from 6 and 7 October. The images reveal changes in storm morphology on $\lesssim$1 day timescales. The lower left panel shows the angle of incidence with respect to the observer.

angle $\mu = \cos\theta$ the distance on the planet subtended by one pixel was $x \approx (210/\mu)$ km. However, the most prominent error sources in determining a single value for the cloud's size are the choice of what constitutes part of the cloud, i.e. whether or not the FWHM value is the proper metric, the assumption that the size of the atmospheric disturbance is well represented by the size of the visible region of the cloud, the filter in which the size is measured (which is loosely tied to the pressure level of the cloud), and the short-timescale variability in the cloud's morphology (see Figure 2.4).

Feature tracking

We determined the speed of the equatorial storm across the planet by tracking its location over multiple observations. To do so, we needed to find the latitude and longitude of the storm's center in each image. Because the physical extent of the storm was much larger than one ShARCS or NIRC2 detector pixel and the bright cloud feature had an irregular shape, it was not sensible to determine its center using a Gaussian or elliptical top-hat fit. Instead, we employed a version of the technique used by Martin et al. (2012), which proceeded as follows. First, we defined a large box around the entire bright cloud region. Second, we computed contours around the brightest region of the storm at many levels (from 68% to 95% in intervals of 0.01%; the particular choice of starting and ending values and step size

Date	Filter	Zonal Extent (km)	Meridional Extent (km)	Error (km)	Zonal Extent (°)	Meridional Extent (°)	Error (°)
2017-06-26	H	8315	7036	345	19.2	16.6	0.8
	Kp	7462	6396	345	17.3	15.1	0.8
2017-07-02	H	8290	8502	236	19.1	20.0	0.6
	Kp	7652	7439	236	17.7	17.5	0.6
2017-07-25	H	15567	9045	368	36.0	21.3	0.9
	Kp	12411	6101	368	28.7	14.4	0.9
2017-10-06 p	H	12165	7341	250	28.1	17.3	0.6
	Kp	11117	6921	250	25.7	16.3	0.6
	F845M	11980	7244	310	27.7	17.1	0.7
2017-10-06 s	H	10907	5244	442	25.2	12.3	1.0
	Kp	-	-	-	-	-	-
	F845M	13930	6408	380	32.2	15.1	0.9

Table 2.3: Sizes of the equatorial storm on all dates the storm was observed to be a discrete feature by Keck or HST. On 6 October, the "p" and "s" refer to the primary and secondary storm feature, respectively. The secondary feature was not detected in Kp band.

had very little effect on the result). Third, we determined the centroid of each contour. Finally, we took the mean of these centroid positions as the derived feature center, and took the standard deviation in the retrieved centers to be the 1σ error on that value. The feature tracking error dominated over the error in the planet's location on the detector (see Section 2.2). We note that this technique found the brightest region of the storm and was therefore sensitive to changes in the storm's morphology, which occur on short timescales ($\lesssim$1 day; see Figure 2.4), and slightly sensitive to the storm's position with respect to the limb due to limb-darkening/brightening effects.

Feature locations in Amateur and PlanetCam images were measured using the WinJupos software, which permits determination of locations of features across the planet. Measurements were obtained by two of us (R.H. and M.D.) and sometimes by the individual observers, and these two or three location determinations were found to be coincident within the estimated uncertainty. The measurement uncertainty was determined by marking the center of the equatorial bright feature bye eye 3-5 times and observing the dispersion in the measurements.

The results of our feature tracking are shown in Figures 2.5 and 2.6. The storm (when present) was stable in latitude, remaining within $\pm5°$ of the equator over the entire time baseline of our observations. The mean latitude of the feature center was found to be 2.2° North, with a standard deviation of $\pm3.7°$.

We derived the longitude drift rate of the storm by fitting our longitude tracking data to a linear model; the details of this process are explained in Appendix 2.8. Over the first six weeks of observations from 10 June to 25 July, we find a best-fit drift rate of 197 $\pm$ 3 m s^{-1}. However, this drift rate provides a relatively poor fit to the storm location on 10 June, 26 June, and 25 July: the predicted location of the feature center lies entirely outside the $\sim20°$ feature. Using instead only the six data points from 2 July to 14 July in the fit, i.e., where the sampling is densest, yields a drift rate of 201.7 $\pm$ 2.2 m s^{-1} and again fails to fit

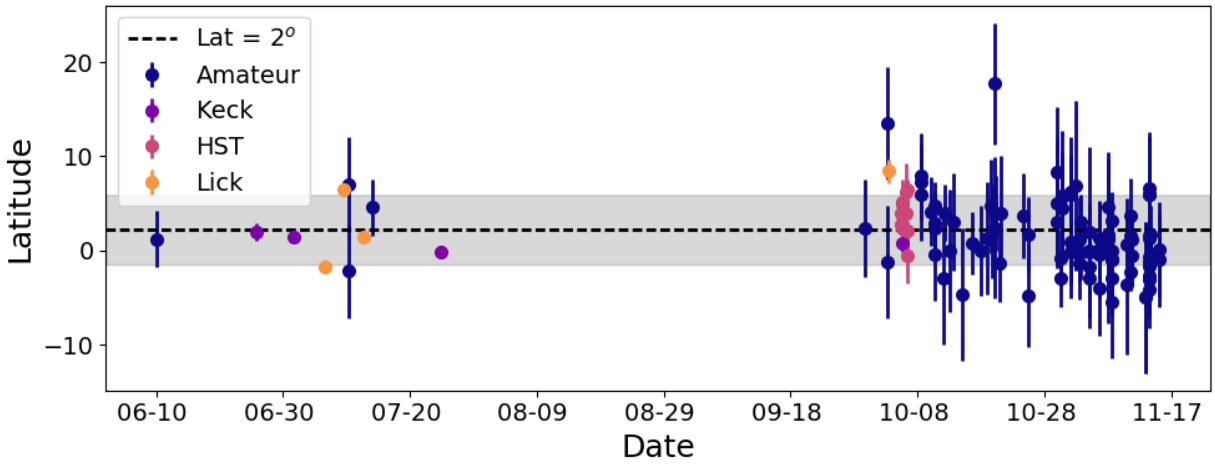

Figure 2.5: Latitude of the bright equatorial feature over time. The gray region represents the 1σ dispersion in the latitude measurements.

the data points before 2 July or after 14 July (see Figure 2.6). This implies that the storm's drift rate varied on timescales of a few to tens of days over the first epoch.

Two distinct bright equatorial storms offset by $\sim 50°$ longitude were visible from 28 September to at least 1 November. The brighter of the two storms is best fit by a constant drift rate of 237.4 ± 0.20 m s^{-1}, and the good fit from 28 September to 1 November implies that a constant drift rate provides a good model for these data. The same drift rate also fits the secondary storm over this epoch, though the data are sparser. On and after 1 November, many equatorial features were observed at different longitudes on the same nights, and the data are not of sufficient resolution or time coverage to track individual features without confusion.

Radiative transfer modeling

The SUNBEAR Radiative Transfer Code

We employed an in-house radiative transfer (RT) code based on the `disort` module (Stamnes et al. 1988), a parallelized RT equation solver. The code, which we call SUNBEAR (Spectra from Ultraviolet to Near-infrared with the BErkeley Atmospheric Retrieval), has been adapted to `Python` based on `pydisort` (Ádámkovics et al. 2016)[11], and used previously for solar system observations on Titan, Uranus, and Neptune (Ádámkovics et al. 2016; de Kleer, Luszcz-Cook, et al. 2015a; Luszcz-Cook, de Kleer, et al. 2016) at infrared wavelengths. SUNBEAR has been extended to visible wavelengths in order to analyze HST data by im-

[11]https://github.com/adamkovics/atmosphere/blob/master/atmosphere/rt/pydisort.py

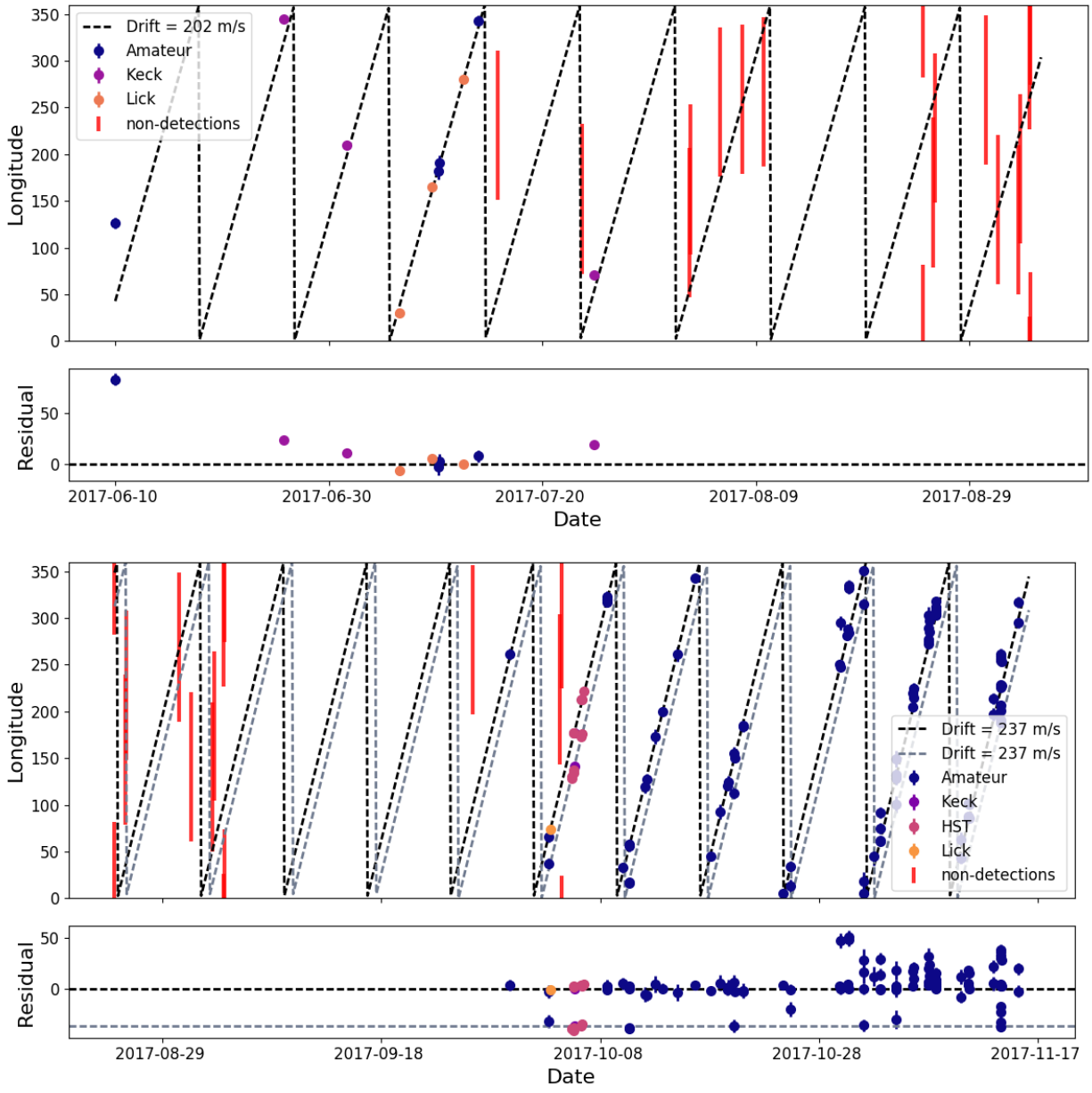

Figure 2.6: Longitude of the bright equatorial feature over time. The longitude coverage (at the equator) of observations in which a bright equatorial storm was not detected are shown as red bars. Observations are split into two epochs to facilitate visualizing the two different wind speed fits. The black and gray lines are wind speed fits to the main equatorial feature and the detached secondary feature, respectively.

plementing several scattering processes that are important at visible wavelengths: Rayleigh scattering, Rayleigh polarization, and Raman scattering. Rayleigh scattering was computed by calculating the total Rayleigh-scattering cross-section per molecule (McCartney 1976), where values for the molecular depolarization and reflective indices came from Allen (1963). Rayleigh polarization, which increases the reflectivity of Neptune's atmosphere at high scattering angles and produces an effect as large as 9% even at zero phase angle (Sromovsky 2005b), was treated following the empirical approximation developed in Sromovsky (2005b). This approximation agrees to the $\lesssim$1% level for cloud-free or cloud-opaque atmospheres. Raman scattering was taken into account using the semi-empirical approximation discussed in Karkoschka (1994, 1998); this technique transforms between the Raman and non-Raman parts of spectra by assuming that the measured geometric albedo is a linear combination of terms involving the spectrum without Raman scattering. Sromovsky (2005a) found that this approximation is accurate at short wavelengths, but underperforms at longer wavelengths within the methane absorption bands. Karkoschka and Tomasko (2009) improved their empirical spectral dependencies based on these results, and we used their parameters within SUNBEAR.

Background Model

We input a temperature-pressure profile and gas abundance profiles appropriate for Neptune's atmosphere (de Pater, Fletcher, et al. 2014; Luszcz-Cook, de Kleer, et al. 2016), along with an optically thin haze at pressures less than 0.6 bar and an optically thick cloud layer at 3.3 bar; see Figure 2.7. This "background" model was identical to the best-fit model of Luszcz-Cook, de Kleer, et al. (2016) (labeled *2L_DISORT* in that paper) retrieved from Keck OSIRIS spectral data of Neptune's dark regions, but with one modification. To account for the increase in haze albedo at visible wavelengths inferred from HST spectroscopic data (e.g., Karkoschka and Tomasko 2011), the single-scattering albedo ϖ of the optically thick cloud at 3.3 bar was allowed to smoothly vary from 0.45 longward of 1.6 microns, consistent with Luszcz-Cook, de Kleer, et al. (2016), to 0.99 shortward of 0.5 microns, consistent with Karkoschka and Tomasko (2011), according to the following equation:

$$\varpi = 0.45 + (0.99 - 0.45)\left[1 + e^{\frac{\lambda - \lambda_t}{0.1}}\right] \tag{2.2}$$

The transition wavelength λ_t between the two ϖ regimes was set to be 0.8 μm, and the 0.1 in the denominator of the exponential, which sets the "sharpness" of the transition between the two albedo values, was also set arbitrarily to a qualitatively reasonable value. Note that the albedo correction at UV wavelengths from Karkoschka and Tomasko (2011) is not important longward of 0.4 μm, so it was ignored here.

We confirmed that the "background" model fit our NIRC2 data in regions where discrete upper tropospheric clouds were not observed by convolving the model spectrum from the RT code with the NIRC2 filter bandpasses[12]. The results of this exercise for our 26 June

[12]https://www2.keck.hawaii.edu/inst/nirc2/filters.html

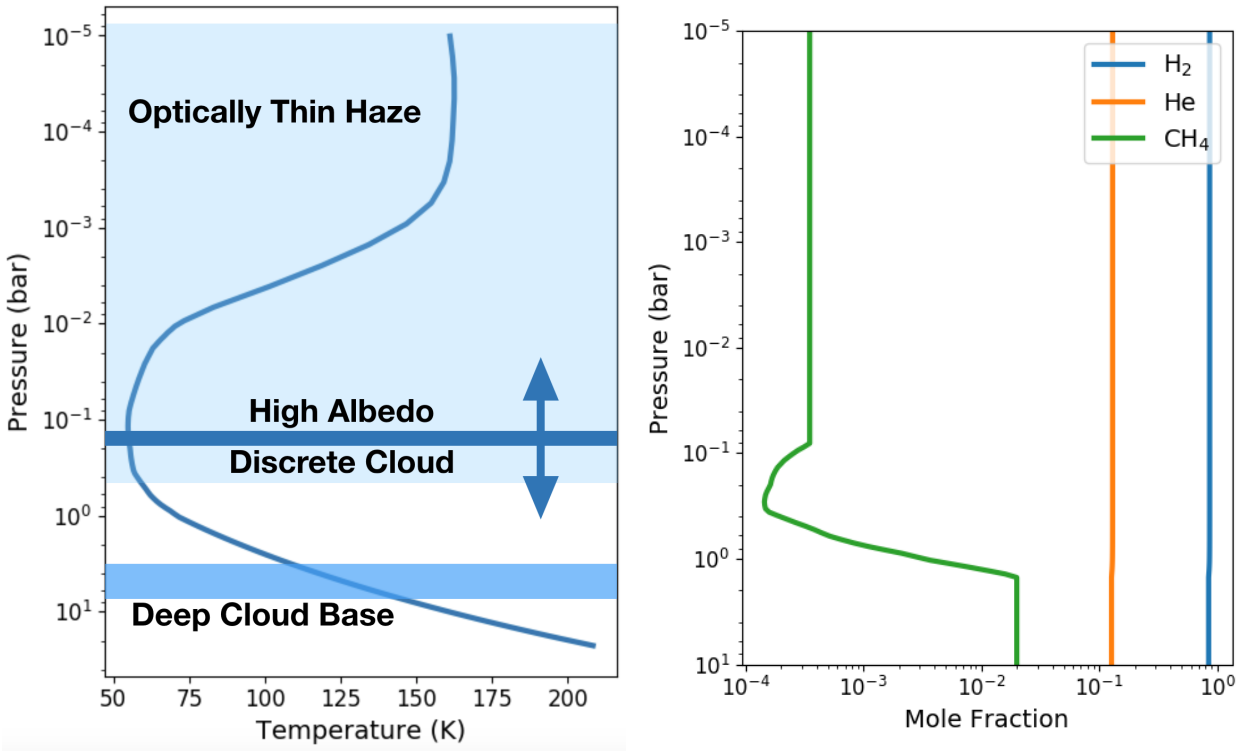

Figure 2.7: **Left:** The temperature-pressure profile of Neptune's atmosphere used in our radiative transfer model. The cloud layers in our radiative transfer model are overlain in blue; the arrows on the high-albedo discrete cloud indicate that we changed the pressure of this layer to fit our observations. **Right:** Vertical abundance profiles of gases in our model.

and 25 July data are shown in Figure 2.8. The model fit within the error bars of the data for all filters except Kp on 25 July. We do not view this as a severe problem for the model because the absolute Kp band I/F values in Neptune's dark regions were so minuscule that small systematic modeling errors may have led to large relative offsets. For example, Irwin, Fletcher, Tice, et al. (2016) noticed short timescale variability in the K band in their VLT SINFONI spectrograph observations, which they attributed to changes in the single-scattering albedo. Scattered light from the bright storms on other regions of Neptune may have also contributed to an observed brightening compared to the model, especially in relatively poor seeing as on 25 July; however, since we are interested in the bright cloud regions themselves, scattered light systematics are not a serious concern.

HST OPAL data and Keck data were taken within two hours of each other on 6 October; however, the Keck data were not photometrically calibrated, so in order to model both datasets together it was necessary to "bootstrap" a photometric calibration to the Keck data. To do so, we assumed that the brightness of the dark regions in the two Keck filters was

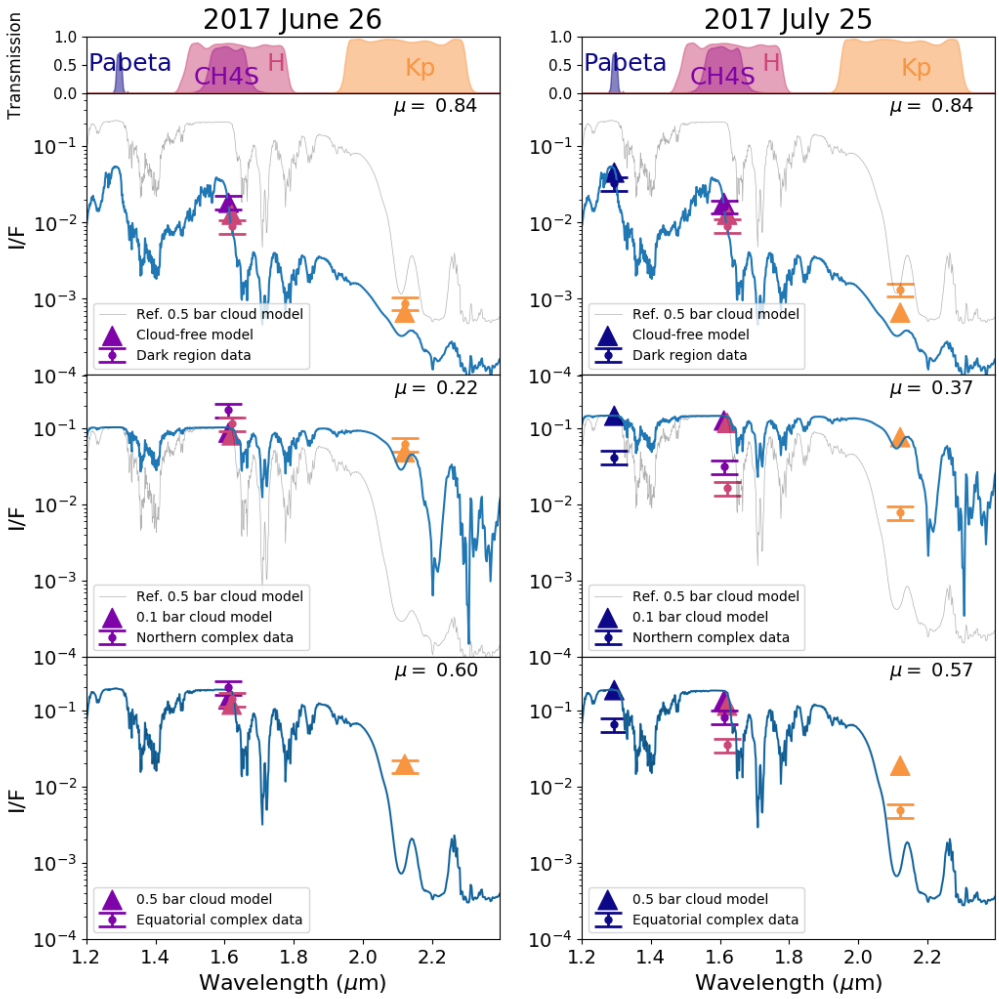

Figure 2.8: Model I/F values compared to data from 26 June (**left**) and 25 July (**right**) for a background region free of discrete upper tropospheric clouds (**top**), the northern cloud complex (**middle**), and the equatorial storm (**bottom**). Triangles represent the model values in each NIRC2 band, derived by convolving the model spectrum (shown here in blue) with the filter passbands. Models in all plots used the reference cloud parameters, varying only pressure and changing μ to the appropriate value for that cloud. The thin gray line in each panel shows a model spectrum generated using the reference parameters and a discrete cloud pressure of 0.5 bar (identical to the bottom panels, but using the appropriate value of μ) to facilitate visualization of differences between the models.

identical (at a given emission angle) on 26 June and 6 October, and then scaled the photon counts in the 6 October images accordingly. This assumption is reasonable because the same background model fit the Keck data on 26 June and 25 July within our uncertainty. Also, the timescale of H-band variability in the haze has been observed to be much longer than the ∼4 months between 26 June and 6 October (Hammel and Lockwood 2007; Karkoschka 2011). The comparison between our "background" model and the combined HST and Keck data is shown in Figure 2.9.

Discrete Cloud Model

We inserted an optically thick discrete cloud layer into the "background" model to simulate the equatorial storm. The cloud layer had the following properties, which we refer to as the "reference" model: $\tau = 10.0$ was the optical depth; $h_f = 0.05$ was the fractional scale height; $g = 0.65$ was the Henyey-Greenstein parameter; $r_p = 1.0$ μm was the peak radius in the Deirmendjian (1964) haze particle size distribution;

$$\varpi = 0.9 + (0.99 - 0.9)\left[1 + e^{\frac{\lambda - \lambda_t}{0.1}}\right] \tag{2.3}$$

was the single-scattering albedo. Since the optical depth, single-scattering albedo, and phase function were all specified, the particle size distribution r_p was only used to set the wavelength dependence of the scattering cross-section and was not truly an independent parameter. The reference cloud model was based on the properties derived by Irwin, Lellouch, et al. (2014) and Irwin, Teanby, et al. (2011), who used the NEMESIS radiative transfer code to model many Neptune infrared cloud spectra observed by the SINFONI spectrograph on the Very Large Telescope (VLT). Their best-fit model spectra varied rather widely in aerosol parameters, and since an equatorial cloud complex similar to what we observed had never been seen before, a good *a priori* guess at the cloud properties was difficult. Nevertheless, those authors favored moderately forward scattering ($g = 0.6 - 0.7$) and moderate- to high-albedo ($\varpi = 0.4 - 1.0$) clouds in most cases. We chose to model a very compact cloud layer because this was the simplest possible assumption in absence of constraining data. A short description of, reference model values of, and bibliographic references for all of the discrete cloud parameters are summarized in Table 2.4, and we refer the reader to Appendix A of Luszcz-Cook, de Kleer, et al. (2016) for additional explanation of the way these parameters were implemented in SUNBEAR.

The pressure P_m of this cloud was varied in steps of $\log P_m = 0.25$ from 10 bar to 0.01 bar to produce a suite of "discrete cloud" spectra for clouds from the deep troposphere to the upper stratosphere. We reran these models for values of the emission angle μ from 0.1 to 1.0 in steps of 0.1, ending up with a grid of spectra in (P_m, μ) space. We then interpolated across this grid to find the spectrum of any (P_m, μ) pair. This technique took advantage of the fact that spectra are continuous functions of their labels; that is, changes in cloud pressure, emission angle, or any other input parameter produce smooth changes in the resulting spectrum. This type of interpolation is widely used to fit stellar spectra (e.g., Rix

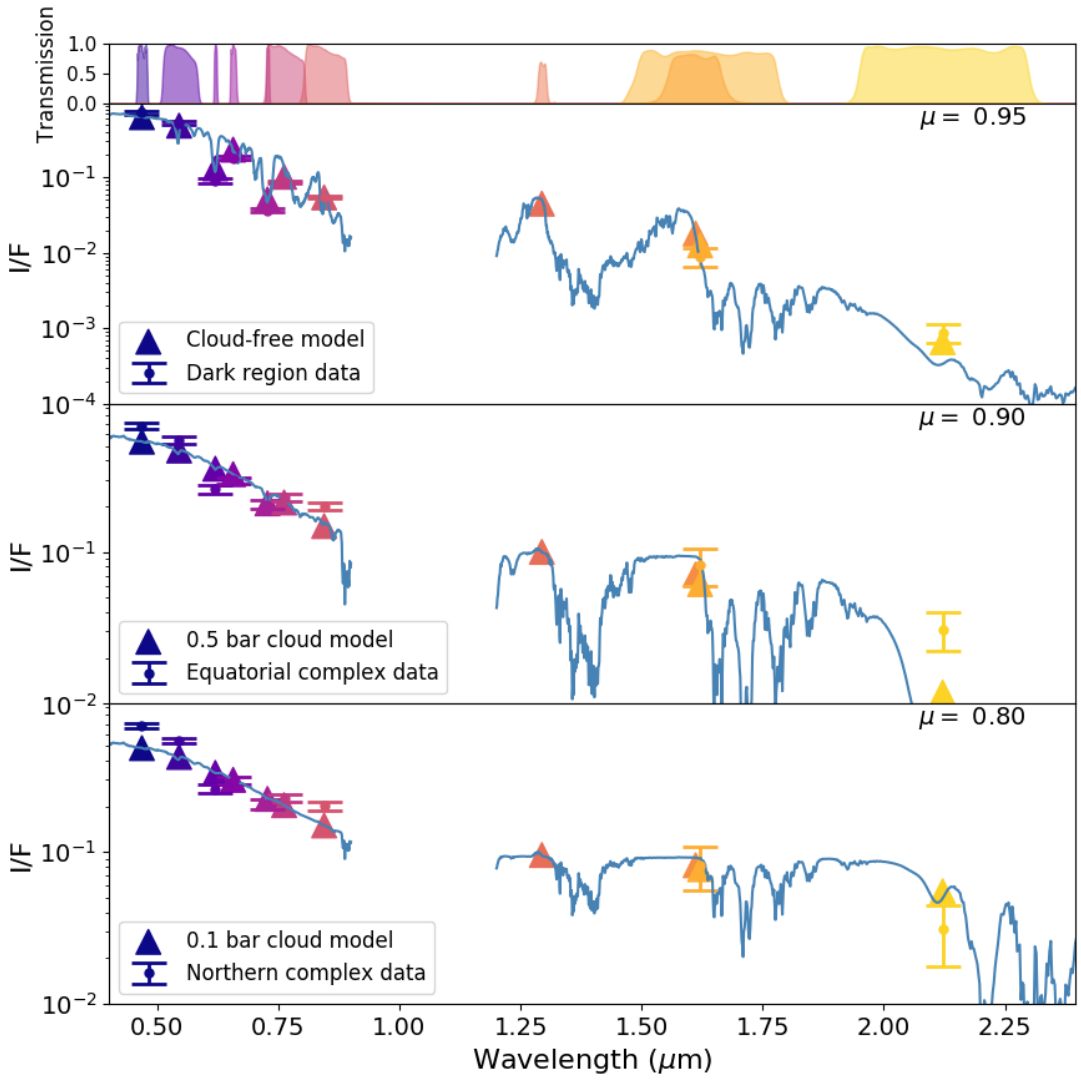

Figure 2.9: Model I/F values compared to combined Keck and HST data from 6 October for a background region free of discrete upper tropospheric clouds (**top**), the northern cloud complex (**middle**), and the equatorial storm (**bottom**). Triangles represent the model values in each filter, derived by convolving the model spectrum (shown here in blue) with the filter passbands. Models in all plots used the reference cloud parameters, varying only pressure and changing μ to the appropriate value for that cloud.

Parameter	Description	Reference Value	Varied?	Reference(s) & Notes
P_m	cloud pressure	-	Yes	-
τ	optical depth	10.0	Yes	assumed optically thick unless poor fit
ϖ_{IR}	single-scattering albedo at IR wavelengths	0.9	No	Irwin, Lellouch, et al. (2014) and Irwin, Teanby, et al. (2011)
ϖ_{vis}	single-scattering albedo at visible wavelengths	0.99	No	Karkoschka and Tomasko (2011)
g	Henyey-Greenstein parameter	0.65	No	Irwin, Lellouch, et al. (2014) and Irwin, Teanby, et al. (2011)
r_p	peak particle radius	1.0 μm	No	Deirmendjian (1964)
h_f	fractional scale height	0.05	No	assume very compact

Table 2.4: Summary of discrete cloud model parameters used in this paper. See Luszcz-Cook, de Kleer, et al. (2016) for more complete descriptions of the meaning of these parameters.

et al. 2016). The model spectra were convolved with the NIRC2 filter bandpasses to produce model reflectivities in each filter for a cloud of a given pressure. Then we determined the average reflectivity of the cloud core in the data by averaging all the pixels in a 90% contour around the brightest pixel in the cloud, and finally compared the model reflectivities to these data; those fits can be seen in Figure 2.8. On 26 June the reference model provided a good fit to both the equatorial storm and northern complex data for tropospheric cloud layers at ∼0.5 bar and ∼0.1 bar, respectively; however, on 25 July the reference model fit neither the equatorial storm nor the northern complex for any values of the cloud pressure. We assumed this difference was caused by a decrease in the opacity of the clouds on 25 July compared to 26 June. This interpretation was favored because the equatorial storm appeared to take on a patchy appearance on 25 July, and changes in microphysical cloud parameters (ϖ, g, r_p) for a given cloud type are relatively small on Earth (e.g. Baum et al. 2005). Good fits to the July 25 data were achieved using optical depths $\tau = 0.1$ for the northern complex and $\tau = 0.5$ for the equatorial storm (see Figure 2.10). We caution that these assumed cloud properties are not a unique fit to the NIRC2 data, as large degeneracies between parameters are present (e.g., de Pater, Fletcher, et al. 2014). It was not possible to retrieve parameters independently, since each of the three haze layers was parameterized by five parameters (ϖ, τ, P_m, h_f, and g) but we only had three or four spectral data points on each observation date. The equatorial storm observed on 6 October with combined HST and bootstrapped Keck data was well fit by the reference discrete cloud model at 0.5 bar pressure (see Figure 2.9), pointing to an increase in reflectivity of the storm at visible wavelengths. In our model, this increase in reflectivity was achieved via an increased single-scattering albedo; however, this solution is not unique. The particle size, optical depth, and Henyey-Greenstein parameter may also change at visible wavelengths compared to infrared wavelengths, and it is possible to fit the sparse available data using many different combinations of these parameters. In addition, the function we used to smoothly vary the single-scattering albedo was purely empirical, and could also be tuned. All of the models we present here should be taken as only one of many possible physical interpretations of the data.

The Kp/H ratio in the upper troposphere depends strongly on the cloud pressure P_m and the opacity τ but only weakly on microphysical cloud properties. Physically, this is because the pressure of a reflecting cloud layer changes the path length of a photon through the atmosphere before it scatters off the cloud. The path length greatly affects the reflectivity in Kp-band near 2.2 μm because methane absorption is very strong at those wavelengths, and therefore a photon traveling through more atmosphere has a higher chance of being absorbed. On the contrary, the path length has little effect on the reflectivity in H and CH4S bands near 1.6 μm because these are much less affected by molecular absorption in the stratosphere and upper troposphere, so the I/F value in those bands is almost entirely governed by scattering off the cloud layer itself. Changing the opacity of the cloud produces a similar effect: a less opaque cloud permits longer path lengths through the atmosphere, and in Kp-band the photons traveling these paths have a high probability of being absorbed whereas in H-band the photons may also backscatter from a haze particle or the deep H_2S cloud base. de Pater, Sromovsky, Hammel, et al. (2011) showed that by subtracting the

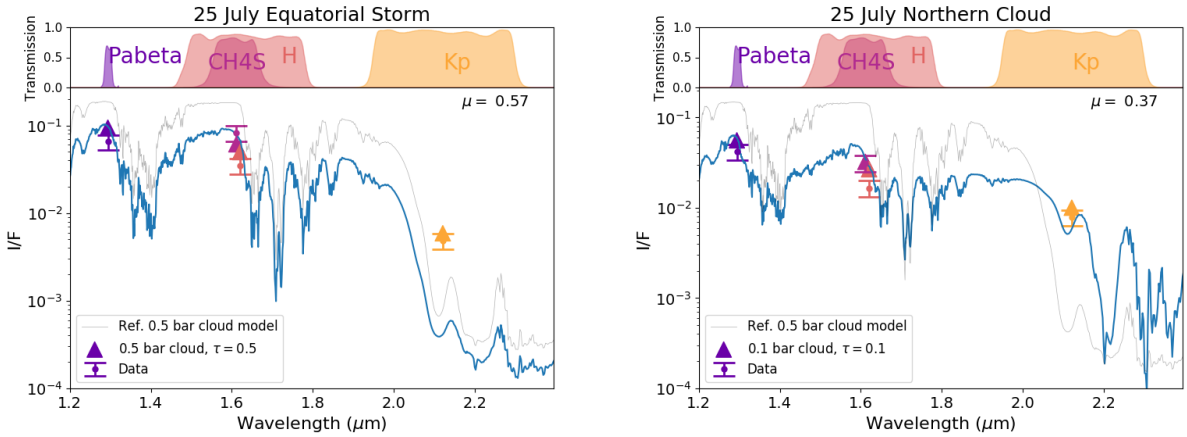

Figure 2.10: Models of the northern cloud complex and equatorial on 25 July. The models were the same as the reference model (see Figure 2.8) but with opacities $\tau = 0.5$ for the equatorial storm and $\tau = 0.1$ for the northern complex. The thin gray line in each panel shows a model spectrum generated using the reference parameters and a discrete cloud pressure of 0.5 bar (identical to the bottom panels in Figure 2.8, but using the appropriate value of μ) to facilitate visualization of differences between the models.

background I/F value from the I/F value of the discrete cloud, the opacity can be eliminated and the ratio equation

$$\frac{I_{c,Kp} - I_{b,Kp}}{I_{c,H} - I_{b,H}} = \frac{I_{Kp}(P_m) - I_{b,Kp}}{I_H(P_m) - I_{b,H}} \tag{2.4}$$

is obtained, where I_c is the intensity at the location of the discrete cloud, I_b is the intensity of the background, and $I(P_m)$ is the radiance of a very optically thick model discrete cloud at pressure P_m (i.e. our reference model cloud). Equation 2.4 can be used to place an approximate constraint on P_m independently of opacity by simply finding the pressure at which the left-hand side and right-hand side of the equation are equal; this idea was applied to clouds on Uranus by de Pater, Sromovsky, Hammel, et al. (2011) and Sromovsky, Hammel, et al. (2012). The solutions to Equation 2.4 as a function of pressure are shown for our data in Figure 2.11. The figure shows that the background-subtracted Kp/H ratio varies from $0.05-1.1$ from 0.1 to 1 bar, defining the pressure range over which this ratio is a useful pressure probe. This technique can also be used to crudely approximate cloud pressures without absolute flux calibration from photometry, as long as the telluric atmospheric transmission between 1.6 μm and 2.2 μm was not strongly wavelength-dependent on the night of the observations. By evaluating Equation 2.4 at every pixel in our Keck images, we produced a rough spatial map of the pressures of Neptune's cloud tops on each date for which the equatorial storm was observed with Keck. These maps are shown in Figure 2.3. The validity of this technique was confirmed by fitting models to data for the two photometrically-calibrated Keck

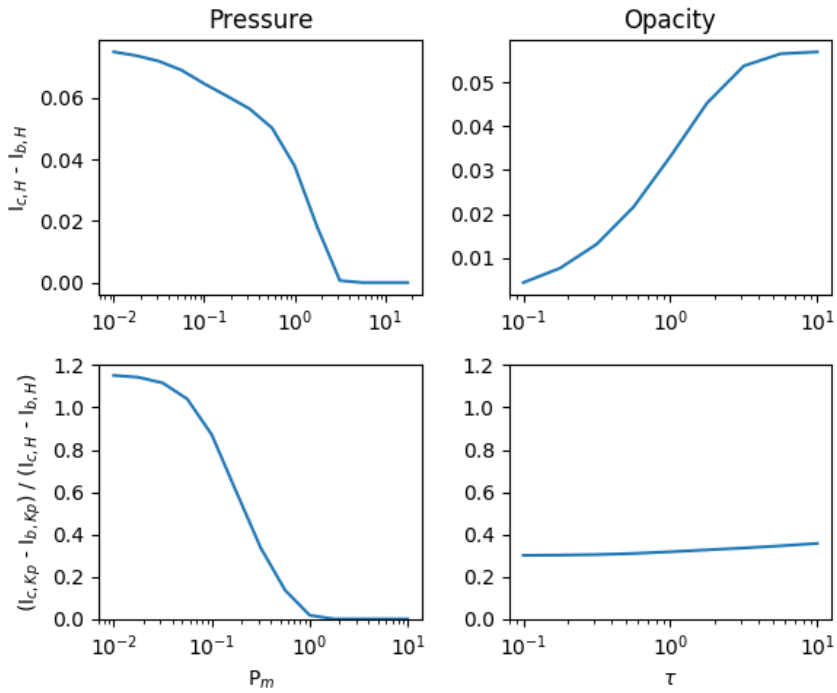

Figure 2.11: Effect of varying the cloud pressure and opacity in our model on the background-subtracted Kp/H ratio. It can be seen in the bottom row that the ratio depended strongly on the cloud pressure but very little on the opacity. The model had microphysical properties $\varpi = 0.75$, $g = 0.65$, $h_f = 0.05$, and $\mu = 1.0$.

datasets. While the overall reflectivity of the clouds changed between 26 June and 25 July, the flux density ratio (inside the 90% contour) between filters did not change significantly—in the equatorial storm the Kp/H ratio was 0.13 on both dates, and in the northern complex the Kp/H ratio was 0.54 on 26 June and 0.47 on 25 July—and Equation 2.4 found cloud pressures of 0.5 bar and $\lesssim$0.1 bar for the equatorial and northern clouds, respectively, in agreement with our radiative transfer modeling. It should be noted that the maps in Figure 2.3 are only valid at locations where a discrete opaque cloud was detected, since they are based on a radiative transfer model that assumes such a cloud is present. Also, some of the clouds in the images lay at pressures less than 0.1 bar or greater than 1.0 bar; in those cases the pressures determined by this technique should be treated as upper or lower limits, respectively.

2.4 Discussion

The size and brightness of the equatorial storm as well as the relatively high cadence of our observations permitted tracking of the storm over several months. The equatorial wind speeds of 202 m s^{-1} and 237 m s^{-1} we derived for the storm are compared to previous determinations of the equatorial wind speed in Figure 2.12. Our wind speeds are around a factor of two smaller than the average equatorial drift rate of ∼400 m s^{-1} derived from Voyager spacecraft measurements at visible wavelengths (combination of green, orange, clear, and methane-U filters—see Table 2.6) (Limaye et al. 1991; Sromovsky, Limaye, et al. 1993), but closer to the average equatorial drift rate of ∼300 m s^{-1} derived from Keck H-band images by Tollefson, Pater, et al. (2018). Both of these average wind speed fits were derived from measurements with relatively high scatter, meaning that a wind speed of 202 m s^{-1} is not a clear outlier in either dataset. This can be seen in the Tollefson, Pater, et al. (2018) points in Figure 2.12, which contain measurements with small error bars ranging from 200 to 450 m s^{-1}. Several other authors (Fitzpatrick et al. 2014; Martin et al. 2012; Sromovsky, Fry, Dowling, et al. 2001a) have tracked equatorial features using Keck or HST observations, and all found similarly large scatter in the equatorial wind speed, with measurements ranging from 150 to 400 m s^{-1}. However, it is worth noting that all of the literature measurements were derived from continuous observations of small cloud features over many hours in a single night, whereas the equatorial feature was tracked occasionally over many weeks. The data are therefore sensitive to different timescales, and the average equatorial drift rate may be the most useful point of comparison to our data. Tollefson, Pater, et al. (2018) found a significant difference in the wind speed they derived from H and Kp band measurements at the equator, which they attributed to vertical wind shear: Kp-bright features were higher in the atmosphere than Kp-faint features and were moving 90 to 140 m s^{-1} more quickly on average. In contrast, the drift rate of the equatorial storm was found to be the same in H and Kp band as well as at the visible and near-IR wavelengths used by amateur observers over several months. The deeper ($\gtrsim$ 0.9 bar - see Figure 2.3) secondary feature observed in the second epoch (after 6 October) also drifted at the same rate, providing evidence that the two features formed part of the same storm system anchored deep in the atmosphere.

Although the equatorial storm with a cloud top at 0.3-0.6 bar was always seen in association with a northern cloud complex, the pressure of the cloud top in the northern complex was significantly lower at $\lesssim$0.1 bar (see Figure 2.3 and Section 2.3). We take this as an upper limit on the pressure because the Kp/H ratio varied little for clouds at even lower pressures (see Figure 2.11). The values we derived agree well with detailed spectroscopic analyses: Irwin, Fletcher, Tice, et al. (2016), Irwin, Lellouch, et al. (2014), and Irwin, Teanby, et al. (2011) found cloud pressures of 0.1-0.2 bar at the northern midlatitudes and 0.3-0.4 bar for small equatorial "intermediate-level" clouds using VLT SINFONI observations. de Pater, Fletcher, et al. (2014) derived pressures of 0.25-0.35 bar for the two equatorial clouds in their analysis of Keck NIRC2 data, but observed mostly stratospheric ($P_m < 0.05$) bar and deep ($P_m \gtrsim 0.5$) bar clouds at the midlatitudes. Gibbard, de Pater, Roe, et al. (2003), who observed Neptune's clouds with the NIRC2 instrument on Keck, favored stratospheric

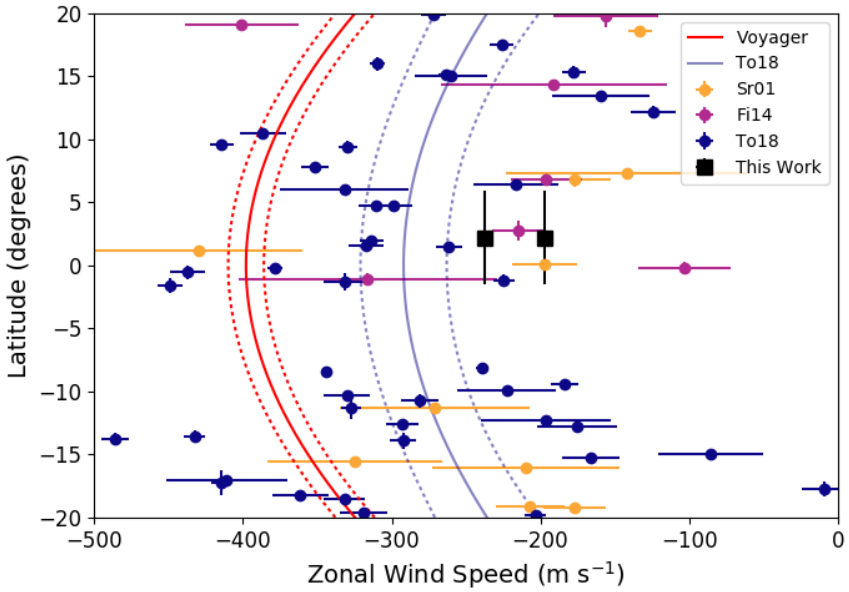

Figure 2.12: Drift rate of cloud features near Neptune's equator measured by various authors. The Voyager profile is the symmetric fourth-order polynomial given by Sromovsky, Limaye, et al. (1993) based on points from Limaye et al. (1991). Sr01 refers to equatorial features tracked by Sromovsky, Fry, Dowling, et al. (2001a) in HST observations. Fi14 refers to Fitzpatrick et al. (2014), whose wind speeds came from Keck H-band observations. To18 refers to the Keck H-band data in Tollefson, Pater, et al. (2018).

(0.02-0.06 bar) clouds at northern midlatitudes but found clouds at 0.1-0.2 bar pressures at southern midlatitudes. Interestingly, on 6 October the fainter secondary equatorial cloud was not detected at all in the Kp filter, pointing to a much deeper cloud pressure of $\gtrsim$0.9 bar.

Dynamical Origin of the Equatorial Storm

Anticyclone Interpretation

The different drift rate of the storms we observed with respect to the Voyager winds, the different drift rates in different epochs, and the similarity in drift rate with pressure may indicate a deep origin of the equatorial and northern clouds; the same kind of effects have been observed in convective storms in Jupiter (Sánchez-Lavega, Orton, et al. 2008; Sánchez-Lavega, Rogers, et al. 2017) and Saturn (Sánchez-Lavega, del Río-Gaztelurrutia, et al. 2011). An upwelling region in an area of the planet predicted by circulation models to be downwelling (e.g. de Pater, Fletcher, et al. 2014) may be caused by an anticyclone-like vortex,

as for the Great Dark Spot (GDS). Infrared-bright cloud features were observed along the southward edge of the southern GDS during the 1989 Voyager flyby (Smith, Soderblom, Banfield, et al. 1989), interpreted as methane condensation produced by upwelling air from the vortex. Prominent companion clouds were also observed in association with the 1994-96 northern dark spots NGDS-15 and NGDS-32 (Hammel and Lockwood 1997; Sromovsky, Fry, and Baines 2002). In most images these companion clouds were only observed poleward of the dark spot; however, on 10 October 1994 a very bright, extended cloud feature was observed to the south of NGDS-32 at latitudes <15°N. Based on this, a companion dark spot might be expected at latitudes $\lesssim$ 15°N; however, neither we (Figure 2.2) nor Wong, Tollefson, et al. (2018) observed a dark spot in the HST OPAL images taken on 6 October 2017, except at ∼45°S. Therefore, if the clouds we observed were supported by a deep vortex, it was either too small to be detectable by HST or was covered by the bright storm clouds even at blue wavelengths (Hueso, de Pater, et al. 2017; Wong, Tollefson, et al. 2018). The fact that the compact cloud remained stable in a region where the Coriolis force approaches zero, that no dark vortex is observed in HST observations in blue wavelengths at these latitudes, and that several similar clouds developed over the studied period, suggest that the bright clouds were not caused by vortices but could have been a manifestation of convective upwelling from different coherent systems in each of the bright equatorial clouds appearing in different epochs.

Moist Convection Interpretation

We explore the possibility that the bright spot was produced by moist convection. In the cloudy regions of the giant and icy planets, moist air is heavier than dry air (at the same temperature) (Guillot 1995; Sánchez-Lavega, Pérez-Hoyos, et al. 2004) and particular conditions are required to trigger moist convection so that latent heat release counteracts the larger density of the moist condensing air. (see, e.g., Hueso and Sánchez-Lavega 2004). Methane moist convection in the upper cloud of Neptune has been studied by Stoker and Toon (1989). We first obtain a crude estimate of the buoyancy of ascending parcels from the temperature difference between saturated updrafts (heated by methane condensation) and dry downdrafts, as given by

$$\Delta T \approx q(L_{CH_4}/C_P) \tag{2.5}$$

where q is the methane mass mixing ratio, $L_{CH_4} = 553$ KJ kg^{-1} is the latent heat of condensation of methane, and $C_P = 1310$ J kg^{-1} K^{-1} is the specific heat of methane at constant pressure. For a methane volume mixing ratio $f_B \approx 0.02 - 0.04$ and an atmospheric molecular weight $\epsilon = 6.97$, $q = \epsilon f_B \approx 0.14 - 0.28$ and Equation 2.5 gives $\Delta T \approx 6 - 12$ K. This value can be taken as an upper limit of the temperature difference between updrafts and the environment. The Convective Available Potential Energy (CAPE) is related to the peak vertical velocity w_{max} reached by the updrafts (Sánchez-Lavega 2011):

$$CAPE = \frac{w_{max}^2}{2} = \int_{Z_f}^{z_n} g\Big(\frac{\Delta T}{T}\Big)dz \approx \frac{g\Delta T}{\langle T\rangle}\Delta z \tag{2.6}$$

where z_f is the height of the free convection level, z_n is the height of the equilibrium (neutral buoyancy) level, and $g = 11.1$ m s^{-2} is the gravitational acceleration in Neptune's troposphere. A parcel that reaches the 0.3 bar altitude level (where cloud tops are observed) having started its motion at the 1.5 bar level within the methane cloud ($\Delta z \approx 35$ km) should have a maximum vertical velocity of

$$w_{max} \approx \sqrt{2g\Big(\frac{\Delta T}{\langle T \rangle}\Delta z\Big)} \tag{2.7}$$

which comes out to $w_{max} \sim 260{-}370$ m s^{-1}. This crude estimation agrees with the peak value in the vertical velocity profiles obtained from a one-dimensional model by Stoker and Toon (1989) and indicates that moist convection, if initiated, can be very vigorous in Neptune. This vertical velocity determination is probably an overestimate for several reasons. First, radiative effects near the tropopause create stable conditions that would reduce CAPE, since the temperature in the convective plume is adiabatic (Guillot 1995). Second, if convective activity is vertically confined within a limited layer, then the amount of CH_4 available for latent heating would be less than q. The temperature difference in Equation 2.5 would then be smaller. Third, including other effects in the updrafts, such as the entrainment of surrounding air on the ascending parcel, turbulent dissipation, and the weight of the condensing methane ice particles, will lower this value, limiting the altitude penetration in the atmosphere. The presence of vertical wind shears, suspected from the low velocity of the feature relative to the Voyager profile (see also Tollefson, Pater, et al. 2018), will also put serious constraints on the vertical propagation of the parcels (Hueso and Sánchez-Lavega 2004). If the bright equatorial spot was convective in origin, it should have been formed by cumulus clusters with a horizontal size similar to Δz, which is ∼35 km. The vigorous ascent of the large number of cumulus clusters necessary to cover the whole storm area, when interacting with the sheared zonal flow, would produce the growth of a zonal disturbance, as observed in Jupiter and Saturn and whose propagation could reach the planetary scale (Sánchez-Lavega, del Río-Gaztelurrutia, et al. 2011; Sánchez-Lavega, Rogers, et al. 2017). However, the images of the equatorial storm and surrounding areas did not show the presence of such a disturbance. It is possible that the disturbance occurred at a deeper cloud level than that of the top of the convective clouds, and perhaps with a lower contrast so as to be hidden at the observed wavelengths.

The energy for moist convection may also be produced by condensation of a water cloud, analogous to observed convective upwelling events in Jupiter and Saturn (Gierasch et al. 2000; Hueso and Sánchez-Lavega 2001, 2004; Hueso, Sánchez-Lavega, and Guillot 2002; Sanchez-Lavega et al. 1987; Stoker 1986). However, this scenario is both unlikely and difficult to model accurately for the following three reasons. First, the deep oxygen and water abundances, as well as the vertical temperature profiles obtained from dry and wet adiabatic extrapolations to the depth of water condensation, are highly uncertain (Luszcz-Cook and de Pater 2013; Mousis et al. 2018; Owen et al. 2006; Wong, Lunine, et al. 2008). Thermochemical models (Atreya and Wong 2005; de Pater, Romani, et al. 1991) predict the formation of water clouds

at pressure levels $P \approx 100 - 500$ bar (depending on the deep abundance of water); that is, about 300-400 km below the observable level of 0.5-1 bar. These uncertainties mean that a simple calculation of the CAPE (Equations 2.5-2.7) at the deep water clouds with updrafts reaching the 0.5 bar level results in uncertain and unrealistically large vertical velocities. Second, other cloud layers, such as NH_4SH, H_2S, and/or NH_3 condensates, are predicted to form in between the upper methane cloud at 0.5-1 bar and the water clouds at 100-500 bar. Updrafts that start at the water clouds and propagate across large vertical distances would interact with these cloud layers in a complicated way. Full 3-D moist convection models that include microphysics and the presence of the stacked layers of different cloud types are necessary to explore this situation, but to our knowledge these models have not yet been developed for Neptune. Third, Cavalié, Venot, Selsis, et al. (2017) have shown based on mixing length theory that H_2O condensation in Neptune would stabilize the atmosphere against convective motions, producing vertical gradients in water molecular weight. This is particularly important in the case of high oxygen (and therefore water) abundance, as some models predict, leading to significant temperature jumps at the water condensation layer.

Wave Interpretation

Another possible interpretation for the nature of this feature is that it formed part of an equatorial wave system. The compactness and brightness of the cloud could be related to the confinement of the moist air mass in a region showing a perturbation in the temperature, geopotential and local wind field caused by the wave. The slow motion of the feature relative to the Voyager profile could represent the zonal phase speed c_x of the wave. Adopting $c_x \approx$ -202 or -237 m s^{-1} and taking from Voyager profile $u \approx -400$ m s^{-1} we get $c_x - u \approx$ 167 or 200 m s^{-1}, i.e. the spot moved eastward relative to the mean flow. A variety of eastward and westward waves have been observed and described at the equator of the atmospheres of Venus, Earth, Mars, Jupiter and Saturn (Allison 1990; Sánchez-Lavega 2011; Simon, Li, et al. 2015). The simplest description of equatorial waves is in the context of the shallow-water model with linearized equations, on an equatorial β-plane for a fluid with a mean depth h (Andrews et al. 1987; Matsuno 1966; Sánchez-Lavega 2011). Three modes of eastward propagating waves result from this analysis: Rossby-gravity or Yanai (RG), inertia-gravity (IG) and Kelvin (K) modes. IG modes have been proposed to explain the temperature oscillations observed at pressures <1 bar during the ingress and egress at mid and high latitudes from Voyager 2 radio-occultation experiment (Hinson et al. 1993). The horizontal (latitude-longitude) velocity structure and vertical (pressure) perturbation patterns for eastward-propagating RG and IG waves shows that they occur at both sides of the Equator with symmetric and antisymmetric patterns, whereas for the Kelvin mode the wave perturbation patterns are centered at the equator and zonally aligned (Matsuno 1966; Wheeler et al. 2000). Identification of the convergence and divergence patterns (Wheeler et al. 2000) with cloud formation suggests that the observed bright Neptune spot would correspond to a Kelvin mode pattern. Due to the lack of data we cannot disregard the possibility that the feature is an RG or IG eastward mode, but here we show that these

data are compatible with a Kelvin mode. Numerical simulations using the shallow water model have shown that Kelvin waves form in Jupiter's equatorial jet (Legarreta et al. 2016). Therefore, we explore the Kelvin wave as responsible for the Neptune spot. The eastward phase speed for the Kelvin wave is given by

$$c_K = \sqrt{gh} \tag{2.8}$$

and using $c_K = 167$ or 200 m s^{-1} we get $h = 2.5 - 3.6$ km or about $H/6$, where $H \sim 18$ km is Neptune's atmospheric scale-height. This Kelvin wave should be confined to a narrow atmospheric layer. In addition, the velocity and geopotential perturbation in the Kelvin wave vary with latitude as a Gaussian function centered at the equator. The e-folding decay width is given by

$$y_K = \left|\frac{2c_k}{\beta}\right|^{1/2} \tag{2.9}$$

and for $\beta = 2\Omega/R_N = 8.72 \times 10^{-12}$ m^{-1} s^{-1} ($\Omega = 1.8 \times 10^{-4}$ s^{-1}; $R_N = 24764$ km) we get $y_K \sim 6500$ km which is consistent with the measured size of the bright spot. The fact that two spots were seen in some cases (see Figure 2.1) with a longitudinal separation between them about the size of the spots themselves also agrees with the horizontal structure derived for a Kelvin wave from such a model (Matsuno 1966).

2.5 Summary

We have discovered a large, long-lived storm at Neptune's equator. Using near-infrared adaptive optics snapshot imaging from Keck and Lick Observatories, optical imaging from HST as part of the OPAL program, and near-infrared imaging from amateur astronomers, we tracked the evolution of the storm from June 2017 to January 2018. Our findings can be summarized as follows:

- This was the first cloud feature of its size and brightness to be observed at low latitudes on Neptune, with an H-band-derived diameter of ∼8500 km in the zonal direction and ∼7000 km in the meridional direction. Its mean latitude remained near 2°N over the course of the observations. Storm activity at the equator persisted at least from 10 June to 31 December 2017 ($\gtrsim$7 months); a discrete feature was observed from 26 June to 25 July but had broken up into a trail of small clouds by 04 September. On 4 October a new storm had appeared, and another breakup into small cloud features was observed on 29 November.

- Feature tracking found best-fit drift rates of 201.7 ± 2.2 m s^{-1} between 7 and 14 July and 237.4 ± 0.10 m s^{-1} between 28 September and 4 November for the storm feature. The feature was found to vary in speed from 10 June to 25 July. The same wind speed was measured at different wavelengths, pointing to a coherent storm system anchored at $\gtrsim$1 bar pressure.

- Radiative transfer modeling suggested a cloud top pressure of 0.3-0.6 bar for the equatorial storm and $\lesssim$0.1 bar for the northern cloud complex for all four Keck observations in which the storm was observed. A decrease in reflectivity of both the northern and equatorial clouds between 26 June and 25 July was interpreted as a decrease in opacity of the clouds between the two dates.

- A secondary equatorial storm feature was observed $\sim$50° longitude away from the main storm and maintained the same drift rate as the main storm from 6 October to at least 4 November. However, the secondary feature was undetected in the Kp filter, meaning its cloud top was at > 0.9 bar pressure, much deeper than the main storm.

- No "dark-spot" vortex was observed near the equator in Hubble images. The upwelling that presumably underlay the storm may therefore have been driven by a Kelvin wave or by moist convection. However, the dynamics of this rare event have yet to be studied in detail.

2.6 Appendix: Proteus Albedo Determination

We determined the total flux of Proteus using a flux bootstrapping method similar to Gibbard, de Pater, and Hammel (2005). Since Proteus was at relatively low signal-to-noise in a background containing considerable scattered light from Neptune, only the flux from the inner core of its point spread function (PSF) could be reliably measured. In order to account for the missing flux in the PSF sidelobes, we measured the flux $F_{0.2}$ from a 0.2″ radius aperture around the standard star, and compared that with the flux from a large aperture containing all the flux F_{tot} from the star. On 25 July a 1.0″ radius aperture was used to compute F_{tot}, and a 0.5″ aperture was used on 26 June. This difference was due to the better atmospheric seeing on 26 June: the bright core of the PSF from HD1160 forced the use of the 128 pixel subarray to avoid saturating the NIRC2 detector, making the field of view too small to use a 1.0″ radius aperture. However, since the PSF was very sharp on 26 June, a 0.5″ radius aperture was sufficient to capture all of the flux. The ratio $F_{0.2}/F_{tot}$ is given in Table 2.2 for each date and band. This correction was then applied to the measured flux from Proteus. The total flux from the moon was also divided by the moon's projected surface area to retrieve an I/F value. We assumed Proteus had a spherical shape with a 210±7 km radius (Karkoschka 2003), which corresponded to ≈0.01″ at our pixel scales of 213 km px^{-1} on 26 June and 210 km px^{-1} on 25 July; this was smaller than Keck's diffraction limit of ≈0.04″ at 1.6 μm, so the moon was unresolved. The final I/F value was simply the geometric albedo and is given in Table 2.2, ignoring phase angle effects. The phase angle was 1.8° on 26 June and 1.2° on 25 July, small enough that Proteus's surface was in near full sun but large enough that coherent backscattering was not yet important (Karkoschka 2001a). The additional error introduced by our flux bootstrapping technique was estimated by varying the inner aperture size from 0.15″ to 0.3″ and recalculating the final I/F value for each; the error was found to be 5-10% except in the Kp filter on 25 July, for which the error was 26%

due to variable atmospheric seeing. The bootstrapping error was added in quadrature to our 20% standard star photometric error, and the total is shown in Table 2.2.

2.7 Appendix: Supplementary Data

Table 2.5 contains information about the amateur and PlanetCam observations used in this paper, and Figure 2.13 shows sample thumbnail images from these observations. Table 2.6 shows central wavelengths and full bandpass widths for all filters referenced in this paper.

2.8 Appendix: Wind Speed Retrievals

The longitude tracking data were fit to a linear wind speed via Markov Chain Monte-Carlo (MCMC) maximum likelihood estimation, implemented by the `emcee` package in `Python` (Foreman-Mackey et al. 2013)[13]. Our application of this technique is explained briefly here.

Assuming a cloud on Neptune drifts at a linear wind speed w, and given a time t_0 at which the cloud's longitude is L_0, the longitude L_m of the cloud at any other time t_n is given by

$$L_m(w, t_n, L_0, t_0) = L_0 + (t_n - t_0)w \tag{2.10}$$

The likelihood function $\ln p$ is then

$$\ln p(L|t, \sigma, w, f) = -\frac{1}{2}\sum_n \left[(L_n - L_m(w, t_n, L_0, t_0))^2 s_n^{-2} + \ln(s_n^{-2})\right] \tag{2.11}$$

where $s_n^2 = \sigma_n^2 + f^2$ is the longitude variance. Writing the variance this way allows for the possibility that the longitude error σ_n (see Section 2.3 for an explanation of how this was determined) was underestimated by some constant amount f. The MCMC algorithm maximizes $\ln p$: in each step of the retrieval, the algorithm chooses values of w and f, uses w to predict longitudes L_m at each time t_n according to Equation 2.10, evaluates how well the longitude data are fit by that model using Equation 2.11, and then chooses a new w and f pair based on the goodness of fit.

Retrievals were carried out separately for the two epochs of observation. Corner plots for both retrievals are shown in Figure 2.14. The retrieval favored nearly Gaussian errors on the wind speed in both epochs, with best-fit values of 201.7 ± 2.2 and 237.4 ± 0.2, respectively. An additional longitude error of $\sim 11^\circ$ was favored by the retrieval in the first epoch (which should be added in quadrature with the original errors), but no additional error term was prescribed in the second epoch. This difference has two possible explanations. First, since half of the measurements in the first epoch were from Lick data whereas most of the measurements in the second epoch were from small telescopes, it is possible that the errors on the Lick data were underestimated while the small telescope errors were correct. The longitude errors from

[13] http://dfm.io/emcee/current/

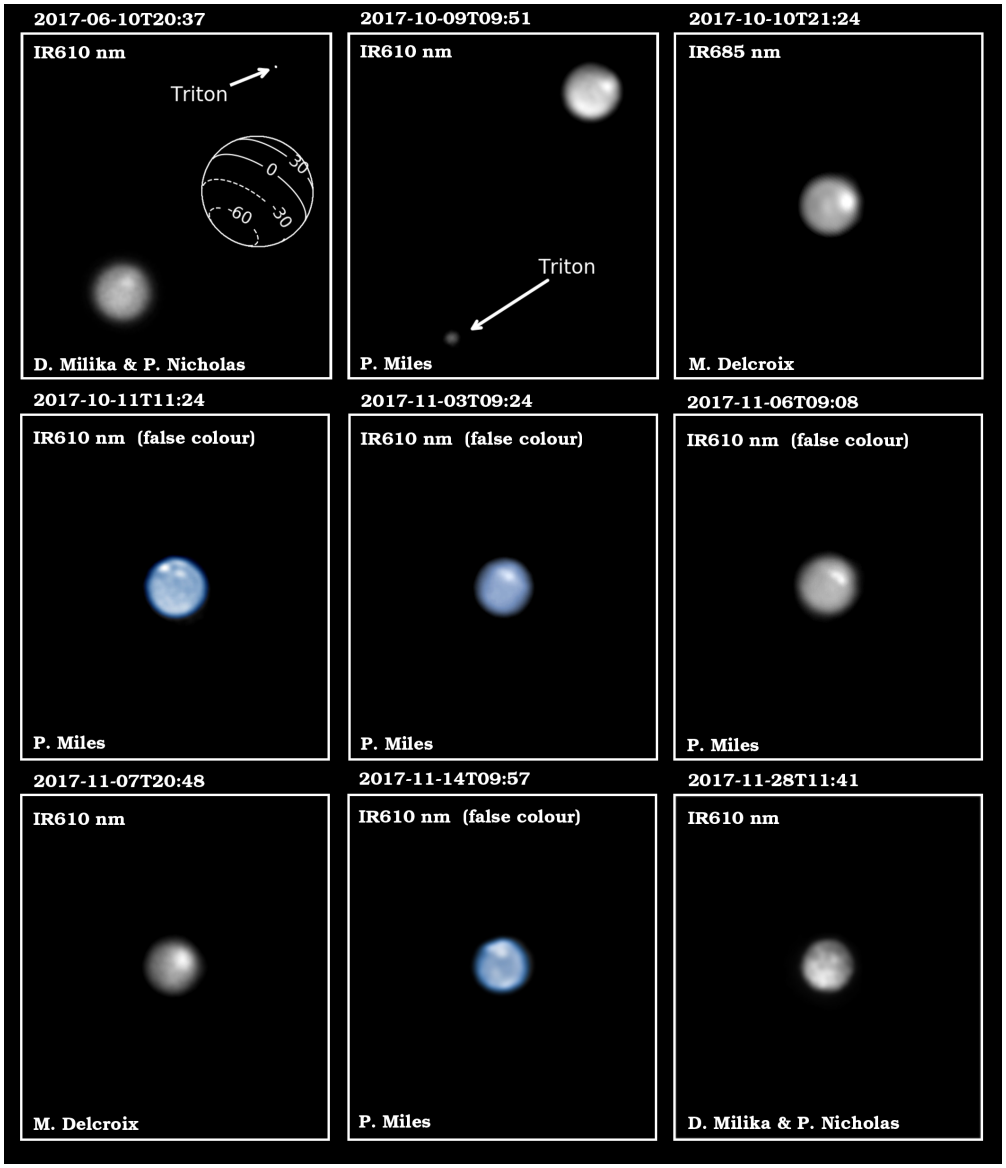

Figure 2.13: Selection of Neptune observations with small telescopes by different observers. Each panel covers a field of view of 29 × 32 arcsec; the orientation is sky North up and sky East to the left in all images. The sequence shows the initial equatorial feature (upper row) since its first observation (upper left panel), and the multiple features observed over November 2017 (middle and bottom rows). All of the images had Triton visible in their original field of view, and the top center panel is offset so that Triton can be seen. Individual observers and filters are identified in each panel.

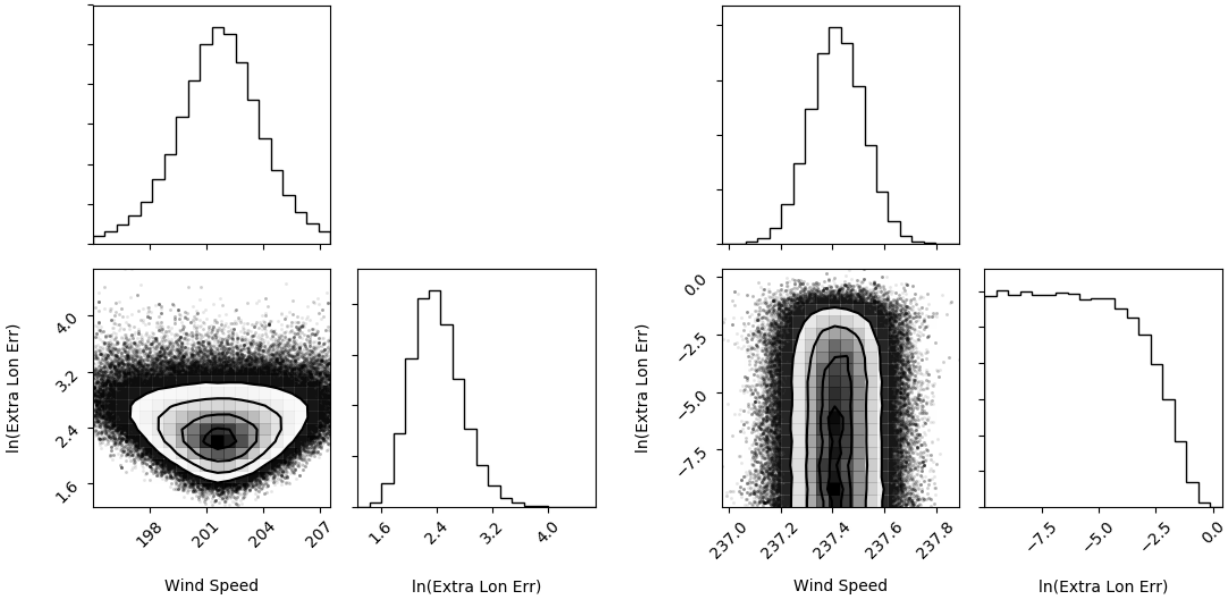

Figure 2.14: "Corner plots" showing the one- and two-dimensional projections of the posterior probability distributions of the MCMC-retrieved parameters for the wind speed retrievals on **Left:** the first epoch of observations, using only the data from 2 to 14 July (where the observations are sampled most densely) and **Right:** the second epoch of observations from 30 September to 26 October.

Lick could be underestimated due to morphological changes in the storm cloud: since Lick resolved the large cloud, the technique used to obtain the storm location actually measured the location of the brightest region of the cloud, which may have changed relative to the rest of the storm over time. The second explanation is simply that a linear wind speed fit did not adequately describe the data over the first epoch; that is, the storm's drift rate was changing over timescales of a few days from 2 to 14 July. This is reasonable because the drift rate certainly changed from 26 June to 25 July, as can be seen by the large residuals in the wind speed fit shown in the first panel of Figure 2.6.

UT Date & Start Time	Observer	Filters
2017-06-10 19:45	Darryl Milika & Pat Nicholas	IR610
2017-07-11 01:53	PlanetCam: Hueso, Ordonez	RG1000
2017-07-11 04:03	PlanetCam: Hueso, Ordonez	M2
2017-07-14 19:22	Darryl Milika & Pat Nicholas	IR610
2017-09-30 13:03	Darryl Milika & Pat Nicholas	IR610
2017-10-04 03:38	Steve Fugardi	IR610
2017-10-09 09:51	Phil Miles	IR610
2017-10-09 10:23	Phil Miles	IR610
2017-10-09 11:13	Phil Miles	IR610
2017-10-10 21:23	Marc Delcroix	IR685
2017-10-11 11:03	Phil Miles	IR610
2017-10-11 11:24	Phil Miles	IR610
2017-10-12 22:40	Martin Lewis	IR610
2017-10-13 02:49	Steve Fugardi	IR610
2017-10-13 20:30	Lucien Polongini	IR610
2017-10-14 12:24	Darryl Milika & Pat Nicholas	IR610
2017-10-15 21:30	Martin Lewis	IR610
2017-10-17 11:07	Darryl Milika & Pat Nicholas	IR610
2017-10-18 21:33	Emmanuel Kardasis	IR610
2017-10-19 17:53	Dimitris Kolovos	IR610
2017-10-20 11:10	Phil Miles	IR610
2017-10-20 11:45	Darryl Milika & Pat Nicholas	IR610
2017-10-21 00:59	Antonio Checco	IR610
2017-10-21 03:13	Steve Fugardi	IR610
2017-10-21 20:30	Dimitri Kolovos	IR610
2017-10-21 20:19	Emmanuel Kardasis	IR610
2017-10-25 13:04	Phil Miles	IR610
2017-10-26 04:36	Blake Estes	IR685
2017-10-26 05:37	Randy Christensen	IR610
2017-10-30 17:14	Clyde Foster	IR610
2017-10-30 17:48	Clyde Foster	IR610
2017-10-31 09:35	Phil Miles	IR610
2017-10-31 11:29	Darryl Milika & Pat Nicholas	IR610
2017-10-31 11:59	Darryl Milika & Pat Nicholas	IR610
2017-10-31 12:23	Darryl Milika & Pat Nicholas	IR610
2017-11-01 21:19	Martin Lewis	IR610
2017-11-02 18:54	Nick Haigh	IR
2017-11-03 09:23	Phil Miles	IR610
2017-11-03 10:26	Phil Miles	IR610
2017-11-04 19:57	Clyde Foster	IR610

2017-11-04 20:10	Clyde Foster	IR610
2017-11-04 20:58	Clyde Foster	IR610
2017-11-06 09:08	Phil Miles	IR610
2017-11-06 10:11	Phil Miles	IR610
2017-11-07 18:36	John Sussenbach	IR685
2017-11-07 18:44	John Sussenbach	IR685
2017-11-07 19:20	Manos Kardasis	IR610
2017-11-07 20:00	Michel Miniou	IR
2017-11-07 20:48	Marc Delcroix	IR610
2017-11-08 11:07	Phil Miles	IR610
2017-11-08 11:36	Darryl Milika & Pat Nicholas	IR610
2017-11-08 11:42	Phil Miles	IR610
2017-11-08 12:25	Phil Miles	IR610
2017-11-10 18:51	Clyde Foster	IR685
2017-11-11 09:48	Phil Miles	IR610
2017-11-11 11:14	Phil Miles	IR610
2017-11-11 12:11	Phil Miles	IR610
2017-11-13 18:04	John Sussenbach	IR685
2017-11-14 09:55	Anthony Wesley	IR610
2017-11-14 09:56	Phil Miles	IR610
2017-11-14 10:08	Phil Miles	IR610
2017-11-14 10:27	Phil Miles	IR610
2017-11-14 10:54	Phil Miles	IR610
2017-11-15 23:30	Almir Germano	IR610

Table 2.5: Description of amateur observations. Filter wavelengths are given in Table 2.6.

Instrument	Filter	λ_c (μm)	$\Delta\lambda$ (μm)
Keck NIRC2	H	1.63	0.30
Keck NIRC2	Kp	2.20	0.35
Keck NIRC2	CH4S	1.59	0.13
Keck NIRC2	PaBeta	1.290	0.019
Lick ShARCS	H	1.66	0.30
Lick ShARCS	Ks	2.15	0.32
HST WFC3	F467M	0.4675	0.0230
HST WFC3	F547M	0.5475	0.0710
HST WFC3	FQ619N	0.6194	0.0062
HST WFC3	F657N	0.6573	0.0094
HST WFC3	F763M	0.7630	0.0780
HST WFC3	F845M	0.8454	0.0870
Calar Alto PlanetCam	RG1000	1.0	0.6
Calar Alto PlanetCam	M2	0.727	0.005
Amateur	IR610	0.610	LP
Amateur	IR685	0.685	LP
Voyager ISS	Clear	0.460	0.360
Voyager ISS	Green	0.585	0.110
Voyager ISS	Orange	0.615	0.050
Voyager ISS	Methane-U	0.540	0.012

Table 2.6: Central wavelengths and full bandpass widths for Keck, Lick, HST, PlanetCam, amateur, and Voyager filters referenced in this paper. "LP" denotes a long-pass filter.

Chapter 3

Thermal Emission from the Uranian Ring System

The published version of this chapter was coauthored by the following individuals, and is included in this thesis with their express permission: Imke de Pater, Michael T. Roman, Leigh N. Fletcher.

The narrow main rings of Uranus are composed of almost exclusively centimeter- to meter-sized particles, with a very small or nonexistent dust component; however, the filling factor, composition, thickness, mass, and detailed particle size distribution of these rings remain poorly constrained. Using millimeter (1.3 - 3.1 mm) imaging from the Atacama Large (sub-)Millimeter Array and mid-infrared (18.7 μm) imaging from the Very Large Telescope VISIR instrument, we observed the thermal component of the Uranian ring system for the first time. The ϵ ring is detected strongly and can be seen by eye in the images; the other main rings are visible in a radial (azimuthally-averaged) profile at millimeter wavelengths. A simple thermal model similar to the NEATM model of near-Earth asteroids is applied to the ϵ ring to determine a ring particle temperature of 77.3 ± 1.8 K. The observed temperature is higher than expected for fast-rotating ring particles viewed at our observing geometry, meaning that the data favor a model in which the thermal inertia of the ring particles is low and/or their rotation rate is slow. The ϵ ring displays a factor of 2-3 brightness difference between periapsis and apoapsis, with $49.1 \pm 2.2\%$ of sightlines through the ring striking a particle. These observations are consistent with optical and near-infrared reflected light observations, confirming the hypothesis that micron-sized dust is not present in the ring system.

3.1 Introduction

To date, observational data for the Uranian ring system were obtained from a combination of Earth-based stellar occultation measurements (French, Nicholson, et al. 1991, and references within), visible-light and radio occultation data from Voyager 2 (e.g., Gresh et al. 1989; Smith, Soderblom, Beebe, et al. 1986; Tyler, Sweetnam, Anderson, Campbell, et al. 1986),

visible-light HST (e.g., Karkoschka 2001b), and ground-based near-IR observations with adaptive optics (e.g., de Kleer, de Pater, et al. 2013; de Pater, Dunn, et al. 2013; de Pater, Gibbard, and Hammel 2006; de Pater, Hammel, et al. 2007). Together, these observations revealed a complex system of ten narrow rings, three broad dusty rings, and at least thirteen associated small satellites (Karkoschka 2001d; Showalter et al. 2006; Smith, Soderblom, Beebe, et al. 1986). The broad spectral coverage of these observations permitted inferences about the particle size distribution of the rings, showing that the narrow rings (except the λ ring) are composed primarily of centimeter- to meter-sized particles, with a very small or nonexistent dust component (Gresh et al. 1989; Karkoschka 2001c). The ϵ ring, the brightest and most massive of the narrow rings, was shown to maintain an appreciable eccentricity ($e = 0.00794$) and an azimuthally-varying width; the ring is five times wider and $\sim$2.5 times brighter in reflected sunlight at apoapsis than at periapsis (French, Elliot, French, et al. 1988; Karkoschka 2001b). However, many fundamental parameters about the ring system remain unknown, including the filling factor, composition, thickness, mass, and detailed particle size distribution of each ring (see review in Nicholson et al. 2018).

In this chapter, we present the first millimeter and mid-infrared observations of the Uranian ring system, obtained in 2017 and 2018 with ALMA at three wavelengths (Band 3; 3.1 mm, Band 4: 2.1 mm, Band 6: 1.3 mm) and the VISIR instrument (Lagage et al. 2004) Q2 filter (18.72 μm) on the Very Large Telescope (VLT). In contrast to images at visible/near-infrared wavelengths, which show the rings in reflected sunlight, our ALMA and VISIR images detect thermal emission from the rings, a component that has never before been imaged. Any contribution from scattered light from Uranus or the Sun is $<$0.01% (see Appendix 3.7). Our observations and data reduction procedures are presented in Section 3.2. We describe how total flux measurements were derived from radial profiles of the rings in Section 3.3, and then compare these total flux measurements to a thermal model of the ϵ ring in Section 3.4. Finally, we present the measured azimuthal structure of the ϵ ring's thermal component in 3.5 before summarizing our results in Section 3.6.

3.2 Observations and Data Reduction

We observed the Uranian ring system at millimeter wavelengths with the Atacama Large (sub-)Millimeter Array (ALMA) and at mid-infrared wavelengths with the VISIR instrument on the VLT between December 2017 and September 2018. An observing log is shown in Table 3.1, and descriptions of our data processing procedures are given in Sections 3.2 and 3.2 for the ALMA and VLT data, respectively. Images of the ring system at all four observed wavelengths are shown in Figure 3.1; each clearly detects the massive ϵ ring.

ALMA Data

The data in each of the three bands were flagged and calibrated by the North American ALMA Science Center using the standard data reduction procedures contained in the

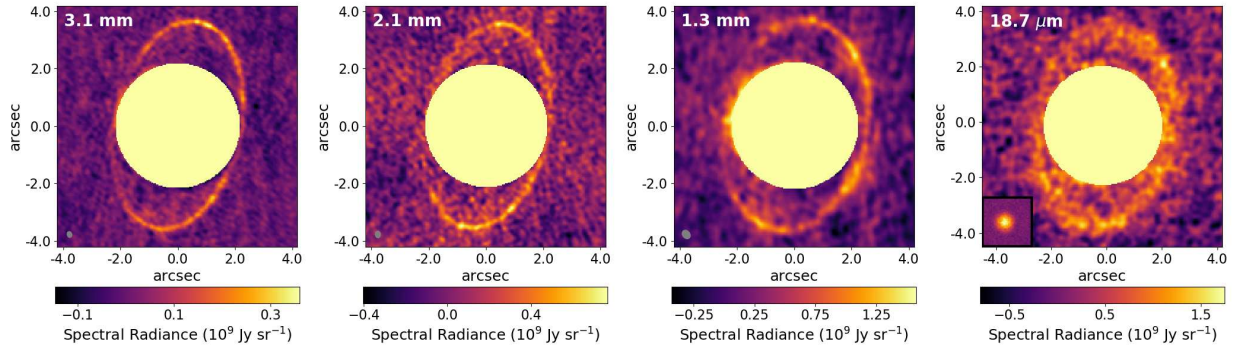

Figure 3.1: Images of the Uranian ring system at 3.1 mm (ALMA Band 3; 97.5 GHz), 2.1 mm (ALMA Band 4; 144 GHz), 1.3 mm (ALMA Band 6; 233 GHz), and 18.7 μm (VLT VISIR; 100 THz). The synthesized beams of the ALMA images are shown as gray ellipses in the bottom left corner of each image, and an image of a point source is shown in the bottom left corner of the VLT 18.7 μm image. The planet itself is masked since it is very bright compared to the rings.

Wavelength	UT Date & Start Time	On-Source Time (min)	Minimum Baseline (m)	Maximum Baseline (m)	Flux & Gain Calibrator	Phase Calibrator
3.1 mm	2017-12-03 23:52	42	41.4	5200	J0238+1636	J0121+1149
3.1 mm	2017-12-06 23:42	42	41.4	3600	J0238+1636	J0121+1149
2.1 mm	2017-12-27 22:56	22	15.1	2500	J0238+1636	J0121+1149
1.3 mm	2018-09-13 07:02	24	15.1	1200	J0237+2848	J0211+1051
18.72 μm	2018-09-04 08:14	42.3	—	—	HD009692 & HD013596	—
18.72 μm	2018-10-03 05:18	42.3	—	—	HD008498 & HD010380	—
18.72 μm	2018-10-13 05:28	42.3	—	—	HD011353 & HD040808	—

Table 3.1: Table of observations.

NRAO's CASA software version 5.1.1. Standard flux and phase calibration procedures were carried out by applying the pipeline using the quasars listed in Table 3.1 as calibrator sources. The CASA pipeline retrieved flux calibration errors of 5.0%, 5.4%, and 5.3% at 3.1 mm, 2.1 mm, and 1.3 mm, respectively. The flux calibration was sanity-checked by comparing the measured total flux of Uranus to previous millimeter-wavelength observations; the result of this exercise is shown in Figure 3.2. To improve the quality of the map, iterative phase-only self-calibration was performed using a procedure similar to that outlined in Brogan et al. (2018) using solution intervals of 20, 10, 5, and 1 minutes in that order. To reduce ringing in the image plane from the presence of a bright planet with sharp edges, a uniform limb-darkened disk model of Uranus was subtracted from the data in the u-v plane, as done in e.g. de Pater, Fletcher, et al. (2014) and de Pater, Sault, Butler, et al. (2016). The disk-subtracted data were inverted into the image plane and deconvolved using CASA's `tclean` function. The ring geometry at the time of observation in each band, taken from

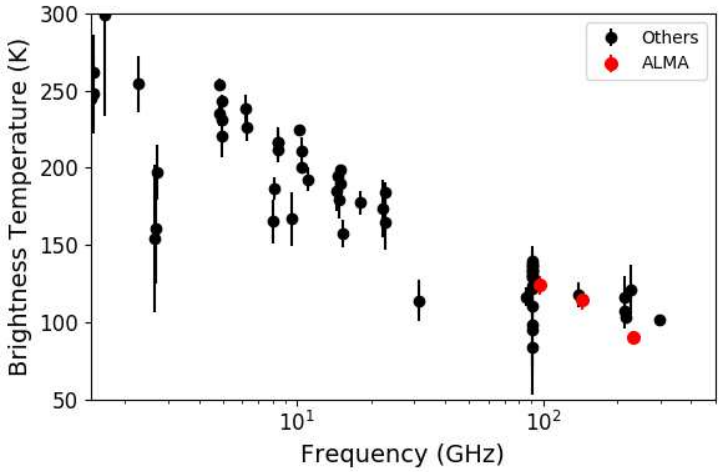

Figure 3.2: ALMA-derived (red; this paper) and literature (black; de Pater and Gulkis 1988; Gulkis and de Pater 1984) measurements of the average millimeter- and radio-wavelength brightness temperature of Uranus's disk.

Wavelength	d (AU)	B_{obs} (degrees)	Ω (degrees)	w (degrees)
3.1 mm	19.2	36.8	192	337 - 341
2.1 mm	19.6	36.4	192	10
1.3 mm	19.1	43.7	190	3
18.72 μm	18.9-19.2	42.7 - 43.9	190	351 - 44

Table 3.2: Observing geometry of the Uranian ring system at the time of our observations. Ω denotes the longitude of the ring plane ascending node, and w denotes the argument of periapsis of the ϵ ring. Ranges of values are shown for the 3.1 mm and 18.7 μm observations because they were taken over the course of several nights.

JPL Horizons[1] and the Planetary Ring Node,[2] are given in Table 3.2.

VLT Data

The 18.72 μm (Q2 filter) VISIR image combined observations from three nights in September and October 2018; details of these observations are listed in Table 3.1. Data from each night were reduced with standard infrared chopping and nodding techniques using the European Southern Observatory VISIR pipeline, and resulting images were flux calibrated via com-

[1]https://ssd.jpl.nasa.gov/horizons.cgi
[2]https://pds-rings.seti.org/

parison to observed standard stars using custom-written `IDL` routines. The three calibrated images were then combined and weighted by the inverse of their errors squared to yield the final, absolutely calibrated mean image. Random errors were estimated from the standard deviation of the background sky, and we estimate a 20% systematic error in radiance due to the uncertainty in the stellar flux and sky subtraction (Dobrzycka et al. 2008).

3.3 Radial Profiles and Total Flux Measurements

We measured the radial profile of the rings in each ALMA image by integrating the rings in azimuth as follows. First, the images were divided into elliptical annuli using the `astropy`-affiliated `photutils` Python package (Bradley et al. 2019). Each annulus was centered at the center of Uranus and given an eccentricity and angle of rotation such that it mimicked a circular annulus projected into Uranus's ring plane. Each annulus was given a ring-plane width of 500 km, and the ring-plane radius of the annulus inner edge was varied in steps of 500 km from 35000 km to 64500 km. The planet Uranus was masked out to a distance equal to its mean radius plus three times the ALMA full beam width at half power in each observing band. The `photutils` package was used to compute the geometric fraction of each pixel contained within a given annulus, weight the flux within that pixel according to that fraction, then sum up the weighted flux of all unmasked pixels. This provided a total flux measurement within the exact elliptical region specified by each annulus (ignoring any masked pixels). The result was a radial flux profile of the ring system in which each unmasked pixel was counted exactly once total, splitting its flux between two annuli if it fell on an annulus edge. The error σ_n on each flux measurement was taken to be the RMS noise in the image (computed far from the planet and rings) times the area of the annulus (not including any masked pixels) in units of the synthesized beam area. The observed profile is shown in Figure 3.3.

The radial flux profile was modeled as the sum of flux contributions from the 6/5/4, α/β, $\eta/\gamma/\delta$, and ϵ ring groups. Each of the narrow main rings (6, 5, 4, α, β, η, γ, δ, ϵ) was projected separately (i.e. one 2-D model per ring, ignoring all other rings) onto a very high resolution (0.01″/pixel) 2-D grid with proper semimajor axis, eccentricity, inclination, and observing geometry[3] using the `PyAstronomy` package in `Python`[4]. These super-resolution model rings were convolved with the Gaussian synthesized beam of ALMA, then summed into a radial profile in the same way as the data (see previous paragraph). The result of this exercise was a 1-D pseudo-Gaussian profile of each ring on each observing date that accounted for its eccentricity. These ring profiles were weighted according to their equivalent widths at visible wavelengths as measured by stellar occultations (French, Elliot, and Levine 1986), added together, and then scaled by eye to match the data to produce an a-priori model radial profile of the ring system. A suite of models was then produced in a Markov Chain

[3]Ephemeris data were taken from JPL Horizons and the Planetary Ring Node.

[4]https://github.com/sczesla/PyAstronomy

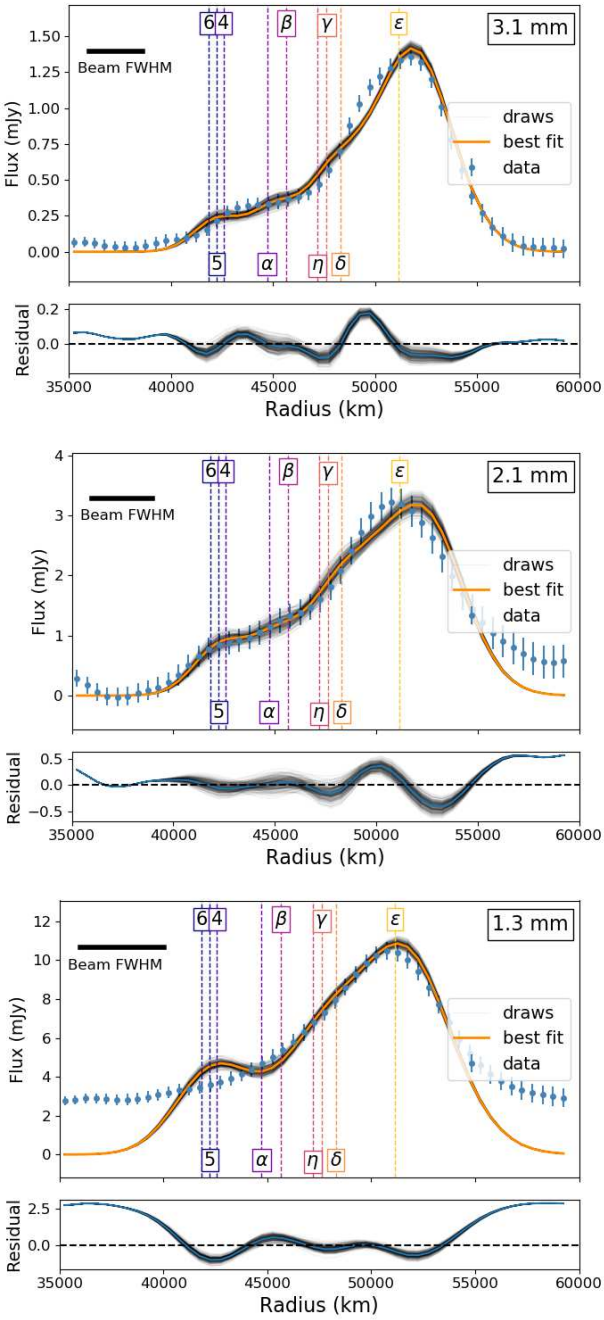

Figure 3.3: Radial flux profiles of the Uranian ring system at 3.1 mm, 2.1 mm, and 1.3 mm. The data, binned into 500 km intervals, are shown as blue dots. The best-fitting model is shown as an orange line, and draws from the distribution of allowed models are shown as thin gray lines. Locations of the main rings are labeled.

Wavelength (mm)	UT Date	B_{obs} (degrees)	Total Flux, F_ν (mJy) 6/5/4	α/β	$\eta/\gamma/\delta$	ϵ
3.1	2017-12-03	36.8	1.29 ± 0.15	1.91 ± 0.19	2.77 ± 0.22	13.73 ± 0.73
2.1	2017-12-27	36.4	5.19 ± 0.67	6.49 ± 0.80	8.15 ± 0.89	36.0 ± 2.2
1.3	2018-09-13	43.7	35.5 ± 2.4	15.5 ± 2.2	44.4 ± 3.2	112.2 ± 6.3

Table 3.3: Total millimeter flux measurements of each ring group. B_{obs} denotes ring opening angle with respect to the observer. Note that two observations were taken at 3.1 mm, on 2017-12-03 and 2017-12-06, and co-added.

Monte Carlo (MCMC) framework implemented using the Python `emcee` package[5] (Foreman-Mackey et al. 2013), wherein the fluxes F_{654}, $F_{\alpha\beta}$, $F_{\eta\gamma\delta}$, and F_ϵ of the four ring groups were allowed to vary freely while the relative contribution from each ring within a group was set according to its visible-wavelength equivalent width (French, Elliot, and Levine 1986). The flux of the 1-D model profile F_m at all radii r was thus fully specified by the fluxes of the four ring groups. Letting $\theta = [F_{654}, F_{\alpha\beta}, F_{\eta\gamma\delta}, F_\epsilon]$, the likelihood function $\ln p$ was given by

$$\ln p(F|r, \sigma, \theta) = -\frac{1}{2}\Sigma_n \Big[(F_n - F_m(\theta))^2 \sigma_n^{-2} + \ln(\sigma_n^{-2})\Big] \tag{3.1}$$

where σ_n^2 was the variance of the measured fluxes at each radius F_n. The MCMC simulation produced posterior probability distributions of F_{654}, $F_{\alpha\beta}$, $F_{\eta\gamma\delta}$, and F_ϵ, which are given in Appendix 3.8 Figures 3.7, 3.8, and 3.9 for images at 3.1 mm, 2.1 mm, and 1.3 mm wavelengths, respectively. The probability distributions show that mild degeneracy between the fluxes of the ring groups is present, and was most apparent at 1.3 mm, where the spatial resolution was poorest. The mean flux values of each group are given in Table 3.3. The uncertainties given in that table are a quadrature sum of the standard deviation of the MCMC-derived probability distribution and the flux calibration error (Section 3.2). Those mean values were used to generate the best-fitting radial profiles shown in orange in Figure 3.3, and random sets of θ values drawn from the MCMC samples were used to produce the light gray model profiles shown in the same figure.

The lower resolution and SNR of the VLT Q2 image precluded retrieval of the ϵ ring flux from a radial profile. We instead measured the total flux within an elliptical annulus of 3 beam-widths thickness ($\sim$33 pixels) centered on the ϵ ring. To minimize contamination from the bright planet, we masked the planet such that the pixels within two beam widths of the planet's outer edge were omitted from the calculated ring flux. The choice of the mask size was informed by line scans through the images along the ansae, where the contributions from the rings and planet were most cleanly separated. Due to the viewing geometry, the PSFs from the ring system and the planet partly overlapped away from the ansae; the masking consequently removed more pixels from these portions of the contributing ellipse and potentially underestimated the flux of the rings. To evaluate the accuracy of our approach,

[5]http://dfm.io/emcee/current/

we applied the same method to synthetic images with azimuthally-uniform rings of known brightness, blurred by the observed PSF of our images and corrupted by different manifestations of synthetic noise. These tests showed that neglecting any attempt at correcting for the planetary contribution overestimated the ring flux by nearly 20%, while the simple mask tended to underestimate the ring flux by less than 10%. We therefore conservatively estimate our measured ring system total flux is accurate to within 20%. Finally, we assumed the contribution of the ϵ ring to the total flux of the ring system was the same at 18.7 μm as at 3 mm to get an approximate ϵ ring flux.

We find the best fit to the 3.1 mm radial profile with total fluxes relative to the ϵ ring of $9.4 \pm 1.4\%$, $13.9 \pm 1.4\%$, and $20.2 \pm 1.6\%$ for the 6/5/4, α/β, and $\eta/\gamma/\delta$ groups. These values are close to the relative equivalent widths at visible wavelengths, which French, Elliot, and Levine (1986) give as 7%, 16%, and 15%, respectively. However, at shorter wavelengths we find the 6/5/4 and $\eta/\gamma/\delta$ groups to be much brighter than expected based on the equivalent width measurements, by factors of 2.1 and 1.5 at 2.1 mm and 4.4 and 2.7 at 1.3 mm. This discrepancy may be due to unmodeled contributions from diffuse millimeter-sized dust between the inner rings, a larger fraction of millimeter-sized grains in those ring groups than in the ϵ ring, or systematic errors due to imperfect subtraction of the PSF around the bright planet. The latter effect may be especially consequential at 1.3 mm due to the poorer resolution of our data at that frequency.

The ring is bathed by the cosmic microwave background (CMB) from every angle, except from the angles where it is blocked by Uranus. The final reported brightness temperature of Uranus was corrected to account for the blocked CMB photons according to the prescription in de Pater, Fletcher, et al. (2014), which gives correction factors of 1.02 K, 0.59 K, and 0.12 K at 3.1 mm, 2.1 mm, and 1.3 mm, respectively. If that CMB correction is undone (that is, Uranus is assumed to be fainter than it really is), then the CMB appears to reach the rings fully isotropically and thus be scattered isotropically. The interferometer is insensitive to scattered CMB photons from the rings since it, too, is bathed isotropically by the CMB; thus, the measured flux from the rings does not need to be corrected for the CMB (Dunn et al. 2005; Zhang et al. 2019).

3.4 Thermal Modeling of the ϵ Ring

We converted the ϵ ring total flux measurements derived in Section 3.3 into spectral radiance (hereafter, "brightness") units to produce a coarse spectrum of the ring. To do so, we simply divided the total flux measurements by the projected geometric area of the ϵ ring, which was computed as follows. Let the measured width of the ring at periapsis and apoapsis be denoted w_p and w_a (19.7 km and 96.4 km for the ϵ ring Karkoschka 2001c). The inner and outer edge of the ring are defined by two ellipses sharing one focus (the center of mass of Uranus) but with semimajor axes a and eccentricities e such that w_p and w_a take their measured values. The inner ellipse has $a_{inner} = a - (w_p + w_a)/4$ and the outer ellipse has $a_{outer} = a + (w_p + w_a)/4$. To keep the focus at the same location requires the equation

$a_{outer} - c_{outer} = a_{inner} - c_{inner} + w_p$ to be satisfied, where $c = ae$ is the focal distance of the ellipse. The equation is satisfied when $c_{outer} - c_{inner} = (w_a - w_p)/2$. Thus the area is given by

$$A_r = \pi a_{outer}^2 \sqrt{1 - e_{outer}^2} - \pi a_{inner}^2 \sqrt{1 - e_{inner}^2} \tag{3.2}$$

Projecting into the observing geometry and scaling to the observer-Uranus distance yields an angular area of $\Omega_{r,obs} = A_r \sin B/d^2 = 1.57 \times 10^{-12}$ steradians.

We compare these four brightness measurements to a simple thermal model modified from the NEATM model for near-earth asteroids (Harris 1998) to constrain the properties of the ϵ ring. The model gives the measured temperature T of a ring particle as

$$T^4 = \frac{L_\odot(1 - A_B)}{4\pi\bar{\eta}\sigma\epsilon d^2} \tag{3.3}$$

where $L_\odot$ is the solar luminosity, d is the heliocentric distance to the asteroid, ϵ is the bolometric emissivity of the asteroid, A_B is the Bond albedo, σ is the Boltzmann constant, and $\bar{\eta}$ is the "beaming factor", a catch-all correction factor for low-phase-angle beaming, rotation, thermal inertia, and geometry (see Section 3.4 for a discussion of how $\bar{\eta}$ differs from the standard NEATM model's η). To translate this temperature into a brightness S_ν we use the equation

$$S_\nu = f(B)B(\nu, T) \tag{3.4}$$

where $B(\nu, T)$ is the Planck function at frequency ν and temperature T, and $f(B)$ is the ring's "fractional visible area", the fraction of paths from the observer through the projected geometric ring area that strike a ring particle (as opposed to passing through to background space).

We performed a Markov Chain Monte Carlo (MCMC) sampling of our model's parameter space using the `emcee` Python package (Foreman-Mackey et al. 2013) to explore the probability distributions of the free parameters in the thermal model. We allowed four parameters to vary: η, ϵ, and A_B in Equation 3.3, and $f(B)$ in Equation 3.4. We treated η, ϵ, and $f(B)$ as completely unknown, but provided a Gaussian prior on A_B with mean value 0.061 and standard deviation 0.006 (Karkoschka 1997). In each MCMC iteration, a set of these parameters was drawn and plugged into the NEATM model, yielding a Planck function. The value of that Planck function at the ALMA- and VLT-observed frequencies was compared with the measured ring group brightness using a likelihood function similar in form to Equation 3.1. The simulation constrains the fractional visible area to $f(B) = 0.491 \pm 0.022$ and the particle temperature to $T = 77.3 \pm 1.8$ K; the best-fit model, as well as a suite of random model draws from the posterior distribution, are plotted against the observed ϵ ring total flux in Figure 3.4. That figure also shows posterior probability distributions for $f(B)$ and T, and a full "corner plot" displaying the one- and two-dimensional projections of the posterior probability distribution is shown in Appendix Figure 3.10. The two figures show that $\bar{\eta}$ and the emissivity are completely degenerate with one another, and the retrieved albedo values are constrained only by the Karkoschka (1997) prior; however, the fractional visible area

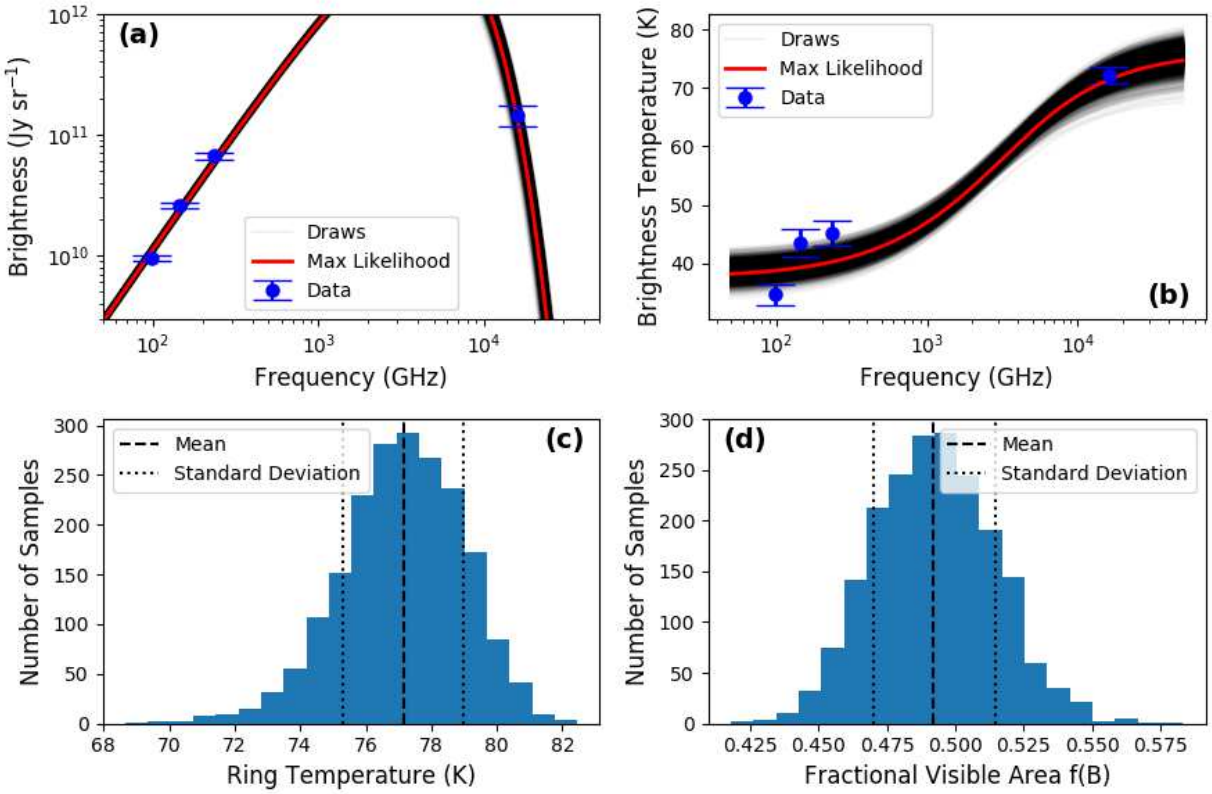

Figure 3.4: **(a)** Brightness and **(b)** brightness temperature comparison between retrieved NEATM model (red line: maximum-likelihood model, translucent black lines: random draws from probability distribution) and ϵ ring brightness measurements (blue points). **c)** Probability distribution function of ϵ ring temperature. **(d)** Probability distribution function of fractional visible area of ϵ ring. The mean value and quartiles are shown as dashed and dotted black lines, respectively.

$f(B)$ and temperature T (derived by combining $\bar{\eta}$, ϵ, and A_B) are strongly constrained and minimally degenerate with one another.

Our derived fractional visible area is consistent with the Karkoschka (2001c) model, which gives $f(B) \approx 0.5$ at zero phase angle for a ring opening angle $B = 40°$ (B ranges from 37° to 44° for our observations). The emissivity of the ring cannot be constrained since it is degenerate with $\bar{\eta}$ and both are unknown a-priori. However, the product of the two quantities is determined to be $\bar{\eta}\epsilon = 1.62 \pm 0.17$. If we assume the ring particles are perfect graybody emitters such that $\epsilon = 1 - A_B$, then $\bar{\eta}$ takes a best-fit value of 1.72. This $\bar{\eta}$ value is larger, and the observed temperature is lower, than expected from the Standard Thermal Model for near-Earth asteroids (STM; Lebofsky, Sykes, et al. 1986), which assumes very low

thermal inertia and/or slow rotation such that all flux is emitted on the sun-facing side of the particle, leading to a predicted temperature $T_{STM} = 79.5$ K. However, $\bar{\eta}$ is smaller and T higher than expected for a particle with thermal timescales long enough and rotation fast enough that the particle's temperature is independent of longitude as in the Fast-Rotating Model (FRM) (Lebofsky and Spencer 1989), which yields $T_{FRM} = 71.5$ K (sub-solar latitude $\approx$40°; see Section 3.4 for a description of our ring particle thermal model). This finding may indicate that the ring particles are closer to STM-like than FRM-like; that is, their thermal inertia is low enough, and their rotation rate is slow enough, that their dayside and nightside temperatures are different at a given latitude. However, beaming due to surface roughness tends to increase the amount of flux an observer sees, leading to lower $\bar{\eta}$ values and higher observed temperatures (Lagerros 1998; Spencer et al. 1989, and references within). Surface roughness is not included in our model, so we cannot disentangle the effects of beaming from the effects of thermal inertia.

Ring Particle Model

The NEATM-like model we employ defines $\bar{\eta}$ as a property of the ring particles as a whole according to Equation 3.3. This differs slightly from the original NEATM model (Harris 1998), which defines η as a function of the temperature at the sub-solar point T_0 such that $T_0^4 \propto \eta$ and $T(\mu) = T_0\mu^{1/4}$, where μ is the cosine of the emission angle. That is, $\bar{\eta}$ represents a geometric average while η does not. To determine the physical meaning of our observed value of $\bar{\eta}$ for the ϵ ring, we produced a toy model of a ring particle. The model assumes a spherical particle with no surface roughness and no lateral heat conduction within the particle. The mean diurnal insolation $\bar{Q}$ for such a particle is given by

$$\bar{Q} = \frac{L_\odot}{4\pi d^2}\frac{1}{\pi}\Big(h_0 \sin\phi \sin\delta + \cos\phi\cos\delta\sin h_0\Big) \tag{3.5}$$

(Pierrehumbert 2010), where δ is the sub-solar latitude of the particle, ϕ is the latitude at a given location on the particle, and h_0 is the hour angle at sunrise and sunset in radians at a given location ($\cos h_0 = -\tan\phi\tan\delta$), which is equal to π times the fraction of the day that location spends in sunlight (note that h_0 is set to π at the summer pole and zero at the winter pole). The temperature at each point is given by $T(\phi) = \bar{Q}^{1/4}$, and the total flux from the particle at the observed frequencies is found by applying a Planck function at each point on the model particle, then taking the mean. We retrieve a blackbody temperature T of the particle as a whole by fitting a single Planck function to these model flux values. Finally, $\bar{\eta}$ is found by comparing T to the subsolar temperature of the STM at the same distance: $1/\bar{\eta} = (T/T_{0,STM})^4$. Taking $T_{0,STM} = 88.3$ K as appropriate at Uranus's distance, this procedure yields $T = 79.5$ and $\bar{\eta} = 1.5$ for the STM as well as $T = 64.1$ and $\bar{\eta} = 3.6$ for the FRM. The FRM-derived temperature depends on the orientation of a particle's rotation axis with respect to the Sun, and the dense packing of the ϵ ring means its particles are likely to undergo frequent collisions that lead to a large spread in rotation axis orientations. However, the total angular momentum of the ring system should dictate that the average

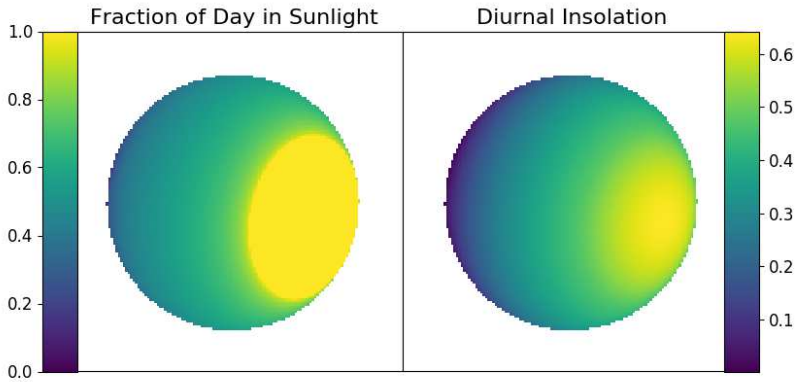

Figure 3.5: **Left:** Fraction h_0/π of one rotation period that a model ring particle spends in sunlight. **Right:** Diurnal mean insolation $\bar{Q}$ of a model ring particle, normalized to the insolation received by a non-rotating (STM-like) model particle at the sub-solar point.

rotation axis is aligned with that of Uranus, so we assume this average rotation axis (sub-solar latitude ≈40°) for all ring particles. Spatial variations in h_0/π and $\bar{Q}$ are mapped in Figure 3.5 for this geometry. In this case, our model yields $T = 71.5$ and $\bar{\eta} = 2.3$. This temperature is lower, and $\bar{\eta}$ is higher, than retrieved from the data.

3.5 Azimuthal Structure

We searched for azimuthal structure in the ϵ ring by breaking the ring into 30 bins, each subtending 12° of azimuth and having a width equal to two times the FWHM of the ALMA point-spread function. The measured brightness in these bins as a function of angle from periapsis is shown in Extended Data Figure 3.6. We find the ϵ ring to be a factor of 2-3 brighter at apoapsis than at periapsis at 3.1 and 2.1 mm, in good agreement with stellar occultation measurements (French, Elliot, and Levine 1986), visible/infrared reflected light observations (de Pater, Dunn, et al. 2013; de Pater, Gibbard, Macintosh, et al. 2002; Karkoschka 1997) and radio occultation measurements (Gresh et al. 1989). No clear periapsis-apoapsis asymmetry is seen at 1.3 mm or 18.7 μm; however, the signal-to-noise ratio is lower in those data, and due to the poorer resolution of those data the measurements are contaminated by the presence of the inner rings to a greater extent. Note that we exclude the portions of the ring nearest (in projection) to Uranus due to contamination by imaging artifacts arising from the very millimeter-bright planet.

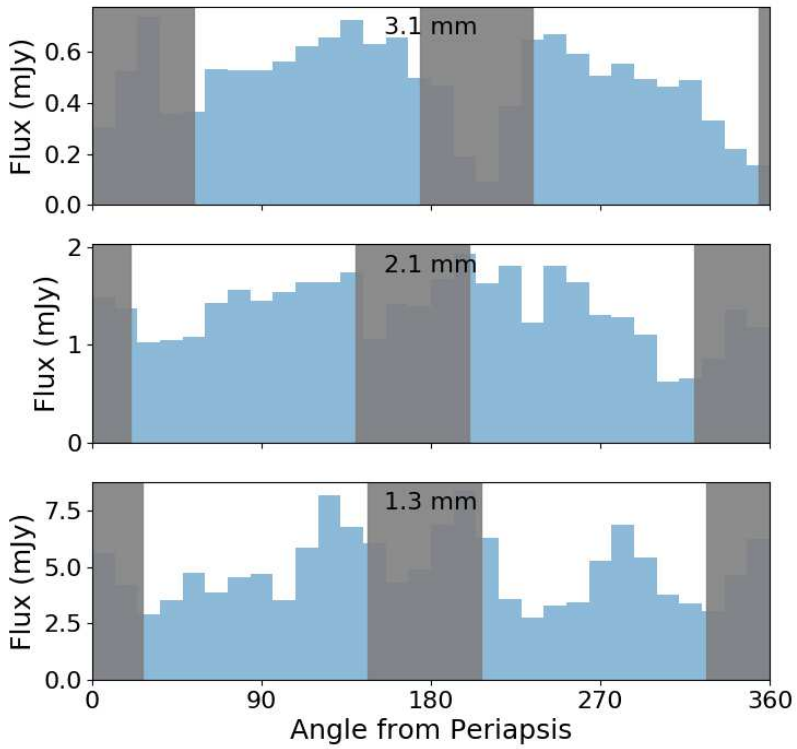

Figure 3.6: ϵ ring brightness as a function of azimuth. The grayed-out regions are contaminated by artifacts from the bright planet. A clear periapsis-apoapsis asymmetry is present at 3.1 mm and 2.1 mm wavelengths.

3.6 Summary

Using ALMA and the VLT VISIR instrument, we have observed the thermal emission component of the Uranian ring system for the first time. Our observations of the ϵ ring agree very well with the Karkoschka (2001c) model, supporting its derivation of the fractional visible area as a function of ring opening angle, and the 3.1 mm brightnesses of the inner main ring groups take the same ratio as observed at visible wavelengths. The consensus between our millimeter and mid-infrared observations and literature visible-wavelength observations shows that the properties of the main rings remain the same at any observed wavelength despite the fact that our observations are not sensitive to micron-sized dust. This finding confirms the hypothesis, proposed based on radio occultation results (Gresh et al. 1989), that the main rings are composed of centimeter-sized or larger particles. A simple thermal

model similar to the NEATM model for asteroids was applied to determine that the ϵ ring particles display roughly black-body behavior at millimeter/mid-infrared wavelengths at a temperature of 77 ± 2 K, suggesting the particles' thermal inertia may be small enough and rotation rate slow enough, to induce longitudinal temperature differences between their day-side and nightside. Observations at higher spatial resolution, achievable using ALMA, would resolve the inner main rings separately and quantify the millimeter-sized dust component if present.

3.7 Appendix: Scattered Light Contribution

We adopt a simple analytical radiative transfer calculation (after Chandrasekhar 1960) to determine the contribution of scattered millimeter-wavelength light from Uranus to the millimeter brightness of the ϵ ring. The radiative transfer equation reads:

$$\frac{dI_\nu}{d\tau_\nu} = S_\nu - I_\nu \tag{3.6}$$

where $S_\nu = j_\nu/\alpha_\nu$ is the source function. For scattered light from direction (θ', ϕ') into direction (θ, ϕ), the source function is given by

$$S_\nu(\theta, \phi) = \varpi_\nu \int_{4\pi} \frac{p(\Theta)}{4\pi} I_\nu(\theta', \phi') d\Omega' \tag{3.7}$$

where $p(\Theta)$ is the scattering phase function, Θ is the scattering angle, ϖ_ν is the single-scattering albedo, and $\int_{4\pi} I_\nu(\theta', \phi') d\Omega'$ is the flux density incident on the rings from the entire 4π steradian sky. Since light from Uranus is the only contributor to the incident radiation at the ϵ ring,

$$\int_{4\pi} I_\nu(\theta', \phi') d\Omega' = I_{\nu,u} \Omega_{u,r} \tag{3.8}$$

where $I_{\nu,u}$ is the specific intensity of Uranus at the observed frequency and $\Omega_{u,r}$ is the solid angle of Uranus as seen from the ring. Then the source function of the rings reads

$$S_\nu = \varpi_\nu \frac{p(\Theta)}{4\pi} I_{\nu,u} \Omega_{u,r} \tag{3.9}$$

To convert this into a flux density as seen from ALMA, we must multiply by the solid angle of the rings with respect to the observer $\Omega_{r,obs}$:

$$F_{\nu,r,obs} = \varpi_\nu \frac{p(\Theta)}{4\pi} I_{\nu,u} \Omega_{u,r} \Omega_{r,obs} \tag{3.10}$$

The specific intensity is the same for any observer, so the same $I_{\nu,u}$ measured by ALMA would be measured by an observer at the ϵ ring, and thus

$$I_{\nu,u} = \frac{F_{\nu,u,r}}{\Omega_{u,r}} = \frac{F_{\nu,u,obs}}{\Omega_{u,obs}} \tag{3.11}$$

where $F_{\nu,u,r}$ and $F_{\nu,u,obs}$ denote the spectral flux density of Uranus as seen from the rings and from Earth, respectively. Substituting Equation 3.11 into Equation 3.10, we have

$$F_{\nu,r,obs} = \varpi_\nu \frac{p(\Theta)}{4\pi} \frac{\Omega_{u,r}\Omega_{r,obs}}{\Omega_{u,obs}} F_{\nu,u,obs} \tag{3.12}$$

The solid angle is defined as $\Omega = A/d^2$, where A is the projected area of an object and d is the distance from that object to the observer, so

$$\frac{\Omega_{u,r}}{\Omega_{u,obs}} = \frac{A_u d_{obs}^2}{A_u r_r^2} = \frac{d_{obs}^2}{r_r^2} \tag{3.13}$$

where A_u is the cross-sectional area of Uranus and r_r is the distance from Uranus to the ϵ ring. Combining this with the fact that $\Omega_{r,obs} = A_{r,obs}/d_{obs}^2$, where $A_{r,obs}$ is the cross-sectional area of the ϵ ring with respect to the observer, we end up with

$$F_{\nu,r,obs} = \varpi_\nu \frac{p(\Theta)}{4\pi} \frac{A_{r,obs}}{r_r^2} F_{\nu,u,obs} \tag{3.14}$$

This derivation assumed that the entire area of the ring is illuminated by light from Uranus as seen by the observer. However, due to shadowing and gaps in the ring, only a fraction of the ring $f(B_u, B)$ is illuminated, where B_u denotes the ring opening angle for an observer on Uranus and B denotes the ring opening angle for an observer on Earth. In reality, the flux comes from a distribution of angles: the diameter of Uranus is roughly 52.6° at the distance to the ϵ ring, giving ring opening angles between −26.3° and 26.3°. To evaluate $f(B_u, B)$ precisely is a difficult task, since one must integrate over many Uranus-ring-observer angles. To simplify the problem, we shall make two assumptions. First, we assume B_u is well represented by the geometric average opening angle $B_u = 18.4°$ (the orbital inclination of the ring with respect to Uranus is $i = 0.001°$, which is negligible). Second, we assume that half of the ring area illuminated by light from Uranus can be seen from Earth, to account for surfaces that point away from the observer. Under these assumptions, $f(B_u, B) = f(B_u)/2$, and we can again use the Karkoschka (2001c) prescription to calculate $f(B_u)$. Since the photons originate from Uranus itself, the phase angle is 0° and the model gives us $f(B_u, B) = f(18.4)/2 = 0.18$. The physical interpretation of such a low value is that at small incident angles particles cast long shadows on each other, blocking much of the flux. Applying this correction to Equation 3.14 gives us

$$F_{\nu,r,obs} = f(B_u, B)\varpi \frac{p(\Theta)}{4\pi} \frac{A_{r,obs}}{r_r^2} F_{\nu,u,obs} \tag{3.15}$$

Since the particles in the ϵ ring are assumed to be $\gtrsim$10 cm in diameter (Gresh et al. 1989; Karkoschka 2001c), we assume a phase function $p(\Theta) = 1$ appropriate for geometric scattering.

Our ALMA observations give the total 3 mm flux density of Uranus to be $F_{\nu,u,obs} = 8.80$ Jy. We assume the ring particles have albedo $\varpi_{3mm} = 1 - \epsilon_{3mm} = 0.05$. For simplicity,

we take $r_r = 51148$ km, the average of the ϵ ring semimajor and semiminor axes. At ring opening angle $B_{obs} = 36.77°$, the projected ring area is $A \sin B_{obs} = 1.11 \times 10^7$ km^2. Plugging these numbers into Equation 3.15 yields $F_{3mm,r,obs} = 28$ μJy. This value is a factor of $\sim$500 smaller than the measured ring flux at 3.1 mm. Since both the planet and rings are at least relatively near the same temperature, the ratio between the reflected thermal emission from the planet and the direct thermal emission from the rings is nearly wavelength-independent, and similarly small values are found in the mid-infrared. While many simplifying assumptions were made in this derivation, such a small scattered light contribution means that scattered light from Uranus can be ignored.

Equation 3.15 can be applied to quantify the contribution of scattered radio flux from the Sun with the following modifications. The fraction $f(B_\odot, B)$ can once again be taken from the Karkoschka (2001c) model, where $B_\odot$ is the ring opening angle as viewed from the Sun (in fact, this geometry is the scenario for which the model was developed). Instead of the Uranus-ring distance r_r, the distance from the Sun to the ring $d_{\odot,r}$ should be used. Finally, the Sun's radio flux at Earth $F_{\nu,\odot,obs}$ replaces $F_{\nu,u,obs}$. Thus we have

$$F_{\nu,r,obs} = f(B_\odot, B)\varpi \frac{p(\Theta)}{4\pi} \frac{A_{r,obs}}{d^2_{\odot,r}} F_{\nu,\odot,obs} \tag{3.16}$$

At the time of our 3.1 mm observations, the phase angle was very nearly 2°, so the Karkoschka (2001c) model gives $f(B_\odot, B) = 0.5$. Alissandrakis et al. (2017) used ALMA observations to find a solar brightness temperature of 7250 ± 170 K at 100 GHz, as well as a solar radius of $964.1 \pm 4.5''$ at 1 AU at 100 GHz. Assuming the same temperature and radius at 97.5 GHz (3.1 mm), we get $F_{\nu,\odot,obs} = 1.45 \times 10^8$ Jy. Finally, taking $d_{\odot,r}$ at the time of observation from JPL Horizons, we find $F_{\nu,r,obs} = 0.38$ μJy, which is $\sim$0.002% of the measured flux. At 18 μm wavelengths, we find $F_{\nu,r,obs} = 7.8$ mJy, or $\sim$2% of the measured flux; this is much smaller than the 20% VLT flux calibration error and so is ignored.

3.8 Appendix: Extended Data

Figures 3.7, 3.8, and 3.9 display "corner plots" for the MCMC-derived total flux measurements discussed in Section 3.3. Figure 3.10 displays a corner plot for the thermal model discussed in Section 3.4.

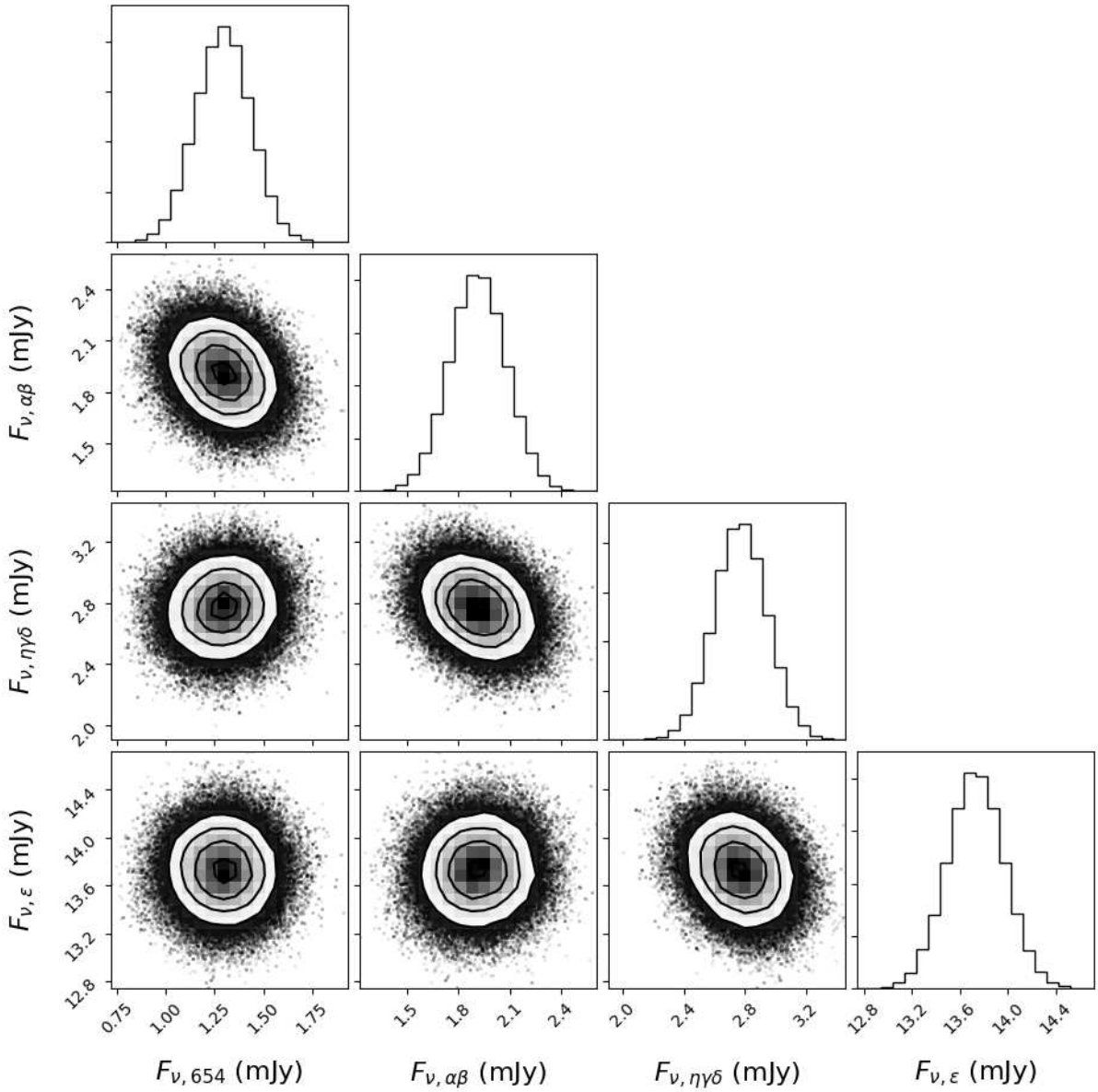

Figure 3.7: "Corner plot" showing the one- and two-dimensional projections of the posterior probability distributions of the MCMC-retrieved total fluxes of each ring group in Band 3 (3.1 mm), derived from comparing our model to the observed the radial profile.

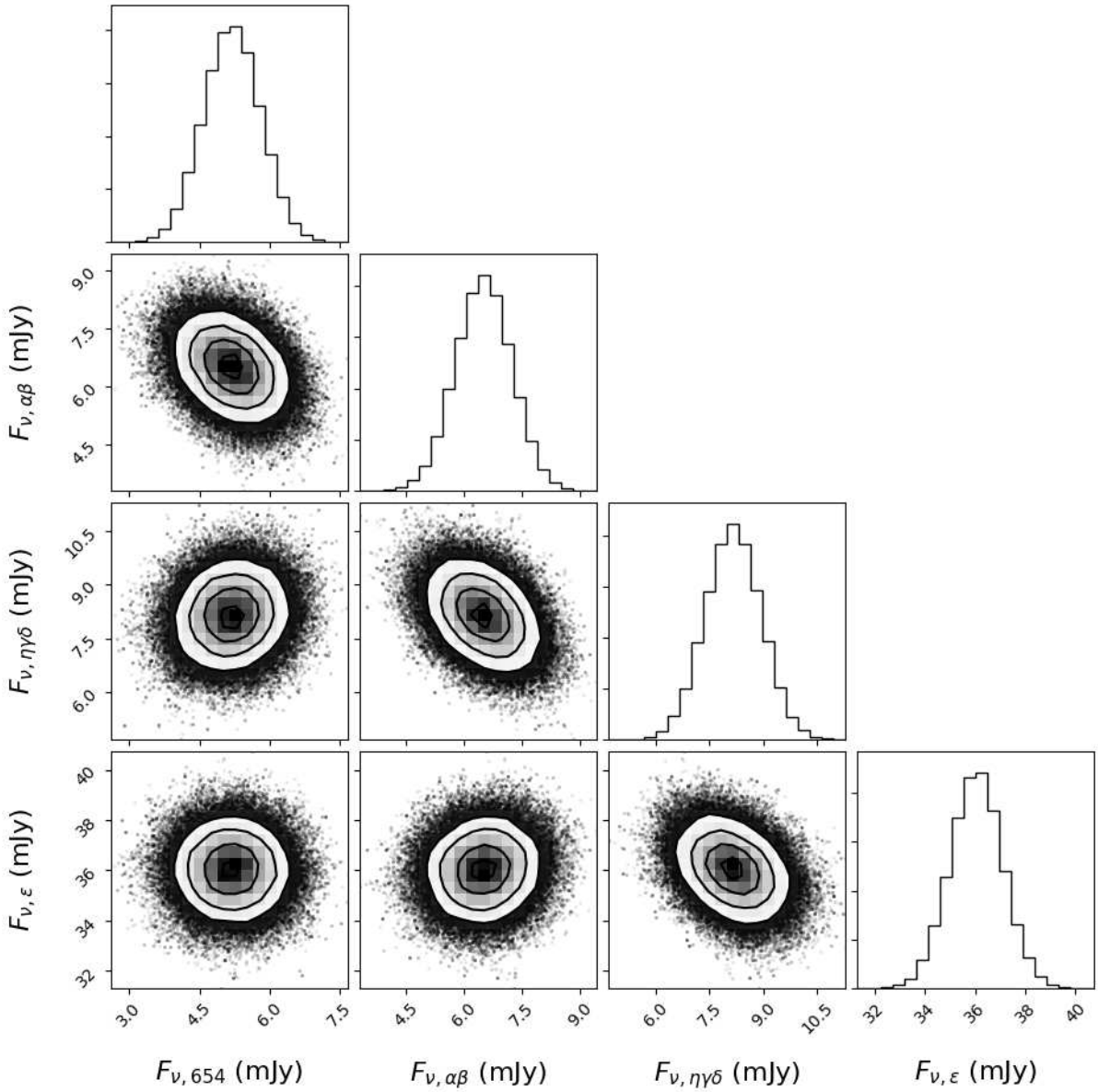

Figure 3.8: "Corner plot" showing the one- and two-dimensional projections of the posterior probability distributions of the MCMC-retrieved total fluxes of each ring group in Band 4 (2.1 mm), derived from comparing our model to the observed the radial profile.

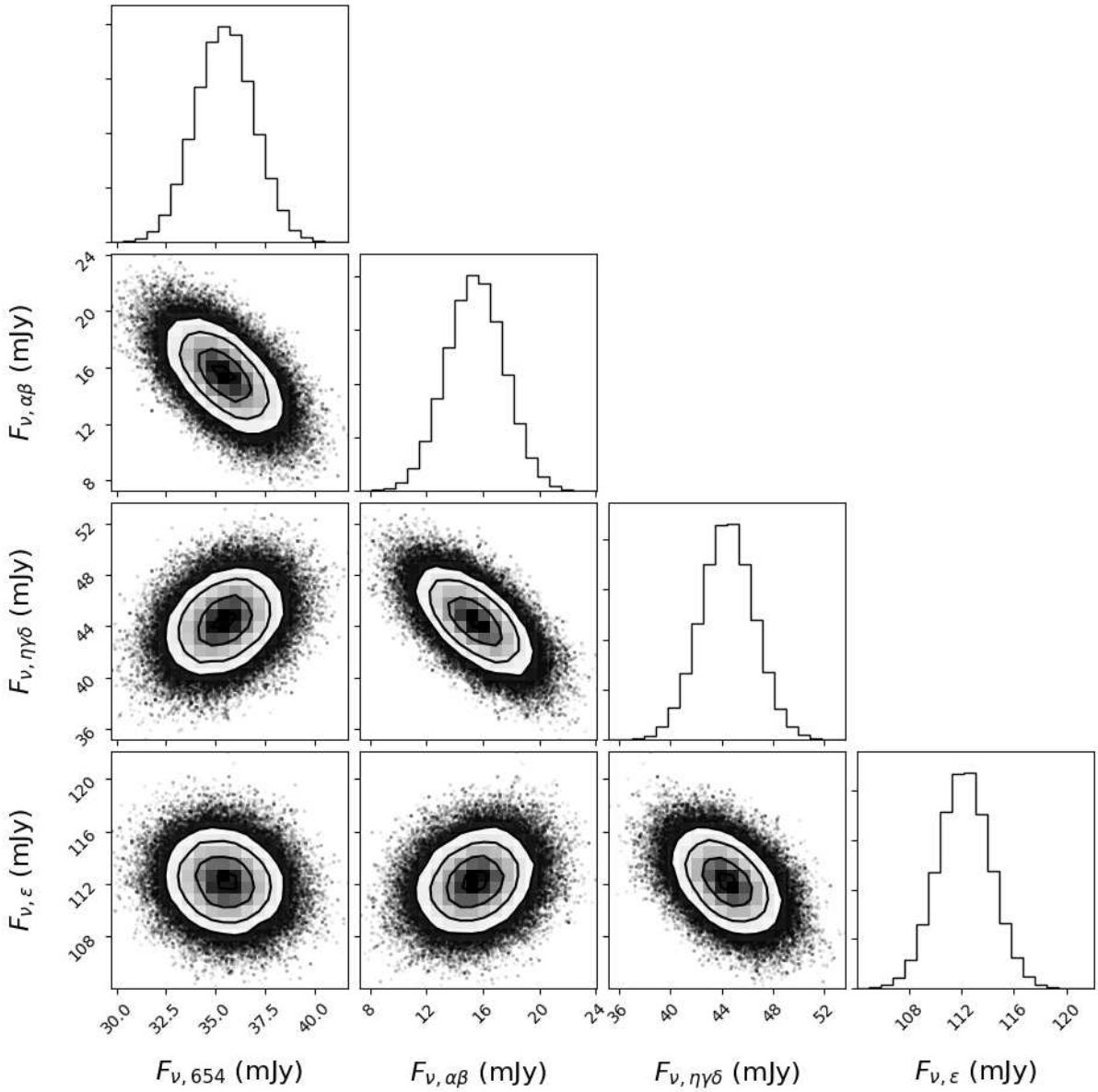

Figure 3.9: "Corner plot" showing the one- and two-dimensional projections of the posterior probability distributions of the MCMC-retrieved total fluxes of each ring group in Band 6 (1.3 mm), derived from comparing our model to the observed the radial profile.

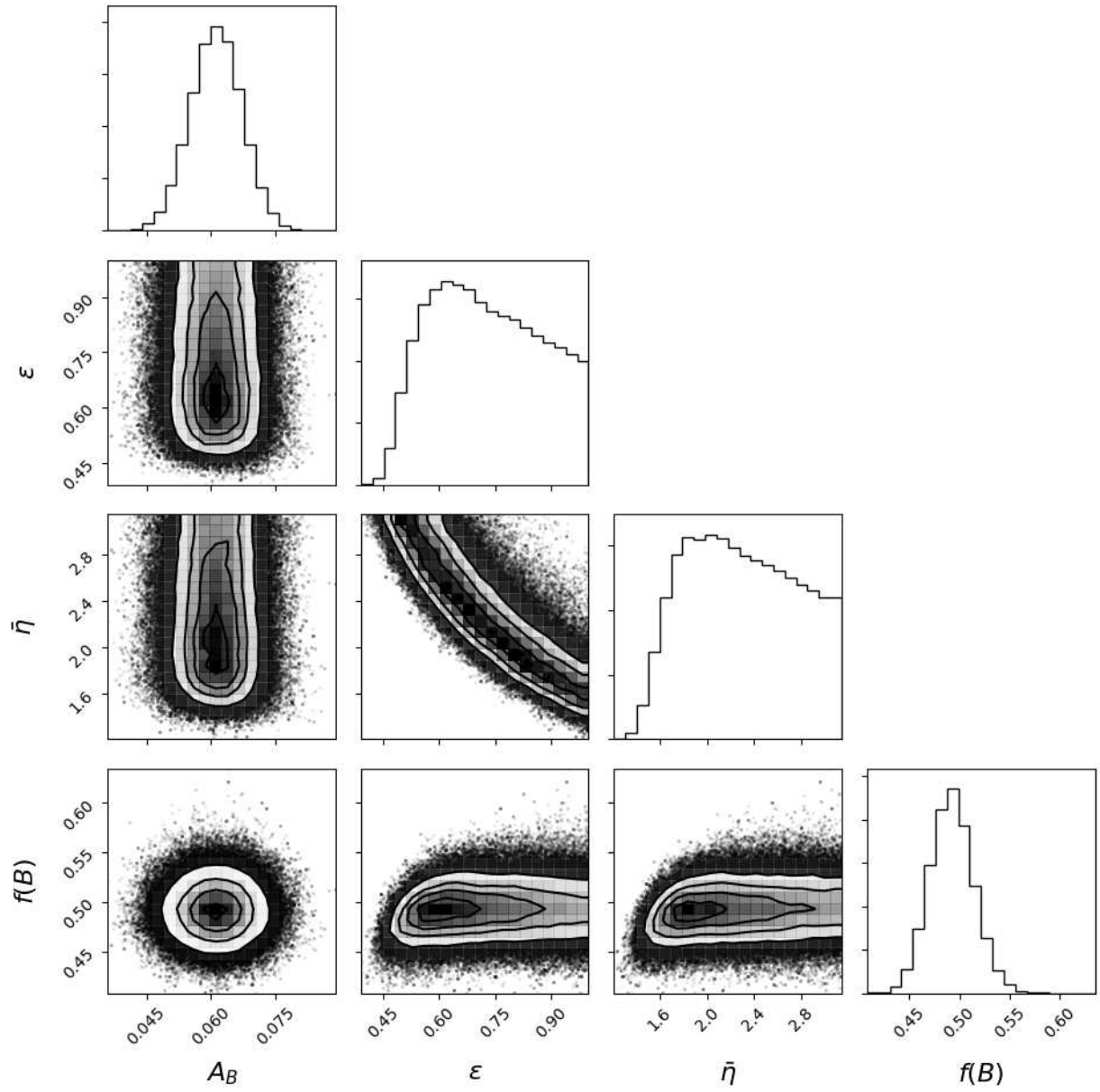

Figure 3.10: "Corner plot" showing the one- and two-dimensional projections of the posterior probability distributions of the MCMC-retrieved thermal model parameters.

Chapter 4

Tropospheric Composition and Circulation of Uranus with ALMA and the VLA

The published version of this chapter was coauthored by the following individuals, and is included in this thesis with their express permission: Imke de Pater, Statia Luszcz-Cook, Joshua Tollefson, Robert J. Sault, Bryan Butler, David de Boer.

We present ALMA and VLA spatial maps of the Uranian atmosphere taken between 2015 and 2018 at wavelengths from 1.3 mm to 10 cm, probing pressures from ∼1 to ∼50 bar at spatial resolutions from 0.1" to 0.8". Radiative transfer modeling was performed to determine the physical origin of the brightness variations across Uranus's disk. The radio-dark equator and midlatitudes of the planet (south of ∼50° N) are well fit by a deep H_2S mixing ratio of $8.7^{+3.1}_{-1.5} \times 10^{-4}$ ($37^{+13}_{-6}\times$ Solar) and a deep NH_3 mixing ratio of $1.7^{+0.7}_{-0.4} \times 10^{-4}$ ($1.4^{+0.5}_{-0.3}\times$ Solar), in good agreement with literature models of Uranus's disk-averaged spectrum. The north polar region is very bright at all frequencies northward of ∼50°N, which we attribute to strong depletions extending down to the NH_4SH layer in both NH_3 and H_2S relative to the equatorial region; the model is consistent with an NH_3 abundance of $4.7^{+2.1}_{-1.8}\times10^{-7}$ and an H_2S abundance of $< 1.9 \times 10^{-7}$ between ∼20 and ∼50 bar. Combining this observed depletion in condensible molecules with methane-sensitive near-infrared observations from the literature suggests large-scale downwelling in the north polar vortex region from ∼0.1 to ∼50 bar. The highest-resolution maps reveal zonal radio-dark and radio-bright bands at 20°S, 0°, and 20°N, as well as zonal banding within the north polar region. The difference in brightness is a factor of ∼10 less pronounced in these bands than the difference between the north pole and equator, and additional observations are required to determine the temperature, composition and vertical extent of these features.

4.1 Introduction

Uranus's 82° obliquity leads to drastic seasonal variations in insolation, with both poles receiving more annual sunlight than the equator. In addition, Uranus is the only giant planet that lacks an apparent internal heat source (Pearl et al. 1990). The unusual pattern of heat flux into the Uranian troposphere resulting from these two characteristics provides an extreme test of our understanding of atmospheric circulation (for recent reviews see Fletcher, de Pater, et al. 2020; Hueso and Sánchez-Lavega 2019). The strong seasonal forcing also plays a role in altering Uranus's atmospheric composition; for example, Uranus's insolation pattern has been invoked to explain the disequilibrium in the H_2 ortho-para fraction in the upper troposphere as well as the seasonal variation in haze properties and/or methane abundance in the stratosphere (Hueso and Sánchez-Lavega 2019). Radio observations provide a unique tool for probing the atmosphere of Uranus beneath its tropospheric cloud layers, permitting inferences about its tropospheric properties (de Pater and Gulkis 1988; de Pater, Romani, et al. 1991; Hofstadter 1992; Hofstadter, Berge, et al. 1990; Hofstadter and Butler 2003; Hofstadter and Muhleman 1989; Jaffe et al. 1984; Klein et al. 2006).

Central to these questions is Uranus's global circulation pattern. Remote-sensing observations probe atmospheric vertical motions indirectly by determining the zonal-mean distribution of condensible gases and clouds. Regions of large-scale upwelling are cloudy and rich in condensible gases up to the condensation pressure of that gas, while downwelling regions are drier and less cloudy. This point can be understood by analogy to the Hadley cell on Earth (see, e.g., Marshall et al. 1989). Water vapor evaporated from the deep reservoir (the ocean) moves equatorward into the Intertropical Convergence Zone (ITCZ), where it rises, condenses as the tropospheric temperature decreases with altitude, and then rains back into the deep reservoir. The air leaving the top of the ITCZ has thus been robbed of its water vapor by the tropopause cold trap, so the divergent upper branch and subsiding subtropical branch of the circulation cell are much drier than the ITCZ both in terms of relative humidity and column-integrated water vapor. The atmospheres of the giant planets organize into a series of alternating thermally direct and thermally indirect circulation cells similar to Earth's Hadley and Ferrel cells, giving rise to the spectacular jets of Jupiter and Saturn. Global circulation models (GCMs) of Jupiter show that the zonal-mean column-integrated abundances of both ammonia and water are indeed higher in the upwelling branches and lower in the downwelling branches (Young, Read, et al. 2019a,b), in agreement with ground-based (e.g., de Pater, Sault, Butler, et al. 2016; de Pater, Sault, Wong, et al. 2019) and spacecraft (Li, Ingersoll, et al. 2017) data. Based on Voyager thermal-infrared measurements, Flasar et al. (1987) suggested a circulation model for Uranus with gas rising at latitudes near 30° and subsiding at the equator and poles. Observations with the Very Large Array (VLA) revealed a bright south pole on Uranus, interpreted as a relative lack of microwave opacity in the deep troposphere down to ∼50 bar, which pointed to large-scale subsidence of dry air (de Pater and Gulkis 1988; de Pater, Romani, et al. 1991; de Pater, Romani, et al. 1989; Hofstadter 1992; Hofstadter, Berge, et al. 1990; Hofstadter and Butler 2003; Jaffe et al. 1984; Klein et al. 2006). A polar depletion in both methane and hydrogen sulfide (H_2S) at higher

altitudes observed at visible and near-infrared wavelengths corroborated this interpretation (Irwin, Toledo, et al. 2018; Karkoschka and Tomasko 2009; Sromovsky, Karkoschka, Fry, de Pater, et al. 2019; Sromovsky, Karkoschka, Fry, Hammel, et al. 2014). Together, these multi-wavelength observations lent further support to the Flasar et al. (1987) non-seasonal equator-to-pole single-cell meridional circulation pattern (de Pater, Romani, et al. 1991; Hofstadter 1992; Sromovsky, Karkoschka, Fry, Hammel, et al. 2014). However, a single-celled model has difficulty explaining the observed bands of clouds at 38° and 58° in both hemispheres. An alternative model prescribing circulation in three vertically stacked layers was proposed by Sromovsky, Karkoschka, Fry, Hammel, et al. (2014), although those authors make clear that the three-layer model has shortcomings of its own. It also remains unclear how the bright storm systems observed occasionally at near-infrared wavelengths, which appear to migrate in latitude (de Pater, Sromovsky, Hammel, et al. 2011; de Pater, Sromovsky, Fry, et al. 2015; Sromovsky, Fry, Hammel, de Pater, Rages, and Showalter 2007), fit into either model.

Previously published radio and millimeter observations of Uranus (e.g. de Pater and Gulkis 1988; Jaffe et al. 1984), mostly taken prior to 1990, have mostly considered the disk-integrated planet and primarily imaged Uranus's southern hemisphere. More recent spatially resolved observations using the VLA have been presented at conferences (e.g., Hofstadter, Orton, et al. 2009) and featured in a recent white paper (de Pater, Butler, et al. 2018). Both the Hofstadter, Orton, et al. (2009) image from 2005 and the de Pater, Butler, et al. (2018) image from 2015, which is analyzed in detail in this paper, show alternating bright and dark zonal bands in the midlatitudes, indicating a more complex circulation pattern than current models. The bright polar regions display similar brightness temperatures and zonal extents in the 2005 image, in which both poles are visible, and in the 2015 image zonal banding is visible within the bright polar region.

Inferences about the vertical cloud structure of giant planets are made by comparing radiative transfer and chemical modeling to observational data across the electromagnetic spectrum. Visible and near-infrared spectroscopy (e.g., de Kleer, Luszcz-Cook, et al. 2015b; Karkoschka and Tomasko 2009; Sromovsky, Karkoschka, Fry, de Pater, et al. 2019; Sromovsky, Karkoschka, Fry, Hammel, et al. 2014; Tice et al. 2013) have identified methane as the major condensible species in the upper troposphere, producing bright clouds and weather readily observed in visible/IR imaging (e.g., de Pater, Sromovsky, Hammel, et al. 2011; de Pater, Sromovsky, Fry, et al. 2015; Sromovsky, de Pater, et al. 2015). At ∼35 bar, gaseous NH_3 and H_2S are expected to precipitate into a cloud of solid NH_4SH, effectively removing either all nitrogen or all sulfur from the upper atmosphere. Gulkis, Janssen, et al. (1978) showed that Uranus must be ammonia-poor above the NH_4SH layer in order to fit the planet's disk-integrated radio spectrum. This finding suggested, contrary to solar composition models, that more H_2S than NH_3 was present in Uranus's deep atmosphere. Further work indicated that H_2S itself was also a major absorber, and new models, still with more sulfur than nitrogen, were developed that improved the fit to the observed spectra (de Pater, Romani, et al. 1991; de Pater 2018). Based on these studies, the uniform cloud layer at ∼3 bar, evident in IR spectroscopy, was long assumed to be composed of H_2S ice particles; this

hypothesis was confirmed recently by the direct detection of H_2S spectral lines above the cloud (Irwin, Toledo, et al. 2018). The chemistry becomes more speculative at pressures deeper than ∼50 bars, as those depths have not been accessed observationally. Models suggest Uranus's oxygen is locked in a water-ice cloud at ∼270 K (∼50 bar), and beneath this, an aqueous nitrogen-, sulfur-, and oxygen-bearing solution is expected to form (Atreya and Romani 1985; Weidenschilling et al. 1973). The effects of phosphine (PH_3) have also been considered in the ice giants. Its condensation pressure is near 80 K (∼1 bar on Uranus), and modeling shows that its absorption at deeper layers may be important to Uranus's infrared and millimeter spectrum (e.g., Fegley et al. 1986; Hoffman et al. 2001), especially near its $J = 1 \rightarrow 0$ rotational transition at 1.123 mm (266.9 GHz). However, its presence has never been confirmed observationally (Moreno et al. 2009; Orton and Kaminski 1989).

In this paper, we present new VLA and ALMA observations of Uranus's atmosphere from 2015 to 2018, representing the highest sensitivity and spatial resolution measurements of the planet at wavelengths from 1.3 mm to 10 cm. In Section 4.2 we outline the observational techniques and data processing procedures used to produce science images of Uranus. We present our results in Section 4.3, including seasonal brightness trends, spatial variations in brightness temperature, and inferred properties of Uranus's troposphere as determined from radiative transfer modeling. Finally, we put our results in a broader context and provide concluding remarks in Section 4.4.

4.2 Observations and Data Reduction

We obtained observations of Uranus with the Karl G. Jansky Very Large Array (VLA) from 0.9-10 cm (3.0-33 GHz) in August 2015 and the Atacama Large (sub-)Millimeter Array (ALMA) from 1.3-3.1 mm (98-233 GHz) between December 2017 and September 2018. A table of observations is provided in Table 4.1. The data-reduction procedures are outlined in the following two subsections.

ALMA Data

The data in each of the three ALMA bands were flagged and calibrated by the North American ALMA Science Center using the standard data-reduction procedures contained in the National Radio Astronomy Observatory (NRAO) Common Astronomy Software Applications (CASA) software version 5.1.1. Standard flux- and phase-calibration procedures were carried out by applying the pipeline using the quasars listed in Table 4.1 as calibrator sources. The CASA pipeline retrieved flux calibration errors of ∼5% in all three bands. Iterative phase-only self-calibration, which is routinely applied to radio observations of bright planets (e.g., Butler et al. 2001; de Pater, Fletcher, et al. 2014; de Pater, Sault, Wong, et al. 2019), was performed using a procedure similar to that outlined in Brogan et al. (2018) using solution intervals of 20, 10, 5, and 1 minutes in that order. To reduce ringing in the image plane from the presence of the bright planet, a uniform limb-darkened disk model of Uranus was

Array	Wavelength (mm)	Frequency (GHz)	UT Date	On-Source Time (min)	Resolution (arcsec)	Resolution (km)	Flux & Gain Calibrator	Phase Calibrator	Sub-Obs Latitude (°)
VLA	95	3.2	2015-08-29	88	0.79	11000	3C48	J0121+422	33
VLA	51	5.8	2015-08-29	89	0.45	6300	3C48	J0121+422	33
VLA	30.	9.9	2015-08-29/30	150	0.26	3600	3C48	J0121+422	33
VLA	20.	15	2015-08-29/30	148	0.17	2400	3C48	J0121+422	33
VLA	9.1	33	2015-08-29/30	160	0.085	1200	3C48	J0121+422	33
ALMA	3.1	98	2017-12-03	42	0.19	2700	J0238+1636	J0121+1149	38
ALMA	3.1	98	2017-12-06	42	0.19	2700	J0238+1636	J0121+1149	38
ALMA	2.1	144	2017-12-27	22	0.21	3000	J0238+1636	J0121+1149	38
ALMA	1.3	233	2018-09-13	24	0.29	4000	J0237+2848	J0211+1051	45

Table 4.1: Table of observations. Note that the VLA observations at 0.9 cm, 2 cm, and 3 cm were taken in two parts over two consecutive days.

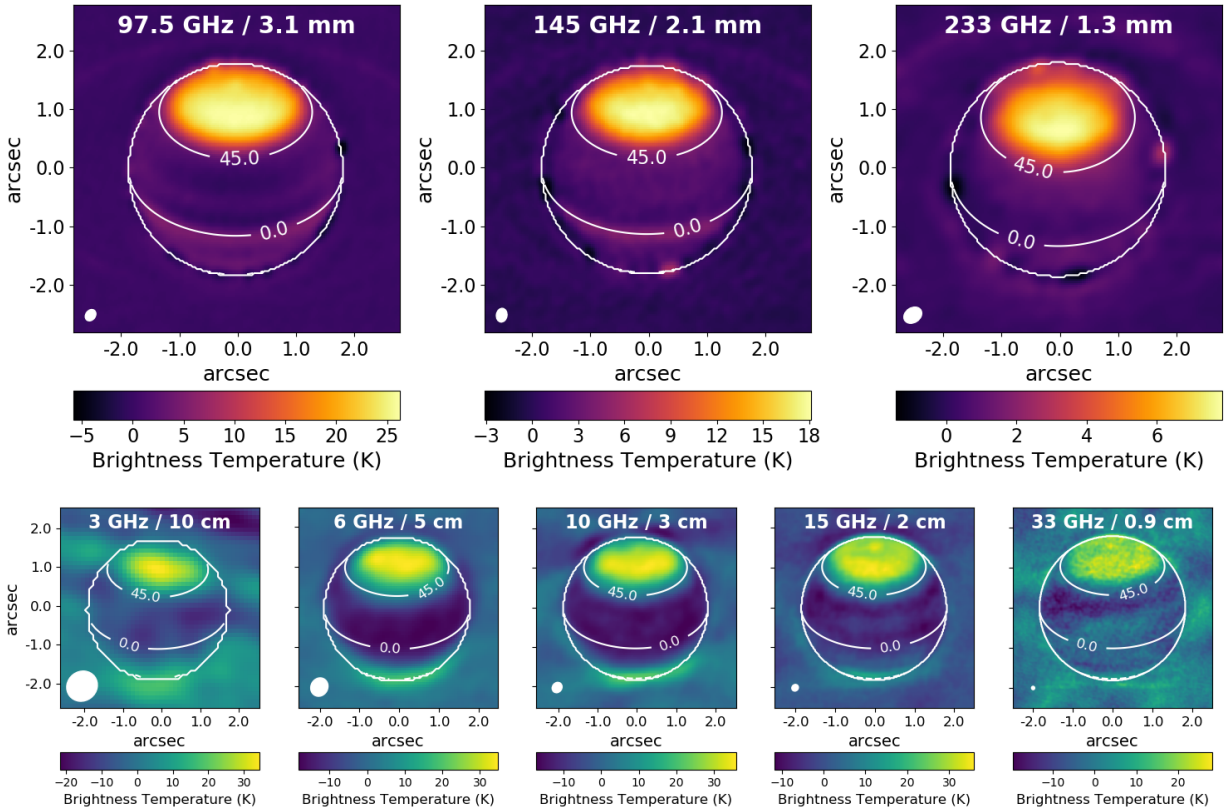

Figure 4.1: Disk-subtracted images of Uranus from ALMA **(top)** at 3.1 mm (Band 3), 2.1 mm (Band 4), and 1.3 mm (Band 6), and the VLA **(bottom)** from 0.9-20 cm. The color bars below each image indicate the brightness temperature residuals in Kelvin. The synthesized beam is shown as a white ellipse in the bottom left corner of each image. The ring of light and dark one-beam-size spots around the planet are artefacts produced by applying a Fourier transform to the UV-plane data near the sharp edges of the bright planet.

subtracted from the data in the UV plane in each band, as done in, e.g., de Pater, Fletcher, et al. (2014) and de Pater, Sault, Butler, et al. (2016). The disk-subtracted data were inverted into the image plane and deconvolved using CASA's `tclean` function. The resulting disk-subtracted images are shown in Figure 4.1. These images are also shown cylindrically projected onto a latitude-longitude grid in Figure 4.2. It should be noted that the planet's rotation smears out features in longitude: the ∼20 minute observations at 2.1 mm and 1.3 mm are smeared by ∼8°, and the 3.1 mm image is a sum of two ∼40 minute observations taken at different sub-observer longitudes.

Images were also produced from the calibrated but non-disk-subtracted data; these images were used to measure absolute fluxes across the disk for radiative transfer modeling.

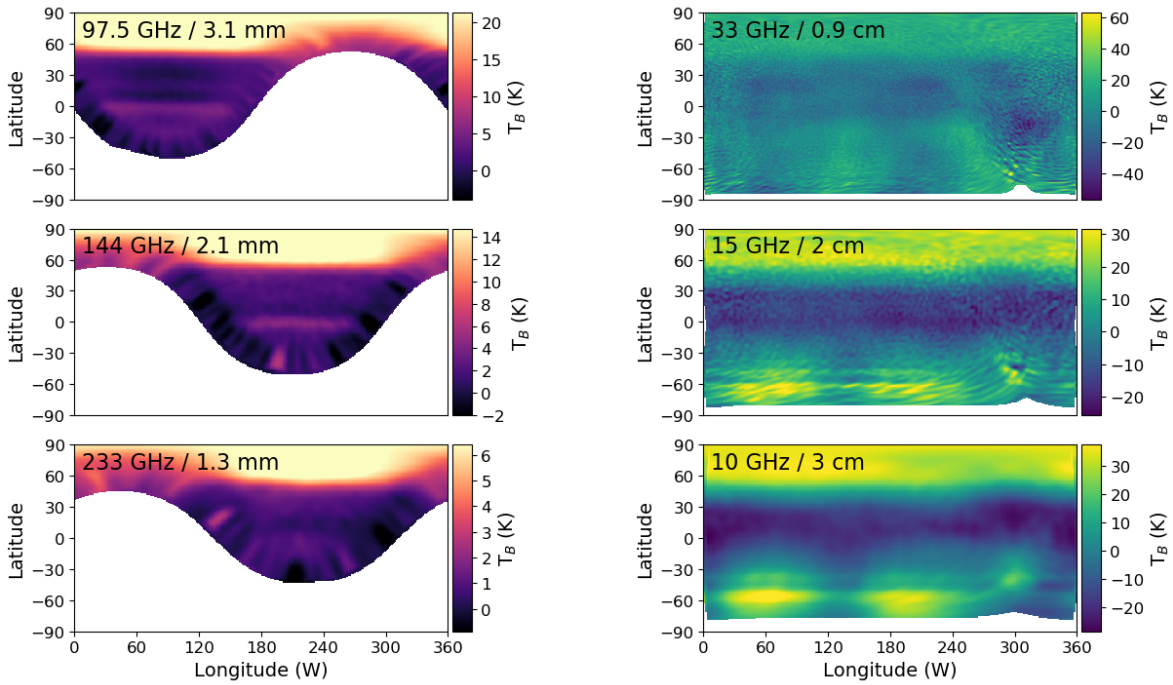

Figure 4.2: **Left:** Reprojected ALMA maps of Uranus. The ∼20-minute observations at 2.1 mm and 1.3 mm are smeared by ∼8°, and the 3.1 mm image is a sum of two ∼40 minute observations taken at different sub-observer longitudes. The alternating bright and dark spots near the planet's limb are due to CLEAN artefacts, induced by attempting to Fourier transform a sharp-edged planet and made larger in apparent size by projection effects. **Right:** Longitude-resolved VLA maps of Uranus, produced using the faceting technique (Sault, Engel, et al. 2004). The distortions near 300°W are due to poor zonal coverage at those longitudes in the observations. The spatial resolution of the 5 cm and 10 cm data is not sufficient to produce reliable longitude-resolved maps, so these are not shown.

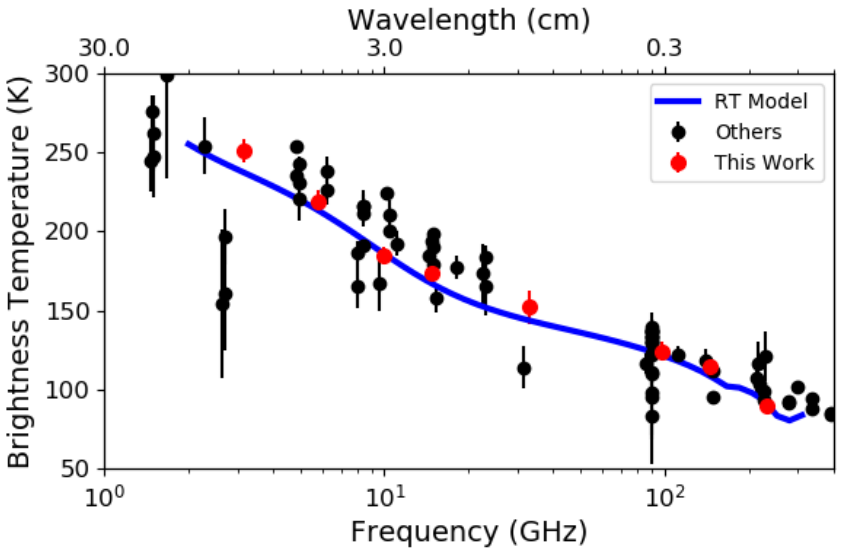

Figure 4.3: Disk-integrated brightness temperatures of Uranus from this work (red points) compared to measurements from the literature (black points; de Pater and Gulkis 1988; Griffin et al. 1993; Gulkis and de Pater 1984; Muhleman et al. 1991; Orton, Griffin, et al. 1986). As shown by those authors (see also Figure 4.4), the scatter in the data is primarily due to real seasonal fluctuations in Uranus's observed brightness temperature as the planet's poles move into and out of view. Our data fall at a lower brightness temperature than the majority of the literature data because those were observed in southern summer, when the bright south polar region made up a large fraction of Uranus's disk. A radiative transfer model with parameters retrieved to match our 25°N data (Section 4.3), shown by a blue line, matches the disk-averaged data quite well.

The ∼3.5" disk of Uranus was smaller than the maximum recoverable scale of the ALMA array configuration in all three observing bands[1]; therefore we have short enough baselines to faithfully measure Uranus's total flux. These flux measurements were confirmed by fitting the visibility data to a Bessel function; the difference between the UV-plane-derived and image-plane-derived total flux measurements was much smaller than the flux calibration error at all wavelengths. The total flux measurements were corrected for the cosmic microwave background (CMB) according to the prescription detailed in Appendix A of de Pater, Fletcher, et al. (2014). Final measurements of Uranus's disk-averaged brightness temperature are plotted against measurements from the literature in Figure 4.3 and tabulated in Table 4.2.

[1]See the ALMA Technical Handbook for further discussion of the maximum recoverable scale https://almascience.nrao.edu/documents-and-tools/cycle5/alma-technical-handbook

Wavelength (mm)	Frequency (GHz)	Disk-averaged T_B (K)	25° N T_B (K)	75° N T_B (K)	Flux Cal Error (K)	RMS per Beam (K)	Latitude Bin Error (K)
95	3.2	251.3	261.3	293.4	7.5	2.2	3.6
51	5.8	219.3	219.2	262.0	6.6	0.8	2.6
30.	9.9	184.5	182.8	224.4	5.5	1.2	2.6
20.	15	173.9	169.4	205.0	5.2	1.3	2.6
9.1	33	152.4	157.8	180.6	10.7	3.4	2.6
3.1	98	140.7	142.6	165.1	7.0	0.3	1.1
2.1	144	122.5	126.5	139.1	6.6	0.1	0.9
1.3	233	91.1	96.0	101.8	4.8	0.1	0.5

Table 4.2: Brightness temperature measurements and errors extracted from the ALMA and VLA maps. See Section 4.2 for discussion of the flux calibration and per-bin RMS errors, and Section 4.3 for discussion of the latitude-bin error.

VLA Data

The data in each of the five VLA bands were flagged and calibrated using the standard data-reduction procedures contained in the `Miriad` software package[2] (Sault, Teuben, et al. 1995). Standard flux- and phase-calibration procedures were carried out using the calibrator sources listed in Table 4.1; the absolute flux calibration error was assumed to be 3% at the longest four wavelengths and 7% at 0.9 cm (Butler et al. 2001; Perley et al. 2013, 2017). Iterative self-calibration, disk subtraction, imaging, and deconvolution were carried out in a similar manner to the ALMA data but using `Miriad`. The CMB correction was applied in the same way as for the ALMA images. The resulting disk-subtracted images are shown in Figure 4.1. It should be noted that the 0.9 cm images are more strongly affected by imaging artefacts than the other bands because this wavelength sits near a telluric water absorption band, leading to relatively poor phase stability. Longitude-resolved images, produced using the faceting technique developed and recently used for VLA observations of Jupiter (de Pater, Sault, Wong, et al. 2019; Sault, Engel, et al. 2004), are shown in Figure 4.2. This represents the first attempt to resolve Uranus in longitude at these wavelengths. Limited UV-plane coverage leads to significant artefacts in these maps, including large-scale alternating bright and dark regions (e.g., bright at 60°W and 200°W in the 2 cm and 3 cm images) that cross many latitude bands. An apparent warping near 300°W is also present, caused by poor zonal coverage at those longitudes. Nevertheless, if any vortex-like disturbances at the scale of Jupiter's Great Red Spot were present on Uranus, these maps should have detected them. No such structures are found, so in this work we focus our analysis on the longitude-smeared maps only.

[2]https://www.atnf.csiro.au/computing/software/miriad/

4.3 Results and Discussion

Seasonal Brightness Variations

We explore long-term trends in Uranus's radio brightness in Figure 4.4, which plots our VLA 3.0 cm data along with 3.5 cm data obtained by Klein et al. (2006) and older disk-averaged data from various telescopes (Gulkis and de Pater 1984) as a function of sub-observer latitude. Our data were taken with Uranus's north pole facing the observer, whereas the Klein et al. (2006) data were taken toward the south pole; nevertheless, Uranus's brightness temperature was the same within the error bars of the data at a sub-observer longitude of $\sim$35°. The $\sim$40 K brightness difference we observe between Uranus's northern midlatitudes and its north pole at 2-3 cm is of the same magnitude as VLA measurements of the difference between the south polar region and southern midlatitudes (e.g., Hofstadter, Berge, et al. 1990). Imaging at 1.3 cm taken near equinox (observers Hofstadter & Butler; de Pater, Butler, et al. 2018), which appears to show that both poles are roughly equally bright, further supports the similarity in brightness temperature between the north and south pole. Any trend in the 3 mm brightness temperature (right panel of Figure 4.4) is much less clear; the error bars are large for all observations taken near equinox, and all data taken at sub-observer latitudes larger than 40° have the same brightness to within the 2σ level. This is confusing given the very large and bright north polar region we observe and the clear brightness temperature variations at longer wavelengths. However, the flux calibration uncertainty from measurements in some older papers (see references in Gulkis and de Pater 1984) have not been reported, and so this result should be treated with caution.

Spatially Resolved Brightness Temperatures

The images in Figures 4.1 and 4.2 reveal complex banding structure in Uranus's troposphere. For better visual comparison of the zonal features in the maps at different frequencies, a vertical slice of width 30° longitude centered on the sub-observer point was taken from the longitude-smeared, disk-subtracted, projected maps (shown in Figure 4.2 for the ALMA data) at each frequency, then averaged into a 1-D brightness versus latitude profile. The resulting profiles are shown normalized relative to one another in Figure 4.5. To extract spatially-resolved brightness temperatures for radiative transfer modeling, we simply averaged non-disk-subtracted latitude profiles over ten degrees latitude; that is, the 25°N region represents latitudes from 20-30°N and the 75°N region represents latitudes from 70-80°N. The error in the extracted brightness temperatures was determined by making latitude profiles over several different 30° longitude ranges and computing the standard deviation in the brightness measurements from those profiles. These "latitude-bin" errors are given in Table 4.2. It is worth noting that they are larger than the per-beam RMS error extracted from background regions of the radio maps (except at 0.9 cm). This is due to systematic errors arising from inverting and CLEANing visibility data of a very bright, extended, and sharp-edged source.

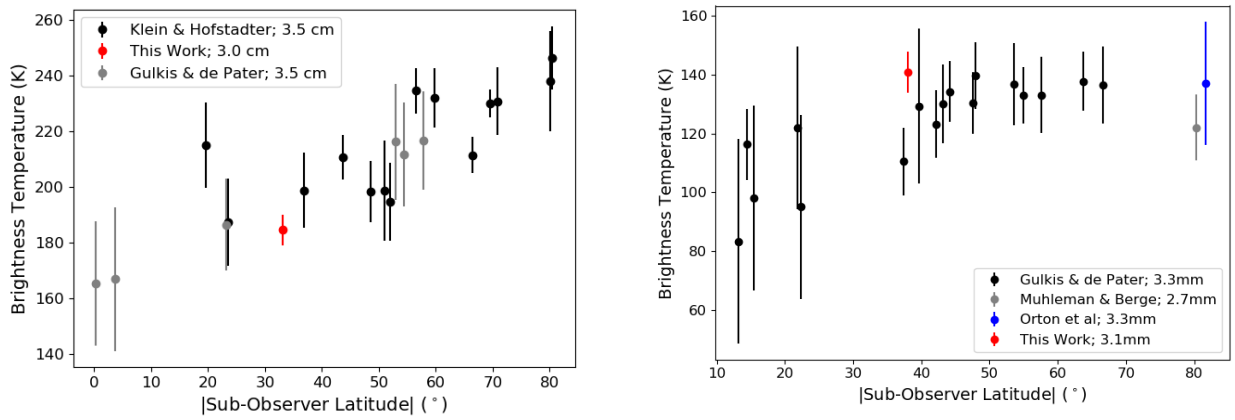

Figure 4.4: **Left:** VLA 3.0 cm total flux measurement of Uranus's disk from this work (red) compared to 3.5 cm flux measurements made with the Goldstone station of NASA's Deep Space Network (DSN) at a range of sub-observer latitudes (Klein et al. 2006), as well as 3.5 cm measurements made prior to 1984 as summarized in Gulkis and de Pater (1984). **Right:** ALMA 3.1 mm total flux measurement of Uranus's disk from this work (red) compared to previous mm-wavelength measurements from various authors (Gulkis and de Pater 1984; Muhleman et al. 1991; Orton, Griffin, et al. 1986). The error bars on the literature measurements in both panels should be treated with caution, as flux calibration errors are often not reported. For the purposes of this plot, we have added 5% flux calibration errors to the points from the Gulkis and Muhleman papers. The x-axis in both panels shows the absolute value of sub-observer latitude; note that all previous measurements were made at negative sub-observer latitudes.

The north polar region is readily observed across the radio and millimeter spectrum as a prominent brightening northward of ∼50°N. At 3.1 mm wavelength, this brightening reaches >25 K, nearly ten times the magnitude of any other brightness variations observed across Uranus's disk. The edge of this brightening appears sharply defined: the transition from the darker midlatitudes to the bright poles occurs over less than a single resolution element in all the observing bands. The magnitude of the polar brightening is much too large to be explained by variations in kinetic temperature (see Appendix 4.5), so we attribute it to downwelling air dry in absorbing species such as NH_3 and H_2S. Keck observations in the methane-sensitive PaBeta and H_2-sensitive He1A filters in 2015 (Sromovsky, Karkoschka, Fry, de Pater, et al. 2019, simultaneous with our VLA observations) revealed a strong polar methane depletion that is spatially correlated with the bright polar region observed in the millimeter and radio data (see Figure 4.5). This implies continuously downwelling dry air over a wide range of pressures from 0.1 to at least 20 bar (see Section 4.3) at latitudes northward of 50°N. However, localized regions of upwelling (i.e. convection) or a temporally

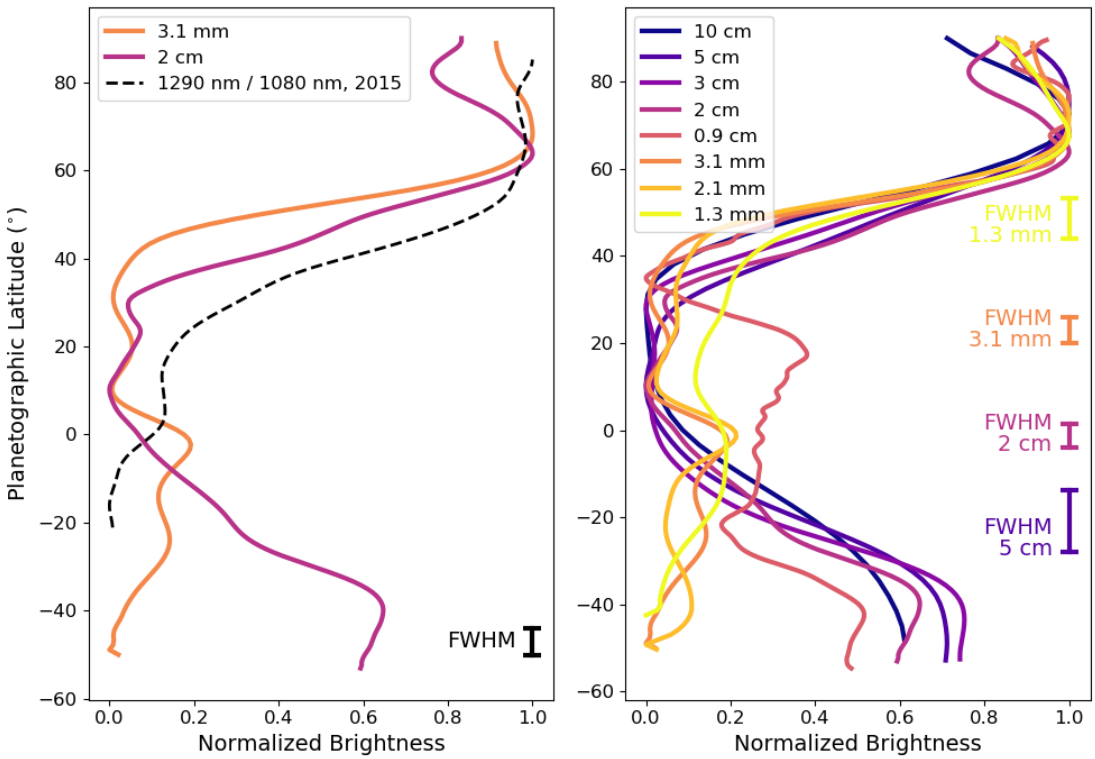

Figure 4.5: Meridional brightness profiles of the zonally-averaged radio/millimeter maps. **Left:** The 3.1 mm ALMA and 2.0 cm VLA data are plotted separately because they provide the best combination of high signal-to-noise ratio and resolution. These are compared to the brightness ratio between the Keck PaBeta (1.29 μm) and He1A (1.08 μm) filters, which is a tracer of the upper tropospheric methane abundance, as derived from 2015 imaging (Sromovsky, Karkoschka, Fry, de Pater, et al. 2019, black dashed line). The PaBeta/He1A ratio curve and VLA 2 cm curve have been convolved with a 1-D Gaussian beam at the ALMA 3.1 mm resolution (0.19 arcsec); the $\sim$6° FWHM of the beam at the sub-observer point is shown in the bottom right corner. **Right:** Latitudinal brightness profiles at all the observed wavelengths are plotted against one another. The FWHM of the beam at the sub-observer point is shown for representative frequencies in the same color as the data for that frequency. To facilitate visual comparison, the brightness temperature units in both panels are normalized so that each band has maximum one.

variable circulation pattern at the north pole cannot be ruled out. At 0.9 cm and 2 cm wavelengths, the highest-resolution VLA bands, a polar collar is observed at ∼60°N, just north of the 45° polar collar seen at near-infrared wavelengths (see also Figure 4.5) but at the same latitude as the transition to solid-body rotation in Uranus's zonal wind profile (Sromovsky, Fry, Hammel, de Pater, and Rages 2012). The polar collar is bounded by a somewhat fainter band at ∼75°N, then another brightening right at the north pole. However, this banding is not observed in the ALMA data despite similar spatial resolutions in the 3 mm and 2 cm data.

Alternating bright and dark bands are observed near Uranus's equator in some of our images, with brighter latitudes at ∼20°S, ∼0°, and ∼20°N. At 3.1 mm, these bands are ∼1 K, ∼4 K, and ∼1 K brighter, respectively, than their surroundings. The banding is visible in all the ALMA data (3.1 mm, 2.1 mm, and 1.3 mm). It is also observed faintly in the 2 cm and 0.9 cm VLA bands, but not at longer wavelengths. Using our radiative transfer model (see Section 4.3), we find that variations in the CH_4 abundance, the PH_3 abundance, the relative humidity of H_2S, or the ortho-para fraction can all produce stronger absorption from 1 to 3 mm than at wavelengths longer than 2 cm. Changes in the kinetic temperature may also be responsible for all or part of the brightness temperature banding; however, this would require unusual atmospheric temperature profiles to fit our radio-millimeter spectrum (see Appendix 4.5 for a discussion of the kinetic temperature as it relates to the polar region). These putative abundance variations suggest downwelling and depletion in condensing species extending at least from ∼1 to 5 bar at the brighter latitudes. The lack of strong banding at longer wavelengths means that either the depletions do not extend deeper than 5-10 bar, the depletions are caused by a species that absorbs more strongly at shorter wavelengths, or the longer-wavelength VLA observations lack the sensitivity and spatial resolution to detect these faint equatorial bands. These observations point to a more complex circulation pattern than predicted by models (Allison et al. 1991; Flasar et al. 1987; Sromovsky, Karkoschka, Fry, Hammel, et al. 2014), which suggested upwelling near 30°N and 30°S and subsidence at the equator and poles. A recent review paper (Fletcher, de Pater, et al. 2020) considered a more complex model that prescribes tropospheric upwelling at the equator and just equatorward of the polar region (∼40°N), and downwelling between these. This model captures the large region of subsidence that we require at the poles. However, the alternating bright and dark bands we see, if indeed tied to upwelling and downwelling, do not match very well the locations prescribed in their model.

Radiative Transfer Modeling

The combined ALMA and VLA datasets comprise a spectrum of Uranus. Here, we use radiative transfer models to fit this spectrum and infer the vertical distribution of condensible species in Uranus's atmosphere. Radiative transfer modeling was carried out using the radio-BEAR (radio-BErkeley Atmospheric Radiative transfer) code[3]. The cloud model and

[3]https://github.com/david-deboer/radiobear

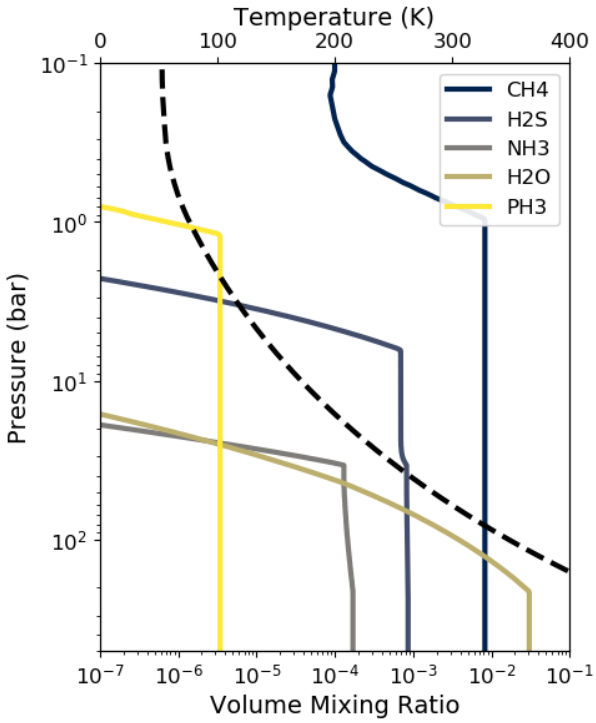

Figure 4.6: Vertical abundance profiles for trace gases in our radiative transfer model. Deep atmospheric abundances are set to 35× Solar except for NH_3, which has an abundance of 1× Solar. The dashed black line plots the assumed temperature-pressure profile, which follows a moist adiabat.

radiative transfer scheme are described in detail in de Pater, Fletcher, et al. (2014), de Pater, DeBoer, et al. (2005), and de Pater, Sault, Wong, et al. (2019). Radio-BEAR assumes that the atmosphere is in local thermodynamic equilibrium; its temperature follows an adiabat with a temperature of 76.4 K at 1 bar as determined by radio-occultation experiments with Voyager 2 (Lindal et al. 1987). At higher altitudes, where radiative effects become important, we used the temperature-pressure profile derived from Voyager/IRIS observations by Orton, Fletcher, et al. (2015). The temperature-pressure profile is shown in Figure 4.6. Cloud densities may affect the millimeter and/or radio spectrum via absorption and scattering; however, too little is known about the cloud properties on Uranus to make an accurate cloud density model and clouds have been shown not to significantly affect the opacity at these wavelengths on Jupiter (de Pater, Sault, Wong, et al. 2019). RadioBEAR therefore ignores cloud opacity and considers only gas absorption.

We started with a nominal disk-averaged model that assumed deep H_2S, H_2O, and CH_4 abundances of 30× Solar and a deep NH_3 abundance of 1× Solar (de Pater, Romani, et al.

1991; de Pater, Butler, et al. 2018).[4] The vertical profiles of these gases were determined using a cloud-physics model (Atreya and Romani 1985; de Pater, Romani, et al. 1991; Romani 1986) that includes prescriptions for a water-solution cloud at $\gtrsim$100 bar and an NH_4SH layer at $\sim$35 bar. We added in PH_3 with a nominal deep abundance of 30$\times$ Solar and a simple prescription for its saturation vapor curve (Orton and Kaminski 1989). Vertical profiles of all the condensible gases included in the radiative transfer code are plotted in Figure 4.6. The observed frequencies are sensitive to the atmospheric abundance and temperature from $\sim$0.1-50 bar; contribution functions at each frequency for the nominal model are shown in Figure 4.7.

We next perturbed many possible variables within this model one at a time to observe their effect on the spectrum, namely: the abundances of NH_3, H_2S, CH_4, and PH_3 from 500 bar up to just below the NH_4SH layer[5]; the relative humidity of the H_2S ice cloud (H_2S h_{rel}); the ortho-para hydrogen fraction; and a wet vs dry adiabat. Only NH_3 and H_2S gas absorb strongly enough to impact the radio spectrum by $\gtrsim$5 K, i.e. above the flux calibration error, at the observed frequencies. We therefore expect strong constraints on only the H_2S and NH_3 abundances and the H_2S relative humidity; the impacts of these three parameters on Uranus's radio spectrum are shown in Figure 4.8. The effect of the NH_4SH cloud can be seen on the spectrum as NH_3 and H_2S are varied (Figure 4.8a and 4.8b): at low H_2S abundances and high NH_3 abundances, NH_3 survives above the NH_4SH cloud and absorbs strongly at long wavelengths, whereas at high H_2S abundances and low NH_3 abundances (including the nominal values), H_2S survives above the NH_4SH cloud and absorbs most strongly at millimeter wavelengths. In the intermediate regime, where the NH_3 and H_2S abundances are nearly equal, the lower H_2S abundance leads to less absorption from 1-3 cm, but at 10 cm the NH_3 absorption deeper than the NH_4SH cloud is still important (see salmon line in Figure 4.8b). Pressure-broadened absorption near the 1.123 mm (266.9 GHz) rotational line of phosphine may also be important in ALMA Band 6, i.e. at 1.3 mm (see Figure 4.8d). Methane has no strong lines at millimeter or radio wavelengths, but alters Uranus's millimeter/radio spectrum at the $\sim 1\sigma$ level by altering the strength of H_2-CH_4 collision-induced absorption (CIA; Borysow et al. 1986). The ortho-para fraction of molecular hydrogen changes the strength of H_2-H_2 CIA as well as modifying the adiabatic lapse rate, and thus also affects the mm/radio spectrum (Trafton 1967; Wallace 1980).[6] Since

[4]Solar abundances are assumed to be the protosolar values given in Asplund et al. (2009) $C/H_2 = 5.90 \times 10^{-4}$; $N/H_2 = 1.48 \times 10^{-4}$; $O/H_2 = 1.07 \times 10^{-3}$; $S/H_2 = 2.89 \times 10^{-5}$; $Ar/H_2 = 5.51 \times 10^{-6}$; $P/H_2 = 5.64 \times 10^{-7}$

[5]This effectively ignores the solution cloud at $\sim$100 bar. However, we are mostly insensitive to the solution cloud's effect on the spectrum, so for practical purposes this is the same as varying the abundances just above the solution cloud. The reason we made this choice and its effects are discussed further in Sections 4.3 and 4.3.

[6]The default ortho-para hydrogen state is "normal" H_2, which denotes high-temperature-limit value of 3:1 orthohydrogen:parahydrogen, which is reached near 300 K. "Equilibrium" H_2 refers to the equilibrium ortho-para fraction at the temperature of each atmospheric layer according to the T-P profile in Figure 4.6. The ortho-para fraction may achieve disequilibrium due to vertical mixing, since the timescale to convert between the ortho- and para-states is much longer than dynamical timescales (Trafton 1967; Wallace 1980).

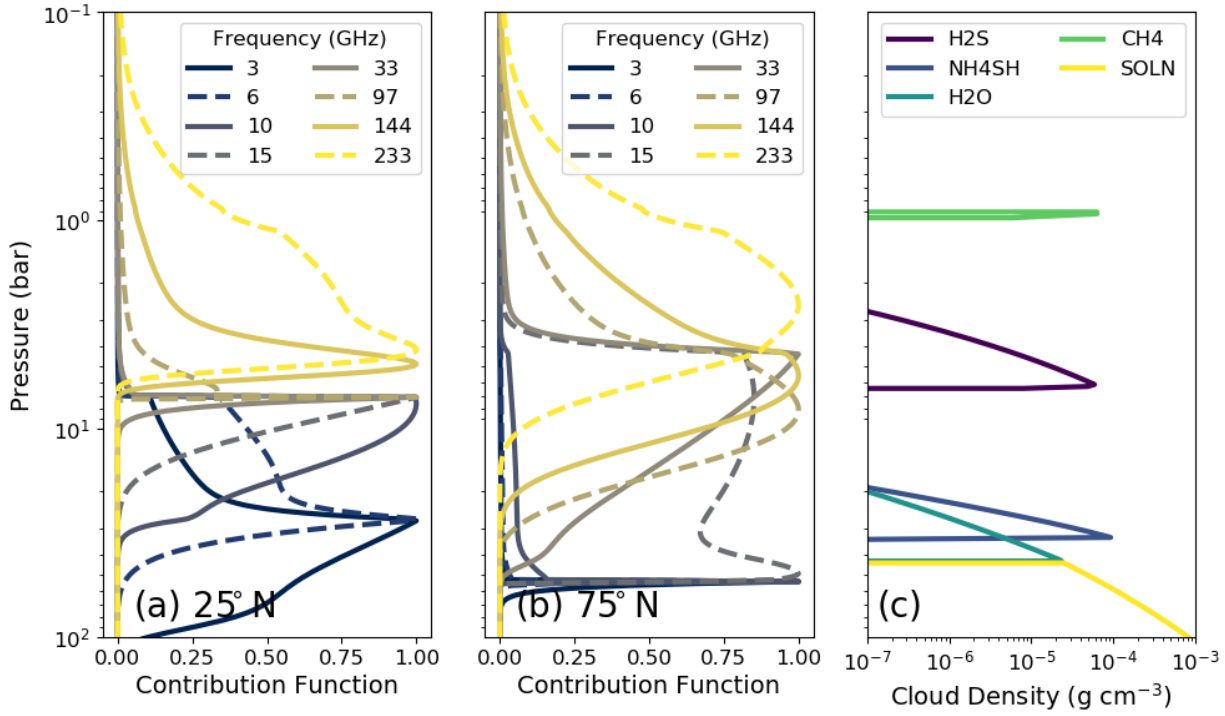

Figure 4.7: Normalized contribution function at each observed frequency for the best-fitting radiative transfer models at **(a)** 25°N and **(b)** 75°N. The spike in panel (b) at ∼40 bar is caused by the discontinuity in the vertical abundance profiles at the retrieved mixing pressure. **(c)** Cloud density as a function of pressure for clouds expected to form under thermochemical equilibrium assuming the abundance profiles in Figure 4.6.

in our model the CH_4 abundance, PH_3 abundance, and ortho-para fraction of H_2 may all affect the spectrum to near the $\sim 1\sigma$ level at some frequencies, we allow them to vary as well. The deep H_2O abundance has no impact on the spectrum because the H_2O cloud forms well below the maximum depth to which we are sensitive; we set the deep H_2O abundance to a fixed 30× Solar. The difference between a wet and dry adiabat is small; we assumed a dry adiabat.

Radiative transfer modeling was carried out within a Markov Chain Monte Carlo (MCMC) framework, implemented using the `emcee` Python package (Foreman-Mackey et al. 2013).[7] Letting θ represent the set of free parameters in the model, the likelihood function $\ln p$ is given by

$$\ln p(T|\nu, \sigma, \theta) = -\frac{1}{2} \sum_n \left[(T_n - T_m(\theta))^2 \sigma_n^{-2} + \ln(2\pi\sigma_n^{-2}) \right] \tag{4.1}$$

[7]https://emcee.readthedocs.io/en/v2.2.1/

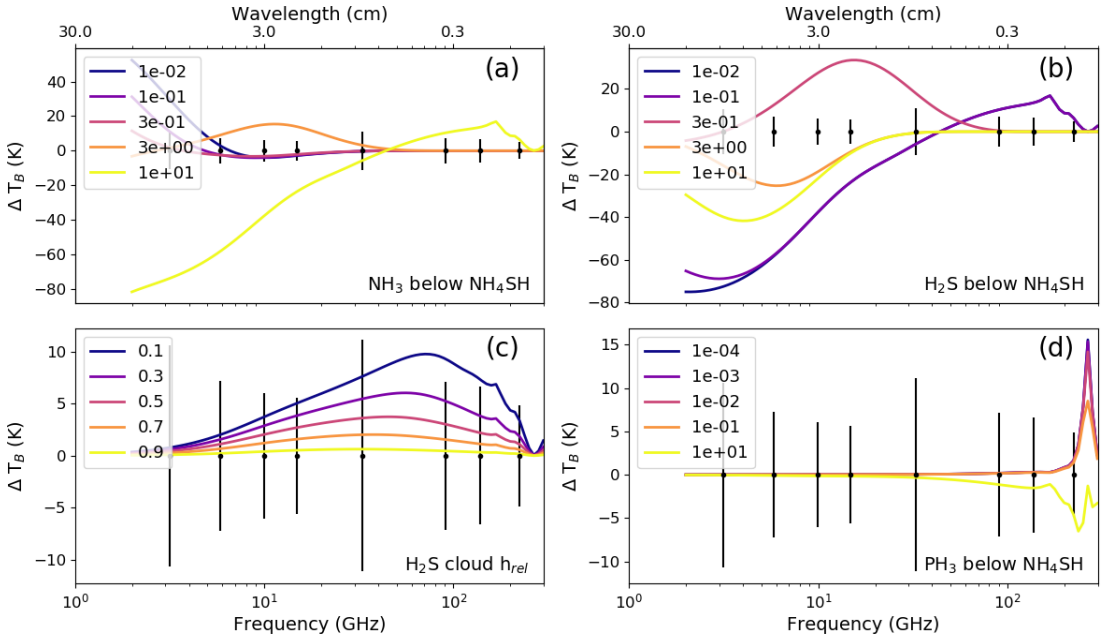

Figure 4.8: Effect of changing radiative transfer model parameters on the radio spectrum of Uranus. In each panel, one parameter was changed from its nominal value; the resulting model spectrum was subtracted from the nominal model such that ΔT_B represents the departure from the nominal model. Legend labels denote a multiplicative factor applied to the model parameter of interest, where 1.0 is the nominal value (30× Solar for H_2S and PH_3; 1× Solar for NH_3, 1.0 for H_2S h_{rel}). The black points plotted along the zero line show the size of the error bars on the data at the observed frequencies. All models were produced assuming viewing geometry from the sub-observer point.

where σ_n^2 is the variance of the measured brightness temperature T_n at each frequency ν_n. At each MCMC step, a set of test parameters θ is selected, a model brightness temperature $T_m(\theta)$ is generated by RadioBEAR at each frequency, and the likelihood function is evaluated. The result of many MCMC iterations is a joint probability distribution over the free parameters in the radiative transfer model. Each of the MCMC runs presented in this paper used 500 iterations and 40 walkers. As is standard practice with MCMC (Foreman-Mackey et al. 2013), we cut out the "burn-in" phase by using only the second half of the iterations to describe the posterior distribution; plotting the parameter values as a function of iteration confirmed that this procedure had worked as intended. We refer the interested reader to Hogg et al. (2018) for an overview of how MCMC works and is used in astrophysics research.

Parameter	2.5% (-2σ)	16% (-1σ)	Median	84% ($+1\sigma$)	97.5% ($+2\sigma$)	Abu./Solar (1σ)
NH_3 below NH_4SH	4.07×10^{-9}	2.63×10^{-7}	7.23×10^{-6}	8.49×10^{-5}	7.40×10^{-4}	$0.06^{+0.6}_{-0.04}$
H_2S below NH_4SH	5.34×10^{-4}	6.88×10^{-4}	8.27×10^{-4}	1.12×10^{-3}	1.50×10^{-3}	$35.2^{+12.5}_{-5.9}$
H_2S h_{rel}	0.005	0.02	0.05	0.13	0.34	—
CH_4 below NH_4SH	2.68×10^{-4}	1.77×10^{-3}	8.29×10^{-3}	2.39×10^{-2}	5.73×10^{-2}	17^{+33}_{-14}
ortho-para	0.03	0.19	0.58	0.87	0.97	—
PH_3 below NH_4SH	4.52×10^{-9}	2.86×10^{-7}	3.43×10^{-6}	1.16×10^{-5}	2.72×10^{-5}	18^{+43}_{-17}
H_2S above NH_4SH	4.29×10^{-4}	6.32×10^{-4}	8.09×10^{-4}	1.00×10^{-3}	1.31×10^{-3}	$34.4^{+8.3}_{-7.7}$
Deep H_2S	5.59×10^{-4}	7.20×10^{-4}	8.65×10^{-4}	1.17×10^{-3}	1.57×10^{-3}	$36.8^{+13.1}_{-6.2}$

Table 4.3: Values and errors for radiative transfer model parameters for the "enriched" region at 25°N. The median values are reported, along with the 16th/84th percentile values, which represent the 1σ interval, and the 2.5/97.5 percentile values, which represent the 2σ interval. The quantities below the horizontal line are not free parameters in the model, but can be determined from the retrieved vertical profiles. The values below the solution cloud are measured at 35 bar. The ortho-para fraction takes a value between 0 and 1, where 1 is "equilibrium" H_2 and 0 is "normal" H_2. The deep H_2S abundance refers to the model abundance below the water solution cloud.

Enriched Region

We first fit the radio-dark region at 25°N, chosen as the representative "enriched" or volatile-rich region because of its location at small emission angles with respect to the observer as well as relatively similar brightnesses at nearby latitudes, minimizing beam smearing effects. For computational efficiency, we simplified the full cloud-physics model to include only prescriptions for the NH_4SH cloud and the H_2S, NH_3, CH_4, and PH_3 ice clouds. The solution cloud beneath the NH_4SH cloud was ignored; this was a reasonable compromise because its location at ∼100 bar pressures is deeper than the observed frequencies probe (see Figure 4.7). The vertical abundance profile of H_2O as well as all other inputs (ortho-para fraction, adiabat) were set to their nominal values. We checked our simplified implementation against the full cloud-physics model, and found that the difference in brightness temperature between them was at least an order of magnitude smaller than the flux calibration errors at all frequencies. However, it should be noted that the MCMC retrieval estimates the NH_3 and H_2S abundances below the NH_4SH layer but above the solution cloud, i.e. at ∼50-100 bar. The solution cloud in the full model removes ∼5% of the deep H_2S and ∼25% of the deep NH_3; this is discussed further in Section 4.3. The retrieved values for all the parameters at 25°N are given in Table 4.3. The best-fitting model is compared to the data in Figure 4.9, and a "corner plot" displaying the one- and two-dimensional projections of the posterior probability distribution of the retrieved parameters is shown in Figure 4.10. The observed disk-averaged brightness temperatures are also reasonably well fit by the 25° model (see Figure 4.3).

The abundance of ammonia below the NH_4SH cloud is only weakly constrained in the enriched region, with a best-fitting value of 6% Solar but a 1σ confidence interval from 0.2%

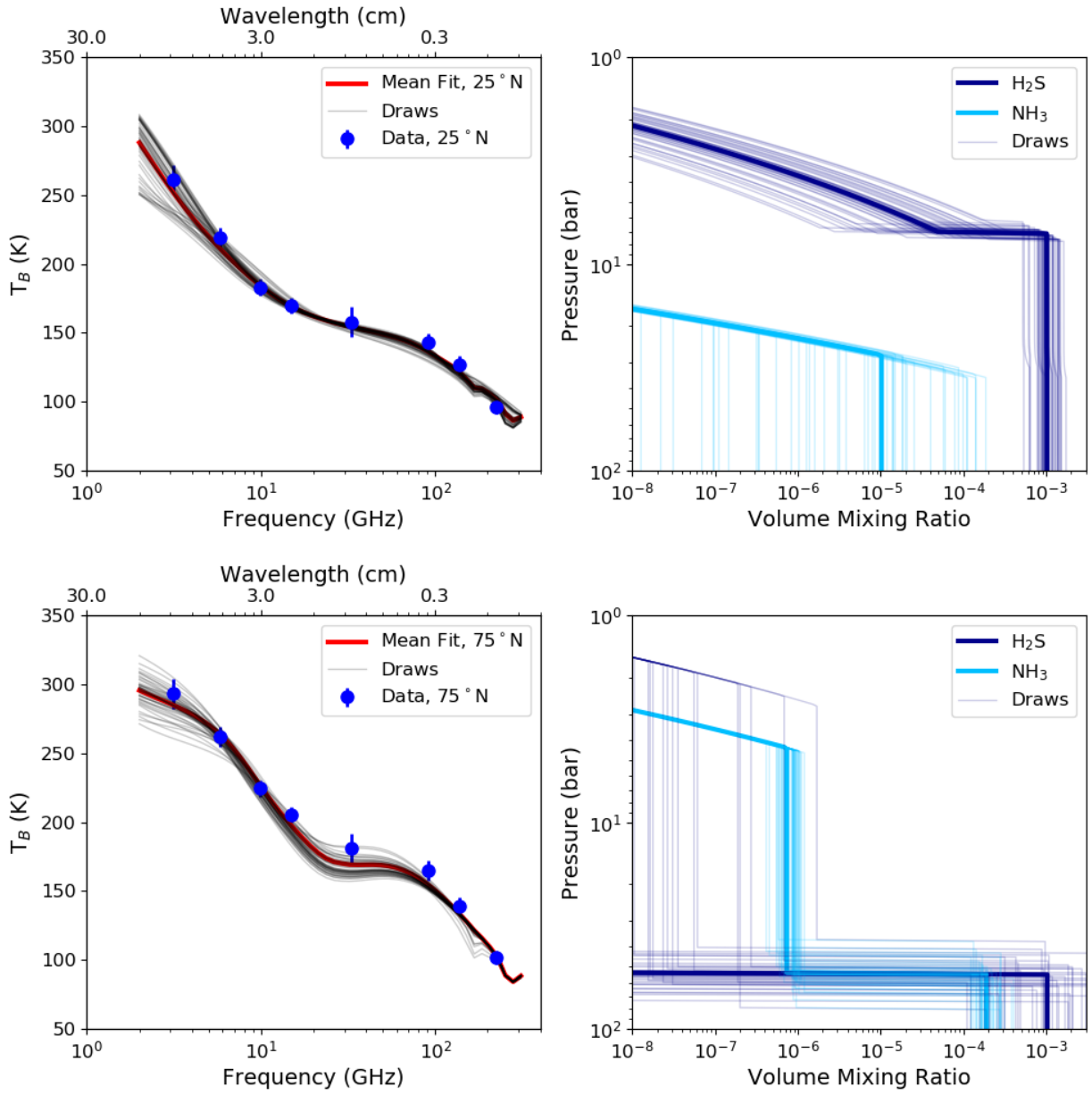

Figure 4.9: **Left:** Brightness temperature measurements of Uranus (blue dots) compared to our radiative transfer models at 25°N (top) and 75°N (bottom). The best-fitting model is shown as a thick red line, and 50 MCMC draws are shown as thin gray lines. **Right:** Abundance profiles of H_2S (dark blue) and NH_3 (light blue) for the best-fitting model (thick line) and the same 50 draws (thin lines) at 25°N (top) and 75°N (bottom). We refer the reader to Hogg et al. (2018) for an explanation of the meaning of model draws.

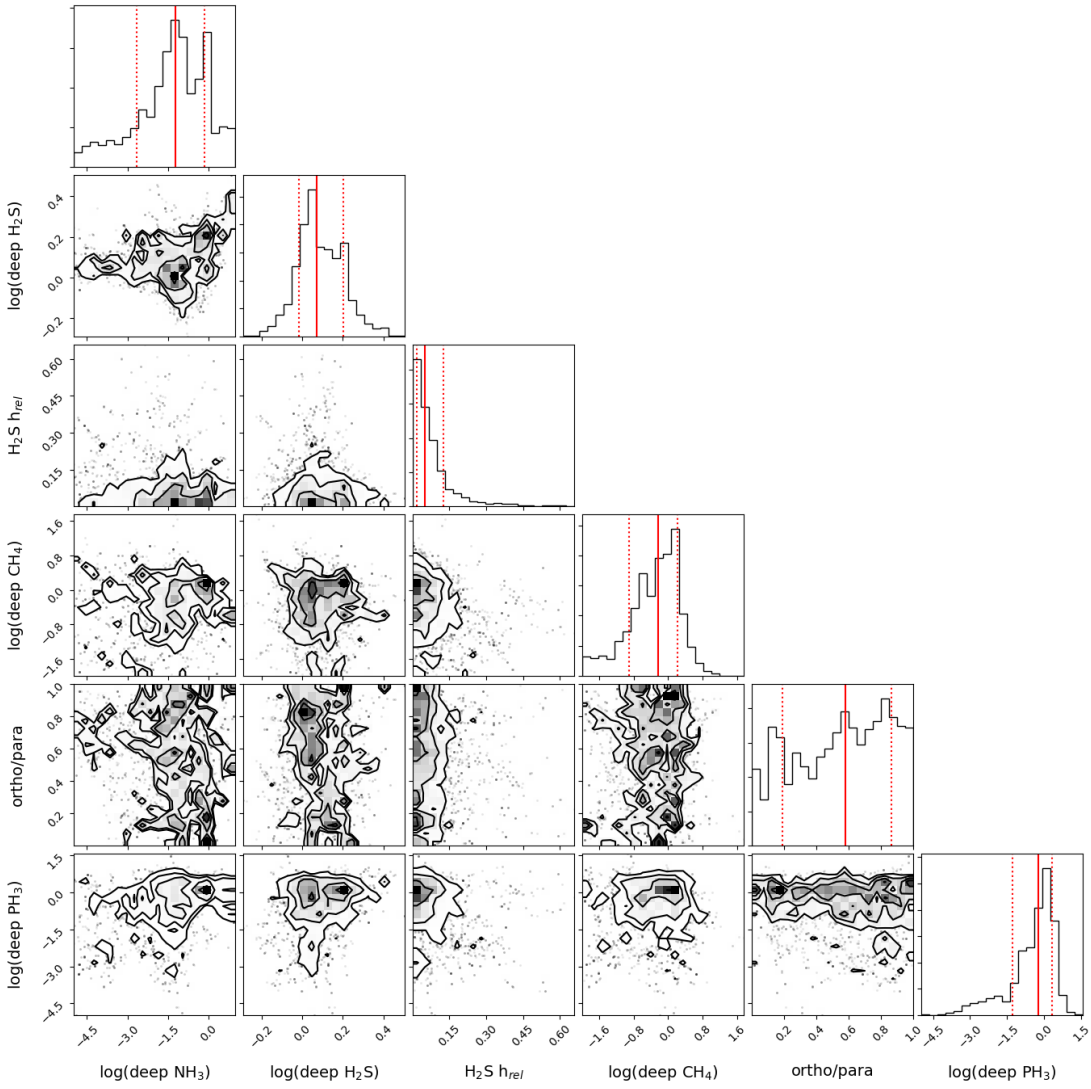

Figure 4.10: "Corner plot" showing the one-dimensional (top panels, corresponding to the label at the bottom of each column) and two-dimensional (other panels) projections of the posterior probability distribution of the MCMC-retrieved parameters for the radiative transfer models at 25°N. The mean value (solid red line) and 16th and 84th percentile (dotted red lines) of each probability distribution are plotted. We refer the reader to Hogg et al. (2018) for an explanation of how to interpret a corner plot.

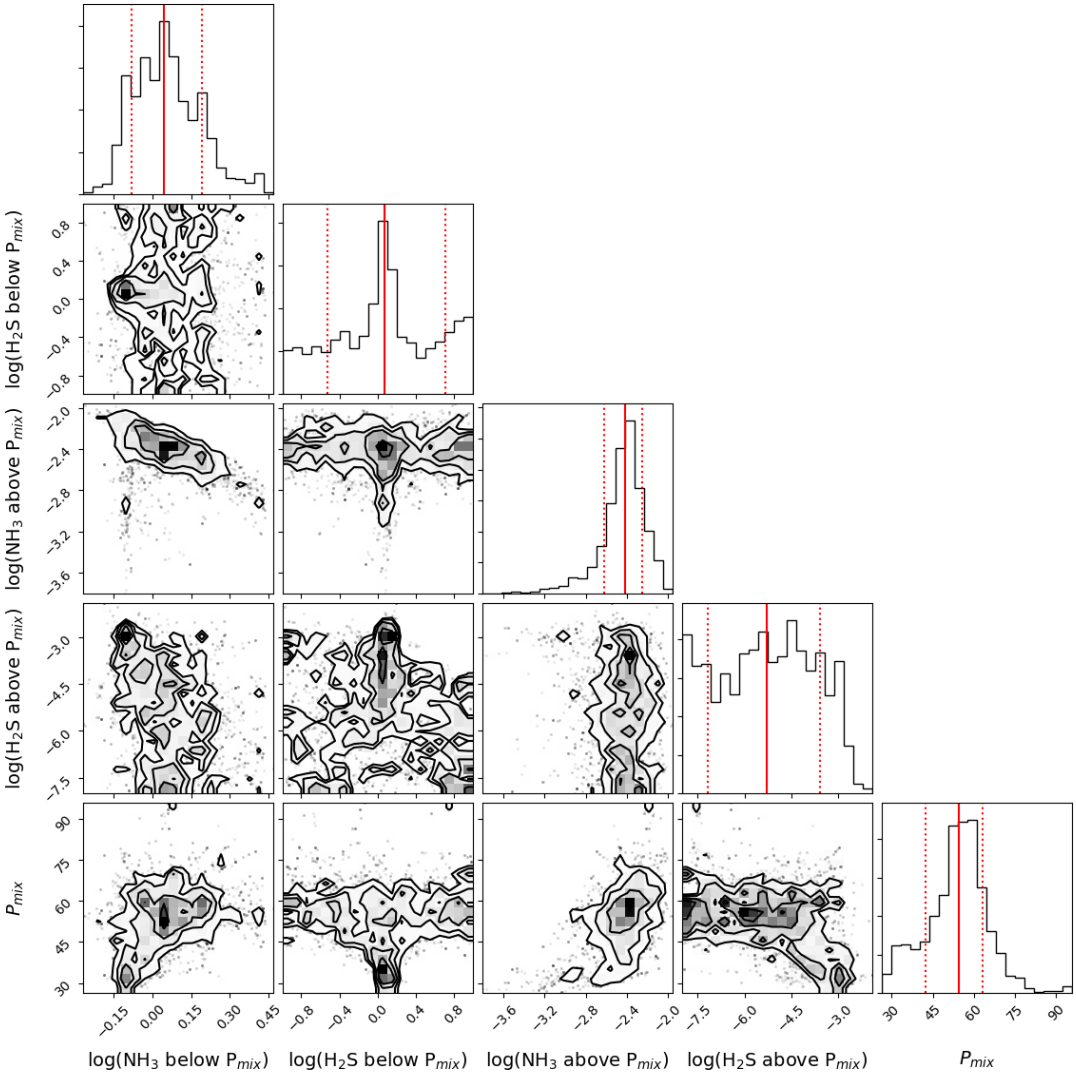

Figure 4.11: Same as Figure 4.10 but for the depleted model and data at 75°N.

to 70% Solar. This quantity is better constrained in the depleted north polar region, where the very low H_2S absorption allows our observations to probe deeper into the atmosphere (see Section 4.3). The hydrogen sulfide abundance takes a 1σ value of $35.2^{+12.3}_{-5.9}\times$ Solar below the NH_4SH cloud, in excellent agreement with previous results (de Pater, Romani, et al. 1991). The relative humidity of the H_2S ice cloud takes an 84th percentile value of 0.13, meaning that $h_{rel} < 13\%$ is preferred to higher values. Models that include at least some PH_3 are preferred, as absorption from the pressure-broadened PH_3 line at 1.123 mm (266.9 GHz) is the only way in our model to decrease the brightness temperature at 1.3 mm relative to 2.1 mm. Indeed, a PH_3 abundance below $\sim$3% Solar is disfavored at the 2σ level. However, the spectral slope within the 1.3 mm ALMA band is more consistent with models lacking phosphine absorption than models including it (see Figure 4.12). A detailed study of Uranus's radio spectrum around the PH_3 $J = 1 \rightarrow 0$ absorption line at 1.123 mm (266.9 GHz) is required to confirm or rule out the presence of significant PH_3 in the Uranian troposphere. The methane abundance is only weakly constrained. Our retrieved abundance agrees with previous measurements at near-infrared and visible wavelengths, which range from $\sim$3 to $\sim$5% in the equatorial regions (Irwin, Fletcher, Teanby, et al. 2019; Karkoschka and Tomasko 2009; Sromovsky, Karkoschka, Fry, de Pater, et al. 2019; Sromovsky, Karkoschka, Fry, Hammel, et al. 2014; Tice et al. 2013), but is not as constraining as these studies. The average spin state of hydrogen (ortho-para) remains completely unconstrained by our data.

North Pole

We then modeled the brightness temperature of the depleted north polar region at 75° N. Physically, the situation in the downwelling depleted region differs from that in the upwelling enriched region: the subsiding air is already depleted in condensible species, so strong subsaturations are likely at certain pressures. In addition, the depletion in abundances does not extend to infinite depth—the atmosphere must be well-mixed deeper than some pressure P_{mix}. Thus the deep abundance should remain the same as retrieved in the enriched region. With these considerations in mind, we employ a model for the depleted region that prescribes a step function in the H_2S and NH_3 abundances. We set the prior probability distribution functions of the deep abundances equal to the posterior probability distribution functions found for the enriched region; that is, the deep abundances are constrained to agree with the enriched region. The H_2S and NH_3 abundances are uniform above some mixing pressure P_{mix} until the species reaches its condensation level; the depletion factor of each species and P_{mix} are allowed to vary freely. The retrieved values for all the parameters at 75°N are given in Table 4.4. The best-fitting model is compared to the data in Figure 4.9, and a "corner plot" displaying the one- and two-dimensional projections of the posterior probability distribution of the retrieved parameters is shown in Figure 4.11.

The MCMC simulation shows that strong depletions in both NH_3 and H_2S are required above the mixing pressure. The results are consistent with zero H_2S above the mixing pressure; the simulation yields a 1σ upper limit of 0.8% Solar, which translates to at least $\sim$4000 times less H_2S above P_{mix} than in the enriched region, i.e., an abundance $\lesssim 2 \times 10^{-7}$.

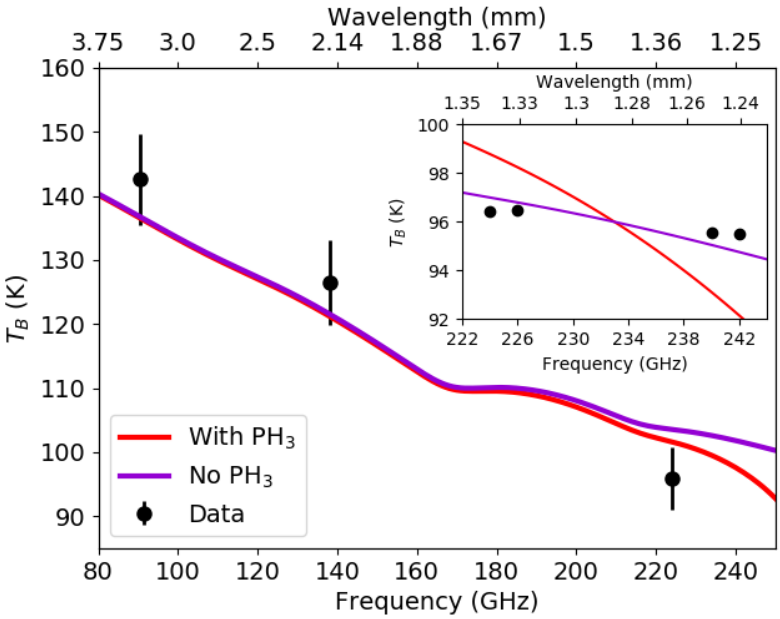

Figure 4.12: **Main:** ALMA data at 25°N (black points) plotted over radiative transfer models with 35× Solar phosphine (red line) and without any phosphine (purple line). The inclusion of phosphine marginally improves the fit. In this plot, the error bars include the flux calibration error and are identical to those in the left panel of Figure 4.9. **Inset:** ALMA data in Band 6 (1.24-1.35 mm) split into its four spectral windows. We plot here only the error due to random noise, which is very small compared to the brightness of Uranus; the error bars are of the same order as the thickness of the data points. The radiative transfer models are normalized so that their value at 1.29 mm (233 GHz) is equal to the mean of the Band 6 data, to facilitate visual comparison of the spectral slopes. The inclusion of phosphine makes the spectral slope agreement poorer.

Parameter	2.5% (-2σ)	16% (-1σ)	Median	84% ($+1\sigma$)	97.5% ($+2\sigma$)	Abu./Solar (1σ)
NH_3 below P_{mix}	8.46×10^{-5}	1.00×10^{-4}	1.31×10^{-4}	1.86×10^{-4}	2.74×10^{-4}	$1.10^{+0.46}_{-0.26}$
H_2S below P_{mix}	8.46×10^{-5}	2.07×10^{-4}	8.46×10^{-4}	3.61×10^{-3}	6.41×10^{-3}	36^{+118}_{-27}
NH_3 above P_{mix}	1.09×10^{-7}	2.88×10^{-7}	4.67×10^{-7}	6.75×10^{-7}	9.53×10^{-7}	$3.9^{+1.7}_{-1.5} \times 10^{-3}$
H_2S above P_{mix}	—	—	—	1.89×10^{-7}	1.11×10^{-6}	<0.008
P_{mix}	30.64	42.23	54.59	63.23	75.58	—
Deep NH_3	1.02×10^{-4}	1.31×10^{-4}	1.71×10^{-4}	2.43×10^{-4}	3.92×10^{-4}	$1.44^{+0.60}_{-0.34}$

Table 4.4: Values and errors for radiative transfer model parameters for the "depleted" north polar region at 75°N. The median values are reported, along with the 16th/84th percentile values, which represent the 1σ interval, and the 2.5/97.5 percentile values, which represent the 2σ interval. The quantities below the horizontal line are not free parameters in the model, but can be determined from the retrieved vertical profiles. The deep NH_3 abundance refers to the model abundance below the H_2O solution cloud.

The results do not constrain the H_2S abundance below P_{mix} any more than did the enriched region model. Because so little H_2S absorption is present, the spectrum of the depleted north polar region is more sensitive than the enriched equatorial region to the NH_3 abundance below the mixing pressure, and this quantity is constrained to $1.10^{+0.45}_{-0.26}\times$ Solar (1σ). Above the mixing pressure, the model is consistent with a factor of $\sim$280 depletion in NH_3 in the north polar region compared to the enriched midlatitude region, i.e., an abundance of $\sim 5 \times 10^{-7}$. The retrieved mixing pressure of 55^{+9}_{-12} (1σ) is somewhat deeper than the level at which the NH_4SH cloud is expected to form in equilibrium ($\sim$35 bar); however, this value remains within the 95% (2σ) confidence interval. It is thus a reasonable guess that the atmosphere transitions from well-mixed to depleted at the NH_4SH cloud.

RT Modeling Discussion

The good fit to the data provided by our cloud-physics model (Figure 4.9) lends strong support to a Uranian atmosphere dominated by H_2S absorption in the upwelling regions, with most or all NH_3 removed from the troposphere by the NH_4SH cloud. This model, which is similar to that of de Pater, Romani, et al. (1991) and de Pater, Romani, et al. (1989), permits significant H_2S above the NH_4SH cloud. The nitrogen-to-sulfur (N/S) ratio does not need to be tuned to very near unity as required by the H_2S-inclusive models of Hofstadter (1992). The midlatitudes are fit by a solar NH_3 abundance below the NH_4SH layer, which forms at a pressure of $\sim$35 bar. This is deeper than the midlatitude mixing pressure of $\sim$22 bar determined by Hofstadter, Berge, et al. (1990); however, those authors did not consider the role of H_2S absorption on Uranus's radio spectrum. In the downwelling north polar region, our model agrees well with the Hofstadter, Berge, et al. (1990) and Hofstadter (1992) south polar region model: those authors required an NH_3 abundance of $\sim 5 \times 10^{-7}$ down to $\sim$50 bar pressures (they ignored H_2S gas opacity). All three of those requirements are within 1σ of our results, providing evidence that the north- and south-polar warm spots may arise from the same chemical processes.

The retrieved abundances derived in the previous subsections came from a simplified cloud-physics model that did not take into account the solution cloud at pressures deeper than 50 bars. Thus, to make inferences about the true deep abundances of nitrogen- and sulfur-bearing species, we returned to the full cloud-physics model of de Pater, Romani, et al. (1991), which includes prescriptions for the deep water and water-solution clouds from Atreya and Romani (1985). We tuned the model such that the NH_3 and H_2S abundances between the solution cloud and the NH_4SH cloud matched our retrieved abundances of those species. For this purpose, we used the best-fitting H_2S abundance below the NH_4SH cloud from the enriched region and the best-fitting NH_3 abundance below P_{mix} from the depleted region, since those were the best-constrained values and the two regions are assumed to be well-mixed below the mixing layer. This procedure yielded abundances in the deep troposphere of $1.7^{+0.7}_{-0.4} \times 10^{-4}$ ($1.4^{+0.6}_{-0.3}\times$ Solar; 1σ) for NH_3 and $8.7^{+3.1}_{-1.5} \times 10^{-4}$ ($37^{+13}_{-6}\times$ Solar; 1σ) for H_2S.

Using the NH_3/H_2S ratio as a proxy for the nitrogen/sulfur (N/S) ratio, our results provide a much stronger constraint on Uranus's bulk atmospheric N/S ratio than previous

work. We find N/S = $0.20^{+0.08}_{-0.07}$ (1σ), in agreement with de Pater, Romani, et al. (1991) and de Pater, Romani, et al. (1989), who required N/S< 0.2. This is a very strong selective enrichment in sulfur considering the Solar N/S value of ∼5. Our observed sulfur-to-nitrogen ratio can be explained by an ice giant formation scenario in which volatiles were trapped as clathrate hydrates and then swept up by planetesimals (Hersant et al. 2004). Those authors argue that in the cold, ice-rich conditions of the outer disk, NH_3 and H_2S would be trapped very efficiently by clathration and accrete onto solid grains, while N_2 would remain in the gas phase. At the temperature and pressure of the outer disk, nearly all sulfur is in the form of H_2S, and the N_2:NH_3 ratio is roughly 10:1. Therefore, Uranus and Neptune should have accreted nearly all available sulfur but only a small fraction of available nitrogen, decreasing the N/S ratio by a factor of ∼20, which is close to what we observe.

4.4 Conclusions

The millimeter and radio observations presented here provide a unique view of Uranus's troposphere: we provide the first published millimeter-wavelength maps of the planet, as well as the first VLA observations taken during northern summer. Our results are summarized as follows.

- High-spatial-resolution maps reveal a complex tropospheric circulation pattern, including thin, bright, likely downwelling bands at ∼0°N, 20°N, and 20°S in the 2 cm VLA and 2.1/3.1 mm ALMA maps. The identity of the absorber in these bands remains unknown, but variations in the relative humidity of H_2S or the methane abundance are good candidates to explain these features. Kinetic temperature variations may also play a role.

- The north polar region is approximately equal in brightness and extent to the south polar region observed three decades ago, with a radio brightness temperature ∼35 K brighter at 2 cm than the midlatitudes. The polar brightening can be observed over a large range of frequencies from 10 cm - 1 mm. Taken together with methane sensitive infrared measurements, this implies a single vertical cell of downwelling air from ∼0.1 to 50 bars. Radiative transfer modeling suggests the north polar region is depleted in ammonia to a similar degree as the south polar region observed 30 years ago; both have an NH_3 volume mixing ratio of $\sim 5 \times 10^{-7}$ above the ∼50 bar level and zero H_2S opacity.

- The radio spectrum of the dark upwelling midlatitude regions between ∼40°S and ∼40°N is consistent with a model in which all NH_3 is removed by the NH_4SH cloud at ∼35 bar, and constrains the deep H_2S abundance to $37^{+13}_{-6}\times$ Solar.

- The radio spectrum of the downwelling north polar region at latitudes north of ∼50°N is consistent with strong depletions in both ammonia and hydrogen sulfide from the

top of the atmosphere down to a mixing pressure $P_{mix} = 55^{+9}_{-12}$. The strong depletion in H_2S in this region permits the deep NH_3 abundance to be well constrained, taking a value of $1.4^{+0.6}_{-0.3}\times$ Solar.

- The deep sulfur-to-nitrogen ratio in Uranus's troposphere is N/S = $0.20^{+0.08}_{-0.07}$ (note protosolar N/S $\sim$ 5), assuming the Atreya and Romani (1985) prescription for the water-solution cloud at pressures deeper than 50 bars and no temperature difference between the equator and the pole. This is the most stringent constraint on that ratio to date.

- The phosphine abundance in the ice giants remains unknown; the observations presented in this work are only sensitive to pressure-broadened phosphine spectral lines at the 2σ level in one band (ALMA Band 6; 1.3 mm), and the spectral slope in this band does not support a pressure-broadened phosphine line.

This paper lays the groundwork for more detailed studies of Uranus's tropospheric circulation and composition with the upcoming next-generation Very Large Array (ngVLA). The ngVLA will perform 10 cm and 20 cm observations at resolutions of $\sim$3 mas and $\sim$10 mas, respectively, permitting a much stronger constraint on the ammonia abundance in the ice giants. Observations from 3 cm to 3 mm at resolutions down to 0.1 mas will resolve the new dark and bright bands discovered in this work well enough to extract robust brightness temperature measurements from those regions; applying radiative transfer models may identify the absorbers responsible for these bands. An outline of the solar system science that will become possible with the ngVLA is given in de Pater, Butler, et al. (2018).

4.5 Appendix: Meridional Temperature Gradients

The radio occultation experiment aboard the Voyager 2 spacecraft determined the temperature-pressure profile in Uranus down to roughly 2.7 bar (Lindal et al. 1987); however, this measurement was made using two occultations between 0° and -10° latitude, so meridional differences were not observed. The IRIS instrument determined the temperature structure down to $\sim$0.6 bar as a function of latitude, finding temperature differences smaller than 2 K (Pearl et al. 1990). Similarly small temperature differences have also been observed in the upper troposphere from more recent ground-based studies (Roman et al. 2020). The latitudinal temperature structure of Uranus has not been directly observed below 1 bar. Most atmospheric models predict that meridional temperature gradients should be small because the orbital period is much shorter than the radiative relaxation time in Uranus's troposphere (Conrath et al. 1990; Friedson et al. 1987; Wallace 1983); however, recent calculations have cast doubt on the radiative timescales used in those papers (Li, Le, et al. 2018). We must therefore consider the possibility that the observed brightness temperature difference between the midlatitude and polar regions is driven primarily by differences in kinetic temperature, instead of differences in composition as assumed in the main text.

The strength of an absorption feature is set by both the abundance profile of the absorbing species and the atmospheric temperature profile. To disentangle temperature and abundance is an underconstrained problem; however, a large midlatitude-to-pole temperature difference between ∼0.6 and 50 bar is generally considered unlikely based on several lines of evidence. These have been summarized convincingly by Hofstadter and Butler (2003), and here we leverage our new data to expand upon the arguments of those authors.

The radio/millimeter spectra at the midlatitudes and poles cannot both be fit with the same composition unless a highly unphysical temperature-pressure profile is assumed. The latent heat of condensation of H_2S (or H_2S/NH_3 in the NH_4SH cloud) at saturation is very small compared to the enthalpy of a parcel of air in Uranus, so the difference between a moist and dry adiabat is very small. However, if the requirement to fit the Voyager data at pressures less than 0.6 bar is relaxed, warmer or cooler adiabats can be considered. Starting with our best-fitting gas abundances and vertical temperature structure in the midlatitude region (Section 4.3), we tried using warmer adiabatic profiles; a sample result is shown in Figure 4.13. No adiabatic profile can effectively fit the north polar data. To achieve a reasonable fit to the observed north polar spectrum using only kinetic temperature changes requires many unphysical kinks in the temperature structure (Figure 4.13). The "solutions" we find require a strongly superadiabatic lapse rate near the H_2S ice cloud level to bring H_2S condensation high in the atmosphere, and a strongly subadiabatic lapse rate deeper than that to keep the NH_4SH cloud deep enough. Overall, we find that the spectra, and in particular the millimeter wavelengths, are highly sensitive to the pressure level of the H_2S and NH_4SH clouds; the kinetic temperature must be tuned very finely to place these at the correct equilibrium level. It is worth noting that a discontinuity in the temperature profile at a condensation layer is possible if a large vertical gradient in atmospheric molecular weight is also present, as has been suggested for both the methane and H_2O cloud layers (Cavalié, Venot, Selsis, et al. 2017; Cavalié, Venot, Miguel, et al. 2020; Guillot 1995). However, the abundances of NH_3 and H_2S have a factor of $\gtrsim$25 less effect on the atmospheric molecular weight than those of CH_4 and H_2O, so this effect is not expected to be important near the NH_4SH or H_2S cloud layers.

Hofstadter and Butler (2003) considered the complementary situation, in which the bright polar region followed an adiabat and the equatorial region was fit using strongly subadiabatic temperature profiles. This goes contrary to most theory, which generally predicts that the pole should be more stably stratified (Briggs et al. 1980; Friedson et al. 1987; Wallace 1983), but shall be considered regardless. In this case, the temperature profiles at the midlatitudes and poles were both forced to fit the Voyager data, but allowed to diverge below. Hofstadter and Butler (2003) note that the temperature differences needed to make this work, which reach 90 K at 20 bar pressure, imply a vertical wind shear of -100 m s^{-1} per scale height at 20 bar by the thermal wind equation. However, they stop short of integrating the thermal wind equation vertically to produce a geostrophic wind profile. We have done this, and find that the winds must be supersonic deeper than ∼20 bar, which is unphysical. It is worth noting that the thermal wind equation assumes a compositionally constant atmosphere wherein density differences are due to temperature only. Significant meridional gradients in

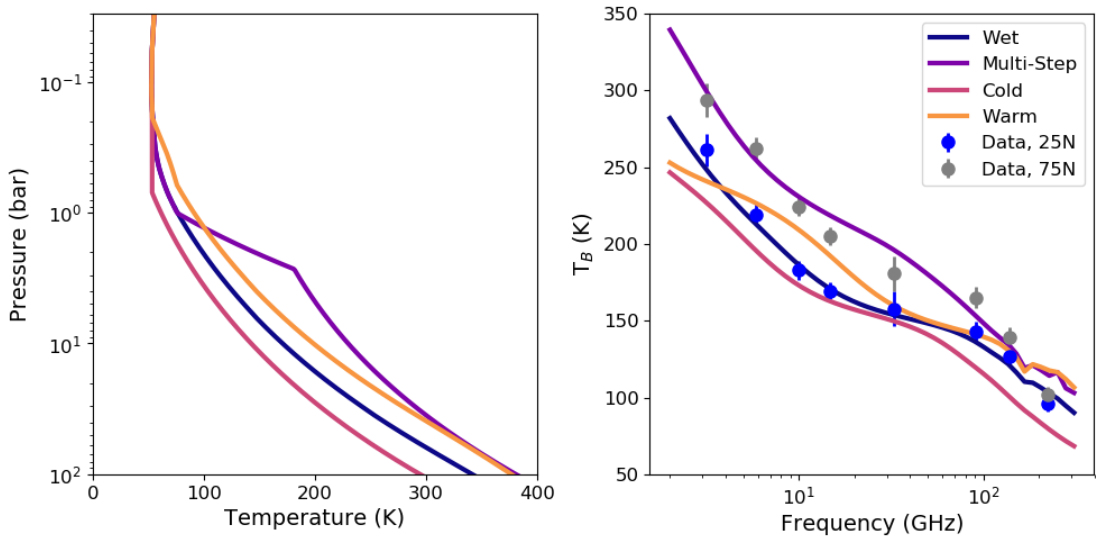

Figure 4.13: Effect of temperature profile perturbations on the radio/millimeter spectrum of Uranus. Using the same chemical abundances as for our best-fitting model at 25°N, we consider a wet adiabat (blue line) and a warmer and cooler adiabat (orange and salmon lines). We also attempt to perturb the temperature profile ad-hoc until a reasonable fit to the north-polar-region data is achieved (purple line).

composition could arise on Uranus via gradients in the methane abundance, since methane accounts for up to 5% of the troposphere by volume and is much heavier than hydrogen and helium (Sun, Schubert, et al. 1991; Tollefson, Pater, et al. 2018). However, methane is observed to be depleted in the poles relative to the midlatitudes (Irwin, Fletcher, Teanby, et al. 2019; Karkoschka and Tomasko 2009; Sromovsky, Karkoschka, Fry, de Pater, et al. 2019; Sromovsky, Karkoschka, Fry, Hammel, et al. 2014; Tice et al. 2013), so the implied compositional (and therefore density) gradients would lead to even larger vertical wind shear. The observed thermal wind (e.g., Sromovsky, de Pater, et al. 2015) also points, again by the thermal wind equation, to a warmer midlatitude region than polar region.

Taken together, these arguments show that composition is the primary driver of the observed brightness temperature differences at millimeter and radio wavelengths. However, the possibility that both temperature and composition change between the midlatitudes and poles cannot be ruled out. A different assumed polar temperature profile would have a relatively small but perhaps non-negligible effect on the deep NH_3 abundance retrieved in this paper.

Chapter 5

Quantitative Precipitation Estimation of Extremes in CONUS with Radar Data

The published version of this chapter was coauthored by the following individuals, and is included in this thesis with their express permission: William D. Collins, Mark D. Risser.

Constructing an accurate, continental, in-situ-based, kilometer-scale, long-term record of the precipitation field and its spatio-temporal changes remains a significant challenge. Here, we determine the extreme-value behavior of the NEXRAD Stage IV radar-based quantitative precipitation estimate (QPE). We find that the climatology of 5-year daily return values in CONUS East of the Rocky Mountains shows only slight variability on spatial scales smaller than ∼100 km. In light of this finding, we test whether rain-gauge-only daily precipitation datasets can produce accurate extreme-value behavior at spatial scales finer than the spacing between gauges. We find that the 5-year daily return values are accurate at locations far from rain gauges only if the interpolation between gauges is carried out appropriately for extremes. Precipitation statistics derived from in-situ rain gauge data are therefore of sufficient spatial resolution to faithfully capture daily extremes over much of the eastern United States.

Plain Language Summary

Accurate measurement of the amount of precipitation that falls within a given region and time period is crucial for environmental modeling, climate change research, and resource and risk management. For all of those applications, it is desirable to understand not only how much precipitation falls on average, but also how much precipitation falls during an extreme event, such as a severe storm. Using data from weather radar, we show that certain statistical properties of extreme rainfall are highly correlated on spatial scales up to 100 kilometers over the eastern United States. This means that rain gauge networks, which have typical inter-gauge spacings of roughly 30 kilometers over the eastern United States, are dense enough

to accurately measure these statistical properties. However, it's imperative to interpolate between the rain gauge measurements in a way that explicitly captures extremes if the application of interest requires capturing extremes accurately. Our research represents a step toward constructing an accurate, continental-scale, long-term, high-resolution precipitation dataset.

5.1 Introduction

Accurate measurement of the amount of precipitation that falls within a given region and time period is crucial for environmental modeling (e.g. Abatzoglou 2013; Jones, Gladkow, et al. 2001; Parra et al. 2004), climate change research (e.g. Alexander et al. 2006; Groisman et al. 1999; Schär et al. 2016), and resource and risk management (e.g. Rosenzweig et al. 2002; Schumann 2011; Vogel et al. 2019). All of these applications require understanding not only the seasonal-mean or annual-mean precipitation, but also the extreme tail of the daily or sub-daily precipitation distribution. Precise measurements of the total rainfall over a specific area at scales of tens of kilometers or less, such as a city or watershed, are often also needed.

Estimating the true spatio-temporal distribution of precipitation from observational data is known as quantitative precipitation estimation (QPE), and is currently obtained from three main data sources: satellite, rain gauges, and ground-based radar. Each source provides unique advantages subject to specific limitations. Satellite observations provide spatially continuous measurements, but are subject to severe uncertainty because precipitation must be inferred from cloud top height or temperature as derived from microwave and/or infrared spectra (Iguchi et al. 2009; Tapiador, Turk, et al. 2012). This uncertainty generally leads to overestimation of extreme precipitation events relative to gauge- or radar-based estimates (AghaKouchak et al. 2011; Mehran et al. 2014). Over the contiguous United States (CONUS), where the density of both rain gauges and radar stations is high, satellite-based QPE products tend to perform compared unfavorably to other estimates. For example, Timmermans et al. (2019) found significant biases in the representation of daily precipitation extremes from satellite-based gridded QPEs compared with rain gauge estimates. Satellite products are therefore not considered further here.

Rain gauges provide the most accurate and temporally continuous point measurements of precipitation despite errors from undercatch, variance in management quality, and changes in location or equipment (see Tapiador, Turk, et al. 2012, for a recent review). They also provide the longest time record of any precipitation measurement by far. However, gauges yield point measurements only, and one must interpolate spatially between them to estimate precipitation over an area. Ground-based radar observations provide very high native spatial and temporal resolution. Each Weather Surveillance Radar 88 Doppler Radar (WSR-88D) radar stations in CONUS (NOAA 2006) completes a full scan of the sky every $\sim$10 minutes, and the station's preprocessing algorithm bins the scan into 1 km range by 1° azimuth sections, amounting to sub-hourly precipitation estimates on a $\lesssim$4 km grid (Fulton et al. 1998).

However, the relationship between radar reflectivity and precipitation rate is degenerate and differs for different types of storms, and therefore it must thus be determined empirically via comparison with rain gauge data (Fulton et al. 1998; Young, Bradley, et al. 2000). Multisensor estimates combine the high spatial and temporal coverage of the radar data with the high fidelity of the gauge data, and hence represent the state-of-the-art in operational QPE. However, experiments to validate these QPEs often take place over small regions and on timescales shorter than a few months (e.g., Seo, Krajewski, et al. 2018; Spies et al. 2018; Willie et al. 2017).

A variety of studies make use of gauge-based QPE and solve the aforementioned spatial interpolation problem in various ways, sometimes making use of elevation corrections or models of climatology (e.g. Daly, Neilson, et al. 1994; Daly, Smith, et al. 2015; Livneh, Rosenberg, et al. 2013; Schaake et al. 2004; Sheridan et al. 2010). We refer to this class of gauge-based analysis of extremes as "grid-then-fit" techniques because they interpolate at the native temporal scale (e.g., daily) and then calculate statistical properties of the interpolated data. These approaches tend to underestimate extreme precipitation, especially at small (0.25°) scales (Behnke et al. 2016; Gervais et al. 2014; Sun and Barros 2010). To rectify this issue, Risser et al. (2019) have developed a statistical "fit-then-grid" technique in which Generalized Extreme-Value (GEV) statistics (see Coles et al. 2001) are calculated at individual rain gauges, the GEV parameters are spatially interpolated, and then the gridded GEV distributions are reconstructed from these interpolated parameters. This method implicitly assumes that the parameters of the GEV distribution vary smoothly in space, such that high-quality inference about extremes can be made in between stations. The optimal gauge interpolation technique depends on both the grid resolution and the application of interest (Chen et al. 2008; Gervais et al. 2014), and best practices for interpolating to smaller scales than the inter-gauge spacing have not been established.

This study seeks to determine whether the extreme statistics of daily precipitation vary smoothly between rain gauges over the CONUS, testing the assumption of Risser et al. (2019) over that domain, and to evaluate the accuracy of this novel fit-then-grid technique as compared with standard grid-then-fit algorithms. To these ends, we consider the GEV statistics of a dataset at very high (4 km) spatial resolution, namely the NEXRAD Stage IV daily dataset (Fulton et al. 1998; Lin 2011; Lin and Mitchell 2005; Seo and Breidenbach 2002), a radar-based multisensor QPE, from 2002-2019. Stage IV is available at hourly, six-hourly, and daily frequencies. We focus on daily maxima here to facilitate comparison with the GHCN-D network, the most extensive network of rain gauges in the CONUS, and to test the results of Risser et al. (2019) directly. Stage IV has been evaluated extensively in the literature, including via the use of percentile-based metrics to capture extreme value behavior (Nelson et al. 2016; Prat et al. 2015). However, percentile-based metrics have been shown to produce different results depending on the specific metric used (Schär et al. 2016). McGraw et al. (2019) previously employed GEV statistics in a comparison between rain gauges and Stage IV data at hourly, 3-hourly, 6-hourly, and daily frequencies. However, they only reported those statistics at the locations of ∼500 rain gauges and did not consider spatial variability in their GEV fits. Our paper is the first (to our knowledge) to publish

GEV statistics at every grid cell in Stage IV.

We describe our data processing and GEV fitting in Section 5.2. In Section 5.3, we use this new data product to explore whether the high spatial resolution of this QPE provides new information on the climatology of extremes at finer spatial scales than accessible using gauge-only estimates. In Section 5.4, our product is compared with the Risser et al. (2019, hereafter R19) gauge-only interpolation technique, as well as with the Mountain Mapper algorithm (Schaake et al. 2004), a more conventional gridded QPE that incorporates the Parameter-elevation Relationships on Independent Slopes Model (PRISM) climatological model (Daly, Smith, et al. 2015) and is widely used for operational weather analyses. Specifically, Mountain Mapper is the official rainfall product distributed by the California-Nevada, Colorado Basin, and Northwest River Forecast Centers of the National Oceanographic and Atmospheric Administration (NOAA). We contextualize our findings within existing literature on the spatial scales of extremes in Section 5.5, then summarize our work in Section 5.6.

5.2 Data Processing

We computed and made use of three distinct extreme-value datasets in this paper; these are summarized below.

Stage IV GEV: We downloaded the 4-km-resolution daily NEXRAD Stage IV gridded multisensor QPE for every day between 1 January 2002 and 31 December 2019, totaling 6573 days (18 years) on a 881×1121 grid. We compared the Stage IV daily measurements to Global Historical Climatology Network Daily (GHCN-D) rain gauge data (Menne et al. 2012) in grid cells that contained a GHCN station. These validation steps are outlined in Supporting Information S1. Stage IV was found to agree very well with GHCN-D in both means and extremes in grid cells that contained a gauge, meaning that the normalization of the radar data to nearby rain gauges in the Stage IV processing pipeline preserves information about extremes.

As noted by other authors (Nelson et al. 2016; Prat et al. 2015), Stage IV is a fundamentally heterogeneous dataset. The product from the three western NOAA River Forecast Centers (California-Nevada, Northwest, and Colorado Basin, hereafter "Western RFCs") differs substantially from that of the nine other RFCs comprising the CONUS (hereafter "Eastern RFCs"). Specifically, the Western RFCs produce their QPE using the gauge-only Mountain Mapper technique discussed below and do not incorporate radar data at all, while the Eastern RFCs use the radar-inclusive procedures outlined in Fulton et al. (1998) and Lin and Mitchell (2005). Data from the Western RFCs are therefore not actually made using a multisensor technique, and so are for the most part not considered further in this paper.

In each grid cell of Stage IV, we extracted seasonal maximum precipitation amounts for each season (DJF, MAM, JJA, and SON), and then fit the GEV distribution to the 18 seasonal maxima over our period of record. This is a fairly short period of record over which to apply GEV statistics; however, in this work we draw our conclusions from the 5-year return values only, which are well sampled by 18 years of data. To assess whether our GEV

fits provided an adequate representation of the data, we performed a 2-sided Kolmogorov-Smirnov (K-S) test to quantify the likelihood that the observed seasonal maxima were drawn from the GEV distribution. We found a p-value of < 0.05 in at least 94% of grid cells in the Eastern RFCs in all seasons, meaning that the data were plausibly drawn from the GEV distribution. We used the GEV fit to generate 5-year return value estimates in each grid cell for each season. Following R19, we assessed the errors in our fit parameters using a bootstrap resampling technique: the seasonal maxima at each grid cell were resampled with replacement and then re-fit 250 times, and the standard deviation of the fit parameters in those 250 fits were used to define the 1-σ error on the parameters.

R19 GEV: We used the same extreme-value dataset as R19, which is based on GHCN-D rain gauge measurements, but extracted 5-year return values instead of 20-year return values as in that paper. To create a mean climatology from the R19 analysis, the exact same procedures described in R19 were applied to GHCN measurements of seasonal average daily precipitation (instead of seasonal maximum daily precipitation), and an ordinary least-squares fit was applied at each station such that the spatially-interpolated parameters were the mean and variance instead of the GEV parameters. We refer to this mean climatology hereafter as the "R19 mean".

Mountain Mapper: The Mountain Mapper dataset (Schaake et al. 2004) is a gauge-only gridded precipitation product at 4-km resolution that is widely used in operational weather analysis. It interpolates from rain gauges to the 4-km grid using an inverse-square weighting scheme, incorporating also the PRISM climatological model (Daly, Smith, et al. 2015). However, the official Mountain Mapper product is not archived at NOAA. Instead, we have created several versions of the dataset using an identical procedure to Schaake et al. (2004). The creation of our own versions of the dataset is beneficial for direct comparison to R19 and Stage IV for three reasons. First, we have used the same rain gauge network as Risser, namely stations from the GHCN-D network in CONUS with at least 66.7% non-missing values over our time period (8097 stations). Second, we can interpolate the gauge network onto any grid we choose. Finally, we can force the long-term mean of Mountain Mapper to equal any chosen climatology; versions of Mountain Mapper constrained to the R19 mean and to the mean of our 18-year slice of Stage IV are employed in this paper. We compute GEV statistics and their errors at each grid cell in the same way as for Stage IV. Our computations using the Mountain Mapper procedure are discussed further in Supporting Information S2.

5.3 Spatial Scales of Extremes

If the hypothesis that the extreme statistics of daily precipitation vary smoothly between rain gauges over the CONUS is true, then a spatial power spectrum of the 5-year return value map should show little power at $\lesssim$50-km scales. We thus used a wavelet decomposition to compute a spatial power spectrum of the 5-year return values in the Stage IV dataset using a 2-D continuous wavelet transform. Following the procedure outlined in Torrence et al.

(1998), we used Morlet wavelets with non-dimensional frequency $\omega_0 = 6$, and 40 widths equally spaced on a log scale from 4 km to ∼2000 km.[1] Maps of the power on various representative spatial scales are shown for JJA and DJF in Figure 5.1 to help visualize the wavelet decomposition. The power spectrum of our 5-year return value map is presented in Figure 5.2. (The same maps and power spectra are shown for the MAM and SON seasons in the Supporting Information.) The spatial scales s plotted on the x-axis are nearly equal to the Fourier wavelength λ for this choice of wavelet (formally $\lambda = 1.02s$, following Torrence et al. 1998), and should be interpreted in the same manner as a Fourier wavelength, namely as the combined length scale of a positive and negative fluctuation about the mean. Note that substantial edge effects obscure any useful information at scales larger than $s = 1000$ km, so these are not plotted.

To aid in understanding the implications of Figure 5.2, we have overplotted the power spectrum of a test dataset that contains pure white noise within the entire domain (the eastern RFCs), correlated at the 25-pixel (100-km) scale; that is, we made a map of pure Gaussian noise then oversampled it by a factor of 25. A log-linear power spectrum takes the form

$$S_\nu(f) = cf^{-\beta} \tag{5.1}$$

where f is the spatial frequency and β is the spectral scaling. The correlated noise test spectrum can be interpreted as transitioning between $\beta = 2$ at the smallest length scales, where the map is highly autocorrelated, and $\beta = 1$ at the largest length scales, where the map is completely uncorrelated and looks like pure white noise. Note that white noise is not spectrally flat on a log-linear scale, but instead follows a $\beta = 1$ scaling. In between these two regimes is stored all the information content in the map, and as such, the power spectrum is strongly peaked at 100 km length scales. This can be seen most clearly after the spectra have been divided by the $P = s^2$ line in the right panel of Figure 5.2. The 5-year return value maps in both JJA and DJF show similar behavior to the correlated noise map, with strong autocorrelation ($P \propto s^2$) at small spatial scales but with a broader, less prominent spike in power that begins near 200-km scales and continues out to 800-km scales. This means that 5-year return values are strongly autocorrelated at $s < 200$ km, confirming the hypothesis that extreme statistics of daily precipitation vary smoothly between rain gauges over the CONUS. The power spectral density is maximized at very large length scales of ∼800 km. The strong autocorrelation at small scales is present in each of the four major Köppen-Geiger climate classes within the eastern CONUS, as shown in the Supplementary Material.

5.4 QPE Product Comparison

Section 5.3 validated the implicit assumption of the R19 fit-then-grid technique that extreme statistics of daily rainfall vary smoothly between rain gauges. It is *a priori* unclear, though,

[1] Using a Morlet wavelet in this way is mathematically identical to a "short-time" Fourier transform using a Gaussian window function

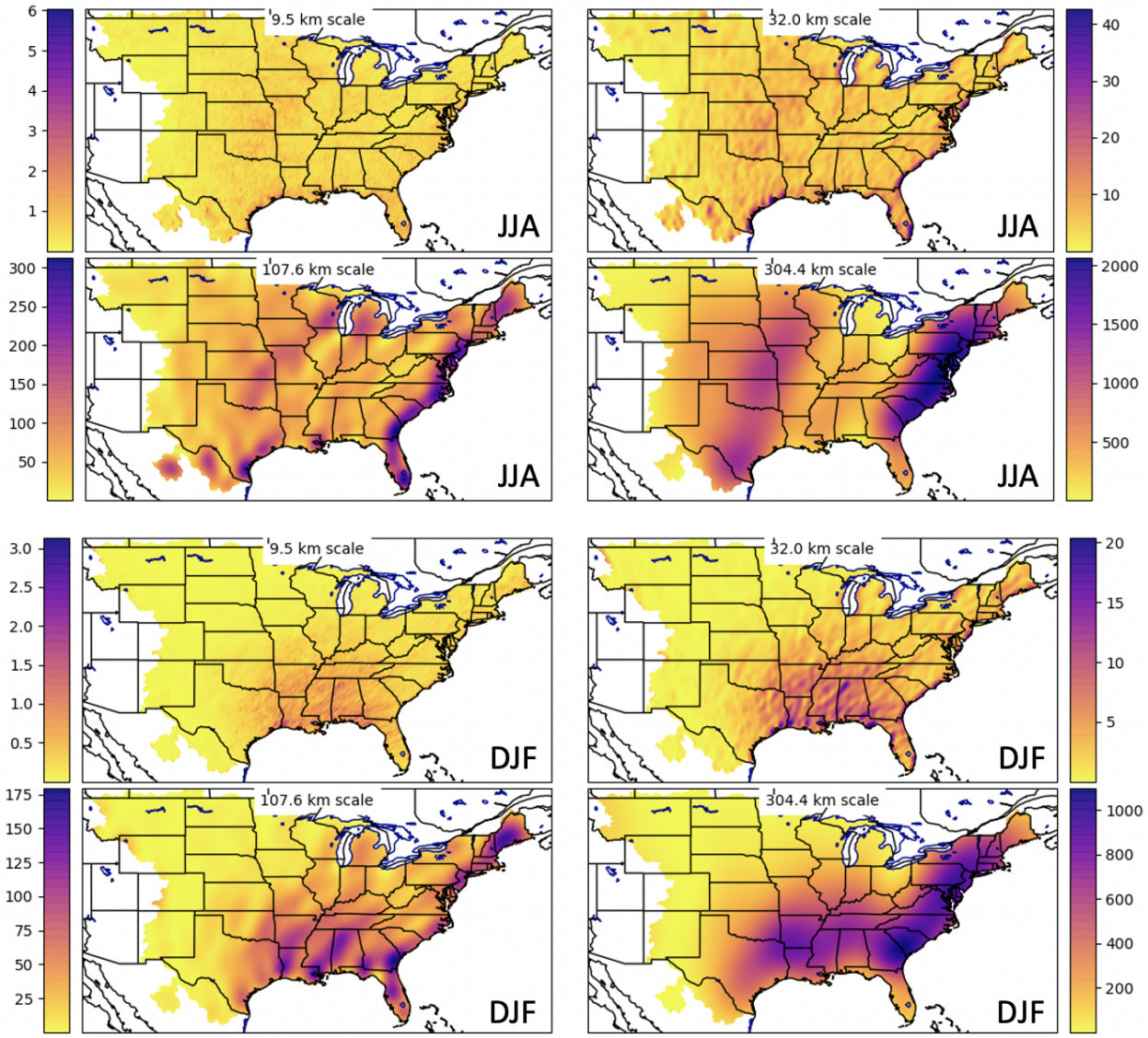

Figure 5.1: Wavelet decomposition of Stage IV 5-year return value map for **(Top:)** DJF and **(Bottom:)** JJA at four representative spatial scales. The colormap denotes power spectral density in arbitrary units.

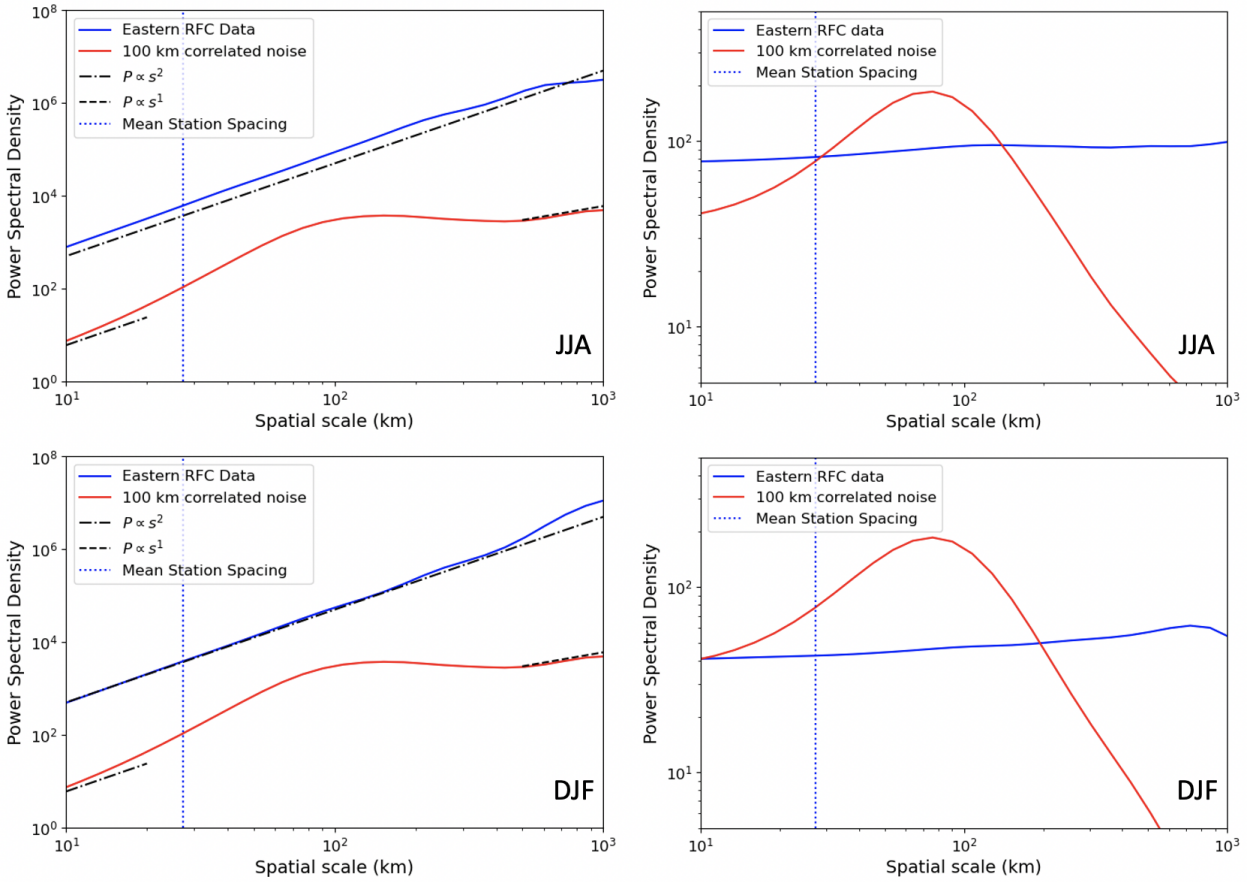

Figure 5.2: Seasonal wavelet power spectrum of the Stage IV 5-year return value map for **Top:** JJA and **Bottom:** DJF over the eastern RFCs only (blue lines). Vertical lines show the mean spacing of 27 km between GHCN stations in the eastern RFC domain. The power spectrum of white noise correlated at the 100 km scale is also shown (red line). The left panels show the raw power spectra; the right panels show the spectra after being divided by the $P = s^2$ line.

whether this fit-then-grid algorithm is actually more accurate than a standard grid-then-fit algorithm when applied to an identical set of rain gauges and given an identical mean climatology. We set up this test by comparing the extreme-value behavior between the Mountain Mapper and R19 datasets. To ensure a direct comparison, we used a version of Mountain Mapper constructed such that its long-term seasonal mean ($\bar{Y}$ in Supporting Information S2) was equal to the R19 mean. As Figure 5.3 shows, the return values are substantially different between the two datasets, with Mountain Mapper underestimating R19 by greater than 10% over much of the CONUS in both DJF and JJA. An assessment of the statistical significance of this difference is given in Supporting Information S3.

We next evaluated the R19 and Mountain Mapper 5-year return values against Stage IV. This comparison is somewhat difficult to probe directly because the long-term means of R19 and Stage IV are not strictly equal, so differences in extremes may be partially caused by differences in the long-term means of those datasets. To get around this, we computed return values from a version of Mountain Mapper that is forced to equal the long-term means of Stage IV, and compared both this Mountain Mapper version and Stage IV itself with R19 (see Figure 5.4). In so doing, any differences are isolated to the treatment of extremes. This Mountain Mapper version is found to underestimate extremes relative to Stage IV over large portions of the Eastern RFCs, whereas R19 agrees more closely.

The difference between Mountain Mapper and R19 is attributable to the grid-then-fit approach taken by Mountain Mapper: using an inverse-square weighting scheme to interpolate between grid points makes it unlikely for extremes to occur at grid points far from any one rain gauge. This hypothesis is confirmed by considering the difference between Mountain Mapper and Stage IV as a function of distance from the nearest rain gauge over the eastern RFCs. The 5-year return values from Mountain Mapper agree well with Stage IV at distances $\lesssim$10 km from the nearest gauge, but begin to underestimate Stage IV at larger distances in both DJF and JJA (Figure 5.5). It is important to note that the spatial averaging inherent in the Mountain Mapper technique is not a deficiency *per se*, and is in fact the appropriate way to measure the spatial average of extremes over a large grid box (Gervais et al. 2014) for comparison to climate models at $\sim$100 km resolution. However, we have shown that the Risser technique provides a more accurate estimate of rainfall extremes at $\sim$25 km scales, assuming the radar-aided Stage IV dataset to be a "ground truth".

5.5 Discussion

The long correlation lengths of 5-year return values in the eastern CONUS derived in Section 5.3 are perhaps unsurprising in the context of the dynamical systems that produce extreme precipitation in that region. In the central and eastern United States, extreme precipitation is most often associated with one of three categories of storm: mesoscale convective systems (MCSs), landfalling tropical cyclones (TCs), and synoptic forcing events (i.e., extratropical cyclones). MCSs are organized groups of thunderstorms that produce distinct circulations at scales longer than 100 km and persist over timescales of 3 hours to 1 day (Feng et al.

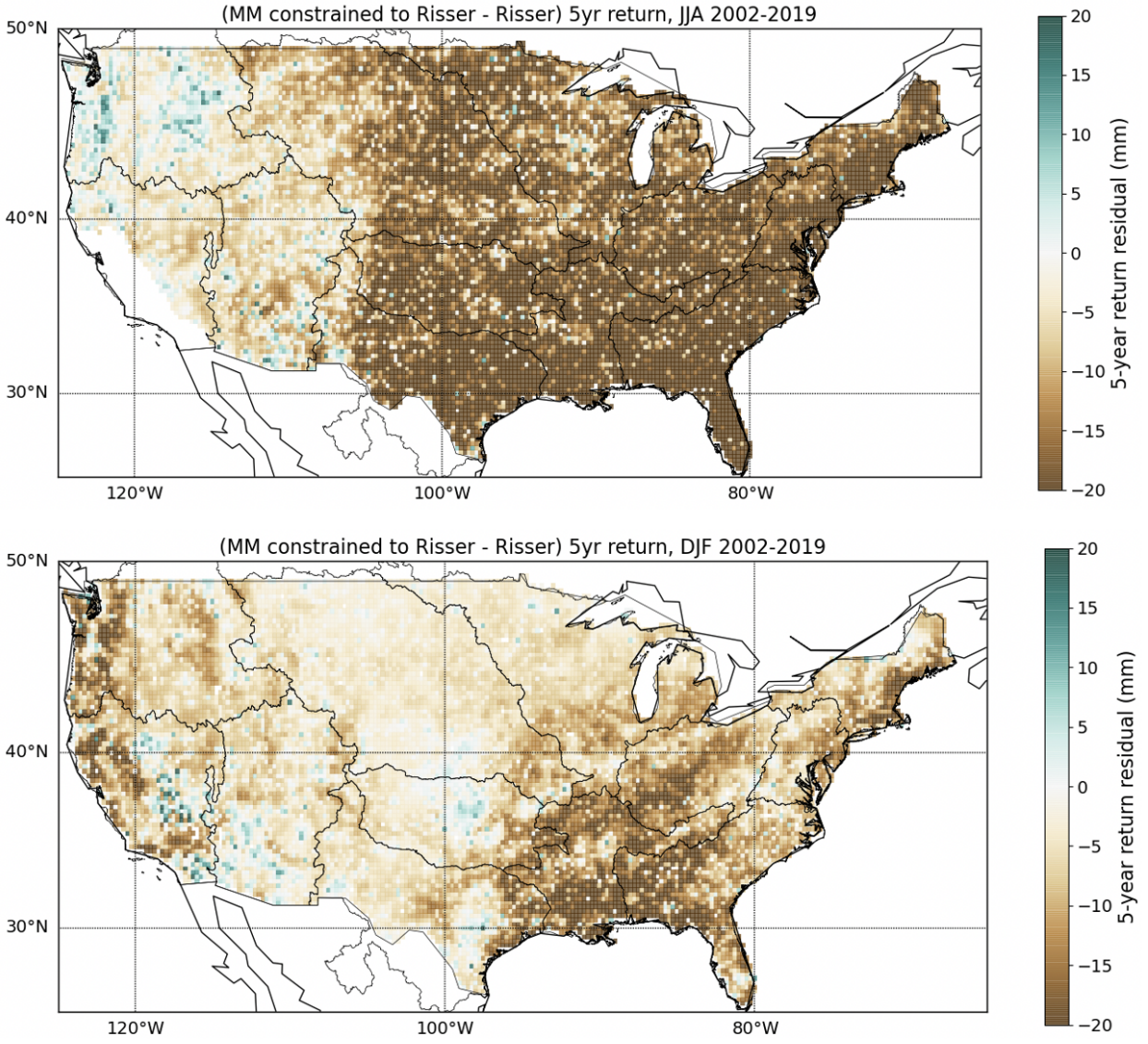

Figure 5.3: Difference between 5-year return value from R19 and our Mountain Mapper implementation constrained to the R19 mean climatology for **Top:** JJA and **Bottom:** DJF. The extremes in Mountain Mapper are lower in magnitude than in R19 over the majority of CONUS in both seasons.

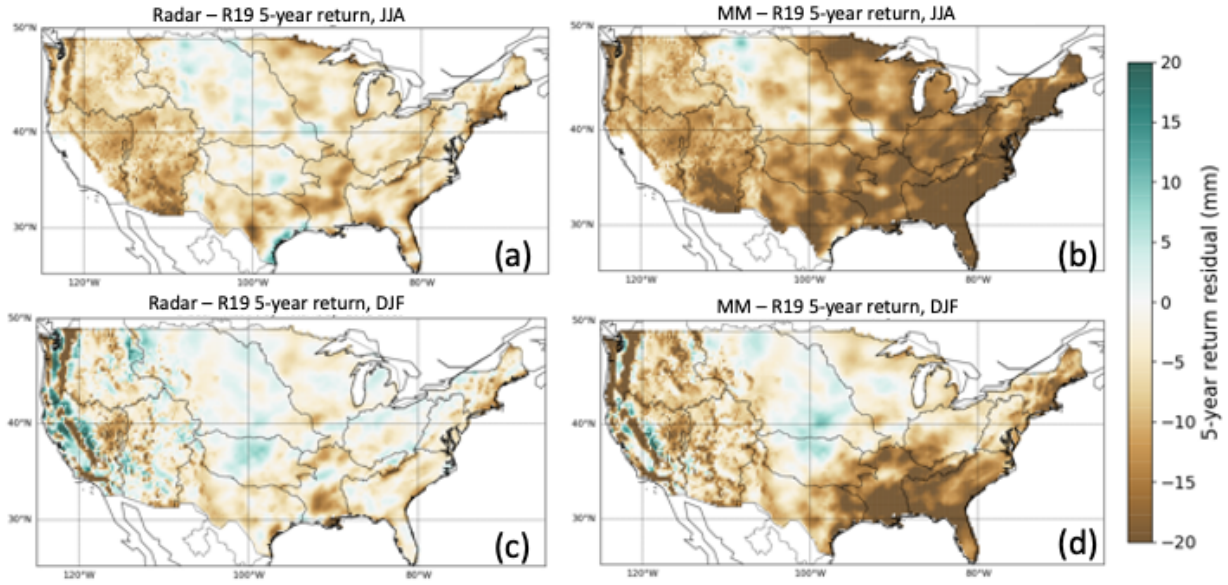

Figure 5.4: Difference between 5-year return value from **(a)** R19 and Stage IV in JJA, **(b)** R19 and Mountain Mapper in JJA, **(c)** R19 and Stage IV in DJF, and **(d)** R19 and Mountain Mapper in DJF. Here the Mountain Mapper datasets have been constrained to the Stage IV mean climatology. The R19 extremes agree more closely with Stage IV than Mountain Mapper in both JJA and DJF (i.e., the discrepancies are smaller in panels **a** and **c** than in panels **b** and **d**), validating the ability of the R19 technique to interpolate extremes to smaller spatial scales.

2019; Houze 2004; Parker et al. 2000). These systems account for over half of extreme rainfall events at 24-h duration in the warm season in these regions (Schumacher et al. 2006; Stevenson et al. 2014). Landfalling tropical cyclones (TCs) also contribute substantially in the summer and fall in the eastern and southeastern United States, especially in coastal regions (Knight et al. 2009; Miniussi et al. 2020; Shepherd et al. 2007). In the cool season, extreme precipitation results primarily from strong synoptic forcing events (Maddox et al. 1979; Schumacher et al. 2006; Stevenson et al. 2014). Although synoptic forcing events occur with nearly unchanging frequency throughout the year, MCSs and TCs are much more seldom present in DJF (Stevenson et al. 2014), and extremes in DJF tend to be of lower magnitude than in JJA (Maddox et al. 1979; Stevenson et al. 2014). Individual storms of these types all tend to produce heavy precipitation over length scales of 100 km or more. The long correlation lengths in the statistics of extreme precipitation presented here can thus be partially attributed to the long correlation lengths of individual events. This interpretation is in good agreement with Touma et al. (2018), who used indicator semivariograms to assess the correlation scales of 90th percentile rainfall days over CONUS. Although that analysis

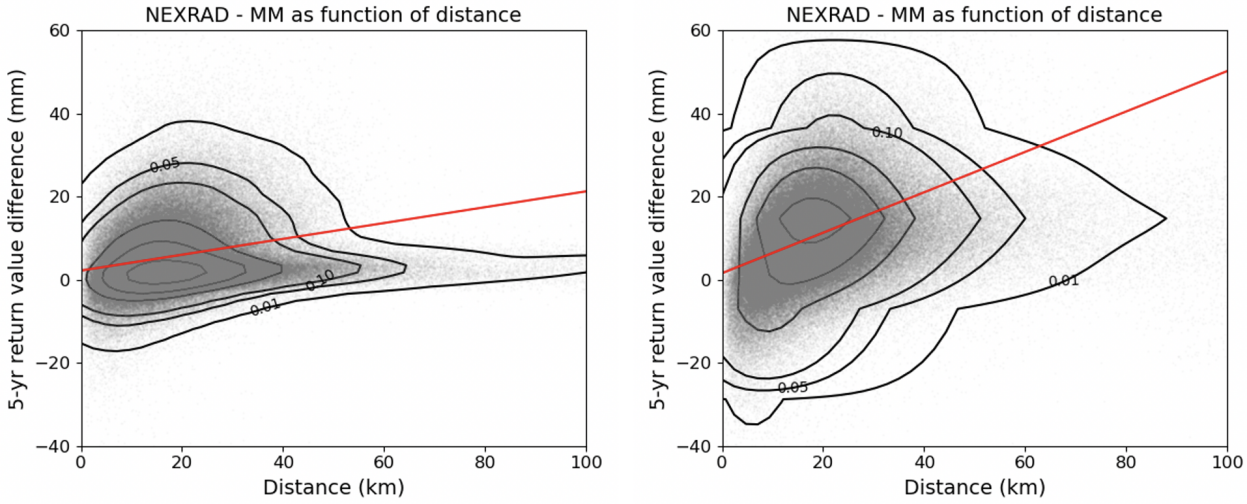

Figure 5.5: Five-year return value difference between Stage IV and Mountain Mapper as a function of distance from the nearest rain gauge used in Mountain Mapper for **Left:** DJF and **Right:** JJA over the eastern CONUS. The small gray points denote individual grid cells; the contours describe the cumulative density of points. The red line shows a least-squares linear fit to the gray points. The return values agree in grid cells near rain gauges, but Mountain Mapper begins to underestimate Stage IV as the distance from a gauge is increased.

was split into more climatological regions, their North, Northeast, South, and Southeast regions all display DJF length scales within 1σ of 300 km.

Previous studies (e.g. Kursinski et al. 2008) have shown, perhaps in apparent tension with the above, that individual extreme storms can be highly localized in both space and time, with heavy precipitation falling over spatial scales of ∼50 km or less. Importantly, though, the spatial statistics of rainfall depend strongly on the time cadence considered. In a case study of the C'evennes-Vivarais region of France, Lebel et al. (1987) and Kirstetter et al. (2010) showed that the decorrelation distance of rainfall amounts increases with lengthening temporal scale from hourly to daily cadence. We wish to stress that our results are only valid at the daily cadence we considered; the assumption of smoothly-varying GEV statistics between rain gauges, and therefore the R19 technique, may not be justified at sub-daily cadences.

It is interesting to consider Figure 5.2 in terms of the fractal properties of rainfall explored by Lovejoy (1982) and Lovejoy and Mandelbrot (1985). Those authors describe the spatial structure of cloud and rain areas according to $N \sim L^{-D}$, where N is the extent to which a fractal fills space as measured at scale L. Bies et al. (2016) explored the relationship between the fractal and power spectrum interpretations of scaling fields, finding that the fractal dimension D and β in Equation 5.1 are related according to $D = 1 + (4 - \beta)/2$ for a

2-dimensional field. (In the terminology of Bies et al. (2016), we measured here a "surface β" and the cited papers use a "coastal edge D".) We find $\beta \approx 2$ (which leads to $D \approx 2$) for this process up to scales of a few hundred km; that is, the extreme precipitation field is 2-dimensional. This is another way of interpreting the high level of autocorrelation on small scales. $D = 2$ is larger than the fractal dimension found by Lovejoy and Mandelbrot (1985) for cloud and rain areas, meaning that the spatial scales over which extreme statistics vary in Stage IV are larger than the spatial scales of individual precipitation events.

5.6 Conclusions

We have tested the assumption that the climatology of extremes varies only minimally at length scales smaller than the average inter-rain-gauge spacing of ∼30 km in the eastern CONUS. We find that this assumption is valid: 5-year daily return values are strongly autocorrelated at scales up to at least 100 km in both DJF and JJA. We also find that the fit-then-grid algorithm of R19 substantially improves the fidelity of daily extreme statistics compared with the grid-then-fit Mountain Mapper technique. On both 4-km and 25-km scales, the grid-then-fit Mountain Mapper technique underestimates extremes relative to the more spatially complete multi-sensor Stage IV QPE in the eastern United States, whereas the Risser et al. (2019) technique measures extremes more accurately than Mountain Mapper at 25 km scales. Taken together, these findings show that rain gauge observations are sufficient to capture the large majority of the extreme-value information in the climatology of the true rain field, but only if interpolated appropriately for the application of interest. This paper improves confidence that appropriately-constructed gauge-only gridded products provide an accurate historical record of daily extreme statistics beyond the years in which radar data are available, an important step toward creating an accurate, continental-scale, in-situ-based, long-term precipitation record for use in hydrological modeling, resource management, and climate change studies. As the resolution of global circulation models continues to increase into the future, QPEs will be required at finer and finer scales, and standard gauge-interpolation techniques will fail to accurately represent precipitation within these grid boxes. The human impacts of extreme events are felt at human scales, e.g. homes (10m), farms (1 km), and watersheds (10 km). Our work moves toward casting measurements of extremes into a risk framework at those scales.

Data Availability Statement

Datasets for this research are available at the following locations:

- The NEXRAD Stage IV data product is described in Lin (2011) and can be accessed online at `https://data.eol.ucar.edu/dataset/21.093`
- The GHCN-Daily data is described in Menne et al. (2012) and can be accessed online at `https://www.ncei.noaa.gov/access/metadata/landing-page/bin/iso?id=gov.noaa.ncdc:C00861`.

- The CNRFC gridded QPE product can be accessed online at `https://www.cnrfc.noaa.gov/arc_search.php`
- The PRISM NORM81 climatology is described in Daly, Smith, et al. (2015) and can be accessed online at `http://www.prism.oregonstate.edu/recent/`

5.7 Appendix: Comparison of GHCN and Stage IV Extremes

Here we provide a direct comparison between the extreme-value behavior of the GHCN-D rain gauge network and the daily Stage IV dataset in the Stage IV grid cells that contain a rain gauge (hereafter "gauge-cell pair"). We also consider the effect of time-of-observation offsets on the representation of extremes in the two datasets.

After Risser et al. (2019), we selected rain gauges from the GHCN-D network within the boundaries of CONUS that had at least 66.7% non-missing daily precipitation measurements over the Stage IV period of record (2002-2019). Measurements were only considered non-missing if the data quality flag ("QFLAG") was blank, meaning that all quality assurance checks passed, and the source quality flag ("SFLAG") was not set to "S" (which would indicate that the measurement may differ significantly from the true value). Any values with MFLAG set to "T" (a trace of precipitation) were set to 0 mm. The resulting dataset consisted of 8097 rain gauges in total.

We first compared the daily precipitation measurements from gauge-cell pairs over our entire period of record by computing the Pearson correlation coefficient (R-value) for each pair. This comparison is complicated by the fact that the GHCN network and the Stage IV dataset define the start and end time of a day differently. The day is defined to run from 12:00-11:59 UTC in the Stage IV dataset, whereas the definition of a day is non-uniform across the GHCN-D dataset, varying according to the "data source code" flag (Menne et al. 2012). The majority of GHCN stations are maintained by volunteers (Flags 0, 7, and N; N is the CoCoRaHS network), who are encouraged to report from 7:00 AM the previous day to 7:00 AM on the recorded day, leading to a 0-3 hour time-of-observation offset from the Stage IV dataset depending on the longitude of the gauge. However, this time offset changes based on the time of year due to daylight savings time, and not all volunteer stations follow the 7:00 AM reporting time convention. The SNOTEL gauge network (Flag T Pepin et al. 2005), prevalent in the western United States, records from 00:00-23:59 UTC, leading to an offset of exactly 12 hours from Stage IV. The USCRN (Flag R Diamond et al. 2013) and ASOS (Flag W NOAA 1998) networks record from 00:00-23:59 LST, leading to a 4-8 hour difference depending on longitude. The effects of these time offsets on the correlation coefficient can be seen clearly in Figure 5.6. The daily measurements from zero-offset pairs are much more tightly correlated on average (left panel), and the correlation coefficients (right panel) are correspondingly higher. Overall, our assessment of the daily precipitation in Stage IV compared to GHCN-D reproduces the findings of (Nelson et al. 2016), who compare Stage IV to the USCRN gauge network, and so we do not expand on those here.

It is instructive to examine the seasonal maxima of each gauge-cell pair, as these seasonal maximum values are the input to the GEV fit; this comparison is shown in Figure 5.7 for zero-time-offset and large-time-offset pairs. The seasonal maxima agree much better between the two datasets than the daily measurements because radar- and gauge-based QPEs agree better at high rain rates than at low rain rates (Nelson et al. 2016; Prat et al. 2015, and

our own analysis). In addition, the difficulties caused by the time-of-observation offsets are ameliorated somewhat if seasonal maximum data are considered instead of daily data.

We next computed generalized extreme value statistics for the two datasets and determined their 5-year return values. The GEV distribution is given by Coles et al. (2001) as

$$\Pr[z > Z] = \exp\Big(- \Big[1 + \xi\Big(\frac{z-\mu}{\sigma}\Big)\Big]^{-1/\xi}\Big) \tag{5.2}$$

where μ is the location parameter, σ is the scale parameter, and ϵ is the shape parameter. At each grid cell or rain gauge, we fit the seasonal maximum daily precipitation measurements to this function using the `climextRemes` package (Paciorek et al. 2018), where σ, μ, and ξ are fitted parameters. This family of extreme distributions encompasses all possible tail behaviors, assuming that each seasonal maximum value is independent of the others and that the underlying distribution does not change over the period of record. Neither of these assumptions are strictly true for Earth's climate; the El Niño-Southern Oscillation and other long-period oscillations lead to possible correlation or anticorrelation from season to season, and climate change amplifies extreme rainfall over time. However, the effects of decadal oscillations and climate change are likely both small over our 18-year period of record (Dai 2013; O'Gorman 2015), so use of the GEV distribution is an acceptable assumption. Any nonstationarity will affect all the different precipitation measurements used in this paper in the same way, and so should not have a noticeable effect on intercomparisons between datasets. As in R19, the errors on the GEV fit parameters were computed via bootstrap resampling. Each set of seasonal maxima was resampled with replacement and then fit to Equation 5.2 250 times; the spread in the fit parameters in these 250 samples was used to define the standard error in σ, μ, and ξ.

The 5-year return values for each gauge-cell pair are shown in Figure 5.8. Linear fits to the GHCN vs Stage IV measurements were computed using two methods: a least-squares technique, which assumes the GHCN data to be the "ground truth" and does not account for the error bars in the GHCN data, and an orthogonal distance regression (ODR) technique, which accounts for errors in both GHCN and Stage IV. The ODR fit shows nearly a perfect one-to-one agreement (slope = 0.98 $\pm$ 0.01) between the 5-year return values in the two datasets, indicating that the measurements agree at the locations of rain gauges within the fitting error. The 1σ spread about that linear fit is almost identical to the average 1σ uncertainty in the return value arising from the GEV fit to the seasonal-maximum data, which was $\sim$7 mm for both the GHCN and Stage IV datasets. This means that almost all of the spread can be explained by the fitting error, lending further support to the conclusion that the fitting noise dominates over any systematic difference between the Stage IV and GHCN return values at the location of rain gauges.

5.8 Appendix: Computation of the Mountain Mapper Algorithm

Here we create our own versions of the Mountain Mapper dataset (Schaake et al. 2004) over the time range 2002-2019. The Mountain Mapper technique uses an inverse distance weighting approach to estimate precipitation at ungauged locations from values at gauged locations while taking into account the long-term climatology of precipitation at the gauged and ungauged locations, as follows. First define $\bar{X}$ as the monthly climatological mean precipitation at a gauge, such that $F_X = X/\bar{X}$ is a precipitation measurement X (mm) in units of the mean precipitation at that gauge. Similarly, define $\bar{Y}$ and $F_Y = Y/\bar{Y}$ so F_Y is the precipitation Y (mm) at the grid point in units of its monthly precipitation climatology. Then we can compute

$$F_Y = \sum_i^n W_i F_{X_i} / \sum_i^n W_i \tag{5.3}$$

where X_i are the precipitation measurements from each of n nearby gauges, and $W_i = d_i^{-2}$ is an inverse-square weight on the distance between gauge and grid point. At each time step, we used the $n = 10$ nearest gauges to each grid point that provided a valid precipitation measurement. The assumption here is that if nearby rain gauges are experiencing a precipitation event of intensity $X_i = k\bar{X}$, then the grid point is experiencing an event of intensity $Y_i = k\bar{Y}$, where k is an arbitrary constant. Finally, to retrieve Y from F_Y we need to know $\bar{Y}$. This cannot be measured directly, so it is taken as some mean monthly precipitation measured another way. In the current version of the official Mountain Mapper, the PRISM climatological model from 1981-2010 is used—this is the PRISM "Norm81" monthly climatology (Daly, Smith, et al. 2015). For the purposes of this paper, we used various seasonal normals as $\bar{Y}$, including the R19 seasonal means and the seasonal mean of the Stage IV dataset, depending on the dataset against which we were evaluating Mountain Mapper.

To validate our implementation of Mountain Mapper, we compared our implementation using the monthly PRISM normals against the Mountain Mapper dataset produced by the California-Nevada River Forecast Center, whose estimate is taken as an input to NEXRAD. Six-hourly accumulation comparisons for five consecutive randomly-chosen 6-hour periods in January are shown in Figure 5.9. It can be seen from the plots that the spatial distribution of rainfall agrees very well between the two datasets. However, an examination of the long-term means revealed small but non-negligible differences in the climatology between our implementation and theirs. These discrepancies are due to the fact that different rain gauges are used: the CNRFC uses a custom list of ∼900 gauges from various sources that are updated periodically, whereas we use a fixed set of gauges from GHCN-D, namely all GHCN-D gauges in CONUS with at least 67% temporal coverage between 2002 and 2019. The choice of rain gauges has important ramifications especially in mountainous regions, where the climatology $\bar{Y}$ varies significantly on spatial scales smaller than the spacing between gauges. Despite these differences, our choice to use GHCN-D gauges is advantageous in that it permits a more direct comparison between Mountain Mapper and the R19 dataset in the eastern United States.

5.9 Appendix: Uncertainty Quantification for Return Value Differences

As shown in Figure 5.3 in the main text, the difference in 5-year return value between Mountain Mapper and R19 exceeds 20 mm over large portions of the eastern RFCs. This difference is on average larger than the error in the 5-year return values due to uncertainty in the GEV fit. In Figure 5.10, we show the data from Figure 5.3 recast into units of the quadrature sum of the 5-year return value errors from Mountain Mapper and R19, confirming that the difference between the two QPEs is greater than 3σ in many locations, especially in JJA.

5.10 Appendix: Spatial Statistics by Region

The wavelet power spectra shown in Figure 5.2 of the main text represent an average over the eastern CONUS, and it is therefore possible that the behavior of this average does not represent the behavior of all climatologies within the domain. To test this, we split the eastern CONUS into Köppen-Geiger climate classes (from Peel et al. 2007). Wavelet power spectra for each of the four classes is shown in Figure 5.11. We found that for all four major classes in the eastern CONUS (steppe; temperate; cold, warm summer; and cold, hot summer), the largest differences in daily extremes were at the largest length scales and there was little power at the smaller scales. Note that since the areas covered by each Köppen-Geiger class are smaller and more irregular than the eastern CONUS itself, substantial edge effects are present in the wavelet power spectrum at the largest scales. Nevertheless, the power spectrum in all four regions is valid out to at least 100 km, and if substantial variability were present at smaller scales it would be detected. The same findings hold for the other seasons (not shown).

5.11 Appendix: Wavelet Power Spectra for MAM and SON

The wavelet decomposition of the Stage IV 5-year return value map for the MAM and SON seasons is shown in Figure 5.12 and the resulting power spectra are shown in Figure 5.13. Just as in DJF and JJA, the power in both MAM and SON has a broad peak at $\gtrsim$200-km scales, meaning that the statistics of extremes vary smoothly at smaller scales.

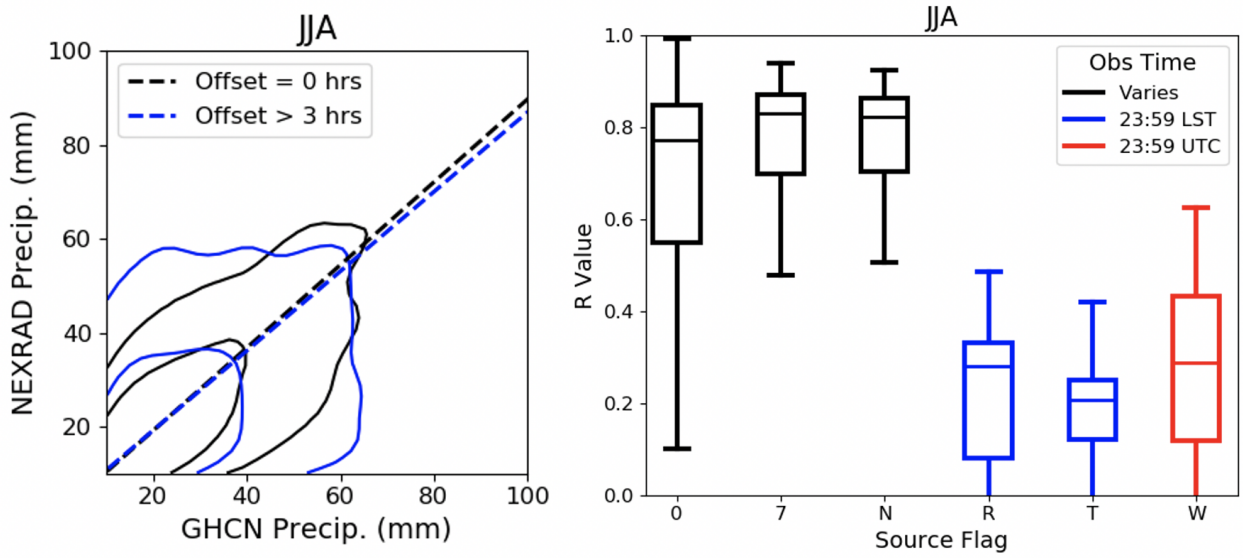

Figure 5.6: **Left:** Density contour plot of daily precipitation measurements for gauge-cell pairs. The pairs are split according to their time-of-observation offset: black contours denote pairs with zero time-of-observation offset between the GHCN and NEXRAD measurements, while blue contours denote pairs with a time-of-observation offset of four or more hours. Contour levels are 84% and 97.5% of all rainy-day (>10 mm) data. Dashed lines show linear fits to each dataset. **Right:** Box-and-whisker plot of NEXRAD-GHCN daily precipitation comparison R-values, split by GHCN station type.

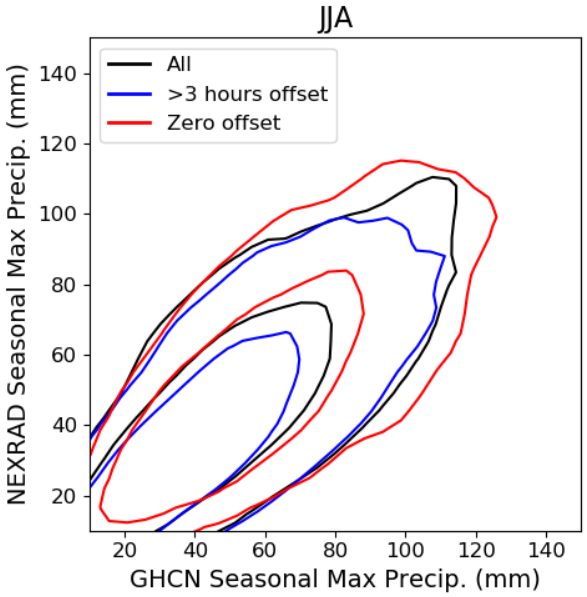

Figure 5.7: Density contour plot of seasonal maximum precipitation measurements for gauge-cell pairs in JJA. The pairs are split according to their time-of-observation offset: red contours denote pairs with zero time-of-observation offset between the GHCN and Stage IV measurements, blue contours denote pairs with a time-of-observation offset of four or more hours, and black contours show the entire dataset. Contour levels are at 84% and 97.5% of each dataset.

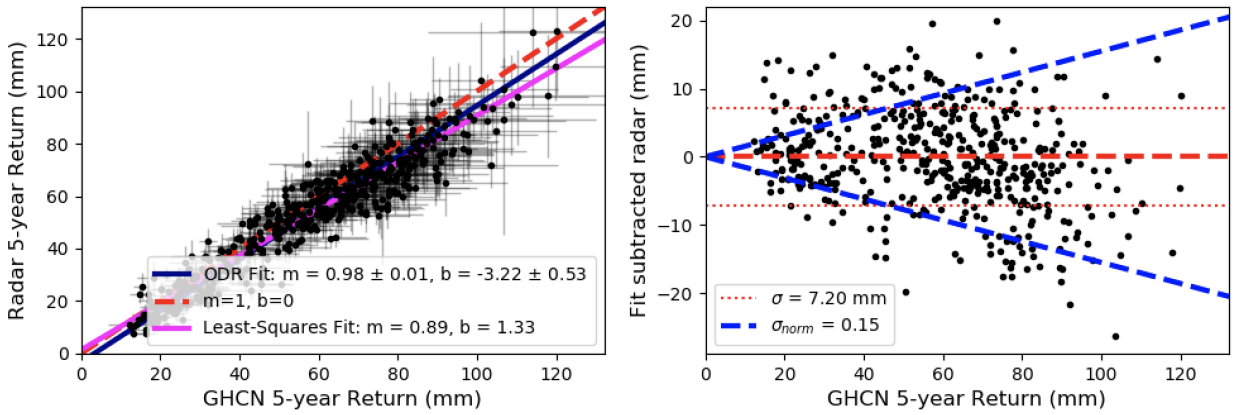

Figure 5.8: **Left:** Five-year return value comparison between GHCN-D and Stage IV in Stage IV grid cells that contain a rain gauge. The red dashed line shows the $y = x$ line; the blue line shows an orthogonal distance regression fit to the data, and the magenta line shows a linear least-squares fit to the data. **Right:** Residual after subtracting the ODR fit (blue line) from the data in the left panel. The blue dashed lines show the 1-σ error assuming errors are proportional to the precipitation level, and the red dotted lines about the zero line (red dashed) show the 1-σ error assuming errors are independent of the precipitation level.

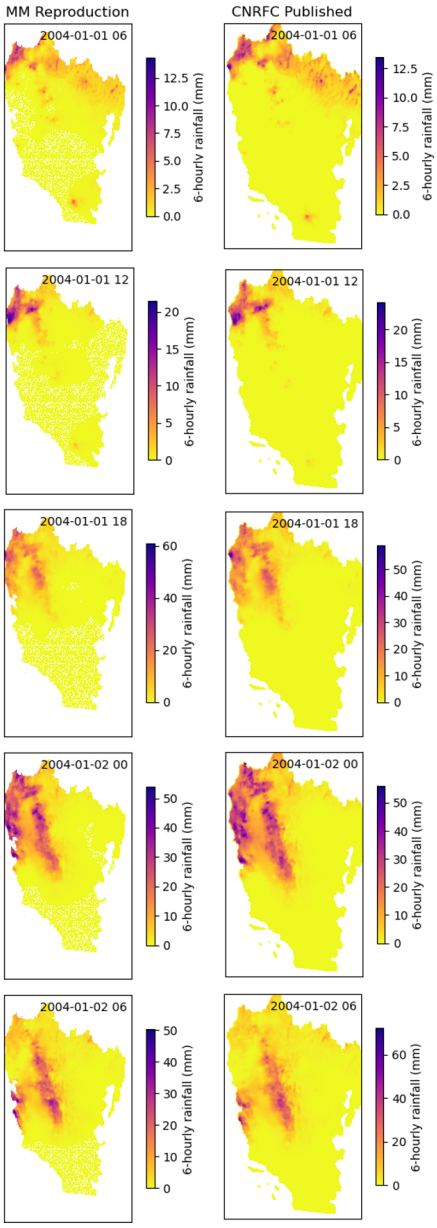

Figure 5.9: Validation of our Mountain Mapper implementation against the official Mountain Mapper product from the California-Nevada River Forecast Center. The spatial distribution and magnitude of 6-hourly and daily rainfall agree between the two datasets to a high degree of accuracy, meaning that our Mountain Mapper implementation operates as expected.

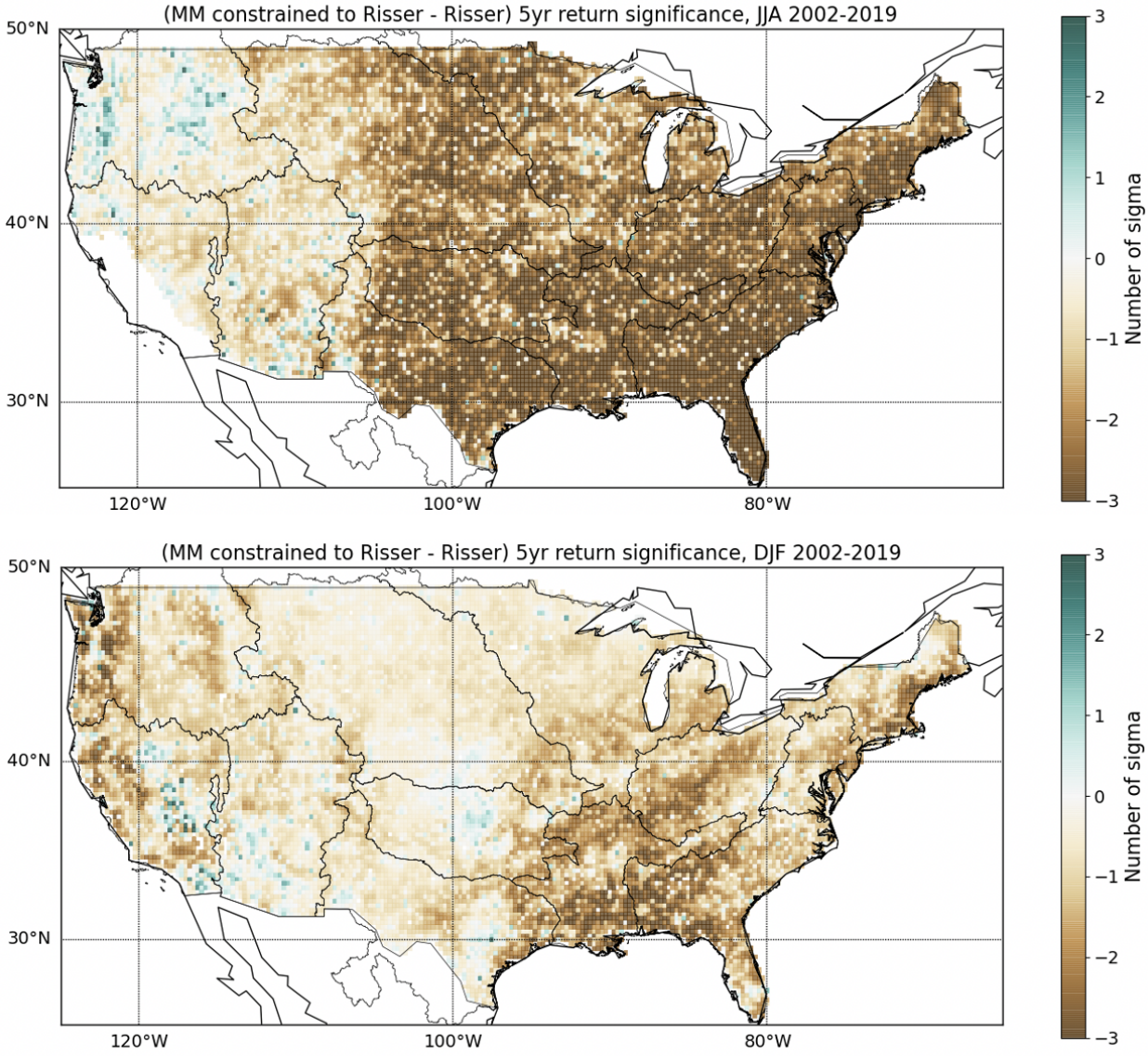

Figure 5.10: Same as Figure 5.3 in the main text, but in units of the 5-year return value error. The differences between MM and R19 are larger than 3σ over large portions of CONUS.

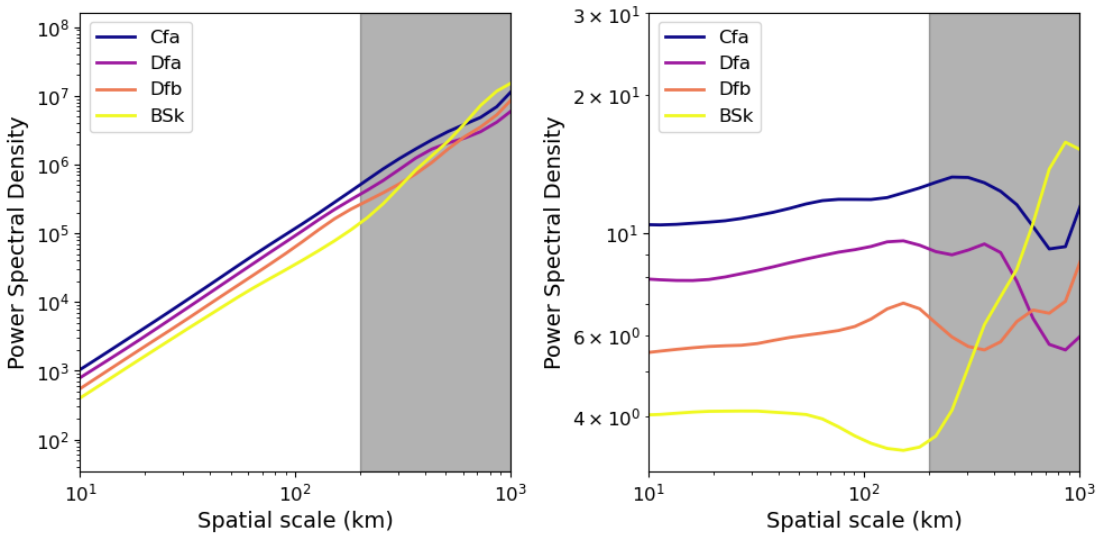

Figure 5.11: Wavelet power spectrum of the Stage IV 5-year return value map for each of the four major Köppen-Geiger climate classes in the eastern CONUS in JJA. The left panel shows the raw power spectra, and the right panel shows the spectra with the $P = s^2$ line subtracted. Note that substantial edge effects lead to unphysical oscillations at the largest scales due to the small size of the Köppen-Geiger regions, so we have greyed out scales larger than 200 km. The climate classes in the legend are: BSk = steppe; Cfa = temperate; Dfb = cold, warm summer; and Dfa = cold, hot summer.

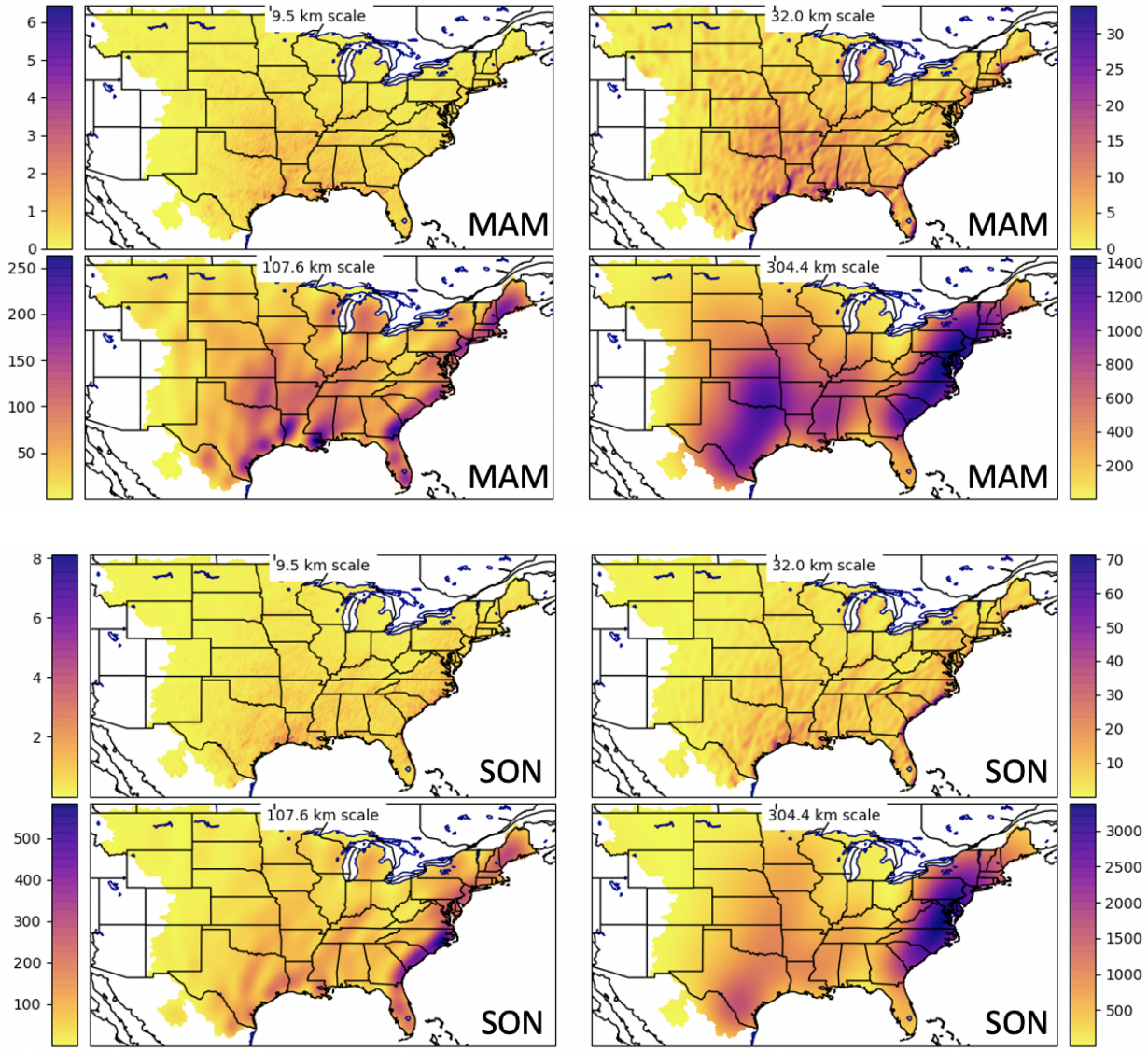

Figure 5.12: Same as main text Figure 5.1, but for **(Top:)** MAM and **(Bottom:)** SON seasons.

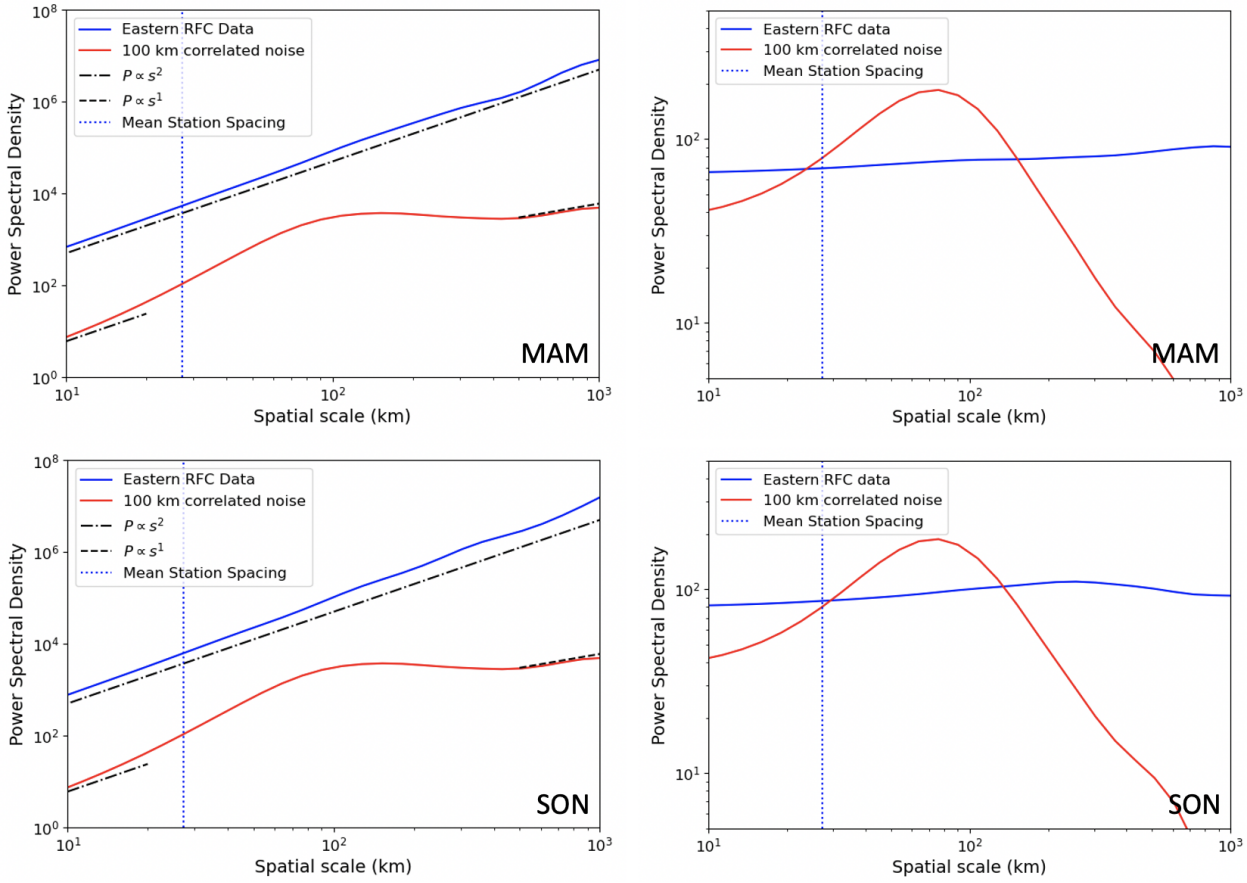

Figure 5.13: Same as main text Figure 5.2, but for **(Top:)** MAM and **(Bottom:)** SON seasons.

Chapter 6

A Storm-Resolving Data Set for Development of Next-Generation Parameterizations

The newest generation of non-hydrostatic, cloud-resolving, global models (i.e., GCRMs) promise to resolve many of the outstanding issues in the way GCMs represent storm events by explicitly resolving atmospheric motion at cloud-system scales. To test whether this promise is realized requires the development of new observational datasets and diagnostics; one must simultaneously measure the meteorological drivers of cloud formation, the cloud properties themselves, and the spatio-temporal distribution of precipitation generated by the clouds. Reanalysis alone fails to provide adequate diagnostics, since reanalysis products typically estimate cloud properties and precipitation using similar convective and microphysical parameterizations to the GCRMs being tested. We present a new, combined dataset at ∼8-km and hourly resolution over the eastern and Midwestern CONUS from 2005-2020 that bridges this gap. The dataset provides ERA-5 reanalysis data for synoptic-scale fields relevant to cloud and precipitation formation, GOES-East geostationary satellite data for cloud structure, and ground-based NEXRAD radar data for precipitation, all on the same space-time grid. We demonstrate the added value in using observed precipitation and cloud fields instead of reanalysis with a particular eye toward capturing extreme events. We also report statistical properties of the cloud and precipitation fields over the CONUS that can be used to benchmark GCMs and GCRMs, including new computations of the precipitation efficiency as a function of surface equivalent potential temperature. The dataset can be leveraged to build and validate realistic stochastic parameterizations in future climate models.

6.1 Introduction

Accurate predictions of how extreme storms will change under the influence of a warming climate are of urgent importance for agricultural forecasts, infrastructure planning and risk assessment, and policymaking (Change 2022). State-of-the-art global circulation models (GCMs) still fail to produce extreme precipitation events that look like the observed atmosphere, despite substantial effort and progress toward that goal in the past 50 years (Arias et al. 2021); GCMs precipitate too often, but at too low intensity (Stephens et al. 2010; Sun, Solomon, et al. 2006). This failure is attributed to the inappropriate representation of two main physical processes taking place at smaller spatial scales than one model grid cell: cloud and precipitation microphysics, and convection (Hourdin et al. 2006; Neggers 2015). GCMs must work around this resolution constraint by parameterizing these processes, but accurate parameterizations are difficult to achieve in practice. Cloud microphysics parameterizations suffer from the severe scaling problem of trying to represent the aggregated effects of μm-scale processes at kilometer scales, and gaps remain in both conceptual understanding of the microphysics and numerical representation of known physics (for a review, see Khain et al. 2000). Both conceptual and computational difficulties arise in convective parameterizations, as well, as summarized nicely by Arakawa (2004): the parameterization scheme must make an artificial separation between resolved and sub-grid atmospheric motions, which follow a continuous spectrum of size scales in nature, and it must formulate the statistical effects of cloud fields given a wide range of initial synoptic-scale conditions without simulating individual clouds. One of the primary drivers toward constructing GCMs with ever higher spatial resolutions has been the promise of ameliorating some of these difficulties by better resolving convective processes (Arias et al. 2021).

Recent advances in computational resources and techniques have led to higher-resolution models of cloud systems, both in regional cloud-resolving models (CRMs) and in a new regime, that of global cloud-resolving models (GCRMs). Regional CRMs have typical spatial resolutions from tens of meters to a few kilometers, resolving non-hydrostatic accelerations, but suffer from sensitivity to their boundary conditions. That is, they are unable to influence or be influenced by the synoptic- and global-scale atmospheric flows in which they are situated, and their ability to reproduce the observed long-term statistics of clouds and precipitation is limited (for a review, see Guichard et al. 2017). GCRMs resolve non-hydrostatic accelerations globally with kilometer-scale resolution, representing moist convection without the need for cumulus parameterization (see review by Satoh et al. 2019). The ability of GCRMs to simulate clouds and precipitation is already being evaluated for the DYnamics of the Atmospheric general circulation On Non-hydrostatic Domains (DYAMOND) experiment (Stevens et al. 2019), the first GCRM ensemble. Roh et al. (2021) intercompare the cloud radiative effects in the DYAMOND ensemble, finding large variations in the net shortwave radiation at the top of the atmosphere. Su et al. (2022) find a large spread in the convective organization in DYAMOND, with most models producing too many small, isolated precipitation events over the tropical ocean as compared with satellite precipitation observations. The same authors also demonstrate a wide range in the ability of the models to

reproduce the observed diurnal cycle of precipitation over land, with many models overestimating its amplitude. Arnold et al. (2020) show that the NASA Goddard Earth Observing System (GEOS) model, one member of DYAMOND, underestimates the amplitude of the diurnal cycle of precipitation at low resolution and produces unphysical small-scale spatial fluctuations in the diurnal cycle at high resolutions compared with satellite data.

The comparisons with satellite precipitation detailed above underscore the importance of evaluating climate models on multiple axes using observational data; however, they paint an incomplete picture. As pointed out by, e.g., Tapiador, Navarro, et al. (2017), satellite precipitation estimates are either temporally sporadic, as in the case of microwave sensors like the Tropical Rainfall Measuring Mission (TRMM), or rely on a simple relationship between infrared cloud-top brightness temperature and precipitation, as in the case of some geostationary observatories. The majority of model evaluation efforts focus on one observed field at a time; this approach makes it difficult to identify the physical processes that are misrepresented in the climate model, especially given that the increased resolution of GCRMs does not appear to be the singular "silver bullet" for modeling convection. A reexamination of the observational quantities and datasets that are used to evaluate the fidelity of models is required in order to understand, for example, whether they accurately represent the clouds and precipitation associated with each individual convective cell within a mesoscale convective system over the lifetime of that system.

In the real atmosphere, a storm is defined not only by a large volume of precipitation deposited onto the surface in a short time, but also by the synoptic-scale meteorological drivers of the flow in which precipitating clouds are embedded, the properties of the clouds and hydrometeors themselves, the fluid dynamics of the atmosphere within the cloud system, and the precipitation that falls to the ground. Cloud and precipitation fields evolve rapidly in time, so continuous, high-cadence monitoring is required to understand the inception and lifetime of storm systems. Internal variability in the climate system alters the large-scale flow year-by-year, and a wide range of meteorological systems are relevant to the production of extreme precipitation over North America (Barlow et al. 2019), so observations over many years are needed to capture the diversity of storms. In this paper, we present a new combination of data on an 8-km grid at hourly resolution over the Eastern and Midwestern CONUS from 2005-present to fill this gap. We combine the European Centre for Medium-Range Weather Forecasts (ECMWF) Reanalysis v5 (ERA-5) reanalysis data, the Geostationary Operational Environmental Satellite East (GOES-East) cloud products, and the ground-based Next-Generation Weather Radar (NEXRAD) Stage IV precipitation dataset to simultaneously track the upstream drivers and downstream effects of cloud formation as well as the clouds themselves.

The paper is organized as follows. We provide a short description of each of our three data sources in Section 6.2, and discuss their benefits and drawbacks. In Section 6.3, we present probability distribution functions (PDFs) for the NEXRAD precipitation data and the GOES cloud liquid/ice water path. We compare these with the precipitation and cloud statistics in ERA-5 to demonstrate the added value of using true observational data instead of reanalysis data alone. We also provide intensity-duration-frequency (IDF) curves for

NEXRAD for several event durations from 1 to 24 hours. Putting all three data sources together, we present a novel statistical analysis of the precipitation efficiency according to the recent definition put forth by Li, Studholme, et al. (2022) in Section 6.4. We explore the implications of the observed characteristic residence times of condensate in the atmosphere in Section 6.5. Finally, in Section 6.5, we contextualize these findings within a broader discussion of the ways in which our dataset can be leveraged to improve predictions of extreme weather in a warmer future climate, and summarize our results in Section 6.6.

6.2 The Dataset

We have put together a new combination of observational data sources with the goal of measuring the structure and evolution of storm systems from inception to dissipation. With this goal in mind, we include a reanalysis product (ERA-5) to probe the meteorological drivers of storms, a satellite cloud product (GOES) to constrain the dynamical and microphysical processes within precipitating cloud systems, and a quantitative precipitation estimate (QPE; NEXRAD) to probe the hydrological and societal impacts of precipitating storms. These three data sources are presented in detail in the next paragraphs. Figure 6.1 shows an example snapshot of selected fields from the dataset over a summer storm in the Midwestern CONUS. Table 6.1 lists the meteorological fields we included in the combined dataset.

The ERA-5 and NEXRAD datasets were regridded conservatively onto the GOES grid using the `TempestRemap` software (Ullrich, Devendran, et al. 2016; Ullrich and Taylor 2015). The resulting combined dataset has ∼8-km horizontal resolution, with the size of grid cells varying slightly over the CONUS based on the geometry of a detector at geostationary orbit projected onto the spheroidal surface of Earth. The choice to remap ERA-5 and NEXRAD to GOES was made for two reasons. First, this choice maintains the maximum resolution of the observational data, which is immutable; reanalysis could later be computed at higher spatial resolutions should the need arise. Second, it is unclear how best to conservatively remap some of the derived cloud fields. It is important to note that this choice of regridding super-resolves the ERA-5 data by an areal factor of ∼15, so the ERA-5 fields really represent an average of the nearest ∼15 grid cells. Conversely, the NEXRAD precipitation data has been spatially averaged, and the interested user could in principle achieve a higher resolution for the precipitation data only. The spatial extent of the dataset is constrained to within the eastern and Midwestern CONUS based on the boundary of the NEXRAD dataset (see Section 6.2).

The temporal resolution of the dataset is hourly, from 1 January 2005 to 31 December 2021; this time range is again constrained by NEXRAD, as 2005 was the first full year when the hourly Stage IV analysis was available. The NEXRAD and ERA-5 variables are reported at the :00 mark of each hour, whereas the GOES data product records instantaneous measurements once per hour at either the :30 or :45 minute mark (:30 for GOES-16; :45 for GOES-12 and GOES-13). For the precipitation field in both NEXRAD and ERA-5 (as well as the MER field), one hour of data represents an assumed rainfall amount in the past hour.

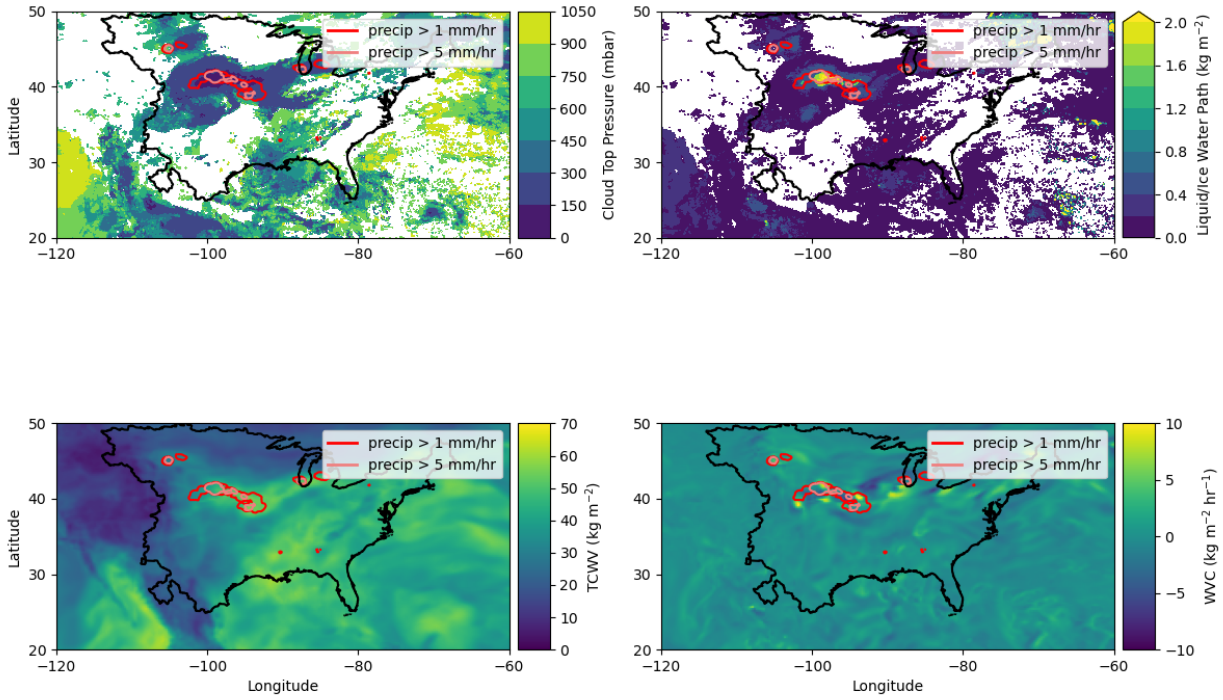

Figure 6.1: Example snapshot of a few of the fields included in our dataset, taken as a storm passed over the U.S. Midwest at 09:00 UT on 19 July 2019. Precipitation contours are overlain in red ($P_s > 1.0mm$) and salmon ($P_s > 5.0mm$). The domain of NEXRAD Stage IV is shown as a black contour. The acronyms on the colorbar labels in the bottom two panels denote ERA-5 Total Column Water Vapor (TCWV) and ERA-5 Water Vapor Convergence (WVC); see also Table 6.1.

Short Name	Full Name	Source	Units
LSP	large-scale precipitation	ERA-5	kg m^{-2}
CP	convective precipitation	ERA-5	kg m^{-2}
MTPR	mean total precipitation Rate	ERA-5	kg m^{-2}
TCWV	total column water vapor	ERA-5	kg m^{-2}
WVD	water vapor divergence	ERA-5	kg m^{-2} s^{-1}
MER	mean evaporation rate	ERA-5	kg m^{-2} s^{-1}
CLWD	column liquid water divergence	ERA-5	kg m^{-2} s^{-1}
CIWD	column ice water divergence	ERA-5	kg m^{-2} s^{-1}
TCLW	total column liquid water	ERA-5	kg m^{-2}
TCIW	total column ice water	ERA-5	kg m^{-2}
2T	two-meter temperature	ERA-5	K
2D	two-meter dew-point temperature	ERA-5	K
	cloud bottom temperature	GOES	K
	cloud top temperature	GOES	K
	cloud bottom height	GOES	km
	cloud effective height	GOES	km
	cloud top height	GOES	km
	cloud bottom pressure	GOES	Pa
	cloud effective pressure	GOES	Pa
	cloud top pressure	GOES	Pa
	cloud effective temperature	GOES	K
LWP/IWP	cloud liquid/ice water path	GOES	g m^{-2}
	cloud particle size	GOES	μm
	cloud visible optical depth	GOES	unitless
	cloud phase	GOES	n/a
P_s	observed precipitation	NEXRAD	mm

Table 6.1: Fields included in the combined dataset. Raw brightness temperatures, pixel counts, and pixel/solar zenith/azimuth information are also available for the GOES data but not listed.

The TCWV, TCIW, TCLW, WVD, CLWD, CIWD, 2T, and 2D fields, like all the GOES variables, are instantaneous quantities. We made no attempt to temporally interpolate the GOES data onto the same time grid as ERA-5 and NEXRAD or vice versa for several reasons. First, interpolation requires averaging, which degrades the information content of the dataset. Second, instantaneous measurements and hourly averages represent fundamentally different quantities, and it is unclear whether the instantaneous measurements would be most useful at the start, end, or middle of an hour. Third, the choice we made is the most flexible, since an interested user could subsequently perform any time interpolation they choose without having to undo any steps.

NEXRAD Quantitative Precipitation Estimate

We quantify precipitation using the operational Next-Generation Radar (NEXRAD) Stage IV radar-based QPE (Fulton et al. 1998; Lin 2011; Lin and Mitchell 2005; Seo and Breidenbach 2002) at hourly cadence on a natively 4-km grid from 1 January 2005 to 31 December 2021. We choose to include the NEXRAD QPE instead of state-of-the-art gauge-based QPEs like PRISM (Daly, Neilson, et al. 1994) or the Livneh product (Livneh, Bohn, et al. 2015) because the inclusion of radar data provides spatially-complete and temporally-continuous coverage without reliance on elevation models or gauge interpolation, which has been shown to underestimate extreme events at locations far from rain gauges (Behnke et al. 2016; Gervais et al. 2014; Molter et al. 2021; Sun and Barros 2010).

As noted by other authors (Molter et al. 2021; Nelson et al. 2016; Prat et al. 2015), Stage IV is a heterogeneous dataset. The product from the three western NOAA River Forecast Centers ("Western RFCs"; California-Nevada, Northwest, and Colorado Basin) do not incorporate radar data, instead using a gauge-based estimate, while the rest of the River Forecast Centers use the radar-inclusive procedures outlined in Fulton et al. (1998) and Lin and Mitchell (2005). Data from the Western RFCs are therefore not included in the dataset. The spatial domain of the dataset is thus defined by the boundary surrounding the rest of the River Forecast Centers; this includes the eastern and Midwestern CONUS westward to, and mostly including, New Mexico, Colorado, Wyoming, and Montana. The boundaries of the Eastern RFCs are plotted in Figure 6.1.

GOES Satellite Cloud Products

We take cloud information from the Advanced Baseline Imager (ABI) instruments aboard the Geostationary Operational Environmental Satellites (GOES) as obtained from the NASA Langley Research Center Atmospheric Science Data Center. We make use of the "pixel-level geostationary cloud products" produced by SatCORPS group at the NASA Langley Data Center. In this product, the multi-spectral imaging from ABI has been converted into estimates of cloud properties such as optical depth, liquid/ice water path, and cloud top height (among many others) using the radiative-transfer retrieval algorithms presented by Minnis, Nguyen, et al. (2008). These retrieval algorithms have a long history of development,

having been first implemented supporting the Tropical Rainfall Measuring Mission (TRMM) as part of the Clouds and the Earth's Radiant Energy System (CERES) project (Wielicki et al. 1998, this paper is also a good overview of the algorithm's steps) and then improved and adapted as new satellites were launched as part of CERES (Minnis, Nguyen, et al. 2008; Minnis, Trepte, et al. 2008). Our time series spans the lifetimes of three different GOES-East satellites: GOES-12, GOES-13, and GOES-16. It should be noted that the ABI was substantially upgraded in the GOES-16 era from 5 spectral bands to 16 spectral bands, splitting the same spectral coverage of from 0.5-13 μm into more channels.

We chose to include GOES instead of low-Earth orbiting (LEO) cloud satellites like TRMM and the Global Precipitation Mapping Mission (GPM) because geostationary satellites have the important advantage of near-continuous hourly monitoring, which permits tracking of cloud evolution within throughout the storm's lifetime. Meanwhile, LEO satellites suffer from sampling biases that limit their ability to capture accurate cloud and precipitation statistics (see Bell et al. 1990; Fiolleau et al. 2013; Nijssen et al. 2004, for further discussion).

ERA-5 Reanalysis

We employ the ERA-5 reanalysis (Hersbach et al. 2020) to measure the synoptic-scale water vapor content and circulation of the atmosphere. The ERA-5 reanalysis was released in the year 2020 and represents several updates over the previous-generation ERA-Interim reanalysis, including 31-km horizontal resolution (compared with 80 km for ERA-Interim), upgraded model physics, a larger suite of assimilated data sources, and full hourly output. One of the upgrades from ERA-Interim is that ERA-5 now incorporates radar precipitation data over land, including NEXRAD (Lopez 2011). This helps to explain the high level of agreement in precipitation statistics between the two datasets at time resolutions coarser than 12 hours, which is the cadence at which ERA5 assimilates new data (Hersbach et al. 2020); this is discussed more in Section 6.3. We incorporate only two-dimensional fields at present; this choice was made for three reasons. First, we limit the computational expense of regridding and the final data volume. Second, the satellite-derived cloud properties and radar precipitation are both two-dimensional fields, and one major objective of this paper is to directly compare these to ERA-5. Third, the large-scale precipitation efficiency definitions we discuss in Section 6.4 rely on column-integrated quantities only.

The ERA-5 fields listed in Table 6.1 represent a mixture of "instantaneous" and "mean" fields. The difference between the two is that instantaneous fields are measured at the single time step in the model corresponding to the start of the hour, whereas mean fields comprise an average over the time steps in the past hour. As discussed at the start of Section 6.2, the preference for one or another of these fields depends on the application of interest, and we have not attempted to alter these fields beyond their conservative remapping. The names given in Table 6.1 are identical to those in the native-resolution ERA-5 dataset, and the reader is referred to the documentation of ERA-5 for additional details.

6.3 Statistical Properties of the Dataset

Comparisons between GOES/NEXRAD and ERA-5

It is natural to wonder whether the use of observational data is really required, given that reanalysis data provides a complete four-dimensional estimate of practically every element of the climate system. However, despite twice-daily nudging of ERA-5 toward observations, the convective and microphysics parameters still misrepresent clouds and precipitation hour-by-hour, even when removing systematic effects due to the difference in spatial resolution between ERA-5 and our dataset. This is shown for precipitation in Figure 6.2; NEXRAD was regridded conservatively to match the resolution of ERA5 using `TempestRemap`. When averaged to timescales near the assimilation cadence, ERA-5 performs very well over the CONUS, but underestimates the magnitude of extreme precipitation at hourly cadence. As pointed out in Section 6.1, this behavior is the same as for most GCMs (Stephens et al. 2010; Sun, Solomon, et al. 2006), which is sensible because reanalysis is simply a forced GCM. We also make a cursory evaluation of the representation of clouds in ERA-5 by comparing the GOES cloud liquid/ice water path with the sum of the ERA-5 total column liquid water (TCLW) and total column ice water (TCIW). The PDFs of condensate path from both data sources are shown in in Figure 6.3. The two datasets agree very well in a time-averaged sense; however, GOES observes more very thick clouds and fewer very thin clouds than ERA-5.

IDF Curves of Precipitation

The hourly cadence and continuous spatio-temporal coverage of the NEXRAD precipitation data permit the computation of extreme statistics on multiple time scales. We achieve this using intensity-duration-frequency (IDF) curves, which are widely employed to quantify extreme-value statistics in the literature. Our computations make use of the `idf-analysis` Python package[1], which follows the procedures outlined by the German Association for Water, Wastewater and Waste (Memo 531; DWA 2012), summarized here. First, a rolling sum is taken at the duration of interest D hours, such that each hourly datum represents the sum of itself and its nearest neighbors. Next, maxima are identified and ordered by intensity, counting only maxima separated by at least D hours. A discretization correction is made to the maximum values that accounts for cases where D is only a few hours; this correction is less than 1% if $D > 4$. The n largest events in the period of record, where n is the ratio of the period of record to the return period of interest, are then fit to a Gumbel distribution. We have computed 1-month, 2-month, 4-month, 6-month, 1-year, 2-year, 3-year, and 5-year return values for the NEXRAD data at 1, 2, 3, 6, 12, and 24-hour duration extremes. These will be made publicly available in the refereed version of this manuscript. An example map of three-year return values at three-hour duration is shown in Figure 6.5, and the average IDF curves over our entire study area are shown in Figure 6.4. Maximum values at each duration and latitude-longitude point were also recorded.

[1] https://github.com/MarkusPic/intensity_duration_frequency_analysis

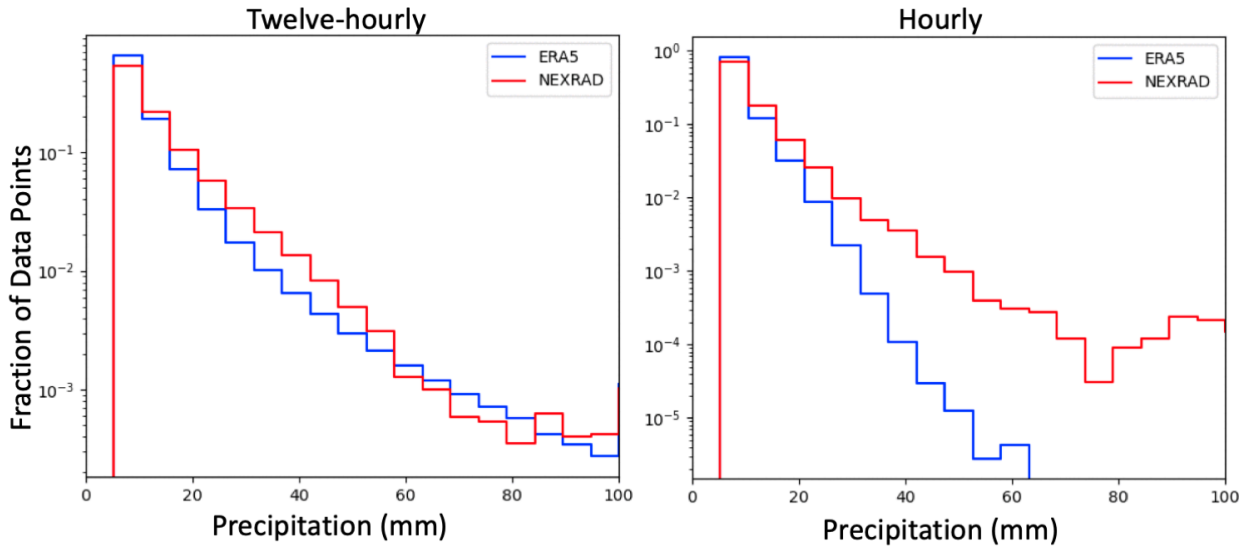

Figure 6.2: (Left:) Twelve-hourly and (Right:) one-hourly probability distribution function of NEXRAD and ERA-5 precipitation over our study region on the native 25-km ERA-5 grid for June, July, and August 2019. The PDF of precipitation agrees to a high degree of accuracy at timescales $\gtrsim$12 hours, but ERA-5 produces too few heavy rainfall events at shorter time scales.

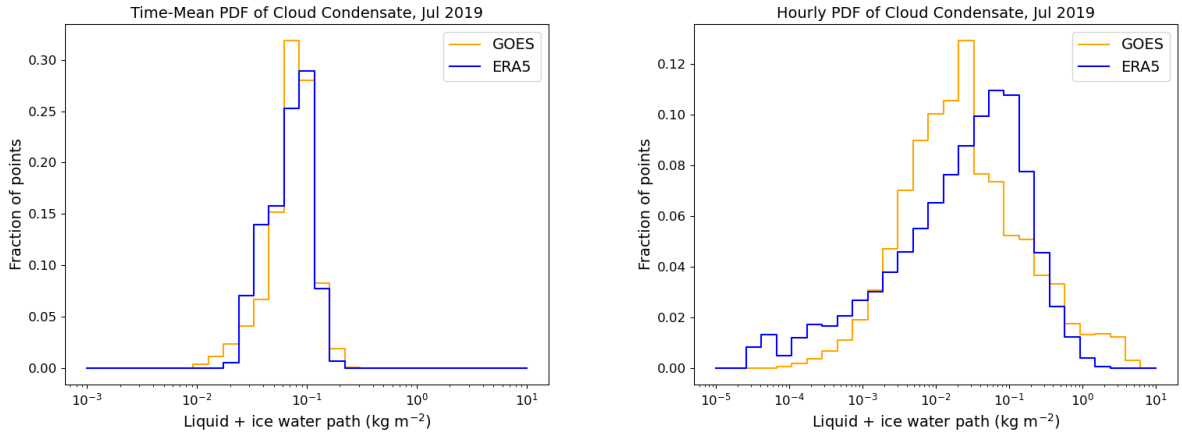

Figure 6.3: (Left:) Time-mean and (Right:) hourly probability distribution function of cloud condensate path from ERA-5 and GOES over our study region in July 2019.

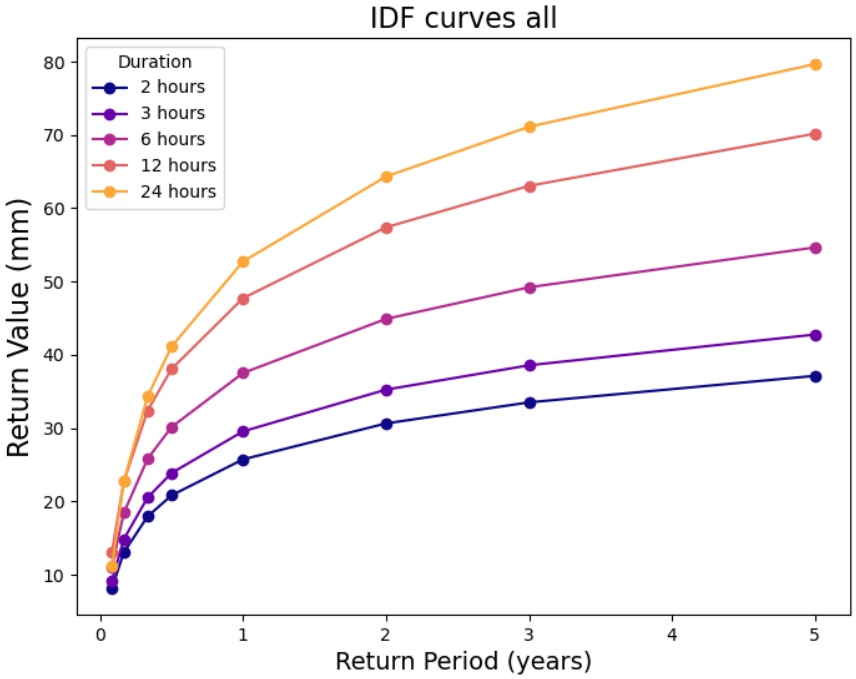

Figure 6.4: Intensity-duration-frequency (IDF) curves for the NEXRAD precipitation data in our dataset, averaged over the full study region.

IDF curves are widely used in hydrological modeling and flood risk assessment, as well as to characterize the climatology of different regions of Earth, including under climate change conditions (e.g., Cronshey 1986; Luo et al. 2018; Mirhosseini et al. 2013; Panziera et al. 2016; Scharffenberg et al. 2006; Yan et al. 2018). Previous studies have computed IDF curves from radar data, showing that radar-based estimates agree well with rain gauge estimates overall, with the primary source of error in radar return values being the short period of record (Eldardiry et al. 2015; Goudenhoofdt et al. 2017; McGraw et al. 2019; Overeem et al. 2009). However, these studies are limited to small regions (e.g., a single radar station) or to daily data only. To our knowledge, this paper is the first to compute IDF curves from an observational precipitation dataset at sub-continental scales on a $\lesssim$10 km grid. In addition to providing inputs to hydrological models, these IDF maps are useful as a benchmark for global circulation models; a successful model should be capable of reproducing these curves for all durations of extreme and for all regions of the CONUS.

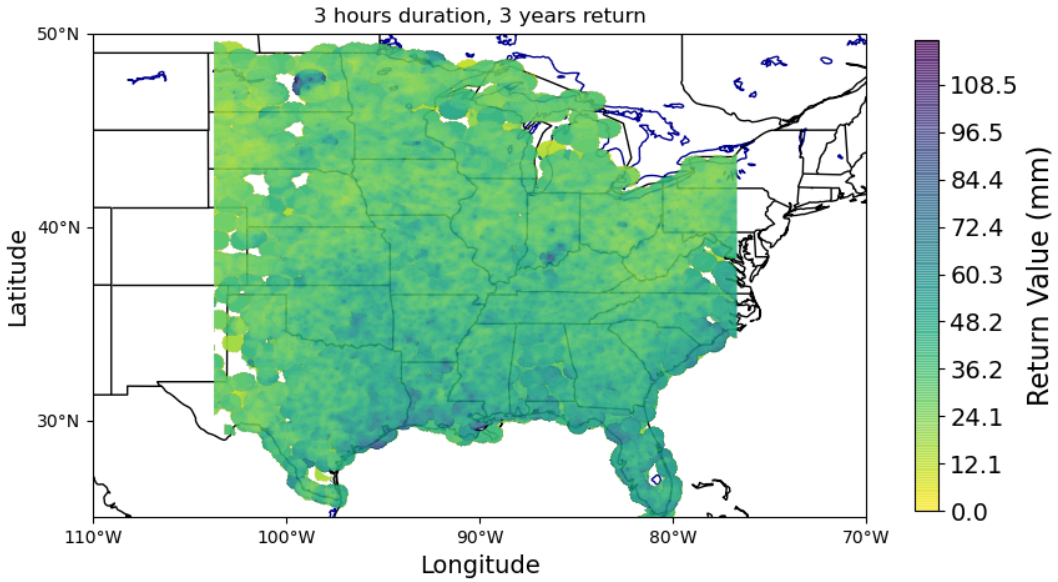

Figure 6.5: Map of three-year return values of three-hourly precipitation over our 15-year period of record. The regions of white space, most prevalent in the far western regions of the map, are regions where a fit to the maximum values could not be computed; this is usually caused by poor radar coverage.

6.4 Results: Precipitation Efficiency

The fraction of cloud condensate that reaches the surface as precipitation is quantified by the precipitation efficiency (PE). PE is related to the energy transport in storms, as a higher PE implies less evaporation of condensate and more net latent heat release into the atmosphere for a given amount of initial condensation. At larger space and time scales, PE can be interpreted as a statistical average of cloud microphysics over many rainstorms. PE is used in various situations in meteorology, including to constrain the physics of individual storm events, as a parameter in cumulus convection schemes, and to make projections of precipitation in future climate; see Sui, Satoh, et al. (2020) for a recent review.

Despite its wide acceptance as a diagnostic parameter for the macroscopic effects of cloud

microphysics, multiple working definitions of PE are found in the literature (Sui, Satoh, et al. 2020). Sui, Li, et al. (2007) define PE based on the condensate budget equation,

$$\frac{dC}{dt} = CONV_c - P_s + SI_{qv} - SO_{qv} \tag{6.1}$$

where $CONV_c$ is the convergence of condensate, P_s is the surface precipitation rate, SI_{qv} is the vapor condensation/deposition rate, and SO_{qv} is the vapor evaporation/melting rate. Their definition of the cloud microphysics precipitation efficiency (CMPE) is then

$$\text{CMPE} = \begin{cases} P_s/(SI_{qv} + Q_{CM}), & \text{if } Q_{CM} > 0 \\ P_s/SI_{qv}, & \text{otherwise} \end{cases}$$

where $Q_{CM} = CONV_c - dC/dt = P_s + SO_{qv} - SI_{qv}$ is the rate of condensate loss from microphysical processes. In words, this means that if clouds are dissipating, the precipitation efficiency is the rate of precipitation divided by the loss of condensate from precipitation and evaporation within clouds; $CMPE = P_s/(P_s+SO_{qv})$. If clouds are forming, the precipitation efficiency is the rate of precipitation divided by the rate of condensate formation. Many other definitions of PE in the literature exhibit the same reliance on microphysical parameters, as they have been developed for cloud-resolving models where these parameters are available (Sui, Satoh, et al. 2020).

The definition of CMPE in Equation 6.4 is difficult to apply to observational data due to its reliance on the microphysical rates of condensate production and loss within the cloud, SI_{qv} and SO_{qv}. Sui, Li, et al. (2007) present the large-scale precipitation efficiency (LSPE) as an alternative that depends only on macroscopic quantities. The LSPE is defined based on the surface rainfall equation (Gao et al. 2005), and reads

$$LSPE = P_s\Big[(-\frac{dq_v}{dt}) + (CONV_{qv}) + (Q_E) + (CONV_C - \frac{dC}{dt})\Big]^{-1} \tag{6.2}$$

where, importantly, terms in parentheses in the denominator are only included if they are positive. In words, this equation says that PE is defined by the amount of water entering the column as vapor compared with the amount of precipitation formed from that vapor. This definition of LSPE is attractive because it correlates closely with CMPE, can be derived from macro-scale quantities only, and has values ranging between zero and unity as one would intuitively expect for an efficiency. Unfortunately, this definition fails for reanalysis data because water vapor is not conserved; the nudging terms artificially add and remove water vapor from grid cells to force agreement between the reanalysis and the observed satellite radiances (Hersbach et al. 2020), and this leads to unphysical values of LSPE that are especially severe at sub-daily timescales like those in our dataset.

Recently, Li, Studholme, et al. (2022) put forth an alternative macroscopic definition of the precipitation efficiency, which they define as

$$\epsilon = \frac{P_s}{\text{CWP}} \tag{6.3}$$

where P_s is the surface precipitation and CWP is the condensed water path. Those authors show that this definition of PE correlates tightly with microphysical PE in a cloud-resolving model. We adopt ϵ as our working definition of PE for the analysis presented here for the following reasons. First, Equation 6.3 can be calculated from NEXRAD and GOES alone, meaning we can observe its value at the dataset's native ∼8-km and hourly resolution. Second, the observational estimates of ϵ can be compared directly with the ERA-5 reanalysis, which also reports condensate path and precipitation. Third, values of ϵ remain meaningful both within a precipitating cloud at short timescales and in a statistically-averaged sense over months to years. Probability density functions of ϵ over our entire study domain are shown in Figure 6.6, calculated hour-by-hour for regions of nonzero precipitation (right panel), and as a temporal mean over both precipitating and non-precipitating times (left panel). In this exploratory study, we compute ϵ for only two months of data, January 2019 and July 2019. The choice of a midsummer month and a midwinter month permits us to make tentative inferences about the differences between the mesoscale convective complexes that dominate summertime precipitation and the baroclinic waves that dominate wintertime precipitation over the CONUS. Future work should expand this analysis to consider the entire time domain of our dataset.

The time-mean values in July are in good agreement between GOES/NEXRAD, ERA-5, and the tropical, annual-mean satellite data of Li, Studholme, et al. (2022), which displays most probable PE values of $4-8\times10^{-4}$ s^{-1}. However, ERA-5 does not make enough low-PE regions in January, even though the most probable values of ϵ are near the same between observations and reanalysis. ERA-5 and NEXRAD/GOES both find larger average PE values in July than in January. In precipitating regions and at hourly cadence, PE is much higher in both calculations: limiting the analysis to precipitating regions removes all non-precipitating clouds from the denominator of Equation 6.3. The spread in PE is large and inclusive of efficiencies approaching 1 s^{-1} in the hourly data; however, the precipitation efficiencies in ERA-5 are systematically far lower than in NEXRAD/GOES. As shown in Section 6.3, this discrepancy is likely driven by two factors: our super-resolution regridding of ERA-5, and the convective and microphysics parameterizations within ERA-5. The hourly ϵ values we derive from GOES/NEXRAD are of the same order of magnitude, albeit somewhat larger, than those calculated from TRMM satellite cloud and precipitation data over the tropical ocean at quarter-degree resolution by Lau et al. (2003); the discrepancy is again likely explicable by differences in spatial resolution.

In Figures 6.7 and 6.8, we plot PE as a function of 2-meter temperature and surface equivalent potential temperature (θ_{e_sfc}), respectively. We computed θ_{e_sfc} according to the formulation of Bolton (1980), using the ERA-5 2-meter temperature and 2-meter dew-point temperature as inputs. θ_{e_sfc} is closely related to the moist static energy, and provides a more complete view of the effects of warming an air parcel than near-surface temperature (Song et al. 2022). Dew-point temperature has also been shown to correlate with extreme precipitation based on gauge observations (Ali et al. 2018). Therefore, we consider θ_{e_sfc} a more useful independent variable for this analysis than 2-meter temperature. We still include the correlation between ϵ and 2-meter temperature for direct comparison with the results of

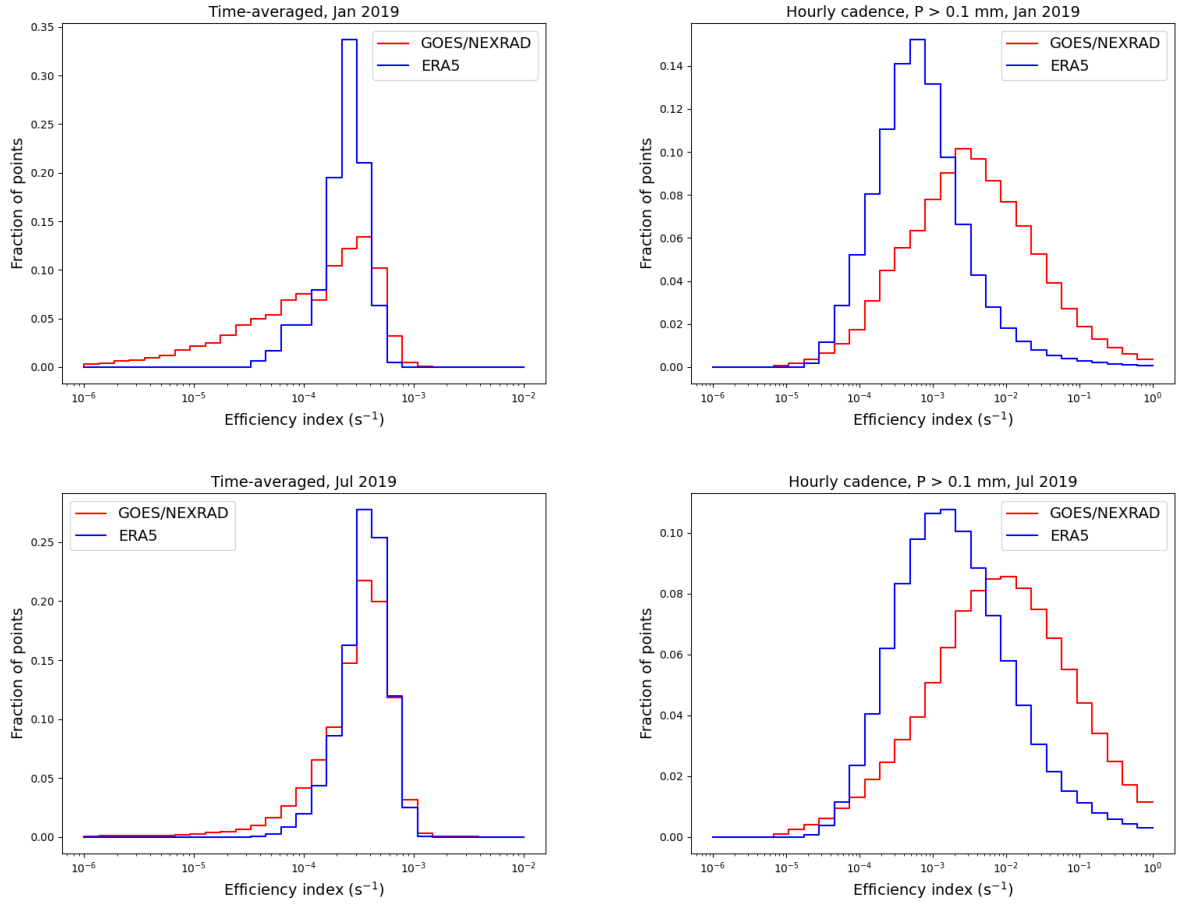

Figure 6.6: (Left:) Time-mean and (Right:) hourly probability distribution function of PE from ERA-5 and GOES/NEXRAD over our study region in (Top:) January 2019 and (Bottom:) July 2019.

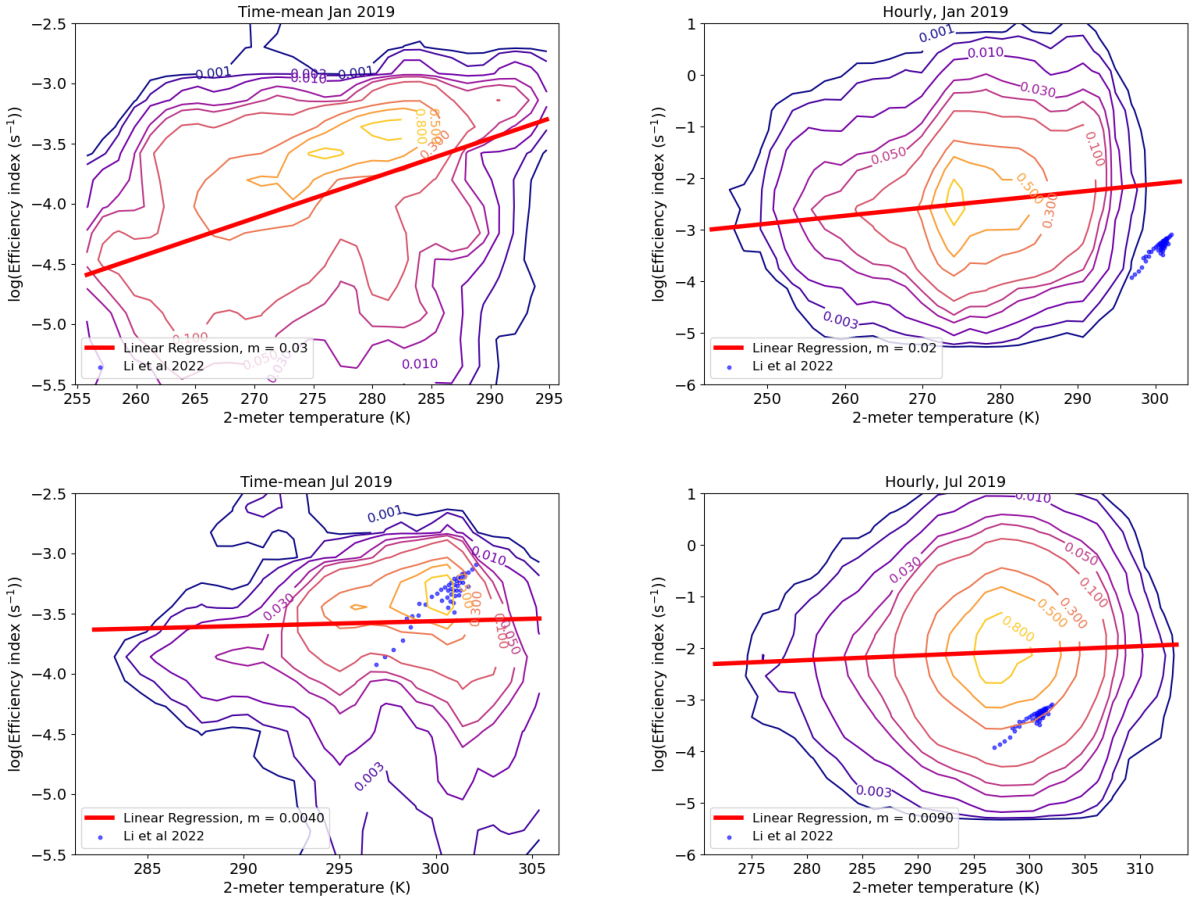

Figure 6.7: GOES/NEXRAD PE plotted against two-meter temperature at (Left:) time-mean and (Right:) hourly cadence over our study region in (Top:) January 2019 and (Bottom:) July 2019. The blue data points denote the satellite-derived annual-mean ϵ values in the Indo-Pacific warm pool from Li, Studholme, et al. (2022).

Li, Studholme, et al. (2022).

We tested for regional differences in PE by splitting our dataset according to Köppen-Geiger climate class (as delineated by Peel et al. 2007); this analysis is presented in Figure 6.9. No significant difference is found between the five regions in summer, but in winter, the tropical Savannah climate region displays substantially higher precipitation efficiencies than the other climate classes.

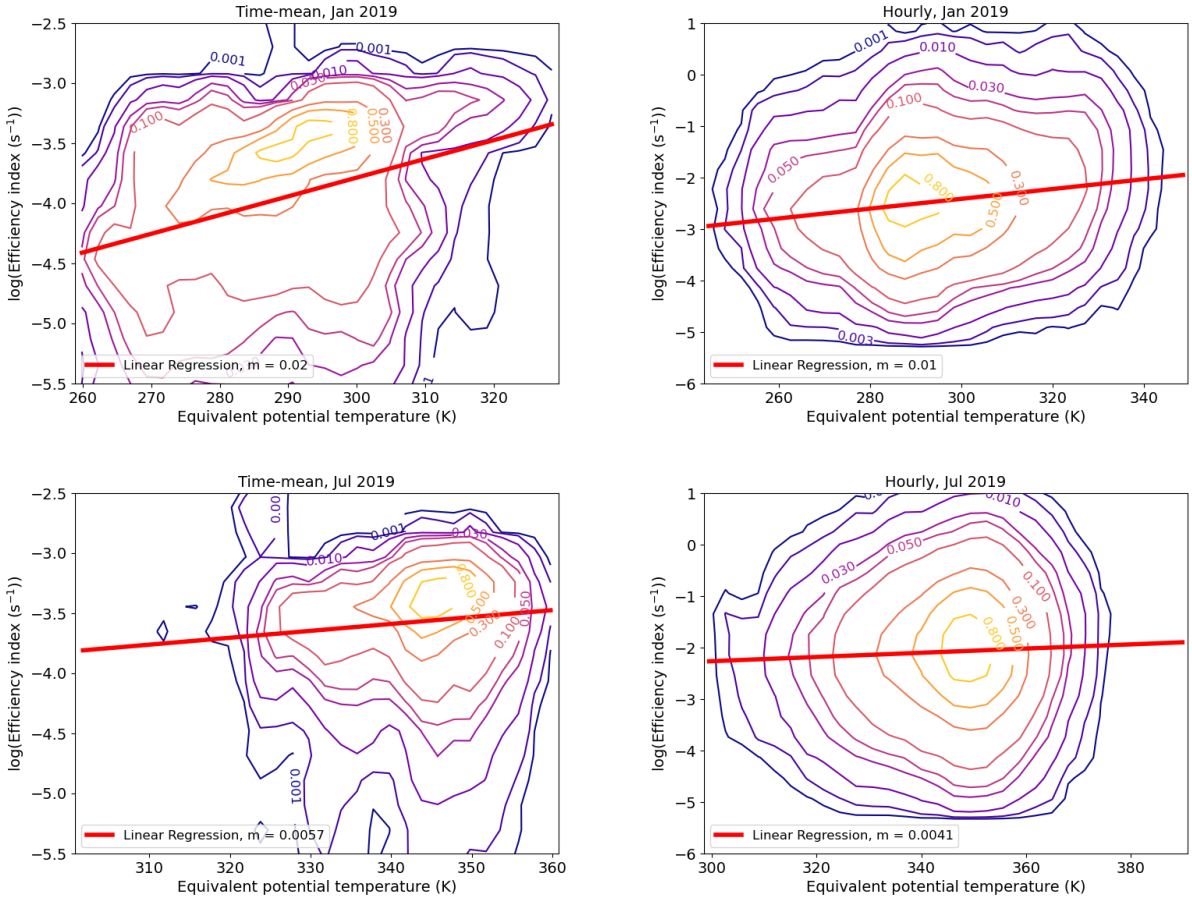

Figure 6.8: GOES/NEXRAD PE plotted against surface equivalent potential temperature at (Left:) time-mean and (Right:) hourly cadence over our study region in (Top:) January 2019 and (Bottom:) July 2019.

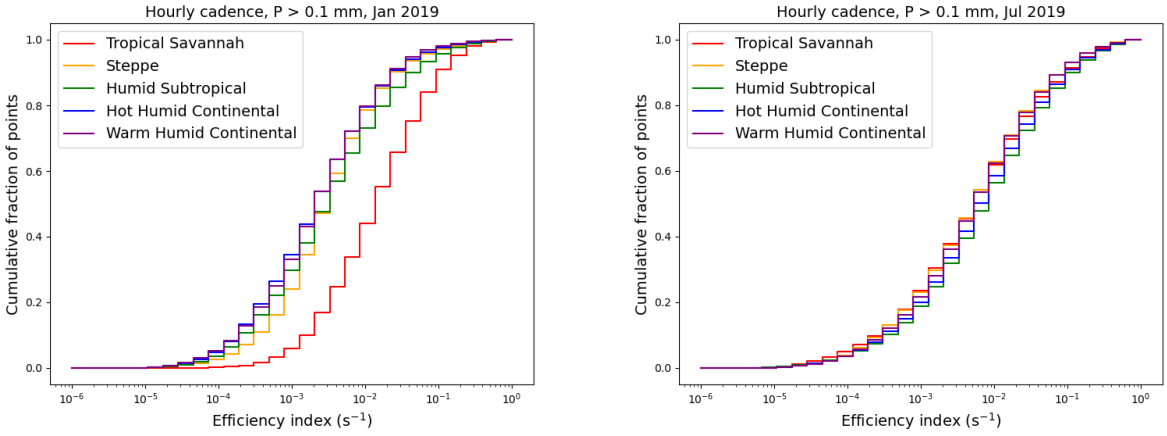

Figure 6.9: Cumulative distribution function of hourly PE from the GOES/NEXRAD data, split into the five Köppen-Geiger climate classes present in our study region for (Left:) January 2019 and (Right:) June 2019.

6.5 Discussion

Precipitation Efficiency

Li, Studholme, et al. (2022) propose ϵ as a metric for evaluating the representation of cloud and precipitation processes within climate models, since ϵ depends sensitively on cloud microphysics parameterizations, but can be calculated easily from large-scale fields. Those authors find a wide range of mean values of $d\epsilon/d\Delta T$ in the Coupled Model Intercomparison Project Phase 6 (CMIP6) ensemble, ranging from -7% to 12%. The positive correlation of ϵ with both near-surface temperature and equivalent potential temperature we find is in agreement with the correlation from Li, Studholme, et al. (2022) observed over the Indo-Pacific warm pool, and persists over a much larger temperature range than those authors probed. This positive correlation is in line with theoretical expectations. PE should be higher within convective aggregations because precipitation is falling through high-humidity columns, inhibiting re-evaporation, and since convective aggregation prefers warmer near-surface temperatures (Bao et al. 2017; Wing et al. 2017), this should lead to high PE at high T. Large eddy simulations have shown that moisture entrained into a cloud through the cloud base is twice as likely to precipitate as moisture entrained laterally (Langhans et al. 2015), raising PE in deep convective towers where vertical moisture transport is large. Given these considerations, the regional difference in wintertime precipitation efficiency between the tropical Savannah and the other K-G classes is expected, as the surface temperatures are consistently warm in this zone (the tropical Savannah climate is only found in the southern half of Florida in our study region). However, the relatively small areal extent of tropical

Savannah in the CONUS means this result should be treated with caution. The lack of any trends with climate class in July is sensible, considering that summer extreme precipitation is driven primarily by deep convection over most of the Eastern and Midwestern CONUS (Schumacher et al. 2006; Stevenson et al. 2014). Future studies of PE as a function of storm type should be undertaken to test whether the temperature dependence is related only to the proportion of rainfall in convective aggregates, or whether PE depends on equivalent potential temperature for two different storms with similar morphological characteristics. Lau et al. (2003) suggest that PE in warm light rain from stratiform clouds over the tropical oceans displays strong sensitivity to sea-surface temperature, but it is unclear whether the same relationship would hold over land.

Unlike other PE definitions, which are mostly non-dimensional, the definition of ϵ has units of inverse time, and a timescale $\tau = 1/\epsilon$ can be defined. Li, Studholme, et al. (2022) interpret τ as the characteristic residence time of condensate in the atmosphere before either precipitating or evaporating, and show its utility as a metric for the latent heat budget in the atmosphere. Within a precipitating cloud, τ is related to the autoconversion timescale $1/C_0$, which is defined as the characteristic timescale for the conversion of cloud droplets to raindrops (Lau et al. 2003). Those authors calculate C_0 from LWP and P_s using a simple parameterization scheme used in climate models (Sundqvist et al. 1989), given by

$$P_s = C_0(\mathrm{LWP})\Big[1 - \exp\Big(-\frac{(\mathrm{LWP})^2}{m_r^2}\Big)\Big] \tag{6.4}$$

where m_r is the typical value of cloud water content beyond which the collision-coalescence autoconversion of cloud drops to raindrops becomes substantial. In practice, m_r is tuned to fit observational data, and Lau et al. (2003) give a best-fitting value for warm rain (rain from liquid-phase clouds) of $m_r = 0.7$ kg m^{-2}. Using this value of m_r, we find a most-probable autoconversion timescale of roughly 10 minutes (600 seconds), in line with the range of 200-1000 seconds published by Lau et al. (2003). The largest precipitation efficiencies, and therefore autoconversion timescales, in our dataset exceed those of Lau et al. (2003), who find typical values of $\tau \sim 5$ minutes for the most intense precipitation events in their data. However, their quarter-degree resolution is insufficient to resolve individual convective cells. Further work is needed to understand whether ϵ can be applied naïvely to very intense convective rainfall, or if the short convergence and advection timescales complicate the interpretation of τ.

Leveraging the Dataset to Prognose Extremes in a Changing Climate

The climate science community has put substantial effort and resources into improving predictions of how precipitation and its extremes will change in a warmer climate in the next hundred years (see, e.g, Fowler et al. 2021, for a recent review). These efforts include theoretical studies of how well the Clausius-Clapeyron (CC) relation should be followed in extreme

storms (e.g., Trenberth et al. 2003), direct measurement of trends in extreme precipitation from observations (e.g., Guerreiro et al. 2018), and analysis of extremes in regional and global climate models. Models disagree on the details of how extremes will change in a warmer climate. Large model spreads are present in predicted regional sensitivities of extremes to global warming, especially in the tropics and during extratropical summer, when deep convective precipitation is prevalent (Akinsanola et al. 2020; Ge et al. 2021; Toreti et al. 2013). The unique combination of data we present in this paper can be leveraged to improve these predictions in several ways, which we discuss briefly below.

The dataset presented here can be used to construct probabilistic (statistical) downscaling relationships. In contrast with dynamical downscaling, in which a smaller-scale but more detailed model is nested within a GCM, probabilistic downscaling links the local scale to the GCM scale using transfer functions calibrated by observed high-resolution data, permitting the inference of local-scale conditions from synoptic-scale model data (see Kallache et al. 2011, for a review). The inclusion of both ERA-5 precipitation estimates (31-km resolution) and NEXRAD precipitation measurements (8-km resolution) permits the use of model output statistics (MOS) downscaling techniques to infer sub-grid rainfall. Similarly, an MOS technique could be used to infer cloud condensate path at the subgrid scale. The large range of synoptic-scale environments and long time baseline of our observations will facilitate the construction of detailed conditional PDFs to apply to these downscaling transfer functions. These statistical downscaling relationships can be applied to generate synthetic weather in a process known as stochastic weather generation (see Wilks et al. 1999, for a review). Weather generators are used in several fields of research, including agriculture, hydrology, and climate vulnerability assessment, but most stochastic weather generators to date are conditioned on daily data only (e.g., Breinl et al. 2017; Evin et al. 2018; Sparks et al. 2018; Steinschneider et al. 2019); our dataset fills a need for hourly data on which to condition those models.

This dataset is designed in parallel to parameterizations for clouds and precipitation in Earth system models (ESMs). In ESMs, the physics of clouds and rainfall processes typically operate on horizontal spatial scales much smaller than the spatial grid onto which the Euler equations governing the atmosphere are discretized. Because of the scale mismatch, it is not possible to represent this physics explicitly, and therefore statistical models calibrated against observations are introduced to mimic the emergent behavior of the cloud and precipitation physics in response to the evolving simulated atmospheric state. In our data set, all three components are replaced by observations: the simulated state with reanalysis, the parameterized clouds with cloud properties retrieved from GOES, and the rainfall from NEXRAD.

Precisely because our dataset has all the requisite components of parameterizations in ESMs, the next stage of research with it will be to construct a stochastic cloud and rainfall parameterization. Parameterizations that respond stochastically rather than deterministically to the resolved-scale atmospheric state better represent the scaling symmetries of the equations of motion (Palmer 2019). One such class of stochastic models are (hidden) Markov Models (MMs and HMMs), and there has already been considerable success with emulating rainfall using HMMs (e.g. Holsclaw et al. 2016). Our plan is to use this stochastic model

to predict rainfall under temperature increases anticipated under a range of IPCC scenarios by 2100. The physical principle underlying this prediction is the Fluctuation Dissipation Theorem (FDT) from statistical physics, which has been proposed as a general mechanism to predict the forced response of a dynamical system based on its unforced internal modes of variability (Leith 1975). There have been several successful demonstrations of FDT to the climate system (e.g. Gritsun et al. 2007), although the assumption of Gaussian statistics underlying these demonstrations has hampered application to, in particular, critical unsolved questions regarding the sensitivity of the Earth system to increasing CO_2. Our adoption of a general HMM framework obviates these limitations. Moreover, it has recently been shown that MMs and therefore HMMs are subject to a discretized version of the FDT (Dembo et al. 2010; Santos Gutiérrez et al. 2020). We will try constructing an HMM of our data set and test its response to several natural "forcings" that have occurred several times in the recent past, namely coupled modes of internal variability driven by physics external to the spatial domain of our data set, e.g. the El Niño Southern Oscillation (ENSO). If FDT is successful in emulating the mean response of rainfall to ENSO etc., we will then compute the response of rainfall to a continuously warming land surface. The advantage of this approach relative to traditional climate projections is that our projection is entirely and rigorously grounded in observations – the primary assumption is that the physics of clouds and rainfall and their connections to resolved-scale meteorology is persistent under such warming.

6.6 Conclusions

We have presented a new combination of data for the analysis of storms at their native scales. The dataset's 8-km and hourly spatio-temporal resolution over a subcontinental and decadal domain make it a multipurpose tool for studying the properties of storms in the current climate and diagnosing model representation of storms. Our conclusions are summarized as follows:

- The dataset presented herein compiles observed cloud, precipitation, and reanalysis fields at storm-relevant length and time scales, and over a synoptic-scale and decade-length domain.
- Observational cloud and precipitation data are imperative for correctly capturing extreme storm behavior at hourly timescales; reanalysis data are not sufficient for this purpose.
- The positive dependence of precipitation efficiency on surface temperature previously observed over the tropical ocean also holds in the mid-latitudes over land, and across a wide range of temperatures in both the warm and cold seasons.
- Our analyses of precipitation IDF and precipitation efficiency can be used as benchmark metrics for current and future GCMs and GCRMs.

Chapter 7

Conclusions & Future Work

This dissertation has focused on interpreting remote-sensing data with radiative transfer models in order to advance our knowledge of the atmospheres of Earth, Uranus, and Neptune. In the first few chapters, I called upon theory and intuition developed for Earth's atmosphere to interpret new high-resolution, multi-wavelength observations of the ice giants. In the latter half of the thesis, I performed statistical analyses of extreme storms in Earth's extratropics, with an eye toward understanding the effects of climate change on extreme precipitation events. The primary results of each chapter, along with open research questions posed by that chapter, are summarized briefly below. I close with a short discussion of future work to be undertaken by the climate science and planetary science communities as a whole.

In Chapter 2, I reported the discovery of a large, long-lived storm system on Neptune, the first of its size ever recorded in Neptune's predominantly quiescent equatorial region. The storm's morphology and persistent activity over a ∼7-month period were reminiscent of Saturn's great storms. Feature tracking and radiative transfer modeling permitted determination of the storm's drift rate and cloud-top pressure, respectively; these parameters, along with the absence of a dark-spot vortex at Neptune's equator in Hubble Space Telescope optical images, represented key observational constraints on the storm's dynamical origin. The storm outbreak was hypothesized to stem from moist convective upwelling, but an equatorial Kelvin wave could not be ruled out as the dynamical origin. Additional theoretical work is needed to understand the dynamics of these rare storm events; it remains to be understood whether the Li and Ingersoll (2015) model for Saturn's episodic storms would also work on the ice giants, and if so, how a convective storm at the water layer in the deep atmosphere would affect the more readily-observed H_2S and CH_4 cloud layers.

Chapter 3 describes the first detection of the thermal component of the narrow main rings of Uranus. Near-simultaneous observations at mid-infrared wavelengths with the Very Large Telescope and millimeter wavelengths with the Atacama Large (sub-)Millimeter Array permitted a precise measurement of the ring particle temperature in the ϵ ring. The derived temperature of 77 ± 2 K suggests that the particles' thermal inertia is small enough (and rotation rate slow enough) to induce longitudinal temperature differences between their day and night sides, in line with the behavior of large particles in Saturn's rings. Currently-

available ground-based millimeter and radio instrumentation has the capability to separate each of the nine inner main rings and perform these same measurements, as well as to measure the thermal component of Uranus's small and mid-sized moons. Future research should focus on using measurements like these to determine whether Uranus's circumplanetary material was sourced from a circumplanetary disk at formation, ejecta from a giant impact, or a combination of the two.

The millimeter and radio maps of Uranus's troposphere presented in Chapter 4 reveal banded structure near the equator of Uranus. I interpreted these bright and dark bands as alternating subsiding and upwelling regions, the result of a global circulation akin to the Hadley-Walker circulation on Earth. Radiative transfer modeling of the H_2S-rich middle latitudes and the H_2S-depleted north polar vortex permitted precise measurements of the H_2S and NH_3 abundances in Uranus, the pressure level of the NH_4SH condensate cloud, and the nitrogen-to-sulfur ratio. I found that ratio to be $0.2^{+0.08}_{-0.07}$, approximately 25 times lower than the protosolar value. At present, it is difficult to confirm or refute any of the competing theories that attempt to explain this strong nitrogen depletion; the two primary explanations are strong selective fractionation during the formation of clathrated water ice in the cold protoplanetary disk, or dissolution of nitrogen-bearing species into a superionic fluid H_2O "ocean" in Uranus's deep interior. Answering this question requires measurements of other elemental abundances in Uranus's troposphere, which can only be achieved by an atmospheric entry probe launched aboard a spacecraft. From the ground, though, future radio observatories like the next-generation Very Large Array (ngVLA) should leverage their increased sensitivity and resolution to unambiguously determine the absorbing species responsible for the banded structure I observed, and make use of their sensitivity to wavelengths longer than 10 cm to further tighten measurements of bulk abundances beneath the NH_4SH layer.

In Chapter 5, the first of two chapters focused on the statistics of extratropical extreme storms on Earth, I used Doppler radar rainfall data to test the assumption, often used when constructing gauge-based quantitative precipitation estimates (QPEs), that the climatology of extremes varies only minimally at length scales smaller than the average inter-rain-gauge spacing. I showed that this assumption does indeed hold, but only if the interpolation technique one uses to represent rain gauge data on a regular grid accounts for extremes in the appropriate manner. This result facilitates extending gridded QPEs back in time to the early 1900s when gauges were the only reliable precipitation estimates, and thus paves the way for creating an accurate, continental-scale, in-situ-based, long-term precipitation record. Such a product is of keen interest for hydrological modeling, resource management, and climate change studies, and future work should prioritize the construction and evaluation of such a dataset.

Chapter 6 presented a new dataset for characterizing storms at ∼8-km and hourly resolution over the Eastern and Midwestern United States from 2002-2020. I used probability density functions and intensity-duration-frequency curves of the cloud and precipitation data to demonstrate the advantage of using radar-observed precipitation and satellite-observed cloud fields instead of reanalysis alone, especially in capturing the intensity of extremes. As an advertisement for the unique capabilities of this particular data combination, I presented

new analysis of the precipitation efficiency and its associated condensate residence times over a wide range of synoptic-scale conditions. The first non-hydrostatic global cloud-resolving models (GCRMs) are now in operation, albeit only over relatively short integrations (<1 simulated year), and the exquisite spatio-temporal resolution of this dataset, along with the metrics we publish, are ideal for evaluating the fidelity of extremes in these GCRMs. However, these comparisons have yet to be carried out, and future work should prioritize this. This combination of observational data sources also hints at novel data-driven approaches to predicting the behavior of extreme weather events under climate change conditions.

Recent and planned advances in technology continue to push atmospheric sciences forward, both on Earth and in the rest of the solar system. Terrestrial climate science must leverage these advances to address one of humanity's most pressing problems—an atmosphere warming under the influence of anthropogenic greenhouse gases. With this societal need as a driver, the climate science community has continued to improve the resolution, complexity, and physical realism of global circulation models. This dissertation laid the groundwork for evaluating the fidelity of such high-resolution models using observational data, especially their representation of extratropical extremes. Much more work is required, though, before accurate predictions of how storms will change in a warming climate are available.

Studies of the ice giants have also been prioritized by the scientific community recently: NASA's Planetary Decadal Survey 2023-2032 (National Academies of Sciences et al. 2022) identified a Uranus mission as its highest-priority flagship mission for the next decade. Such a mission will resolve fundamental questions about the conditions of the protoplanetary disk during planetesimal formation, the migration and bombardment history of protoplanets, the origin and history of the circumplanetary environment (including the diffuse outer rings), and the structure and dynamics of ice giant atmospheres. To maximize the scientific return of such a mission requires making as much progress as possible using existing observatories, and this dissertation represents a small piece of that progress. With a flagship mission on the horizon, the next few decades promise a revolution in our understanding of the outer solar system; there are nearly limitless questions to answer.

Bibliography

Abatzoglou, John T (2013). "Development of gridded surface meteorological data for ecological applications and modelling". In: *International Journal of Climatology* 33.1, pp. 121–131. DOI: 10.1002/joc.3413.

Ádámkovics, M. et al. (May 2016). "Meridional variation in tropospheric methane on Titan observed with AO spectroscopy at Keck and VLT". In: *Icarus* 270, pp. 376–388. DOI: 10.1016/j.icarus.2015.05.023. arXiv: 1509.08835 [astro-ph.EP].

AghaKouchak, A et al. (2011). "Evaluation of satellite-retrieved extreme precipitation rates across the central United States". In: *Journal of Geophysical Research: Atmospheres* 116.D2, p. D02115. DOI: 10.1029/2010JD014741.

Akinsanola, AA et al. (2020). "Projected changes in seasonal precipitation extremes over the United States in CMIP6 simulations". In: *Environmental Research Letters* 15.10, p. 104078.

Alexander, Lisa Victoria et al. (2006). "Global observed changes in daily climate extremes of temperature and precipitation". In: *Journal of Geophysical Research: Atmospheres* 111.D5, p. D05109. DOI: 10.1029/2005JD006290.

Ali, Haider, Hayley J Fowler, and Vimal Mishra (2018). "Global observational evidence of strong linkage between dew point temperature and precipitation extremes". In: *Geophysical Research Letters* 45.22, pp. 12–320.

Alissandrakis, C. E. et al. (Sept. 2017). "Center-to-limb observations of the Sun with ALMA . Implications for solar atmospheric models". In: *A&A* 605, A78, A78. DOI: 10.1051/0004-6361/201730953.

Allen, C. W. (1963). *Astrophysical quantities*.

Allison, M. (Feb. 1990). "Planetary waves in Jupiter's equatorial atmosphere". In: *Icarus* 83, pp. 282–307. DOI: 10.1016/0019-1035(90)90069-L.

Allison, Michael et al. (1991). "Uranus atmospheric dynamics and circulation." In: *IN: Uranus (A92-18701 05-91). Tucson, AZ, University of Arizona Press, 1991, p. 253-295.* Ed. by Jay T. Bergstralh, Ellis D. Miner, and Mildred S. Matthews, pp. 253–295.

Andrews, D. G., J. R. Holton, and C. B. Leovy (1987). "Middle Atmospheric Dynamics". In: *Academic Press (Orlando, Florida)*.

Arakawa, Akio (July 2004). "The Cumulus Parameterization Problem: Past, Present, and Future". In: *Journal of Climate* 17.13, pp. 2493–2525. DOI: 10.1175/1520-0442(2004)

017<2493:ratcpp>2.0.co;2. URL: https://doi.org/10.1175/1520-0442(2004)017%3C2493:ratcpp%3E2.0.co;2.

Arias, Paola et al. (2021). "Climate Change 2021: The Physical Science Basis. Contribution of Working Group14 I to the Sixth Assessment Report of the Intergovernmental Panel on Climate Change; Technical Summary". In.

Arnold, Nathan P, William M Putman, and Saulo R Freitas (2020). "Impact of resolution and parameterized convection on the diurnal cycle of precipitation in a global nonhydrostatic model". In: *Journal of the Meteorological Society of Japan. Ser. II*.

Asplund, Martin et al. (Sept. 2009). "The Chemical Composition of the Sun". In: *ARA&A* 47.1, pp. 481–522. DOI: 10.1146/annurev.astro.46.060407.145222. arXiv: 0909.0948 [astro-ph.SR].

Atreya, S. K. and P. N. Romani (1985). "Photochemistry and clouds of Jupiter, Saturn and Uranus." In: *IN: Recent advances in planetary meteorology (A86-37166 17-91). Cambridge and New York, Cambridge University Press, 1985, p. 17-68. NASA-supported research.* Ed. by G. E. Hunt, pp. 17–68.

Atreya, S. K. and A.-S. Wong (Jan. 2005). "Coupled Clouds and Chemistry of the Giant Planets - A Case for Multiprobes". In: *Space Sci. Rev.* 116, pp. 121–136. DOI: 10.1007/s11214-005-1951-5.

Bao, Jiawei et al. (2017). "The robust relationship between extreme precipitation and convective organization in idealized numerical modeling simulations". In: *Journal of Advances in Modeling Earth Systems* 9.6, pp. 2291–2303.

Barlow, Mathew et al. (2019). "North American extreme precipitation events and related large-scale meteorological patterns: a review of statistical methods, dynamics, modeling, and trends". In: *Climate Dynamics* 53.11, pp. 6835–6875.

Barry, Leon, George C Craig, and John Thuburn (2002). "Poleward heat transport by the atmospheric heat engine". In: *Nature* 415.6873, pp. 774–777.

Baum, Bryan A. et al. (2005). "Bulk Scattering Properties for the Remote Sensing of Ice Clouds. Part I: Microphysical Data and Models". In: *Journal of Applied Meteorology* 44.12, pp. 1885–1895. DOI: 10.1175/JAM2308.1. eprint: https://doi.org/10.1175/JAM2308.1. URL: https://doi.org/10.1175/JAM2308.1.

Behnke, R et al. (2016). "Evaluation of downscaled, gridded climate data for the conterminous United States". In: *Ecological applications* 26.5, pp. 1338–1351. DOI: 10.1002/15-1061.

Bell, Thomas L et al. (1990). "Sampling errors for satellite-derived tropical rainfall: Monte Carlo study using a space-time stochastic model". In: *Journal of Geophysical Research: Atmospheres* 95.D3, pp. 2195–2205.

Bies, Alexander J et al. (2016). "Relationship between fractal dimension and spectral scaling decay rate in computer-generated fractals". In: *Symmetry* 8.7, p. 66. DOI: 10.3390/sym8070066.

Bohren, Craig F and Eugene E Clothiaux (2006). *Fundamentals of atmospheric radiation: an introduction with 400 problems*. John Wiley & Sons.

Bolton, David (1980). "The computation of equivalent potential temperature". In: *Monthly weather review* 108.7, pp. 1046–1053.

Borysow, A. and L. Frommhold (May 1986). "Theoretical Collision-induced Rototranslational Absorption Spectra for the Outer Planets: H 2-CH 4 Pairs". In: *ApJ* 304, p. 849. DOI: 10.1086/164221.

Bradley, Larry et al. (Jan. 2019). *astropy/photutils: v0.6*. DOI: 10.5281/zenodo.2533376. URL: https://doi.org/10.5281/zenodo.2533376.

Breinl, Korbinian et al. (2017). "Can weather generation capture precipitation patterns across different climates, spatial scales and under data scarcity?" In: *Scientific Reports* 7.1, pp. 1–12.

Briggs, F. H. and B. H. Andrew (Feb. 1980). "Microwave radiometry and interferometry of Uranus". In: *Icarus* 41.2, pp. 269–277. DOI: 10.1016/0019-1035(80)90010-X.

Brogan, C. L., T. R. Hunter, and E. B. Fomalont (May 2018). "Advanced Gain Calibration Techniques in Radio Interferometry". In: *arXiv e-prints*. arXiv: 1805.05266 [astro-ph.IM].

Butler, Bryan J. et al. (Dec. 2001). "Accurate and Consistent Microwave Observations of Venus and Their Implications". In: *Icarus* 154.2, pp. 226–238. DOI: 10.1006/icar.2001.6710.

Cavalié, T., O. Venot, F. Selsis, et al. (July 2017). "Thermochemistry and vertical mixing in the tropospheres of Uranus and Neptune: How convection inhibition can affect the derivation of deep oxygen abundances". In: *Icarus* 291, pp. 1–16. DOI: 10.1016/j.icarus.2017.03.015. arXiv: 1703.04358 [astro-ph.EP].

Cavalié, Thibault, Olivia Venot, Yamila Miguel, et al. (May 2020). "The Deep Composition of Uranus and Neptune from In Situ Exploration and Thermochemical Modeling". In: *Space Sci. Rev.* 216.4, 58, p. 58. DOI: 10.1007/s11214-020-00677-8. arXiv: 2004.13987 [astro-ph.EP].

Chandrasekhar, S. (1960). *Radiative transfer*.

Change, IPCC Climate (2022). "Impacts, Adaptation, and Vulnerability. Contribution of Working Group II to the Sixth Assessment Report of the Intergovernmental Panel on Climate Change; Pörtner, H". In: *O., Roberts, DC, Tignor, M., Poloczanska, ES, Mintenbeck, K., Alegría, A., Craig, M., Langsdorf, S., Löschke, S., Möller, V., et al., Eds.*

Chen, Cheng-Ta and Thomas Knutson (Apr. 2008). "On the Verification and Comparison of Extreme Rainfall Indices from Climate Models". In: *Journal of Climate* 21.7, pp. 1605–1621. DOI: 10.1175/2007jcli1494.1. URL: https://doi.org/10.1175/2007jcli1494.1.

Coles, Stuart et al. (2001). *An introduction to statistical modeling of extreme values*. Vol. 208. Springer. DOI: 10.1007/978-1-4471-3675-0.

Conrath, B. J., P. J. Gierasch, and S. S. Leroy (Feb. 1990). "Temperature and circulation in the stratosphere of the outer planets". In: *Icarus* 83.2, pp. 255–281. DOI: 10.1016/0019-1035(90)90068-K.

Cronshey, Roger (1986). *Urban hydrology for small watersheds*. Tech. rep. US Dept. of Agriculture, Soil Conservation Service, Engineering Division.

Cutri, R. M. et al. (June 2003). "VizieR Online Data Catalog: 2MASS All-Sky Catalog of Point Sources (Cutri+ 2003)". In: *VizieR Online Data Catalog* 2246.

Dai, Aiguo (2013). "The influence of the inter-decadal Pacific oscillation on US precipitation during 1923–2010". In: *Climate dynamics* 41.3-4, pp. 633–646. DOI: 10.1007/s00382-012-1446-5.

Daly, Christopher, Ronald P. Neilson, and Donald L. Phillips (1994). "A Statistical-Topographic Model for Mapping Climatological Precipitation over Mountainous Terrain". In: *Journal of Applied Meteorology* 33.2, pp. 140–158. DOI: 10.1175/1520-0450(1994)033<0140:ASTMFM>2.0.CO;2.

Daly, Christopher, Joseph I. Smith, and Keith V. Olson (2015). "Mapping Atmospheric Moisture Climatologies across the Conterminous United States". In: *PLOS ONE* 10.10, pp. 1–33. DOI: 10.1371/journal.pone.0141140.

de Kleer, K., I. de Pater, et al. (Sept. 2013). "Near-infrared spectra of the uranian ring system". In: *Icarus* 226, pp. 1038–1044. DOI: 10.1016/j.icarus.2013.07.016.

de Kleer, K., S. Luszcz-Cook, et al. (Aug. 2015a). "Clouds and aerosols on Uranus: Radiative transfer modeling of spatially-resolved near-infrared Keck spectra". In: *Icarus* 256, pp. 120–137. DOI: 10.1016/j.icarus.2015.04.021.

de Kleer, Katherine, Statia Luszcz-Cook, et al. (Aug. 2015b). "Clouds and aerosols on Uranus: Radiative transfer modeling of spatially-resolved near-infrared Keck spectra". In: *Icarus* 256, pp. 120–137. DOI: 10.1016/j.icarus.2015.04.021.

de Pater, I., D. E. Dunn, et al. (Nov. 2013). "Keck and VLT AO observations and models of the uranian rings during the 2007 ring plane crossings". In: *Icarus* 226, pp. 1399–1424. DOI: 10.1016/j.icarus.2013.08.001.

de Pater, I., L. N. Fletcher, et al. (July 2014). "Neptune's global circulation deduced from multi-wavelength observations". In: *Icarus* 237, pp. 211–238. DOI: 10.1016/j.icarus.2014.02.030.

de Pater, I., S. G. Gibbard, and H. B. Hammel (Jan. 2006). "Evolution of the dusty rings of Uranus". In: *Icarus* 180, pp. 186–200. DOI: 10.1016/j.icarus.2005.08.011.

de Pater, I., S. G. Gibbard, B. A. Macintosh, et al. (Dec. 2002). "Keck Adaptive Optics Images of Uranus and Its Rings". In: *Icarus* 160, pp. 359–374. DOI: 10.1006/icar.2002.6966.

de Pater, I. and S. Gulkis (Aug. 1988). "VLA observations of Uranus at 1.3-20 CM". In: *Icarus* 75, pp. 306–323. DOI: 10.1016/0019-1035(88)90007-3.

de Pater, I., H. B. Hammel, et al. (Sept. 2007). "The Dark Side of the Rings of Uranus". In: *Science* 317, p. 1888. DOI: 10.1126/science.1148103.

de Pater, I., P. N. Romani, and S. K. Atreya (June 1991). "Possible microwave absorption by H2S gas in Uranus' and Neptune's atmospheres". In: *Icarus* 91, pp. 220–233. DOI: 10.1016/0019-1035(91)90020-T.

de Pater, I., R. J. Sault, B. Butler, et al. (June 2016). "Peering through Jupiter's clouds with radio spectral imaging". In: *Science* 352, pp. 1198–1201. DOI: 10.1126/science.aaf2210.

de Pater, I., L. A. Sromovsky, H. B. Hammel, et al. (Sept. 2011). "Post-equinox observations of Uranus: Berg's evolution, vertical structure, and track towards the equator". In: *Icarus* 215, pp. 332–345. DOI: 10.1016/j.icarus.2011.06.022.

de Pater, Imke (Apr. 2018). "Selective enrichment of volatiles confirmed". In: *Nature Astronomy* 2, pp. 364–365. DOI: 10.1038/s41550-018-0457-5.

de Pater, Imke, B. Butler, et al. (2018). "Potential for Solar System Science with the ngVLA". In: *Science with a Next Generation Very Large Array, ASP Conference Series, Vol. 517. ASP Monograph 7. Edited by Eric Murphy., p.49*. Ed. by Eric Murphy. Vol. 517. Astronomical Society of the Pacific Conference Series, p. 49.

de Pater, Imke, David DeBoer, et al. (Feb. 2005). "Retrieval of water in Jupiter's deep atmosphere using microwave spectra of its brightness temperature". In: *Icarus* 173.2, pp. 425–438. DOI: 10.1016/j.icarus.2004.06.019.

de Pater, Imke, Paul N. Romani, and Sushil K. Atreya (Dec. 1989). "Uranus deep atmosphere revealed". In: *Icarus* 82.2, pp. 288–313. DOI: 10.1016/0019-1035(89)90040-7.

de Pater, Imke, R. J. Sault, Michael H. Wong, et al. (Apr. 2019). "Jupiter's ammonia distribution derived from VLA maps at 3-37 GHz". In: *Icarus* 322, pp. 168–191. DOI: 10.1016/j.icarus.2018.11.024. arXiv: 1902.07294 [astro-ph.EP].

de Pater, Imke, L. A. Sromovsky, P. M. Fry, et al. (May 2015). "Record-breaking storm activity on Uranus in 2014". In: *Icarus* 252, pp. 121–128. DOI: 10.1016/j.icarus.2014.12.037. arXiv: 1501.01309 [astro-ph.EP].

Deirmendjian, D. (Feb. 1964). "Scattering and polarization properties of water clouds and hazes in the visible and infrared". In: *Appl. Opt.* 3, p. 187. DOI: 10.1364/AO.3.000187.

Dembo, Amir and Jean-Dominique Deuschel (2010). "Markovian perturbation, response and fluctuation dissipation theorem". In: *Annales de l'Institut Henri Poincaré, Probabilités et Statistiques* 46.3, pp. 822–852. DOI: 10.1214/10-AIHP370. URL: https://doi.org/10.1214/10-AIHP370.

Diamond, "Howard J. et al. (2013). "US climate reference network after one decade of operations status and assessment". In: *Bulletin of the American Meteorological Society* 94, pp. 485–498. DOI: 10.1175/BAMS-D-12-00170.1.

Dobrzycka, Danuta and Leonardo Vanzi (2008). "Calibrating mid-infrared standard stars". In: *The 2007 ESO Instrument Calibration Workshop*. Springer, pp. 139–144.

Dritschel, DG and ME McIntyre (2008). "Multiple jets as PV staircases: The Phillips effect and the resilience of eddy-transport barriers". In: *Journal of the Atmospheric Sciences* 65.3, pp. 855–874.

Dumas, C., B. A. Smith, and R. J. Terrile (Aug. 2003). "Hubble Space Telescope NICMOS Multiband Photometry of Proteus and Puck". In: *AJ* 126, pp. 1080–1085. DOI: 10.1086/375909.

Dunn, D. E. et al. (Feb. 2005). "High-Quality BIMA-OVRO Images of Saturn and its Rings at 1.3 and 3 Millimeters". In: *AJ* 129, pp. 1109–1116. DOI: 10.1086/424536.

DWA (2012). *Arbeitsblatt DWA-A 531: Starkregen in Abhängigkeit von Wiederkehrzeit und Dauer, Deutsche Vereinigung für Wasserwirtschaft, Abwasser und Abfall e.V. (DWA)*. ISBN: 978-3-942964-28-9.

Eldardiry, Hisham, Emad Habib, and Yu Zhang (2015). "On the use of radar-based quantitative precipitation estimates for precipitation frequency analysis". In: *Journal of Hydrology* 531, pp. 441–453.

Evin, Guillaume, Anne-Catherine Favre, and Benoit Hingray (2018). "Stochastic generation of multi-site daily precipitation focusing on extreme events". In: *Hydrology and Earth System Sciences* 22.1, pp. 655–672.

Fegley B., Jr. and R. G. Prinn (Aug. 1986). "Chemical Models of the Deep Atmosphere of Uranus". In: *ApJ* 307, p. 852. DOI: 10.1086/164472.

Feng, Zhe et al. (Sept. 2019). "Spatiotemporal Characteristics and Large-Scale Environments of Mesoscale Convective Systems East of the Rocky Mountains". In: *Journal of Climate* 32.21, pp. 7303–7328. DOI: 10.1175/jcli-d-19-0137.1.

Fiolleau, Thomas and Rémy Roca (2013). "Composite life cycle of tropical mesoscale convective systems from geostationary and low Earth orbit satellite observations: Method and sampling considerations". In: *Quarterly Journal of the Royal Meteorological Society* 139.673, pp. 941–953.

Fitzpatrick, P. J. et al. (Mar. 2014). "Dispersion in Neptune's zonal wind velocities from NIR Keck AO observations in July 2009". In: *Ap&SS* 350, pp. 65–88. DOI: 10.1007/s10509-013-1737-2. arXiv: 1312.2676 [astro-ph.EP].

Flasar, F. M. et al. (Dec. 1987). "Voyager infrared observations of Uranus' atmosphere: Thermal structure and dynamics". In: *J. Geophys. Res.* 92.A13, pp. 15011–15018. DOI: 10.1029/JA092iA13p15011.

Fletcher, L. N., B. E. Hesman, et al. (June 2011). "Thermal Structure and Dynamics of Saturn's Northern Springtime Disturbance". In: *Science* 332, p. 1413. DOI: 10.1126/science.1204774.

Fletcher, Leigh N., Imke de Pater, et al. (Feb. 2020). "Ice Giant Circulation Patterns: Implications for Atmospheric Probes". In: *Space Sci. Rev.* 216.2, 21, p. 21. DOI: 10.1007/s11214-020-00646-1. arXiv: 1907.02901 [astro-ph.EP].

Foreman-Mackey, D. et al. (Mar. 2013). "emcee: The MCMC Hammer". In: *PASP* 125, p. 306. DOI: 10.1086/670067. arXiv: 1202.3665 [astro-ph.IM].

Fowler, Hayley J et al. (2021). "Anthropogenic intensification of short-duration rainfall extremes". In: *Nature Reviews Earth & Environment* 2.2, pp. 107–122.

French, R. G., J. L. Elliot, L. M. French, et al. (Feb. 1988). "Uranian ring orbits from earth-based and Voyager occultation observations". In: *Icarus* 73, pp. 349–378. DOI: 10.1016/0019-1035(88)90104-2.

French, R. G., J. L. Elliot, and S. E. Levine (July 1986). "Structure of the Uranian rings. II - Ring orbits and widths". In: *Icarus* 67, pp. 134–163. DOI: 10.1016/0019-1035(86)90181-8.

French, R. G., P. D. Nicholson, et al. (1991). "Dynamics and structure of the Uranian rings". In: *Uranus*. Ed. by J. T. Bergstralh, E. D. Miner, and M. S. Matthews, pp. 327–409.

Friedson, J. and A. P. Ingersoll (Jan. 1987). "Seasonal meridional energy balance and thermal structure of the atmosphere of Uranus: A radiative-convective-dynamical model". In: *Icarus* 69.1, pp. 135–156. DOI: 10.1016/0019-1035(87)90010-8.

Fulton, Richard A et al. (1998). "The WSR-88D rainfall algorithm". In: *Weather and forecasting* 13.2, pp. 377–395. DOI: 10.1175/1520-0434(1998)013<0377:TWRA>2.0.CO;2.

Gao, Shouting et al. (2005). "Surface rainfall processes as simulated in a cloud-resolving model". In: *Journal of Geophysical Research: Atmospheres* 110.D10.

Ge, Fei et al. (2021). "Future changes in precipitation extremes over Southeast Asia: insights from CMIP6 multi-model ensemble". In: *Environmental Research Letters* 16.2, p. 024013.

Gervais, Melissa et al. (2014). "Representing extremes in a daily gridded precipitation analysis over the United States: Impacts of station density, resolution, and gridding methods". In: *Journal of Climate* 27.14, pp. 5201–5218. DOI: 10.1175/JCLI-D-13-00319.1.

Gibbard, S. G., I. de Pater, and H. B. Hammel (Mar. 2005). "Near-infrared adaptive optics imaging of the satellites and individual rings of Uranus". In: *Icarus* 174, pp. 253–262. DOI: 10.1016/j.icarus.2004.09.008.

Gibbard, S. G., I. de Pater, H. G. Roe, et al. (Dec. 2003). "The altitude of Neptune cloud features from high-spatial-resolution near-infrared spectra". In: *Icarus* 166, pp. 359–374. DOI: 10.1016/j.icarus.2003.07.006.

Gierasch, P. J. et al. (Feb. 2000). "Observation of moist convection in Jupiter's atmosphere". In: *Nature* 403, pp. 628–630. DOI: 10.1038/35001017.

Goody, Richard et al. (1989). "The correlated-k method for radiation calculations in nonhomogeneous atmospheres". In: *Journal of Quantitative Spectroscopy and Radiative Transfer* 42.6, pp. 539–550.

Goudenhoofdt, Edouard, Laurent Delobbe, and Patrick Willems (2017). "Regional frequency analysis of extreme rainfall in Belgium based on radar estimates". In: *Hydrology and Earth System Sciences* 21.10, pp. 5385–5399.

Gresh, D. L. et al. (Mar. 1989). "Voyager radio occultation by Uranus' rings. I - Observational results". In: *Icarus* 78, pp. 131–168. DOI: 10.1016/0019-1035(89)90074-2.

Griffin, M. J. and G. S. Orton (Oct. 1993). "The Near-Millimeter Brightness Temperature Spectra of Uranus and Neptune". In: *Icarus* 105.2, pp. 537–547. DOI: 10.1006/icar.1993.1147.

Gritsun, Andrey and Grant Branstator (2007). "Climate Response Using a Three-Dimensional Operator Based on the Fluctuation–Dissipation Theorem". In: *Journal of the Atmospheric Sciences* 64.7, pp. 2558–2575. DOI: 10.1175/JAS3943.1. URL: https://journals.ametsoc.org/view/journals/atsc/64/7/jas3943.1.xml.

Groisman, Pavel Ya. et al. (1999). "Changes in the Probability of Heavy Precipitation: Important Indicators of Climatic Change". In: *Climatic Change* 42.1, pp. 243–283. DOI: 10.1023/A:1005432803188.

Guerreiro, Selma B et al. (2018). "Detection of continental-scale intensification of hourly rainfall extremes". In: *Nature Climate Change* 8.9, pp. 803–807.

Gueymard, C. A. (Apr. 2004). "The sun's total and spectral irradiance for solar energy applications and solar radiation models". In: *Solar Energy* 76, pp. 423–453. DOI: 10.1016/j.solener.2003.08.039.

Guichard, Françoise and Fleur Couvreux (2017). "A short review of numerical cloud-resolving models". In: *Tellus A: Dynamic Meteorology and Oceanography* 69.1, p. 1373578.

Guillot, T. (Sept. 1995). "Condensation of Methane, Ammonia, and Water and the Inhibition of Convection in Giant Planets". In: *Science* 269, pp. 1697–1699. DOI: 10.1126/science.7569896.

Gulkis, S. and I. de Pater (Oct. 1984). "A review of the millimeter and centimeter observations of Uranus". In: *NASA Conference Publication*. Ed. by J. T. Bergstralh. Vol. 2330. NASA Conference Publication.

Gulkis, S., M. A. Janssen, and E. T. Olsen (Apr. 1978). "Evidence for the depletion of ammonia in the Uranus atmosphere". In: *Icarus* 34.1, pp. 10–19. DOI: 10.1016/0019-1035(78)90120-3.

Hammel, H. B., K. H. Baines, and J. T. Bergstralh (Aug. 1989). "Vertical aerosol structure of Neptune - Constraints from center-to-limb profiles". In: *Icarus* 80, pp. 416–438. DOI: 10.1016/0019-1035(89)90149-8.

Hammel, H. B. and G. W. Lockwood (Oct. 1997). "Atmospheric Structure of Neptune in 1994, 1995, and 1996: HST Imaging at Multiple Wavelengths". In: *Icarus* 129, pp. 466–481. DOI: 10.1006/icar.1997.5764.

— (Jan. 2007). "Long-term atmospheric variability on Uranus and Neptune". In: *Icarus* 186, pp. 291–301. DOI: 10.1016/j.icarus.2006.08.027.

Harris, A. W. (Feb. 1998). "A Thermal Model for Near-Earth Asteroids". In: *Icarus* 131, pp. 291–301. DOI: 10.1006/icar.1997.5865.

Hersant, F., D. Gautier, and J. I. Lunine (June 2004). "Enrichment in volatiles in the giant planets of the Solar System". In: *Planet. Space Sci.* 52.7, pp. 623–641. DOI: 10.1016/j.pss.2003.12.011.

Hersbach, Hans et al. (2020). "The ERA5 global reanalysis". In: *Quarterly Journal of the Royal Meteorological Society* 146.730, pp. 1999–2049.

Hinson, D. P. and J. A. Magalhães (Sept. 1993). "Inertio-Gravity Waves in the Atmosphere of Neptune". In: *Icarus* 105, pp. 142–161. DOI: 10.1006/icar.1993.1115.

Hoffman, James P., Paul G. Steffes, and David R. DeBoer (July 2001). "Laboratory Measurements of the Microwave Opacity of Phosphine: Opacity Formalism and Application to the Atmospheres of the Outer Planets". In: *Icarus* 152.1, pp. 172–184. DOI: 10.1006/icar.2001.6622.

Hofstadter, M. D. (Dec. 1992). "Microwave observations of Uranus". PhD thesis. California Institute of Technology, Pasadena.

Hofstadter, M. D., G. L. Berge, and D. O. Muhleman (Mar. 1990). "Vertical motions in the Uranian atmosphere: an analysis of radio observations". In: *Icarus* 84.1, pp. 261–267. DOI: 10.1016/0019-1035(90)90170-E.

Hofstadter, M. D. and Bryan J. Butler (Sept. 2003). "Seasonal change in the deep atmosphere of Uranus". In: *Icarus* 165.1, pp. 168–180. DOI: 10.1016/S0019-1035(03)00174-X.

Hofstadter, M. D. and D. O. Muhleman (Oct. 1989). "Latitudinal variations of ammonia in the atmosphere of Uranus: An analysis of microwave observations". In: *Icarus* 81.2, pp. 396–412. DOI: 10.1016/0019-1035(89)90060-2.

Hofstadter, M. D., G. Orton, et al. (Sept. 2009). "Infrared and Microwave Observations of Uranus: Implications for Temperature, Composition, Circulation and a Standard Cali-

bration Model for Herschel". In: *AAS/Division for Planetary Sciences Meeting Abstracts #41*. AAS/Division for Planetary Sciences Meeting Abstracts, 28.03, p. 28.03.

Hogg, David W. and Daniel Foreman-Mackey (May 2018). "Data Analysis Recipes: Using Markov Chain Monte Carlo". In: *ApJS* 236.1, 11, p. 11. DOI: 10.3847/1538-4365/aab76e. arXiv: 1710.06068 [astro-ph.IM].

Holsclaw, Tracy et al. (2016). "A Bayesian Hidden Markov Model of Daily Precipitation over South and East Asia". In: *Journal of Hydrometeorology* 17.1, pp. 3–25. DOI: 10.1175/JHM-D-14-0142.1. URL: https://journals.ametsoc.org/view/journals/hydr/17/1/jhm-d-14-0142_1.xml.

Holton, James R (1973). "An introduction to dynamic meteorology". In: *American Journal of Physics* 41.5, pp. 752–754.

Hourdin, Frédéric et al. (2006). "The LMDZ4 general circulation model: climate performance and sensitivity to parametrized physics with emphasis on tropical convection". In: *Climate Dynamics* 27.7, pp. 787–813.

Houze, Robert A. (2004). "Mesoscale convective systems". In: *Reviews of Geophysics* 42.4, RG4003. DOI: 10.1029/2004rg000150.

Hueso, R., I. de Pater, et al. (Oct. 2017). "Neptune long-lived atmospheric features in 2013-2015 from small (28-cm) to large (10-m) telescopes". In: *Icarus* 295, pp. 89–109. DOI: 10.1016/j.icarus.2017.06.009. arXiv: 1709.08854 [astro-ph.EP].

Hueso, R. and A. Sánchez-Lavega (June 2001). "A Three-Dimensional Model of Moist Convection for the Giant Planets: The Jupiter Case". In: *Icarus* 151, pp. 257–274. DOI: 10.1006/icar.2000.6606.

— (Nov. 2004). "A three-dimensional model of moist convection for the giant planets II: Saturn's water and ammonia moist convective storms". In: *Icarus* 172, pp. 255–271. DOI: 10.1016/j.icarus.2004.06.010.

Hueso, R., A. Sánchez-Lavega, and T. Guillot (Oct. 2002). "A model for large-scale convective storms in Jupiter". In: *Journal of Geophysical Research (Planets)* 107, 5075, p. 5075. DOI: 10.1029/2001JE001839.

Hueso, Ricardo and Agustín Sánchez-Lavega (Nov. 2019). "Atmospheric Dynamics and Vertical Structure of Uranus and Neptune's Weather Layers". In: *Space Sci. Rev.* 215.8, 52, p. 52. DOI: 10.1007/s11214-019-0618-6.

Iguchi, Toshio et al. (2009). "Uncertainties in the rain profiling algorithm for the TRMM precipitation radar". In: *Journal of the Meteorological Society of Japan. Ser. II* 87, pp. 1–30. DOI: 10.2151/jmsj.87A.1.

Irwin, P. G. J., L. N. Fletcher, D. Tice, et al. (June 2016). "Time variability of Neptune's horizontal and vertical cloud structure revealed by VLT/SINFONI and Gemini/NIFS from 2009 to 2013". In: *Icarus* 271, pp. 418–437. DOI: 10.1016/j.icarus.2016.01.015.

Irwin, P. G. J., E. Lellouch, et al. (Jan. 2014). "Line-by-line analysis of Neptune's near-IR spectrum observed with Gemini/NIFS and VLT/CRIRES". In: *Icarus* 227, pp. 37–48. DOI: 10.1016/j.icarus.2013.09.003.

Irwin, P. G. J., N. A. Teanby, et al. (Nov. 2011). "Multispectral imaging observations of Neptune's cloud structure with Gemini-North". In: *Icarus* 216, pp. 141–158. DOI: 10.1016/j.icarus.2011.08.005.

Irwin, Patrick G. J., Leigh Fletcher, Nicholas Teanby, et al. (Sept. 2019). "Latitudinal distribution of hydrogen sulphide and methane in the atmospheres of Uranus and Neptune". In: *EPSC-DPS Joint Meeting 2019*. Vol. 2019, EPSC-DPS2019-430, EPSC-DPS2019–430.

Irwin, Patrick G. J., Daniel Toledo, et al. (Apr. 2018). "Detection of hydrogen sulfide above the clouds in Uranus's atmosphere". In: *Nature Astronomy* 2, pp. 420–427. DOI: 10.1038/s41550-018-0432-1.

Jaffe, W. J. et al. (Aug. 1984). "Uranus: Microwave Images". In: *Science* 225.4662, pp. 619–621. DOI: 10.1126/science.225.4662.619.

Jones, Eric, Travis Oliphant, Pearu Peterson, et al. (n.d.). *SciPy: Open source scientific tools for Python*. [Online; accessed 28 August 2018]. URL: http://www.scipy.org/.

Jones, Peter G, A Gladkow, and Annie L Jones (2001). *FloraMap: A computer tool for predicting the distribution of plants and other organisms in the wild [CD-ROM]*. Centro Internacional de Agricultura Tropical (CIAT).

Kallache, Malaak et al. (2011). "Nonstationary probabilistic downscaling of extreme precipitation". In: *Journal of Geophysical Research: Atmospheres* 116.D5.

Karkoschka, E. (Sept. 1994). "Spectrophotometry of the jovian planets and Titan at 300- to 1000-nm wavelength: The methane spectrum". In: *Icarus* 111, pp. 174–192. DOI: 10.1006/icar.1994.1139.

— (Feb. 1997). "Rings and Satellites of Uranus: Colorful and Not So Dark". In: *Icarus* 125, pp. 348–363. DOI: 10.1006/icar.1996.5631.

— (May 1998). "Methane, Ammonia, and Temperature Measurements of the Jovian Planets and Titan from CCD-Spectrophotometry". In: *Icarus* 133, pp. 134–146. DOI: 10.1006/icar.1998.5913.

— (May 2001a). "Comprehensive Photometry of the Rings and 16 Satellites of Uranus with the Hubble Space Telescope". In: *Icarus* 151, pp. 51–68. DOI: 10.1006/icar.2001.6596.

— (May 2001b). "Comprehensive Photometry of the Rings and 16 Satellites of Uranus with the Hubble Space Telescope". In: *Icarus* 151, pp. 51–68. DOI: 10.1006/icar.2001.6596.

— (May 2001c). "Photometric Modeling of the Epsilon Ring of Uranus and Its Spacing of Particles". In: *Icarus* 151, pp. 78–83. DOI: 10.1006/icar.2001.6598.

— (May 2001d). "Voyager's Eleventh Discovery of a Satellite of Uranus and Photometry and the First Size Measurements of Nine Satellites". In: *Icarus* 151, pp. 69–77. DOI: 10.1006/icar.2001.6597.

— (Apr. 2003). "Sizes, shapes, and albedos of the inner satellites of Neptune". In: *Icarus* 162, pp. 400–407. DOI: 10.1016/S0019-1035(03)00002-2.

— (Oct. 2011). "Neptune's cloud and haze variations 1994-2008 from 500 HST-WFPC2 images". In: *Icarus* 215, pp. 759–773. DOI: 10.1016/j.icarus.2011.06.010.

Karkoschka, E. and M. Tomasko (July 2009). "The haze and methane distributions on Uranus from HST-STIS spectroscopy". In: *Icarus* 202, pp. 287–309. DOI: 10.1016/j.icarus.2009.02.010.

Karkoschka, E. and M. G. Tomasko (Jan. 2011). "The haze and methane distributions on Neptune from HST-STIS spectroscopy". In: *Icarus* 211, pp. 780–797. DOI: 10.1016/j.icarus.2010.08.013.

Kaspi, Yohai et al. (June 2020). "Comparison of the Deep Atmospheric Dynamics of Jupiter and Saturn in Light of the Juno and Cassini Gravity Measurements". In: *Space Sci. Rev.* 216.5, 84, p. 84. DOI: 10.1007/s11214-020-00705-7. arXiv: 1908.09613 [astro-ph.EP].

Khain, A et al. (2000). "Notes on the state-of-the-art numerical modeling of cloud microphysics". In: *Atmospheric Research* 55.3-4, pp. 159–224.

Kirstetter, Pierre-Emmanuel et al. (2010). "Toward an error model for radar quantitative precipitation estimation in the Cévennes–Vivarais region, France". In: *Journal of Hydrology* 394.1-2, pp. 28–41. DOI: 10.1016/j.jhydrol.2010.01.009.

Klein, M. J. and M. D. Hofstadter (Sept. 2006). "Long-term variations in the microwave brightness temperature of the Uranus atmosphere". In: *Icarus* 184, pp. 170–180. DOI: 10.1016/j.icarus.2006.04.012.

Knight, David B. and Robert E. Davis (2009). "Contribution of tropical cyclones to extreme rainfall events in the southeastern United States". In: *Journal of Geophysical Research* 114.D23, p. D23102. DOI: 10.1029/2009jd012511.

Kursinski, Ana L and Steven L Mullen (2008). "Spatiotemporal variability of hourly precipitation over the eastern contiguous United States from stage IV multisensor analyses". In: *Journal of Hydrometeorology* 9.1, pp. 3–21. DOI: 10.1175/2007JHM856.1.

Lagage, PO et al. (2004). "Successful Commissioning OF". In: *The Messenger* 117, p. 12.

Lagerros, J. S. V. (Apr. 1998). "Thermal physics of asteroids. IV. Thermal infrared beaming". In: *A&A* 332, pp. 1123–1132.

Langhans, Wolfgang, Kyongmin Yeo, and David M Romps (2015). "Lagrangian investigation of the precipitation efficiency of convective clouds". In: *Journal of the Atmospheric Sciences* 72.3, pp. 1045–1062.

Lau, KM and HT Wu (2003). "Warm rain processes over tropical oceans and climate implications". In: *Geophysical Research Letters* 30.24.

LeBeau, R. P. and T. E. Dowling (Apr. 1998). "EPIC Simulations of Time-Dependent, Three-Dimensional Vortices with Application to Neptune's Great Dark SPOT". In: *Icarus* 132, pp. 239–265. DOI: 10.1006/icar.1998.5918.

Lebel, T. et al. (1987). "On the accuracy of areal rainfall estimation: A case study". In: *Water Resources Research* 23.11, pp. 2123–2134. DOI: 10.1029/wr023i011p02123.

Lebofsky, L. A. and J. R. Spencer (1989). "Radiometry and a thermal modeling of asteroids". In: *Asteroids II*. Ed. by R. P. Binzel, T. Gehrels, and M. S. Matthews, pp. 128–147.

Lebofsky, L. A., M. V. Sykes, et al. (Nov. 1986). "A refined 'standard' thermal model for asteroids based on observations of 1 Ceres and 2 Pallas". In: *Icarus* 68, pp. 239–251. DOI: 10.1016/0019-1035(86)90021-7.

Legarreta, J. et al. (Feb. 2016). "A large active wave trapped in Jupiter's equator". In: *A&A* 586, A154, A154. DOI: 10.1051/0004-6361/201526197.

Leith, C. E. (1975). "Climate Response and Fluctuation Dissipation". In: *Journal of Atmospheric Sciences* 32.10, pp. 2022–2026. DOI: 10.1175/1520-0469(1975)032<2022:CRAFD>2.0.CO;2. URL: https://journals.ametsoc.org/view/journals/atsc/32/10/1520-0469_1975_032_2022_crafd_2_0_co_2.xml.

Li, C. and A. P. Ingersoll (May 2015). "Moist convection in hydrogen atmospheres and the frequency of Saturn's giant storms". In: *Nature Geoscience* 8, pp. 398–403. DOI: 10.1038/ngeo2405.

Li, Cheng, Andrew Ingersoll, et al. (June 2017). "The distribution of ammonia on Jupiter from a preliminary inversion of Juno microwave radiometer data". In: *Geophys. Res. Lett.* 44.11, pp. 5317–5325. DOI: 10.1002/2017GL073159.

Li, Cheng, Tianhao Le, et al. (Sept. 2018). "A high-performance atmospheric radiation package: With applications to the radiative energy budgets of giant planets". In: *J. Quant. Spec. Radiat. Transf.* 217, pp. 353–362. DOI: 10.1016/j.jqsrt.2018.06.002. arXiv: 1806.02573 [astro-ph.EP].

Li, Ryan L, Joshua HP Studholme, et al. (2022). "Precipitation efficiency constraint on climate change". In: *Nature Climate Change* 12.7, pp. 642–648.

Limaye, S. S. and L. A. Sromovsky (Oct. 1991). "Winds of Neptune - Voyager observations of cloud motions". In: *J. Geophys. Res.* 96, p. 18. DOI: 10.1029/91JA01701.

Lin, Y. (2011). *GCIP/EOP Surface: Precipitation NCEP/EMC 4KM Gridded Data (GRIB) Stage IV Data. Version 1.0*. DOI: 10.5065/D6PG1QDD. URL: https://data.eol.ucar.edu/dataset/21.093.

Lin, Ying and Kenneth E. Mitchell (Jan. 2005). "The NCEP Stage II/IV hourly precipitation analyses: development and applications". In: *Proceedings of the 19th Conference on Hydrology*. Vol. 1.2. URL: https://ams.confex.com/ams/Annual2005/techprogram/paper_83847.htm.

Lindal, G. F. (Mar. 1992). "The atmosphere of Neptune - an analysis of radio occultation data acquired with Voyager 2". In: *AJ* 103, pp. 967–982. DOI: 10.1086/116119.

Lindal, G. F. et al. (Dec. 1987). "The atmosphere of Uranus: Results of radio occultation measurements with Voyager 2". In: *J. Geophys. Res.* 92.A13, pp. 14987–15001. DOI: 10.1029/JA092iA13p14987.

Livneh, Ben, Theodore J Bohn, et al. (2015). "A spatially comprehensive, hydrometeorological data set for Mexico, the US, and Southern Canada 1950–2013". In: *Scientific data* 2.1, pp. 1–12.

Livneh, Ben, Eric A Rosenberg, et al. (2013). "A long-term hydrologically based dataset of land surface fluxes and states for the conterminous United States: Update and extensions". In: *Journal of Climate* 26.23, pp. 9384–9392. DOI: 10.1175/JCLI-D-12-00508.1.

Lopez, Philippe (2011). "Direct 4D-Var assimilation of NCEP stage IV radar and gauge precipitation data at ECMWF". In: *Monthly Weather Review* 139.7, pp. 2098–2116.

Lovejoy, S (1982). "Area-perimeter relation for rain and cloud areas". In: *Science* 216.4542, pp. 185–187. DOI: 10.1126/science.216.4542.185.

Lovejoy, S and Benoit B Mandelbrot (1985). "Fractal properties of rain, and a fractal model". In: *Tellus A* 37.3, pp. 209–232. DOI: 10.3402/tellusa.v37i3.11668.

Luo, P et al. (2018). "Impact assessment of rainfall scenarios and land-use change on hydrologic response using synthetic Area IDF curves". In: *Journal of Flood Risk Management* 11, S84–S97.

Luszcz-Cook, S. H., K. de Kleer, et al. (Sept. 2016). "Retrieving Neptune's aerosol properties from Keck OSIRIS observations. I. Dark regions". In: *Icarus* 276, pp. 52–87. DOI: 10.1016/j.icarus.2016.04.032. arXiv: 1706.05049 [astro-ph.EP].

Luszcz-Cook, S. H. and I. de Pater (Jan. 2013). "Constraining the origins of Neptune's carbon monoxide abundance with CARMA millimeter-wave observations". In: *Icarus* 222, pp. 379–400. DOI: 10.1016/j.icarus.2012.11.002. arXiv: 1301.1990 [astro-ph.EP].

Maddox, R. A., C. F. Chappell, and L. R. Hoxit (1979). "Synoptic and Meso-α Scale Aspects of Flash Flood Events". In: *Bulletin of the American Meteorological Society* 60.2, pp. 115–123. DOI: 10.1175/1520-0477-60.2.115.

Marshall, John and R Alan Plumb (1989). *Atmosphere, ocean and climate dynamics: an introductory text*. Academic Press.

Martin, S. C., I. de Pater, and P. Marcus (Jan. 2012). "Neptune's zonal winds from near-IR Keck adaptive optics imaging in August 2001". In: *Ap&SS* 337, pp. 65–78. DOI: 10.1007/s10509-011-0847-y.

Matsuno, T. (1966). "Quasi-geostrophic Motions in the Equatorial Area". In: *J. Met. Soc. Japan* 44, pp. 25–43.

Max, C. E. et al. (Jan. 2003). "Cloud Structures on Neptune Observed with Keck Telescope Adaptive Optics". In: *AJ* 125, pp. 364–375. DOI: 10.1086/344943.

McCartney, E. J. (1976). *Optics of the atmosphere: Scattering by molecules and particles*.

McGraw, Daniel et al. (2019). "Precipitation frequency analyses based on radar estimates: An evaluation over the contiguous United States". In: *Journal of Hydrology* 573, pp. 299–310. DOI: 10.1016/j.jhydrol.2019.03.032.

Mehran, Ali, Amir AghaKouchak, and Thomas J Phillips (2014). "Evaluation of CMIP5 continental precipitation simulations relative to satellite-based gauge-adjusted observations". In: *Journal of Geophysical Research: Atmospheres* 119.4, pp. 1695–1707. DOI: 10.1002/2013JD021152.

Mendikoa, I. et al. (Mar. 2016). "PlanetCam UPV/EHU: A Two-channel Lucky Imaging Camera for Solar System Studies in the Spectral Range 0.38-1.7 μm". In: *PASP* 128.3, p. 035002. DOI: 10.1088/1538-3873/128/961/035002.

Menne, Matthew J et al. (2012). "An overview of the global historical climatology network-daily database". In: *Journal of Atmospheric and Oceanic Technology* 29.7, pp. 897–910. DOI: 10.1175/JTECH-D-11-00103.1.

Miniussi, Arianna, Gabriele Villarini, and Marco Marani (2020). "Analyses Through the Metastatistical Extreme Value Distribution Identify Contributions of Tropical Cyclones to Rainfall Extremes in the Eastern United States". In: *Geophysical Research Letters* 47.7, e2020GL087238. DOI: 10.1029/2020gl087238.

Minnis, Patrick, Louis Nguyen, et al. (2008). "Near-real time cloud retrievals from operational and research meteorological satellites". In: *Remote Sensing of Clouds and the Atmosphere XIII*. Vol. 7107. SPIE, pp. 19–26.

Minnis, Patrick, Qing Z Trepte, et al. (2008). "Cloud detection in nonpolar regions for CERES using TRMM VIRS and Terra and Aqua MODIS data". In: *IEEE Transactions on Geoscience and Remote Sensing* 46.11, pp. 3857–3884.

Mirhosseini, Golbahar, Puneet Srivastava, and Lydia Stefanova (2013). "The impact of climate change on rainfall Intensity–Duration–Frequency (IDF) curves in Alabama". In: *Regional Environmental Change* 13.1, pp. 25–33.

Molter, Edward M, William D Collins, and Mark D Risser (2021). "Quantitative precipitation estimation of extremes in conus with radar data". In: *Geophysical Research Letters* 48.16, e2021GL094697.

Morcrette, JJ et al. (2008). "Impact of a new radiation package, McRad, in the ECMWF Integrated Forecasting System". In: *Monthly weather review* 136.12, pp. 4773–4798.

Moreno, Raphael, A. Marten, and E. Lellouch (Sept. 2009). "Search for PH3 in the Atmospheres of Uranus and Neptune at Millimeter Wavelength". In: *AAS/Division for Planetary Sciences Meeting Abstracts #41*. AAS/Division for Planetary Sciences Meeting Abstracts, 28.02, p. 28.02.

Moses, Julianne I., Mark Allen, and Yuk L. Yung (Oct. 1992). "Hydrocarbon nucleation and aerosol formation in Neptune's atmosphere". In: *Icarus* 99.2, pp. 318–346. DOI: 10.1016/0019-1035(92)90149-2.

Mousis, O. et al. (June 2018). "Scientific rationale for Uranus and Neptune in situ explorations". In: *Planet. Space Sci.* 155, pp. 12–40. DOI: 10.1016/j.pss.2017.10.005. arXiv: 1708.00235 [astro-ph.EP].

Muhleman, Duane O. and Glenn L. Berge (Aug. 1991). "Observations of Mars, Uranus, Neptune, Io, Europa, Ganymede, and Callisto at a wavelength of 2.66 mm". In: *Icarus* 92.2, pp. 263–272. DOI: 10.1016/0019-1035(91)90050-4.

National Academies of Sciences, Engineering, Medicine, et al. (2022). "Origins, Worlds, and Life: A Decadal Strategy for Planetary Science and Astrobiology 2023-2032". In.

Neggers, RAJ (2015). "Attributing the behavior of low-level clouds in large-scale models to subgrid-scale parameterizations". In: *Journal of Advances in Modeling Earth Systems* 7.4, pp. 2029–2043.

Nelson, Brian R. et al. (2016). "Assessment and Implications of NCEP Stage IV Quantitative Precipitation Estimates for Product Intercomparisons". In: *Weather and Forecasting* 31.2, pp. 371–394. DOI: 10.1175/WAF-D-14-00112.1.

Nicholson, P. D. et al. (Feb. 2018). "The Rings of Uranus". In: *Planetary Ring Systems. Properties, Structure, and Evolution*. Ed. by M. S. Tiscareno and C. D. Murray, pp. 93–111. DOI: 10.1017/9781316286791.004.

Nijssen, Bart and Dennis P Lettenmaier (2004). "Effect of precipitation sampling error on simulated hydrological fluxes and states: Anticipating the Global Precipitation Measurement satellites". In: *Journal of geophysical research: atmospheres* 109.D2.

NOAA (1998). *Automated surface observing system users guide*. ASOS Program Office, National Weather Service, National Oceanographic and Atmospheric Administrations. Silver Spring, MD. URL: https://www.weather.gov/media/asos/aum-toc.pdf.

NOAA (2006). *Federal Meteorological Handbook No. 11, Doppler Radar Meteorological Observations, Part C, WSR-88D Products and Algorithms*. FCM-H11C-2006. Office of the Federal Coordinator for Meteorological Services and Supporting Research, NOAA. Washington, DC. URL: https://www.ofcm.gov/publications/fmh/FMH11/FMH-11-PartC-April2006.pdf.

O'Gorman, Paul A (2015). "Precipitation extremes under climate change". In: *Current climate change reports* 1.2, pp. 49–59. DOI: 10.1007/s40641-015-0009-3.

Orton, G. S., Leigh N. Fletcher, et al. (Nov. 2015). "Thermal imaging of Uranus: Upper-tropospheric temperatures one season after Voyager". In: *Icarus* 260, pp. 94–102. DOI: 10.1016/j.icarus.2015.07.004.

Orton, G. S., M. J. Griffin, et al. (Aug. 1986). "Submillimeter and millimeter observations of Uranus and Neptune". In: *Icarus* 67.2, pp. 289–304. DOI: 10.1016/0019-1035(86)90110-7.

Orton, G. S. and C. D. Kaminski (Jan. 1989). "An exploratory 5-μm spectrum of Uranus". In: *Icarus* 77.1, pp. 109–117. DOI: 10.1016/0019-1035(89)90010-9.

Overeem, Aart, TA Buishand, and Iwan Holleman (2009). "Extreme rainfall analysis and estimation of depth-duration-frequency curves using weather radar". In: *Water resources research* 45.10.

Owen, T. and T. Encrenaz (Oct. 2006). "Compositional constraints on giant planet formation". In: *Planet. Space Sci.* 54, pp. 1188–1196. DOI: 10.1016/j.pss.2006.05.030.

Paciorek, Christopher J, Dáithí A Stone, and Michael F Wehner (2018). "Quantifying statistical uncertainty in the attribution of human influence on severe weather". In: *Weather and climate extremes* 20, pp. 69–80. DOI: 10.1016/j.wace.2018.01.002.

Palmer, T. N. (2019). "Stochastic weather and climate models". In: *Nature Reviews Physics* 1.7, pp. 463–471. DOI: 10.1038/s42254-019-0062-2. URL: https://doi.org/10.1038/s42254-019-0062-2.

Panziera, Luca et al. (2016). "A radar-based regional extreme rainfall analysis to derive the thresholds for a novel automatic alert system in Switzerland". In: *Hydrology and earth system sciences* 20.6, pp. 2317–2332.

Parker, Matthew D. and Richard H. Johnson (Oct. 2000). "Organizational Modes of Midlatitude Mesoscale Convective Systems". In: *Monthly Weather Review* 128.10, pp. 3413–3436. DOI: 10.1175/1520-0493(2001)129<3413:omommc>2.0.co;2.

Parra, Juan L, Catherine C Graham, and Juan F Freile (2004). "Evaluating alternative data sets for ecological niche models of birds in the Andes". In: *Ecography* 27.3, pp. 350–360.

Pauluis, Olivier and Isaac M Held (2002). "Entropy budget of an atmosphere in radiative–convective equilibrium. Part I: Maximum work and frictional dissipation". In: *Journal of the Atmospheric sciences* 59.2, pp. 125–139.

Pearl, J. C. et al. (Mar. 1990). "The albedo, effective temperature, and energy balance of Uranus, as determined from Voyager IRIS data". In: *Icarus* 84.1, pp. 12–28. DOI: 10.1016/0019-1035(90)90155-3.

Peel, M. C., B. L. Finlayson, and T. A. McMahon (Oct. 2007). "Updated world map of the Köppen-Geiger climate classification". In: *Hydrology and Earth System Sciences* 11.5,

pp. 1633–1644. DOI: 10.5194/hess-11-1633-2007. URL: https://doi.org/10.5194/hess-11-1633-2007.

Pepin, N. C. et al. (2005). "A Comparison of SNOTEL and GHCN/CRU Surface Temperatures with Free-Air Temperatures at High Elevations in the Western United States: Data Compatibility and Trends". In: *Journal of Climate* 18.12, pp. 1967–1985. DOI: 10.1175/JCLI3375.1.

Perley, R. A. and B. J. Butler (Feb. 2013). "An Accurate Flux Density Scale from 1 to 50 GHz". In: *ApJS* 204.2, 19, p. 19. DOI: 10.1088/0067-0049/204/2/19. arXiv: 1211.1300 [astro-ph.IM].

— (May 2017). "An Accurate Flux Density Scale from 50 MHz to 50 GHz". In: *ApJS* 230.1, 7, p. 7. DOI: 10.3847/1538-4365/aa6df9. arXiv: 1609.05940 [astro-ph.IM].

Pierrehumbert, R. T. (Dec. 2010). *Principles of Planetary Climate*.

Prat, O. P. and B. R. Nelson (2015). "Evaluation of precipitation estimates over CONUS derived from satellite, radar, and rain gauge data sets at daily to annual scales (2002-2012)". In: *Hydrology and Earth System Sciences* 19.4, pp. 2037–2056. DOI: 10.5194/hess-19-2037-2015.

Ralph, F Martin, Paul J Neiman, and Gary A Wick (2004). "Satellite and CALJET aircraft observations of atmospheric rivers over the eastern North Pacific Ocean during the winter of 1997/98". In: *Monthly Weather Review* 132.7, pp. 1721–1745.

Rhines, Peter B (1975). "Waves and turbulence on a beta-plane". In: *Journal of Fluid Mechanics* 69.3, pp. 417–443.

Risser, Mark D. et al. (2019). "A probabilistic gridded product for daily precipitation extremes over the United States". In: *Climate Dynamics* 53.5-6, pp. 2517–2538. DOI: 10.1007/s00382-019-04636-0. arXiv: 1807.04177 [stat.AP].

Rix, H.-W. et al. (Aug. 2016). "Constructing Polynomial Spectral Models for Stars". In: *ApJ* 826, L25, p. L25. DOI: 10.3847/2041-8205/826/2/L25. arXiv: 1603.06574 [astro-ph.SR].

Roddier, F. et al. (Aug. 1997). "First ground-based adaptive optics observations of Neptune and Proteus". In: *Planet. Space Sci.* 45, pp. 1031–1036. DOI: 10.1016/S0032-0633(97)00026-3.

Roe, H. G. et al. (Sept. 2001). "Near-Infrared Observations of Neptune's Tropospheric Cloud Layer with the Lick Observatory Adaptive Optics System". In: *AJ* 122, pp. 1636–1643. DOI: 10.1086/322125.

Roh, Woosub, Masaki Satoh, and Cathy Hohenegger (2021). "Intercomparison of cloud properties in DYAMOND simulations over the Atlantic Ocean". In: *Journal of the Meteorological Society of Japan. Ser. II*.

Roman, Michael T. et al. (Feb. 2020). "Uranus in Northern Midspring: Persistent Atmospheric Temperatures and Circulations Inferred from Thermal Imaging". In: *AJ* 159.2, 45, p. 45. DOI: 10.3847/1538-3881/ab5dc7. arXiv: 1911.12830 [astro-ph.EP].

Romani, Paul Nichols (Jan. 1986). "Clouds and Methane Photochemical Hazes on the Outer Planets." PhD thesis. THE UNIVERSITY OF MICHIGAN.

Rosenzweig, Cynthia et al. (2002). "Increased crop damage in the US from excess precipitation under climate change". In: *Global Environmental Change* 12.3, pp. 197–202. DOI: 10.1016/S0959-3780(02)00008-0.

Rybicki, George B and Alan P Lightman (1991). *Radiative processes in astrophysics*. John Wiley & Sons.

Sanchez-Lavega, A. and E. Battaner (Oct. 1987). "The nature of Saturn's atmospheric Great White Spots". In: *A&A* 185, pp. 315–326.

Sánchez-Lavega, A. (2011). "An Introduction to Planetary Atmospheres". In: *Boca Raton: CRC Press*.

Sánchez-Lavega, A., T. del Río-Gaztelurrutia, et al. (July 2011). "Deep winds beneath Saturn's upper clouds from a seasonal long-lived planetary-scale storm". In: *Nature* 475, pp. 71–74. DOI: 10.1038/nature10203.

Sánchez-Lavega, A., G. S. Orton, et al. (Feb. 2008). "Depth of a strong jovian jet from a planetary-scale disturbance driven by storms". In: *Nature* 451, p. 1022. DOI: 10.1038/nature06807.

Sánchez-Lavega, A., S. Pérez-Hoyos, and R. Hueso (June 2004). "Clouds in planetary atmospheres: A useful application of the Clausius-Clapeyron equation". In: *American Journal of Physics* 72, pp. 767–774. DOI: 10.1119/1.1645279.

Sánchez-Lavega, A., J. H. Rogers, et al. (May 2017). "A planetary-scale disturbance in the most intense Jovian atmospheric jet from JunoCam and ground-based observations". In: *Geophys. Res. Lett.* 44, pp. 4679–4686. DOI: 10.1002/2017GL073421.

Santos Gutiérrez, Manuel and Valerio Lucarini (2020). "Response and Sensitivity Using Markov Chains". In: *Journal of Statistical Physics* 179.5, pp. 1572–1593. DOI: 10.1007/s10955-020-02504-4. URL: https://doi.org/10.1007/s10955-020-02504-4.

Satoh, Masaki et al. (2019). "Global cloud-resolving models". In: *Current Climate Change Reports* 5.3, pp. 172–184.

Sault, R. J., C. Engel, and I. de Pater (Apr. 2004). "Longitude-resolved imaging of Jupiter at λ=2 cm". In: *Icarus* 168, pp. 336–343. DOI: 10.1016/j.icarus.2003.11.014. eprint: astro-ph/0612769.

Sault, R. J., P. J. Teuben, and M. C. H. Wright (1995). "A Retrospective View of MIRIAD". In: *Astronomical Data Analysis Software and Systems IV*. Ed. by R. A. Shaw, H. E. Payne, and J. J. E. Hayes. Vol. 77. Astronomical Society of the Pacific Conference Series, p. 433. eprint: astro-ph/0612759.

Schaake, J, A Henkel, and S Cong (2004). "Application of PRISM climatologies for hydrologic modeling and forecasting in the western US". In: *Preprints, 18th Conf. on Hydrology, Seattle, WA*. Vol. 5. Amer. Meteor. Soc. URL: https://ams.confex.com/ams/84Annual/techprogram/paper_72159.htm.

Schär, Christoph et al. (2016). "Percentile indices for assessing changes in heavy precipitation events". In: *Climatic Change* 137.1-2, pp. 201–216. DOI: 10.1007/s10584-016-1669-2.

Scharffenberg, William A and Matthew J Fleming (2006). *Hydrologic modeling system HEC-HMS: user's manual*. US Army Corps of Engineers, Hydrologic Engineering Center.

Schumacher, Russ S. and Richard H. Johnson (Feb. 2006). "Characteristics of U.S. Extreme Rain Events during 1999–2003". In: *Weather and Forecasting* 21.1, pp. 69–85. DOI: 10.1175/waf900.1.

Schumann, Andreas H (2011). *Flood risk assessment and management: How to specify hydrological loads, their consequences and uncertainties*. Springer Science & Business Media. ISBN: 978-90-481-9917-4. DOI: 10.1007/978-90-481-9917-4.

Seo, Bong-Chul, Witold F Krajewski, et al. (2018). "Comprehensive evaluation of the IFloodS Radar rainfall products for hydrologic applications". In: *Journal of Hydrometeorology* 19.11, pp. 1793–1813. DOI: 10.1175/JHM-D-18-0080.1.

Seo, Dong-Jun and JP Breidenbach (2002). "Real-time correction of spatially nonuniform bias in radar rainfall data using rain gauge measurements". In: *Journal of Hydrometeorology* 3.2, pp. 93–111.

Service, M. et al. (Sept. 2016). "A New Distortion Solution for NIRC2 on the Keck II Telescope". In: *PASP* 128.9, p. 095004. DOI: 10.1088/1538-3873/128/967/095004.

Shepherd, J. Marshall, Andrew Grundstein, and Thomas L. Mote (2007). "Quantifying the contribution of tropical cyclones to extreme rainfall along the coastal southeastern United States". In: *Geophysical Research Letters* 34.23, p. L23810. DOI: 10.1029/2007gl031694.

Sheridan, Peter et al. (2010). "A simple height-based correction for temperature downscaling in complex terrain". In: *Meteorological Applications* 17.3, pp. 329–339. DOI: 10.1002/met.177.

Showalter, M. R. and J. J. Lissauer (Feb. 2006). "The Second Ring-Moon System of Uranus: Discovery and Dynamics". In: *Science* 311, pp. 973–977. DOI: 10.1126/science.1122882.

Simon, A. A., L. Li, and D. C. Reuter (Apr. 2015). "Small-scale waves on Jupiter: A reanalysis of New Horizons, Voyager, and Galileo data". In: *Geophys. Res. Lett.* 42, pp. 2612–2618. DOI: 10.1002/2015GL063433.

Simon, A. A., M. H. Wong, and G. S. Orton (Oct. 2015). "First Results from the Hubble OPAL Program: Jupiter in 2015". In: *ApJ* 812, 55, p. 55. DOI: 10.1088/0004-637X/812/1/55.

Smith, B. A., L. A. Soderblom, D. Banfield, et al. (Dec. 1989). "Voyager 2 at Neptune: Imaging Science Results". In: *Science* 246, pp. 1422–1449. DOI: 10.1126/science.246.4936.1422.

Smith, B. A., L. A. Soderblom, R. Beebe, et al. (July 1986). "Voyager 2 in the Uranian system - Imaging science results". In: *Science* 233, pp. 43–64. DOI: 10.1126/science.233.4759.43.

Song, Fengfei et al. (2022). "Trends in surface equivalent potential temperature: A more comprehensive metric for global warming and weather extremes". In: *Proceedings of the National Academy of Sciences* 119.6, e2117832119.

Sparks, Nathan J et al. (2018). "IMAGE: a multivariate multi-site stochastic weather generator for European weather and climate". In: *Stochastic environmental research and risk assessment* 32.3, pp. 771–784.

Spencer, J. R., L. A. Lebofsky, and M. V. Sykes (Apr. 1989). "Systematic biases in radiometric diameter determinations". In: *Icarus* 78, pp. 337–354. DOI: 10.1016/0019-1035(89)90182-6.

Spies, Ryan R, Thomas M Over, and Terry W Ortel (2018). *Comparison of NEXRAD multisensor precipitation estimates to rain gauge observations in and near DuPage County, Illinois, 2002–12*. Open-File Report 2018–1061. 30 p., doi:10.3133/ofr20181061. Reston, Virginia 2018: U.S. Geological Survey.

Sromovsky, L. A. (Jan. 2005a). "Accurate and approximate calculations of Raman scattering in the atmosphere of Neptune". In: *Icarus* 173, pp. 254–283. DOI: 10.1016/j.icarus.2004.08.008. arXiv: 1504.02726 [astro-ph.EP].

— (Jan. 2005b). "Effects of Rayleigh-scattering polarization on reflected intensity: a fast and accurate approximation method for atmospheres with aerosols". In: *Icarus* 173, pp. 284–294. DOI: 10.1016/j.icarus.2004.07.016.

Sromovsky, L. A., I. de Pater, et al. (Sept. 2015). "High S/N Keck and Gemini AO imaging of Uranus during 2012-2014: New cloud patterns, increasing activity, and improved wind measurements". In: *Icarus* 258, pp. 192–223. DOI: 10.1016/j.icarus.2015.05.029. arXiv: 1512.05009 [astro-ph.EP].

Sromovsky, L. A. and P. M. Fry (Dec. 2005). "Dynamics of cloud features on Uranus". In: *Icarus* 179, pp. 459–484. DOI: 10.1016/j.icarus.2005.07.022.

Sromovsky, L. A., P. M. Fry, and K. H. Baines (Mar. 2002). "The Unusual Dynamics of Northern Dark Spots on Neptune". In: *Icarus* 156, pp. 16–36. DOI: 10.1006/icar.2001.6761.

Sromovsky, L. A., P. M. Fry, K. H. Baines, and T. E. Dowling (Feb. 2001). "Coordinated 1996 HST and IRTF Imaging of Neptune and Triton. II. Implications of Disk-Integrated Photometry". In: *Icarus* 149, pp. 435–458. DOI: 10.1006/icar.2000.6563.

Sromovsky, L. A., P. M. Fry, T. E. Dowling, et al. (Feb. 2001a). "Coordinated 1996 HST and IRTF Imaging of Neptune and Triton. III. Neptune's Atmospheric Circulation and Cloud Structure". In: *Icarus* 149, pp. 459–488. DOI: 10.1006/icar.2000.6564.

— (Apr. 2001b). "Neptune's Atmospheric Circulation and Cloud Morphology: Changes Revealed by 1998 HST Imaging". In: *Icarus* 150, pp. 244–260. DOI: 10.1006/icar.2000.6574.

Sromovsky, L. A., P. M. Fry, H. B. Hammel, I. de Pater, and K. A. Rages (Aug. 2012). "Post-equinox dynamics and polar cloud structure on Uranus". In: *Icarus* 220.2, pp. 694–712. DOI: 10.1016/j.icarus.2012.05.029. arXiv: 1503.00592 [astro-ph.EP].

Sromovsky, L. A., P. M. Fry, H. B. Hammel, I. de Pater, K. A. Rages, and M. R. Showalter (Dec. 2007). "Dynamics, evolution, and structure of Uranus' brightest cloud feature". In: *Icarus* 192.2, pp. 558–575. DOI: 10.1016/j.icarus.2007.05.015.

Sromovsky, L. A., H. B. Hammel, et al. (July 2012). "Episodic bright and dark spots on Uranus". In: *Icarus* 220, pp. 6–22. DOI: 10.1016/j.icarus.2012.04.009.

Sromovsky, L. A., E. Karkoschka, P. M. Fry, I. de Pater, et al. (Jan. 2019). "The methane distribution and polar brightening on Uranus based on HST/STIS, Keck/NIRC2, and

IRTF/SpeX observations through 2015". In: *Icarus* 317, pp. 266–306. DOI: 10.1016/j.icarus.2018.06.026. arXiv: 1806.01154 [astro-ph.EP].

Sromovsky, L. A., E. Karkoschka, P. M. Fry, H. B. Hammel, et al. (Aug. 2014). "Methane depletion in both polar regions of Uranus inferred from HST/STIS and Keck/NIRC2 observations". In: *Icarus* 238, pp. 137–155. DOI: 10.1016/j.icarus.2014.05.016. arXiv: 1502.06480 [astro-ph.EP].

Sromovsky, L. A., S. S. Limaye, and P. M. Fry (Sept. 1993). "Dynamics of Neptune's Major Cloud Features". In: *Icarus* 105, pp. 110–141. DOI: 10.1006/icar.1993.1114.

— (Nov. 1995). "Clouds and circulation on Neptune: Implications of 1991 HST observations." In: *Icarus* 118, pp. 25–38. DOI: 10.1006/icar.1995.1175.

Stamnes, K. et al. (June 1988). "Numerically stable algorithm for discrete-ordinate-method radiative transfer in multiple scattering and emitting layered media". In: *Appl. Opt.* 27, pp. 2502–2509. DOI: 10.1364/AO.27.002502.

Steinschneider, Scott et al. (2019). "A weather-regime-based stochastic weather generator for climate vulnerability assessments of water systems in the western United States". In: *Water Resources Research* 55.8, pp. 6923–6945.

Stephens, Graeme L et al. (2010). "Dreary state of precipitation in global models". In: *Journal of Geophysical Research: Atmospheres* 115.D24.

Stevens, Bjorn et al. (2019). "DYAMOND: the DYnamics of the Atmospheric general circulation Modeled On Non-hydrostatic Domains". In: *Progress in Earth and Planetary Science* 6.1, pp. 1–17.

Stevenson, Stephanie N. and Russ S. Schumacher (2014). "A 10-Year Survey of Extreme Rainfall Events in the Central and Eastern United States Using Gridded Multisensor Precipitation Analyses". In: *Monthly Weather Review* 142.9, pp. 3147–3162. DOI: 10.1175/mwr-d-13-00345.1.

Stoker, C. R. (July 1986). "Moist convection - A mechanism for producing the vertical structure of the Jovian equatorial plumes". In: *Icarus* 67, pp. 106–125. DOI: 10.1016/0019-1035(86)90179-X.

Stoker, C. R. and O. B. Toon (Aug. 1989). "Moist convection on Neptune". In: *Geophys. Res. Lett.* 16, pp. 929–932. DOI: 10.1029/GL016i008p00929.

Su, Chun-Yian, Wei-Ting Chen, Chien-Ming Wu, et al. (2022). "Object-Based Evaluation of Tropical Precipitation Systems in DYAMOND Simulations over the Maritime Continent". In: *Journal of the Meteorological Society of Japan. Ser. II.*

Sui, Chung-Hsiung, Xiaofan Li, and Ming-Jen Yang (2007). "On the definition of precipitation efficiency". In: *Journal of the Atmospheric Sciences* 64.12, pp. 4506–4513.

Sui, Chung-Hsiung, Masaki Satoh, and Kentaroh Suzuki (2020). "Precipitation efficiency and its role in cloud-radiative feedbacks to climate variability". In: *Journal of the Meteorological Society of Japan. Ser. II.*

Sun, Zi-Ping, Gerald Schubert, and Carol R. Stoker (May 1991). "Thermal and humidity winds in outer planet atmospheres". In: *Icarus* 91.1, pp. 154–160. DOI: 10.1016/0019-1035(91)90134-F.

Sun, Xiaoming and Ana P Barros (2010). "An evaluation of the statistics of rainfall extremes in rain gauge observations, and satellite-based and reanalysis products using universal multifractals". In: *Journal of Hydrometeorology* 11.2, pp. 388–404. DOI: 10.1175/2009JHM1142.1.

Sun, Ying, Susan Solomon, et al. (2006). "How often does it rain?" In: *Journal of climate* 19.6, pp. 916–934.

Sundqvist, Hilding, Erik Berge, and Jón Egill Kristjánsson (1989). "Condensation and cloud parameterization studies with a mesoscale numerical weather prediction model". In: *Monthly Weather Review* 117.8, pp. 1641–1657.

Tapiador, FJ, A Navarro, et al. (2017). "Global precipitation measurements for validating climate models". In: *Atmospheric Research* 197, pp. 1–20.

Tapiador, Francisco J, Francis J Turk, et al. (2012). "Global precipitation measurement: Methods, datasets and applications". In: *Atmospheric Research* 104, pp. 70–97. DOI: 10.1016/j.atmosres.2011.10.021.

The Astropy Collaboration et al. (Sept. 2018). "The Astropy Project: Building an Open-science Project and Status of the v2.0 Core Package". In: *AJ* 156, 123, p. 123. DOI: 10.3847/1538-3881/aabc4f. arXiv: 1801.02634 [astro-ph.IM].

Thomas, Gary E and Knut Stamnes (2002). *Radiative transfer in the atmosphere and ocean*. Cambridge University Press.

Tice, Dane S. et al. (Apr. 2013). "Uranus' cloud particle properties and latitudinal methane variation from IRTF SpeX observations". In: *Icarus* 223.2, pp. 684–698. DOI: 10.1016/j.icarus.2013.01.006.

Timmermans, Ben et al. (2019). "An evaluation of the consistency of extremes in gridded precipitation data sets". In: *Climate dynamics* 52.11, pp. 6651–6670. DOI: 10.1007/s00382-018-4537-0.

Tollefson, J., I. d. Pater, et al. (Sept. 2018). "Vertical wind shear in Neptune's upper atmosphere explained with a modified thermal wind equation". In: *Icarus* 311, pp. 317–339. DOI: 10.1016/j.icarus.2018.04.009.

Tollefson, Joshua, Imke de Pater, et al. (June 2021). "Neptunes Spatial Brightness Temperature Variations from the VLA and ALMA". In: *PSJ* 2.3, 105, p. 105. DOI: 10.3847/PSJ/abf837. arXiv: 2104.06554 [astro-ph.EP].

Toreti, Andrea et al. (2013). "Projections of global changes in precipitation extremes from Coupled Model Intercomparison Project Phase 5 models". In: *Geophysical Research Letters* 40.18, pp. 4887–4892.

Torrence, Christopher and Gilbert P Compo (1998). "A practical guide to wavelet analysis". In: *Bulletin of the American Meteorological society* 79.1, pp. 61–78. DOI: 10.1175/1520-0477(1998)079<0061:APGTWA>2.0.CO;2.

Touma, Danielle et al. (2018). "Characterizing the spatial scales of extreme daily precipitation in the United States". In: *Journal of Climate* 31.19, pp. 8023–8037. DOI: 10.1175/JCLI-D-18-0019.1.

Trafton, L. M. (Feb. 1967). "Model atmospheres of the major planets". In: *ApJ* 147, pp. 765–781. DOI: 10.1086/149052.

Trenberth, Kevin E et al. (2003). "The changing character of precipitation". In: *Bulletin of the American Meteorological Society* 84.9, pp. 1205–1218.

Tyler, G. L., D. N. Sweetnam, J. D. Anderson, S. E. Borutzki, et al. (Dec. 1989). "Voyager radio science observations of Neptune and Triton". In: *Science* 246, pp. 1466–1473. DOI: 10.1126/science.246.4936.1466.

Tyler, G. L., D. N. Sweetnam, J. D. Anderson, J. K. Campbell, et al. (July 1986). "Voyager 2 radio science observations of the Uranian system Atmosphere, rings, and satellites". In: *Science* 233, pp. 79–84. DOI: 10.1126/science.233.4759.79.

Ullrich, Paul A, Dharshi Devendran, and Hans Johansen (2016). "Arbitrary-order conservative and consistent remapping and a theory of linear maps: Part II". In: *Monthly Weather Review* 144.4, pp. 1529–1549.

Ullrich, Paul A and Mark A Taylor (2015). "Arbitrary-order conservative and consistent remapping and a theory of linear maps: Part I". In: *Monthly Weather Review* 143.6, pp. 2419–2440.

Vallis, Geoffrey K (2019). *Essentials of atmospheric and oceanic dynamics*. Cambridge university press.

van Dokkum, P. G. (Nov. 2001). "Cosmic-Ray Rejection by Laplacian Edge Detection". In: *PASP* 113, pp. 1420–1427. DOI: 10.1086/323894. eprint: astro-ph/0108003.

Vogel, Elisabeth et al. (2019). "The effects of climate extremes on global agricultural yields". In: *Environmental Research Letters* 14.5, p. 054010. DOI: 10.1088/1748-9326/ab154b.

Wallace, John M and Peter V Hobbs (2006). *Atmospheric science: an introductory survey*. Vol. 92. Elsevier.

Wallace, L. (Sept. 1980). "The structure of the Uranus atmosphere". In: *Icarus* 43.3, pp. 231–259. DOI: 10.1016/0019-1035(80)90172-4.

— (Apr. 1983). "The seasonal variation of the thermal structure of the atmosphere of Uranus". In: *Icarus* 54.1, pp. 110–132. DOI: 10.1016/0019-1035(83)90073-8.

Walt, Stéfan van der et al. (June 2014). "scikit-image: image processing in Python". In: *PeerJ* 2, e453. ISSN: 2167-8359. DOI: 10.7717/peerj.453. URL: http://dx.doi.org/10.7717/peerj.453.

Weidenschilling, S. J. and J. S. Lewis (Dec. 1973). "Atmospheric and cloud structures of the Jovian planets". In: *Icarus* 20.4, pp. 465–476. DOI: 10.1016/0019-1035(73)90019-5.

Wheeler, M., G. N. Kiladis, and P. J. Webster (Mar. 2000). "Large-Scale Dynamical Fields Associated with Convectively Coupled Equatorial Waves." In: *Journal of Atmospheric Sciences* 57, pp. 613–640. DOI: 10.1175/1520-0469(2000)057<0613:LSDFAW>2.0.CO;2.

Wielicki, Bruce A et al. (1998). "Clouds and the Earth's Radiant Energy System (CERES): algorithm overview". In: *IEEE Transactions on Geoscience and Remote Sensing* 36.4, pp. 1127–1141.

Wilks, Daniel S and Robert L Wilby (1999). "The weather generation game: a review of stochastic weather models". In: *Progress in physical geography* 23.3, pp. 329–357.

Willie, Delbert et al. (2017). "Evaluation of multisensor quantitative precipitation estimation in Russian River basin". In: *Journal of Hydrologic Engineering* 22.5, E5016002. DOI: 10.1061/(ASCE)HE.1943-5584.0001422.

Wing, Allison A et al. (2017). "Convective self-aggregation in numerical simulations: A review". In: *Shallow clouds, water vapor, circulation, and climate sensitivity*, pp. 1–25.

Wong, M. H., J. Tollefson, et al. (Mar. 2018). "A New Dark Vortex on Neptune". In: *AJ* 155, 117, p. 117. DOI: 10.3847/1538-3881/aaa6d6.

Wong, Michael H., Jonathan I. Lunine, et al. (2008). "Oxygen and Other Volatiles in the Giant Planets and their Satellites". In: *Reviews in Mineralogy and Geochemistry* 68.1, p. 219. DOI: 10.2138/rmg.2008.68.10. eprint: /gsw/content_public/journal/rimg/68/1/10.2138_rmg.2008.68.10/3/219_wong_etal.pdf. URL: http://dx.doi.org/10.2138/rmg.2008.68.10.

Yan, Hongxiang et al. (2018). "Next-generation intensity-duration-frequency curves for hydrologic design in snow-dominated environments". In: *Water Resources Research* 54.2, pp. 1093–1108.

Young, C Bryan, A Allen Bradley, et al. (2000). "Evaluating NEXRAD multisensor precipitation estimates for operational hydrologic forecasting". In: *Journal of Hydrometeorology* 1.3, pp. 241–254. DOI: 10.1175/1525-7541(2000)001<0241:ENMPEF>2.0.CO;2.

Young, Roland M. B., Peter L. Read, and Yixiong Wang (July 2019a). "Simulating Jupiter's weather layer. Part I: Jet spin-up in a dry atmosphere". In: *Icarus* 326, pp. 225–252. DOI: 10.1016/j.icarus.2018.12.005.

— (July 2019b). "Simulating Jupiter's weather layer. Part II: Passive ammonia and water cycles". In: *Icarus* 326, pp. 253–268. DOI: 10.1016/j.icarus.2018.12.002.

Zhang, Z. et al. (Jan. 2019). "VLA multi-wavelength microwave observations of Saturn's C and B rings". In: *Icarus* 317, pp. 518–548. DOI: 10.1016/j.icarus.2018.08.014.

Zhu, Yong and Reginald E Newell (1998). "A proposed algorithm for moisture fluxes from atmospheric rivers". In: *Monthly weather review* 126.3, pp. 725–735.